

ABSTRACT

CAKMAK, ENES. Dielectric and Electromechanical Properties of Polyurethane and Polydimethylsiloxane Blends and Nanocomposites. (Under the direction of Dr. Tushar K. Ghosh.)

Conventional means of converting electrical energy to mechanical work are generally considered too noisy and bulky for many contemporary technologies such as microrobotic, microfluidic, and haptic devices. Dielectric electroactive polymers (D-EAPs) constitute a growing class of electroactive polymers (EAP) that are capable of producing mechanical work induced by an applied electric field. D-EAPs are considered remarkably efficient and well suited for a wide range of applications, including ocean-wave energy harvesters and prosthetic devices. However, the real-world application of D-EAPs is very limited due to a number of factors, one of which is the difficulty of producing high actuation strains at acceptably low electric fields.

D-EAPs are elastomeric polymers and produce large strain response induced by external electric field. The electromechanical properties of D-EAPs depend on the dielectric properties and mechanical properties of the D-EAP. In terms of dielectric behavior, these actuators require a high dielectric constant, low dielectric loss, and high dielectric strength to produce an improved actuation response. In addition to their dielectric properties, the mechanical properties of D-EAPs, such as elastic moduli and hysteresis, are also of importance. Therefore, material properties are a key feature of D-EAP technology.

DE actuator materials reported in the literature cover many types of elastomers and their composites formed with dielectric fillers. Along with polymeric matrix materials, various ceramic, metal, and organic fillers have been employed in enhancing dielectric behavior of DEs.

This work describes an effort to characterize elastomer blends and composites of different matrix and dielectric polymer fillers according to their dielectric, mechanical, and electromechanical responses. This dissertation focuses on the development and characterization of polymer-polymer blends and composites from a high-k polyurethane (PU) and polydimethylsiloxane (PDMS) elastomers. Two different routes were followed with respect to elastomer processing: The first is a simple solution blending of the two types of elastomers, and the second is based on preparation of composites from PU nanofiber webs and PDMS elastomer. Both the blends and the nanofiber web composites showed improved dielectric and actuation characteristics.

© Copyright 2014 Enes Cakmak

All Rights Reserved

Dielectric and Electromechanical Properties of Polyurethane and Polydimethylsiloxane
Blends and their Nanocomposites

by
Enes Cakmak

A dissertation submitted to the Graduate Faculty of
North Carolina State University
in partial fulfillment of the
requirements for the degree of
Doctor of Philosophy

Fiber & Polymer Science

Raleigh, North Carolina

2014

APPROVED BY:

Dr. Tushar K. Ghosh
Committee Chair

Dr. Richard J. Spontak

Dr. Stephen Michielsen

Dr. Joseph Tracy

DEDICATION

To Mom and Dad,

It's impossible to thank them adequately for everything they have done.

BIOGRAPHY

Enes Cakmak is a Ph.D. student in the Fiber and Polymer Science Department at North Carolina State University. He received his B.S. and master's degree in Textile Engineering in 2003 and 2006, respectively, both from Süleyman Demirel University, Turkey. He joined Süleyman Demirel University as a research assistant in 2005 and worked on applications of new computer software techniques for weaving. He was awarded the Turkish Higher Education Council Scholarship for his Ph.D. studies in the U.S. and joined North Carolina State University to pursue his Ph.D. in Fiber and Polymer Science with a minor in Materials Science and Engineering in 2009.

ACKNOWLEDGMENTS

First and foremost, I sincerely thank Professor Tushar K. Ghosh for his patience and direction during my doctoral program at North Carolina State University. He not only provided the necessary guidance but also encouraged an unrestrained approach to research that fostered an extremely creative environment, which allowed me to expand my knowledge in many areas of polymer science.

I would also like to sincerely thank the members of my committee, Dr. Rich Spontak, Dr Stephen Michielsens, and Dr. Joseph Tracy. Their knowledge and experience in this field were essential in completing this project.

I thank to Dr. Julie Willoughby for her support and my colleagues Syamal, Ali, Krishna, Mehmet and Xiaomeng for their helpful comments on my Ph.D. thesis.

I would like to acknowledge the financial support I've received from the Turkish government and Süleyman Demirel University. I would especially like to thank the academic and administrative staff of Süleyman Demirel University for their endorsements in all stages of my doctoral studies and the Textile Engineering department staff for making necessary and felicitous provisions for my career.

Finally, I am grateful to my wife, Yasemin, for her generous support; my son, Kerem, for his cheery wave; and my parents and parents-in-law for their extensive support. Without their sacrifice, this work would have never have been possible.

TABLE OF CONTENTS

LIST OF TABLES	ix
LIST OF FIGURES	x
CHAPTER 1 Introduction	1
1.1 References	4
CHAPTER 2 Electroactive Polymers and Dielectric Elastomers	8
Abstract.....	8
2.1 Introduction.....	8
2.1.1 Ionic EAPs	11
2.1.2 Electronic EAPs.....	16
2.2 Dielectric Elastomers	21
2.2.1 Actuation Mechanism of D-EAPs	22
2.2.2 DE Materials	25
2.2.3 D-EAP Electrodes.....	30
2.2.4 Electromechanical Instability of D-EAPs.....	32
2.2.5 The Effect of Prestrain on D-EAPs	32
2.2.6 Response Time of D-EAPs	36
2.2.7 DE-based Energy Harvesting	37
2.3 Summary.....	38
2.4 References.....	38
CHAPTER 3 Dielectric Composites.....	52
Abstract.....	52
3.1 Dielectric Properties of Polymers	52
3.1.1 Dielectric Constant and Polarization	53
3.1.2 Dielectric Loss	58
3.1.3 Dielectric Spectroscopy of Polymers.....	60
3.1.4 Dielectric Breakdown	62
3.1.5 Charge Transport in Polymers and Nanocomposites.....	65

3.2 Dielectric Constant Enhancement	69
3.2.1 Interfacial Polarization.....	70
3.2.2 Coulomb Blockade (CB) Effect of Metal Nanoparticles.....	72
3.3 Dielectric Polymer Nanocomposites	73
3.3.1 Polymer Nanocomposites	74
3.3.2 Ferroelectric Ceramic/Polymer Composites.....	75
3.3.3 Metal Filler-Polymer Composites.....	82
3.3.4 Organic Filler-Polymer Composites	89
3.4 High-Dielectric Constant Elastomer Composites	94
3.4.1 Ceramic Fillers.....	94
3.4.2 All-Organic Composites	96
3.4.3 Polymer Synthesis for Dielectric Elastomers	102
3.5 Dielectric Mixing Theories	103
3.6 Concluding Remarks	108
3.7 References	110
CHAPTER 4 Synthesis and Phase Behavior of PDMS/PU Blends	126
Abstract.....	126
4.1 Introduction.....	126
4.2 Materials and Experimental Methods	136
4.2.1 Materials	136
4.2.2 Polymer Blend Preparation.....	142
4.2.3 Compatibility Estimation.....	144
4.2.4 Dynamic Mechanical Property Characterization.....	145
4.2.5 Differential Scanning Calorimeter (DSC) Analysis	146
4.2.6 Fourier-Transform Infrared Spectroscopy (FTIR) Analysis.....	147
4.2.7 Morphological Property Characterization	147
4.3 Results	148
4.3.1 Compatibility Estimation.....	148
4.3.2 Dynamic Mechanical Analysis (DMA)	149

4.3.3 Differential Scanning Calorimetry (DSC) Analysis	156
4.3.4 FTIR Analysis.....	161
4.3.5 Morphological Characterization	166
4.3.6 Dielectric Characterization	171
4.3.7 Evaluation of Dielectric Properties.....	174
4.4 Conclusions.....	175
4.5 References.....	176
CHAPTER 5 Electromechanical Response of Blends of PU and PDMS.....	189
Abstract.....	189
5.1 Introduction.....	190
5.2 Theoretical Background.....	194
5.3 Materials and Methods.....	197
5.3.1 Materials	197
5.3.2 Blend Preparation	199
5.3.3 Dielectric Characterization	200
5.3.4 Mechanical Characterization	201
5.3.5 Electromechanical Characterization	201
5.4 Results and Discussion.....	202
5.4.1 Mechanical Properties	202
5.4.2 Electromechanical Properties	207
5.4.3 Actuator Performance.....	215
5.5 Conclusions.....	218
5.6 References.....	219
CHAPTER 6 Electromechanical Response of PU-PDMS Composite Films.....	227
Abstract.....	227
6.1 Introduction.....	227
6.2 Materials and Methods.....	231
6.2.1 Materials	231
6.2.2 Composite Preparation.....	233

6.1.1 Dielectric Characterization	235
6.2.3 Mechanical Characterization	236
6.2.4 Electromechanical Characterization	236
6.2.5 Morphological Characterization	237
6.3 Results and Discussion	237
6.3.1 Morphology	238
6.3.2 Dielectric Properties	238
6.3.3 Mechanical Properties	240
6.3.4 Electromechanical Properties	242
6.4 Conclusions	249
6.5 References	250
CHAPTER 7 Summary and Future Work	255
7.1 Summary	255
7.2 Future Work	256
7.3 References	257

LIST OF TABLES

Table 2.1 Comparison of alloy, ceramic, and polymer actuators.	10
Table 2.2 Comparison of ferroelectric actuator performance.	19
Table 2.3 Actuation response of common dielectric elastomers.	29
Table 4.1 PDMS matrix elastomer composition comparison of types I and type II for blend materials formulation.	140
Table 4.2 E_{coh} (internal energy) and V_g (internal molar volume) of constitutes of PU and PDMS.	148
Table 4.3 Glass transition temperature (T_g) of polymer blends and their pure polymer constitutes.	155
Table 4.4 Crystallinity and crystallinity peak temperatures of elastomers with different PDMS/PU ratios in casting solutions.	158
Table 4.5 FTIR assignments of PU and PDMS polymers.	162
Table 6.1 Mechanical properties of the neat and composite film samples.	241
Table 6.2 Mechanical properties of the neat and composite film samples.	249

LIST OF FIGURES

Figure 2.1 Multi-field coupling of smart materials/structures	9
Figure 2.2 Actuation mechanism of an IPMC.	13
Figure 2.3 Example of actuation displacement of an IPMC over time.....	13
Figure 2.4 Polyaniline, a conjugated polymer: leucoemeraldine ($y = 1$), emeraldine ($y = 0.5$), and pernigraniline ($y = 0$).	14
Figure 2.5 CNT-bending actuator	15
Figure 2.6 PVDF. Left: tg+tg-; right: all trans.....	17
Figure 2.7 The reorientation of liquid crystals bonded to an elastomer network.	21
Figure 2.8 Schematic representation of D-EAPs' actuation mechanism.....	22
Figure 2.9 Effects of hardener amount on actuation strain for DC3481 silicone elastomer... 28	
Figure 2.10 A circular actuator with fixture. The elastomer is attached to a circular fixture after a nominal prestrain application.....	33
Figure 2.11 Mechanical effects of prestrain on actuation performance: a) mechanical deformation, b) electrical deformation, c) electrical deformation with prestrain.	34
Figure 2.12 Actuation behavior of PDMS elastomers under various strains (a) Strain vs electric field for PDMS actuators. The dotted line drawn perpendicular to $40\text{V}/\mu\text{m}$ is guide for eye. The numbers at the tops of the plots show the level of prestrain. (b) Effect of prestrain levels on electrical breakdown (PDMS elastomer). Strain-prestrain plot was plotted from reference.	35
Figure 2.13 Relative actuation performance versus electrical field for various prestrained PDMS films.	36

Figure 2.14 Speed response plots of a) PDMS, b) acrylic elastomer actuators.	37
Figure 3.1 Schematic representation of the five types of polarizations: a) $P_{electronic}$, b) P_{ionic} , c) $P_{molecular}$, d) $P_{interfacial}$, e) $P_{hyperelectronic}$	55
Figure 3.2 Dielectric behavior versus frequency.	58
Figure 3.3 Dielectric loss spectra of polymethylacrilate.	61
Figure 3.4 A wide variety of charge transports in an insulator.....	67
Figure 3.5 a) Schematic representation of p - and n -type regions of an insulating polymer; b) the accumulation of heterocharges and homocharges over an insulator in the first 10 sec of voltage application under various electrical fields. Right: cathode; left: anode.	68
Figure 3.6 Stern diffuse double layer produced by nanoparticles on a charged surface within a dielectric composite.	69
Figure 3.7 Effect of particle interface size (in nm) on intensity of physical properties.	70
Figure 3.8 Increase of interface volume (a) Relationship between filler diameter versus interface volume, representation of relationship given in plot. (b) In image A is filler B is matrix'	71
Figure 3.9 The O'Konski model assumes a conductive interface layer on a particle: (a) $E = 0$, (b) $E \neq 0$	72
Figure 3.10 a) Schematic representation of a Coulomb blockade; b) model of the structure as two capacitors in a series; c) capacitance performance versus voltage results computed theoretically.....	73
Figure 3.11 TEM image of BaTiO ₃ /PI composite film made through in situ polymerization with BaTiO ₃	79
Figure 3.12 Electrical field alignment of fillers in a polymer composite.	81

Figure 3.13 Dielectric behavior of silver (20 nm) epoxy nanocomposites.....	85
Figure 3.14 Curing of composite samples under external magnetic and electrical fields.	87
Figure 3.15 Effect of Ni-C core-shell particle weight fraction and external fields on dielectric constant and resistivity.....	88
Figure 3.16 Surface conductivity of PDPH polymer: (a) V-I characteristics; (b) sample with two polymer layers (1 st line in plot (a)); (c) sample with one polymer layer, where the electrodes are on the surface of the polymer (2 nd in the plot (a)); (d) sample with one polymer layer, where the electrodes are under the polymer film (3 rd in the plot (a)).	93
Figure 3.17 Actuation performances of NBR elastomer composite with the addition of varying a) DOP, b) TiO ₂ concentrations:	96
Figure 3.18 Dielectric constant vs. actuation strain for CPO-PDMS elastomer composites ¹⁰⁹ . a) Dielectric constant-CuPc weight concentration- plot b) Strain-electric field plot.....	97
Figure 3.19 Schematic of oligomer copper-phthalocyanine (CuPc).....	98
Figure 3.20 Actuation response of a) thick, b) thin samples of polyurethane-carbon black elastomer composites	99
Figure 3.21 Representation of periodic layered-design EAPs for FE analysis.....	102
Figure 3.22 The geometry for modelling core-shell filled composites for their dielectric behavior: (a) particle, (b) interphase, and (c) matrix parts in dielectric composites.	107
Figure 4.1 Chemical Formulation PDMS elastomer networks, Type I (a,b,c) and Type II (d,e,f). Polymer (a) is a hydride functional PDMS fluid, crosslinker (b) is a multi-functional crosslinker, (c) is a PDMS elastomer network, (d) is hydroxyl functional PDMS fluid, crosslinker (e) is a multi-functional crosslinker, and (f) is the PDMS elastomer network. The catalyst is tin, and the reaction takes place in a humid environment.....	141

Figure 4.2 Possible routes of interaction between PDMS and PU elastomers: (a) schematic of network formation of Type I elastomer; (b) schematic of network formation of Type II elastomer; (c) chemical structure of 3-isocyanatopropyltriethoxy-silane crosslinker; (d) chemical structure of polyurethane elastomer with end groups shaded. 142

Figure 4.3 Schematic of blend elastomer preparation: (a) mixing PU/THF and PDMS/THF mixture and addition of the PDMS crosslinking agent to the mixture for film formation, (b) use of planetary mixer for overall mixing and curing film preparation..... 144

Figure 4.4 DMFA Analysis of Type I PDMS and Type II PDMS and blend: (a) Storage modulus and loss modulus with varying frequency of Type I elastomers, (b) $\tan(\delta)$ of blends for varying frequency of Type I elastomers, (c) storage modulus and loss modulus with varying frequency for Type II elastomers, (d) $\tan(\delta)$ of blends for varying frequency Type II elastomers. Symbols are as follows: (●) represents pure PDMS; (■) represents 10/90 PU/PDMS blends; and (◆) represents 20/80 PU/PDMS blends. Open symbols correspond to the loss modulus of the samples. 150

Figure 4.5 DMTA Analysis of homopolymers of PU, Type I PDMS, and Type II PDMS. Storage modulus and $\tan(\delta)$ were plotted from -130 °C to 200 °C. PU sample breaks at ca. 120 °C. Red line (—) represents the Type I PDMS; blue line (—) represents the Type II PDMS; green line (—) represents PU elastomer. 151

Figure 4.6 DMA Analysis of Type I elastomer and its blends. Red line (—) represents pure PDMS; blue line (—) represents the 10 PU wt% concentration blend sample; green line (—) represents the 20 PU wt% concentration blend sample: (a) storage modulus and loss modulus with varying temperature from -130 °C to 200 °C for PDMS elastomer Type I and blends with 10 and 20 wt% PU concentrations; (b) storage modulus and loss modulus with varying temperature from -130 °C to 200 °C for PDMS elastomer Type II and blends with 10 and 20 wt% PU concentrations..... 152

Figure 4.7 DSC Analysis of Types I and II elastomer and their blends. Red (—) represents pure PDMS; blue line (—) represents PU polymer; green line (—) represents 20 PU wt% concentration blend sample; and black line (—) represents 40 PU wt% concentration blend sample: (a) storage modulus and loss modulus with varying temperature from -120 °C to 200 °C for PDMS elastomer Type I and its blends with 20 wt% and 40 wt% concentrations; (b) storage modulus and loss modulus with varying temperature from -120 °C to 200 °C for PDMS elastomer Type II and its blends with 20 and 40 wt% concentrations..... 157

Figure 4.8 FTIR Spectrum for Type I PDMS, PU, and its blends. Red (—) represents pure PDMS; blue (—) represents pure PU; green (—) represents 20 PU wt% concentration Type I blend..... 163

Figure 4.9 FTIR Spectrum for Type II PDMS, PU, and its blends: red (—) represents pure PDMS; blue (—) represents pure PU; green (—) represents 20 PU wt% concentration Type II blend..... 164

Figure 4.10 Morphological views of PU/PDMS blend elastomers with (a) representative 10% PU filler concentration and (b) spherical PU distributed throughout the PDMS matrix. (image taken from 10 wt% PU / Type I PDMS blends.) 167

Figure 4.11 Representative morphological electron microscope images of PU/PDMS blend elastomers with (a) a film cross-section of 2% PU filler concentration; (b) spherical 10% PU fillers distributed throughout the PDMS matrix; (c) spherical 20% PU fillers distributed throughout the PDMS matrix; (d) spherical and ovoid 40% PU fillers distributed throughout the PDMS matrix. 168

Figure 4.12 Morphological cross-sections of blend Type I elastomers. Images (a) and (b) show the dispersion of spherical PU elastomer fillers throughout the PDMS matrix; this points to the separation of spherical PU fillers from the PDMS matrix. These images were taken after a fracture of blends occurred in liquid nitrogen. The interphases between the species are pointed out in the images above. 169

Figure 4.13 Morphology of blend elastomers with 2 wt% PU concentration: (a) cross-sectional view of Type II elastomer blends and (b) spherical PU fillers diffused throughout PDMS..... 170

Figure 4.14 Analysis of morphological cross-sectional images of blends for both Type I and Type II elastomers. SEM images were analyzed for filler dimensions: (a) Type I distribution of size of filler diameter blends and (b) Type II distribution of approximate filler size diameter blends. 171

Figure 4.15 The dielectric constant (effective permittivity, ϵ') as a function of frequency for Type I blends. (\blacktriangledown)PU, (Δ) 40 wt% PU, (\diamond) 20 wt% PU, (\square) 10 wt% PU, (\circ) 2 wt% PU, (\blacktriangle)PDMS. 172

Figure 4.16 Dielectric loss, ($\tan \Delta$) as a function of frequency for the Type II blends. (\blacktriangledown)PU, (Δ) 40 wt% PU, (\diamond) 20 wt% PU, (\square) 10 wt% PU, (\circ) 2 wt% PU, (\blacktriangle)PDMS..... 173

Figure 4.17 Effective permittivity as a function of weight fraction of polyurethane (a) at a low-frequency measurement (100 Hz) and (b) at a high-frequency measurement (10^6 Hz). The dashed lines represent the theoretically predicted results based on weight concentration. Dashed lines represent (—) series, (---) logarithmic, (-·-) parallel, and (- - -) Maxwell Garnet theoretical prediction of mixing for dielectric constant, in order from bottom to top. Data connected with dots serve guide to eye..... 174

Figure 5.1 A circular actuator preparation from elastomers: (a) application of prestrain to a DE, (b) operation principle for D-EAP actuators, (c) fractured cross-section electron microscope image of a 5 wt% composition blend elastomer. PU fillers are 1-2 μm in size and spherical in shape..... 193

Figure 5.2 Scheme of blend elastomer preparation. Mixing of the PU/THF and PDMS/THF mixtures and addition of the PDMS crosslinking agent to the mixture for film formation.. 200

Figure 5.3 Mechanical properties of PU and PDMS samples: Stress-strain curve for pristine PU and PDMS elastomers: The red dot (●) Type I PDMS elastomer; blue square (■) Type II PDMS elastomer; and green plus (+) represents PU elastomer. 203

Figure 5.4 Mechanical properties of blends. (a) Young’s modulus (filled symbols) of the blend elastomer versus PU weight concentration. The open red circles (●) represent the Type I blend elastomers’ tensile modulus; the filled blue squares (■) represent the Type II blend elastomers’ tensile modulus. (b) Ultimate strain (open symbols) values for blend elastomers. The open red circles (○) represent the Type I blend elastomers’ tensile strain; the open blue squares (□) represent the Type II blend elastomers’ tensile strain. 204

Figure 5.5 The dependence of actuation strain on electric field or the the Type I blend elastomers for various filler concentrations (wt%): (a) actuation strain versus electrical field for films of Type I PDMS (▲), Type I blends of 2 wt% PU (□) , 10 wt% (△), 20 wt% (◇), 40 wt% PU compositions (○). Type I PDMS (▲) reached to a maximum actuation strain of ~25 at ~180 V/μm, which was excluded from the plot. Lines are guides for eye. (b) Electromechanical breakdown field versus PU weight percentage for Type I blends. All lines serve as guide for eye..... 207

Figure 5.6 Dielectric strength of the Type I blend elastomers and the Type I PDMS elastomer. The dielectric breakdown electrical fields were plotted from electromechanical actuation tests of the elastomers. The dashed lines serve to connect data points. (b) Dielectric constant of blends versus PU weight concentration. Dashed lines represent (—) series, (---) logarithmic, (-.-) parallel, and (---) Maxwell Garnet theoretical prediction of mixing for dielectric constant, in order from bottom to top. 209

Figure 5.7 The dependence of actuation strain for the Type II blend elastomers at various filler concentrations: (a) actuation strain versus electrical field for concentrations (Pure Type II, 20 wt% and 40 wt%) (b) electromechanical breakdown field versus PU weight percentage for the Type II blends for 50 V/μm..... 210

Figure 5.8 Actuation strain versus electrical field for (a) Type I and (b) Type II blends. (a) Type I PDMS (\blacktriangle), (\square) Type I blends of 2 wt% PU, (\blacktriangle) 10 wt%, (\blacklozenge) 20 wt%, (\odot) 40 wt% PU concentrations. (b) Pure Type II PDMS, 20 wt% and 40 wt% PU concentrations. 211

Figure 5.9 (a) Dielectric strength of the blends and the PDMS elastomer. The dielectric breakdown electrical fields were plotted from the ultimate electromechanical actuations of the elastomers. Red open dots (\circ) represent the Type I blends' tensile strains; blue open squares (\square) represent the Type II blends' tensile strains. (b) Young's modulus of the blends elastomer versus PU weight concentration. Red filled dots (\bullet) represent the Type I blends' tensile modulus; blue filled squares (\blacksquare) represent the Type II blends' tensile modulus. 212

Figure 5.10 Dielectric strength of the blend elastomers and the PDMS elastomer: (a) dielectric constant versus PU weight percentage in the Type II blends and b) actuation strain at $60 \text{ V}/\mu\text{m}$ as a function of PU weight concentration. Breakdown electrical fields were plotted based on electromechanical actuation tests of elastomers. The solid and dashed lines serve to connect..... 213

Figure 5.11 The actuator performance of blends: (a) electromechanical coupling efficiency (K^2), (b) compressive (Maxwell) stress, (c) electromechanical energy density given by $-P_{\text{Maxwell}}(1+S_z)/2$ on a unit volume basis, and (d) elastic energy density (E_L) displayed in terms of PU weight concentration. In all cases, the magnitude of the electric field is $60 \text{ V}/\mu\text{m}$. The solid and dashed lines are linear fits to the data; these serve as guides for the eye..... 215

Figure 6.1 (a) A dielectric elastomer actuator and its actuation mechanism ; (b) DE circular actuator configuration. 231

Figure 6.2 Analysis of an electrospun PU fiber web: (a) an SEM image of fibers (the nanofibers after mixing in to hexane solvent is shown in the inset image and (b) analysis of fiber diameter distribution. Fibers had an average diameter of 125 nm. 232

Figure 6.3 Preparation steps of the nanofiber composite elastomer films. 234

Figure 6.4 Preparation of nanofiber composite: (a) electrospinning of PU, (b) infusion of PDMS into PU fiber webs, (c) 3D schematic of final composite structure, and (d) cross-section image of elastomer composite; nanofibers and part of fibers are an apparent in the image..... 235

Figure 6.5 Cross-sectional view of the PU-PDMS nanofiber composite: (a) low-magnification view of a composite film’s cross-section and (b) high-magnification image of composite films. Inset image shows a single PU electrospun fiber edge. 238

Figure 6.6 Dielectric properties of fiber-infused composites: (a) effective permittivity as a function of frequency; (b) dielectric loss factor, $\tan(\Delta)$, as a function of PU fibers..... 239

Figure 6.7 Actuation strain versus electric field for (a) Type I and (b) Type II PU/PDMS composite films. 243

Figure 6.8 Plots of actuator performance of composites: (a) electromechanical coupling efficiency (K^2); (b) compressive (Maxwell) stress; (c) electromechanical energy density, as given by $[-PMaxwellsz^2]$ on a unit-volume basis; (d) electric energy density, E_L , $[-Ysz - \ln 1 + sz]$, displayed in terms of PU weight concentration. For all plots, the magnitude of the electric field was $50 \text{ V}/\mu\text{m}$. The lines serve as visual guides to eye..... 245

CHAPTER 1 Introduction

Electroactive polymers (EAPs) change their shape under an applied electric field. Dielectric elastomers (DEs) form a class of EAPs that offer highly promising electromechanical characteristics and are particularly suitable for many of today's and future technologies. Dielectric electroactive polymer (D-EAP) actuators are known for their unique properties of large actuation stress (up to 7Pa)¹, large actuation strain (>200%)²⁻⁸, high specific energy density (~0.15 J/g)¹, high coupling efficiency, fast response time (<3 sec)⁶, and reliable actuation control^{9,10}. They are also lightweight, flexible, easy to process, and inexpensive.

DEs have been used to create low cost, lightweight, and noiseless mechanisms in the emerging technologies of bio-inspired robots¹¹⁻¹³, prosthetic devices^{14,15}, adaptive structures¹⁶, electroactive fluid pumps^{17,18}, conformable skins, refreshable braille devices^{19,20}, autofocus lens positioners^{21,22}, speakers, shape and texture systems^{23,24}, active smart textiles¹⁵, sensors²⁵, and energy-harvesting systems²⁶⁻³⁶. The use of DEs in these diverse fields requires interdisciplinary expertise in chemistry, materials science, electronics, applied mechanics, and computer science.

Actuators made of dielectric elastomers are basically parallel plate capacitors with a passive elastomer film separating two compliant electrodes. The electromechanical response of a the resulting D-EAP actuator depends largely on both its dielectric and mechanical properties. The dielectric constant of an elastomer affects the charge storage properties of the actuator and, as a result, the stress/strain generated by the material. The dielectric elastomer's mechanical properties, such as stiffness, are particularly important in translating stress into

material strain and therefore are a key factor in impedance matching of the actuator and the system.

Ideal DE materials should have the mechanical properties of elastomers along with a high dielectric constant and low dielectric loss. They should have high energy density and dielectric breakdown strength. However, most common elastomers (e.g., silicone and polyurethane) have relatively low dielectric constant, so ceramics, metals, and organic materials with significantly higher dielectric properties have been introduced to a variety of polymer matrices to fabricate composites with enhanced electrical and mechanical properties. In general, the results reported in the literature paint a mixed picture. In most cases, significant improvement in the elastomer's dielectric constant was accompanied by unacceptable increase in dielectric loss and/or in stiffness of the material.

Polymer-polymer blends and composite systems offer a promising route in the development of materials with improved dielectric behavior because of their ease of processing, low cost, low weight, and potentially better compatibility. In comparison with ceramic and metallic filled composites, polymer-polymer systems seem to offer a more attractive route for the development of D-EAP materials because of their potential compatibility in mechanical properties.

The work described in this thesis aims to develop a material with improved dielectric behavior as well as acceptable mechanical properties for use in dielectric elastomer actuator applications. The approach in this research includes the use of a relatively high-dielectric

constant polymer, polyurethane (PU), as a filler in the forms of blends and nanofibers in two types of polydimethylsiloxane (PDMS) matrix material.

This dissertation is organized such that each chapter represents a potential publication. All chapters, with the exceptions of 2-3 are written in the form of reviews or research articles. A short description of each follows;

Chapter 1. Introduces the thesis topic of elastomer blends and composites as dielectric elastomers.

Chapter 2. Includes a literature review on electroactive polymers, with particular emphasis on dielectric elastomers.

Chapter 3. Includes a literature review of dielectric materials and polymer composites, with particular focus on dielectric elastomer materials; also includes classification of these materials in terms of composite formation and application.

Chapter 4. Describes the synthesis and dielectric properties of the blends of polyurethane and polydimethylsiloxanes investigated in this research.

Chapter 5. Describes the electromechanical properties of the blends of polyurethane and polydimethylsiloxanes investigated in this research.

Chapter 6. Presents the results and a discussion of the fabrication and characterization of nanofiber-based elastomer composites formed from polyurethane nanofibers and polydimethylsiloxane elastomers.

Chapter 7. Summarizes the findings of this study.

1.1 References

1. Pelrine, R., Kornbluh, R., Pei, Q. & Joseph, J. High-speed electrically actuated elastomers with strain greater than 100%. *Science* **287**, 836–839 (2000).
2. Ma, W. & Cross, L. E. An experimental investigation of electromechanical response in a dielectric acrylic elastomer. *Appl. Phys. Mater. Sci. Process.* **78**, 1201–1204 (2004).
3. Carpi, F., Mazzoldi, A. & De Rossi, D. High-strain dielectric elastomer for actuation. in *Smart Struct. Mater. 2003 Electroact. Polym. Actuators Devices EAPAD* **5051**, 419–422 (2003).
4. Jordi, C., Schmidt, A., Kovacs, G., Michel, S. & Ermanni, P. Performance evaluation of cutting-edge dielectric elastomers for large-scale actuator applications. *Smart Mater. Struct.* **20**, 075003 (2011).
5. Goulbourne, N. C., Mockensturm, E. M. & Frecker, M. I. Electro-elastomers: Large deformation analysis of silicone membranes. *Int. J. Solids Struct.* **44**, 2609–2626 (2007).
6. Michel, S., Zhang, X. Q., Wissler, M., Löwe, C. & Kovacs, G. A comparison between silicone and acrylic elastomers as dielectric materials in electroactive polymer actuators. *Polym. Int.* **59**, 391–399 (2010).
7. O'Halloran, A., O'Malley, F. & McHugh, P. A review on dielectric elastomer actuators, technology, applications, and challenges. *J. Appl. Phys.* **104**, 071101–10 (2008).
8. Zhu, L. H., Zhu, X. L., E, S. J., Hui, A. F. & Cao, J. B. Influence of prestrain on output characteristic of dielectric elastomer film actuators. *Key Eng. Mater.* **455**, 81–86 (2010).

9. Shankar, R., Ghosh, T. K. & Spontak, R. J. Dielectric elastomers as next-generation polymeric actuators. *Soft Matter* **3**, 1116 (2007).
10. Stoyanov, H., Kollosche, M., Risse, S., McCarthy, D. N. & Kofod, G. Elastic block copolymer nanocomposites with controlled interfacial interactions for artificial muscles with direct voltage control. *Soft Matter* **7**, 194 (2011).
11. Anderson, I. A., Ieropoulos, I. A., McKay, T., O'Brien, B. & Melhuish, C. Power for robotic artificial muscles. *Mechatronics, IEEE/ASME Transactions on* **16**, 107–111 (2011).
12. Hyouk Ryeol Choi *et al.* Biomimetic soft actuator: design, modeling, control, and applications. *IEEE/ASME Transactions on Mechatronics* **10**, 581–593 (2005).
13. Taya, M. Bio-inspired design of intelligent materials. in *Smart Structures and Materials* **5051**, 54–65 (2003).
14. Biddiss, E. & Chau, T. Dielectric elastomers as actuators for upper limb prosthetics: Challenges and opportunities. *Med. Eng. Phys.* **30**, 403–418 (2008).
15. Carpi, F. & De Rossi, D. Electroactive polymer-based devices for e-textiles in biomedicine. *Inf. Technol. Biomed. IEEE Trans. On* **9**, 295–318 (2005).
16. Prahlad, H. *et al.* Programmable surface deformation: thickness-mode electroactive polymer actuators and their applications. in *Electroactive Polymer Actuators and Devices* **5759**, 102–113 (2005).
17. Arthur, G. G., McKeon, B. J., Dearing, S. S., Morrison, J. F. & Cui, Z. Manufacture of micro-sensors and actuators for flow control. *Microelectron. Eng.* **83**, 1205–1208 (2006).

18. Carpi, F., Menon, C. & De Rossi, D. Electroactive elastomeric actuator for all-polymer linear peristaltic pumps. *IEEE/ASME Trans. Mechatron.* **15**, 460–470 (2010).
19. Chakraborti, P. *et al.* A compact dielectric elastomer tubular actuator for refreshable Braille displays. *Sens. Actuators Phys.* **179**, 151–157 (2012).
20. Mazzone, A., Zhang, R. & Kunz, A. Novel Actuators for Haptic Displays Based on Electroactive Polymers. in *Proceedings of the ACM Symposium on Virtual Reality Software and Technology* 196–204 (ACM, 2003).
21. Choi, S. T., Lee, J. Y., Kwon, J. O., Lee, S. & Kim, W. Varifocal liquid-filled microlens operated by an electroactive polymer actuator. *Opt. Lett.* **36**, 1920–1922 (2011).
22. Shian, S., Diebold, R. M. & Clarke, D. R. Tunable lenses using transparent dielectric elastomer actuators. *Opt. Express* **21**, 8669–8676 (2013).
23. Ouyang, G., Wang, K., Henriksen, L., Akram, M. N. & Chen, X. Y. A novel tunable grating fabricated with viscoelastic polymer (PDMS) and conductive polymer (PEDOT). *Sens. Actuators Phys.* **158**, 313–319 (2010).
24. Ouyang, G. M., Wang, K. Y. & Chen, X. Y. Enhanced electro-mechanical performance of TiO₂ nano-particle modified polydimethylsiloxane (PDMS) as electroactive polymers. in *Solid-State Sensors* 614–617 (2011).
25. Toth, L. Design and development of dielectric elastomer transducers with dual actuation and sensory functionality. (University of Toronto, 2002).
26. Davies, D. K. Charge generation on dielectric surfaces. *J. Phys. Appl. Phys.* **2**, 1533–1537 (1969).

27. Lo, H. C., McKay, T., O'Brien, B. M., Calius, E. & Anderson, I. Circuit design considerations for regulating energy generated by dielectric elastomer generators. in *SPIE Proceedings* **7946**, 79760C–79760C–8 (2011).
28. Koh, S. J., Keplinger, C., Li, T., Bauer, S. & Suo, Z. Dielectric elastomer generators: How much energy can be converted? *Mechatron. IEEE/ASME Trans.* **16**, 33–41 (2011).
29. Jean-Mistral, C., Basrour, S. & Chaillout, J.-J. Dielectric polymer: scavenging energy from human motion. in *Electroactive Polymer Actuators and Devices* **6927**, 1–16 (SPIE, 2008).
30. Putson, C. *et al.* Effects of copper filler sizes on the dielectric properties and the energy harvesting capability of nonpercolated polyurethane composites. *J. Appl. Phys.* **109**, 024104 (2011).
31. Guyomar, D. *et al.* Electrostrictive energy conversion in polyurethane nanocomposites. *J. Appl. Phys.* **106**, 014910 (2009).
32. Beeby, S. P., Tudor, M. J. & White, N. M. Energy harvesting vibration sources for microsystems applications. *Meas. Sci. Technol.* **17**, R175–R195 (2006).
33. Cao, J. *et al.* in *Advanced Electrical and Electronics Engineering* (ed. Lee, J.) 201–207 (Springer, 2011).
34. Ogden, R. & Steigmann, D. *Mechanics and electrodynamics of magneto-and electro-elastic materials.* **527** (Springer, 2011).
35. Kang, G., Kim, K.-S. & Kim, S. Note: Analysis of the efficiency of a dielectric elastomer generator for energy harvesting. *Rev. Sci. Instrum.* **82**, 046101 (2011).
36. McKay, T. G., O'Brien, B. M., Calius, E. P. & Anderson, I. A. Soft generators using dielectric elastomers. *Appl. Phys. Lett.* **98**, 142903 (2011).

CHAPTER 2 Electroactive Polymers and Dielectric Elastomers

Abstract

This literature review outlines the most current research on electroactive polymers (EAPs), a category of smart materials that exhibit physical changes when subjected to an electrical field, with particular focus on dielectric elastomer transducers (sensors, actuators, energy generators, etc.). The review begins with a general discussion of dielectric elastomer actuators and continues with a more detailed discussion of their mechanism of actuation and performance. The dielectric behavior of materials and polymers is discussed, with particular emphasis on dielectric composites.

2.1 Introduction

Electroactive materials constitute a class of “smart” materials—that possess one or more qualities that can be significantly altered by external stimuli. These include piezoelectrics, shape-memory materials, electro- and magneto-strictive materials, superconductors, pyroelectrics, photostriction-active materials, and photo-ferroelectrics. The idea of using smart materials as in situ sensors and actuators for a wide variety of engineering applications emerged in the mid-1980s. Figure 2.1 displays the multi-field stimuli and responses of these materials.

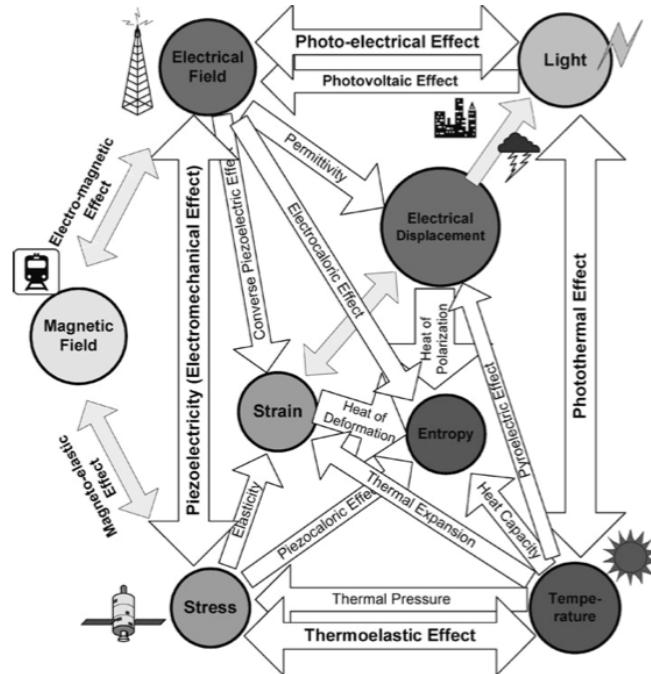


Figure 2.1 Multi-field coupling of smart materials/structures⁷.

An electroactive material responds to an external electrical stimulus with a change in a certain property in a reproducible and stable manner. This type of material, which is emerging as one of the largest and most fundamental subgroups of active materials, includes organic transistors, photovoltaic cells, and electroluminescent materials. In this review, as is widely accepted in the field, the broader term *electroactive material* is used to refer to materials that serve as electromechanical transducers and produce stress and strain as a result of electrical input. As defined here, electroactive materials therefore include shape-memory alloys, polymers, and some ceramics. Electroactive ceramics produce small strains (~1%) but have the advantage of high and precise stress generation¹⁻³. Shape-memory alloys are known for high stress, long response time, and hysteresis⁴⁻⁶. Electroactive polymers (EAPs) are

lightweight, relatively inexpensive, and mechanically robust, and they exhibit a rapid response time. The force generated by EAPs is less than that generated by ceramics and metal alloys, but EAPs are capable of producing larger displacements. A broad comparison of various electroactive materials is presented in Table 2.1.

Table 2.1 Comparison of alloy, ceramic, and polymer actuators⁷.

Property	EAC	SMA	EAP
Areal actuation strain (%)	0.1-3	< 8	> 200
Blocking force (MPa)	30-40	7000	1-3
Actuation speed (sec)	10 ⁻⁶ -1	1-100	10 ⁻⁶ -100
Mass density (g/cm ³)	6-85	5-6	0.9-2.5
Electrical field (V/μm)	50	n/a ^a	100-300
Power consumption (W)	1	1	10 ⁻³
Material property	Fragile	Elastic	Elastic, resilient

^a SMAs are not field-driven actuators

The use of polymeric materials has increased in almost every part of our lives due to their remarkable properties (i.e., low weight, low cost, and ease of processing) and other benefits. Polymer composites have had applications in many areas of engineering as replacements for

metals, ceramics, and glasses. One particular emerging field that stands to benefit greatly from polymeric composites is that of electroactive actuator materials.

The actuation mechanism of EAPs relies on electrostatic forces, electrostriction, ion insertion, and molecular conformational changes. EAPs are broadly classified into one of two different groups—ionic and electronic—according to their actuation mechanism.

2.1.1 Ionic EAPs

Actuation of the ionic type of EAP occurs through ion displacement within the polymer upon application of electrical bias. The actuation rate of ionic EAPs is relatively slow, but compared to the electronic types of electroactive polymers, these usually require low voltage to operate (or to hold the displacement). However, constant energy must be applied to ionic EAPs to keep the system in an active state. Ionic EAPs include ionic polymer gels, ionic polymer-metal composites (IPMCs), conductive polymers, and carbon nanotubes.

2.1.1.1 Ionic Polymer Gels

Ionic polymer gels, a class of ionic EAPs, carry ionic groups in the main or side chain, and these ionic groups are counterbalanced by oppositely charged ions. These ions can diffuse in and out of the polymer chains under an electrical field, with the formation of an alkaline environment on the cathode side and an acidic environment on the anode side. The change of the gel's pH results in an ionic repulsion of like charges and serves to swell the polymer chains. This chain and gel swelling is the actuation mechanism in this type of actuator. Common polymers in this group include polyacrylic acid, polymethacrylic acid, polystyrene sulfonic acid, and polyvinylphosphonic acid^{7,8}.

2.1.1.2 Ionic Polymer-Metal Composites

Ionic polymer-metal composites (IPMCs) are bending actuators made of ionic polymers. They consist of a perfluorinated ionomer polymer membrane and metal electrodes. The polymer membrane is a solvent-swollen material, and the electrodes have a coating of metal, such as Platinum. The membrane materials for IPMCs are often Nafion (sulfonated tetrafluoroethylene-based fluoropolymer-copolymer) and Flemion (perfluorocarboxylate). IPMCs require an ionic liquid or wet operating condition. Ionic liquid tetra-n-butylammonium (TBA⁺) is also used to prepare IPMCs; Na⁺, K⁺, Li⁺, and Cs⁺ are typical cations for the water solution.

When a cantilever strip of a solvated Nafion-based IPMC sample is subjected to an electric potential of several volts (1-3 V) applied across its faces, it bends toward the anode with stresses of 30 MPa and strains of 3%. This operation is described in Figure 2.2. Under the same electrical potential, a backward relaxation is observed in these materials after they reach maximum strain. The actuation and backward relaxation response are plotted in Figure 2.3.

The mechanical bending of the IPMC composite strip produces charge storage that is opposite to the charge generation mechanism of fuel cells⁹. Typical actuation strains of ~10% have been reported under an average applied voltage of 5 V¹⁰. IPMCs have been proposed for use in biomedical, aerospace, and oceanic robotics applications. They can serve as vibration-sensing transducers, motion sensors, tactile sensors, micro pumps, fuel cells, and

hydrogen sensors^{11,12}. IPMCs also display self-sensing of actuation achieved by evaluating the electrical potential during actuation^{13,14}.

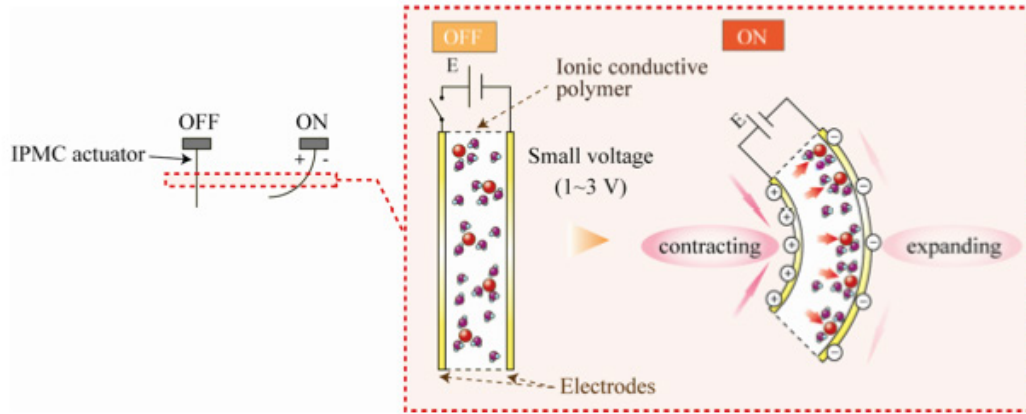


Figure 2.2 Actuation mechanism of an IPMC¹³.

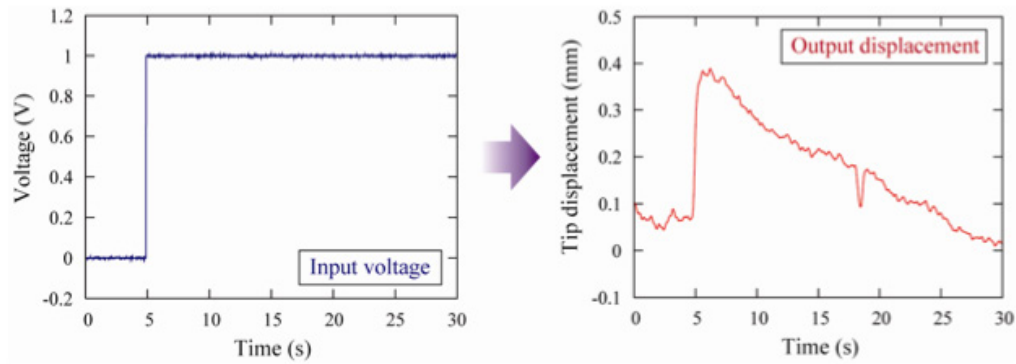


Figure 2.3 Example of actuation displacement of an IPMC over time¹¹.

2.1.1.3 Conductive Polymer Actuators

Conductive electroactive polymer actuators are conjugated polymers. They are capable of alterations in chemical, electrical, and mechanical (shape, size, etc.) properties under an

electrical impulse¹⁰. Conductive polymer actuators operate in an electrolyte environment. Actuation is caused by the ingress and egress of ions, contained in an electrolyte bath, into and out of the porous structure of the polymer. The process is driven by the conducting polymer working as an electrode, along with another suitable nonreactive counter-electrode¹⁵. Under a typical operating voltage of 1-5 V, first the addition of the ion causes the polymer to swell, and then the removal of the ion causes the entire system to contract during the redox cycles. This swelling and contraction causes the bending deformation¹⁶. The chemical structure of a common conductive polymer, polyaniline, is shown in Figure 2.4. The ratio of blocks determines the conductivity of the polyaniline.

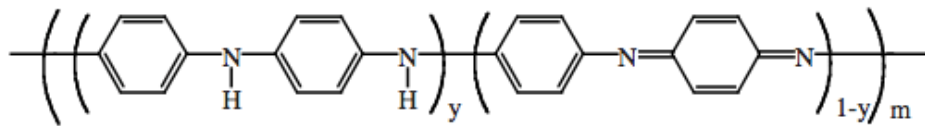


Figure 2.4 Polyaniline, a conjugated polymer: leucoemeraldine ($y = 1$), emeraldine ($y = 0.5$), and pernigraniline ($y = 0$).

Conducting polymer actuators have been reported to produce stresses of around 40 MPa with a power-to-mass ratio of about 39 W/kg¹⁷. The actuation strain produced by conducting polymer actuators is not more than 2%¹⁷. This strain limitation is due to ionic diffusion rates inside the polymer and a limiting molecular backbone conformation under ionic diffusion¹⁸. In addition to the low voltage requirement, the linear strain characteristics of conductive

polymer actuators make them useful for precise motion control in many applications in biomedicine and other fields¹⁸.

2.1.1.4 Carbon Nanotubes

Carbon nanotubes (CNTs) are hollow cylindrical particles that have extreme mechanical and electrical properties due to their chemical structure and geometrical form. Typically the CNTs have outer diameters in the range of 5-100nm and lengths in the range of 0.3-3 μm ¹⁹. As actuators, CNTs, immersed in an electrolyte solution (e.g., NaCl), act as electromechanical active electrodes. Upon the application of electrical potential between the CNTs and a counter-electrode, ions are attracted to the nanotubes, leading to the accumulation of charges on the CNT surface. These charges are balanced by the electronic charge within the CNTs, and the accumulation of the charges on the CNT surface leads to an increase in the C-C bond length of the nanotube. This increase results in a bending actuation as depicted in Figure 2.5.

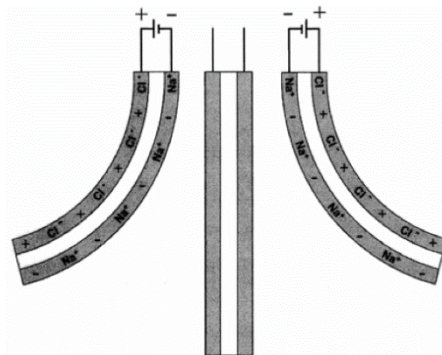


Figure 2.5 CNT-bending actuator²².

The theoretically predicted limitation of axial strain is 1% for double-layer electrolyte CNT actuators²⁰, however a 0.2% axial strain was reported recently in an observed experimental

actuation^{20,21}. CNT actuators provide higher stress than any ferroelectrics or any natural muscle, at around a 1 V potential^{20,22}, and have very small actuation strains. Compared to CNT actuators, graphene paper actuators made of two layers reportedly produced three times more actuation strain, around 0.8%¹⁵. Response time is slow for both systems because of the liquid electrolytes used²³.

The charge injection to CNT actuators is implemented using solid electrolytes, which increases response time and potential application areas. A randomly and magnetically oriented buckypaper²⁴ produced from single-walled CNTs has been tested up to 1500 V. A fast response with 0.22% strain has been reported using magnetically aligned CNTs under positive bias. A maximum of 10% bending actuation strain has been theoretically predicted for this buckypaper CNT actuator²³.

2.1.2 Electronic EAPs

Electronic EAPs are active polymers that respond to compressive electrostatic forces when placed between two electrodes. Electronic EAPs require higher voltages to operate and produce faster responses than ionic EAPs. Their actuation mechanism is also distinct from that of ionic EAPs and can be either electrostatic or electrostrictive.

The two main groups of electronic EAPs are ferroelectric polymers and dielectric elastomers.

2.1.2.1 Ferroelectric Polymers

Ferroelectric polymers are crystalline polar polymers that maintain a permanent electric polarization of dipoles. They generate strain due to spontaneous reverse polarization of permanent dipoles under electrical fields. These crystalline polar polymers produce potential

with the application of compression in a process known as piezoelectricity. While non-centrosymmetric materials exhibit piezoelectricity, nonconductive crystals and dielectric materials display spontaneous and permanent electric polarization, called ferroelectricity, in which an external electric field reverses the permanent polarization^{25,26}.

In ferroelectric polymers, randomly oriented dipoles are aligned through the application of an electrical field. This alignment of dipoles leads to a change in molecular transformation and, as a result, a change in the length of the polymer, as shown in Figure 2.6. The cumulative increase in molecular length induces a strain along a particular axis and is known as electrostriction. This ferroelectric behavior is observed in ferroelectric materials in temperatures below their Curie temperatures.

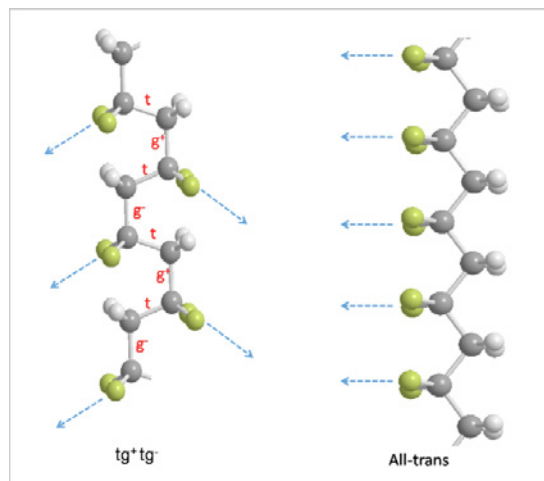


Figure 2.6 PVDF. Left: tg+tg-; right: all trans.

Poly-vinylidene fluoride (PVDF), polytrifluoroethylene, and odd-numbered nylons are examples of ferroelectric polymers. PVDF and its copolymers have been widely studied for

their ferroelectric properties. These substances' highly crystalline structure increases their moduli and mechanical energy density. Recently, the typical 2% electrostrictive actuation of P(VDF-TrFE) was increased to 4% by using electron irradiation to induce trans and gauche formation in all chains of the ferroelectric polymer²⁷. Moreover, the use of blends has increased the dielectric constant of these materials by up to 300 at a frequency of 1 MHz. Ferroelectric materials' linear strain behavior also makes them useful as sensors and transducers within the limits of their voltages²⁷. Table 2.2 gives detailed information about the PVDF molecular actuation system and achieved strain energy densities.

The configuration of a ferroelectric actuator is identical to that of other electronic EAPs. A ferroelectric polymer surface coated with compliant electrodes forms the actuator. These materials are often considered as high-dielectric constant fillers for the production of high-dielectric constant composites.

Table 2.2 Comparison of ferroelectric actuator performance⁹.

Material	Y(GPa)	Typical s_m	$Ys_m^2/2(\text{J}/\text{cm}^3)$	$Ys_m^2/2p(\text{J}/\text{kg})$
Piezoceramic	64	0.1%	0.13	4.25
Magnetostrictor	100	0.2%	0.12	21.16
Pzn-Pt Single Crystal	7.7	1.7%	1	131
Polyurethane Elastomer	0.02	4%	0.016	13
P(VDF-TrFE) Ferroelectric Polymer	0.38	4%	0.3	160

2.1.2.2 Other Electrostrictive Polymers

Electrostrictive actuator materials—electronic EAPs similar to ferroelectric polymers—have many benefits, including easy methods of production and high actuation performance. Graft elastomers, electrostriction papers, and liquid crystal elastomers (LCEs) are examples of electrostrictive materials.

Graft elastomers consist of a flexible backbone and grafted side crystal structures. The electric field produces polar regions over the crystalline side chains. The orientations of crystal regions move the polymer backbone and lead to actuation. These actuators show up to a 4% actuation strain⁹.

Electrostrictive paper is a chemically modified paper used for electrostriction. The application of an electrical field produces a bending displacement within the paper. The actuation efficiency varies depending on voltage, frequency, and assembly adhesives. Electrostrictive paper is used in various applications, such as flexible speakers, sound-absorbing materials, and smart shape-control devices.

Liquid crystal elastomers are elastomeric composites with liquid crystals fixed to elastomer chains. Their actuation mechanism is triggered by heat, an electric field, or UV light²⁸⁻³⁰. The actuation involves bending or shrinking, depending on the type of stimulus. The shrinking actuation mechanism is occurred with a phase transition between nematic and isotropic phases of mesogens²⁸. The phase transition changes the elastomer network configuration, as depicted in Figure 2.7. One cycle of an actuation takes approximately 20 sec³¹. The electrical fields needed for liquid crystal elastomers are up to two orders of magnitude smaller (1.5 to 25 MV/m) than those needed for dielectric electroactive polymer (D-EAP) or ferroelectric polymers, and dielectric constant enhancement decreases this further²⁹. The achieved strain is 4%, much smaller than that achieved by thermally actuated types of LCEs (45%)²⁹.

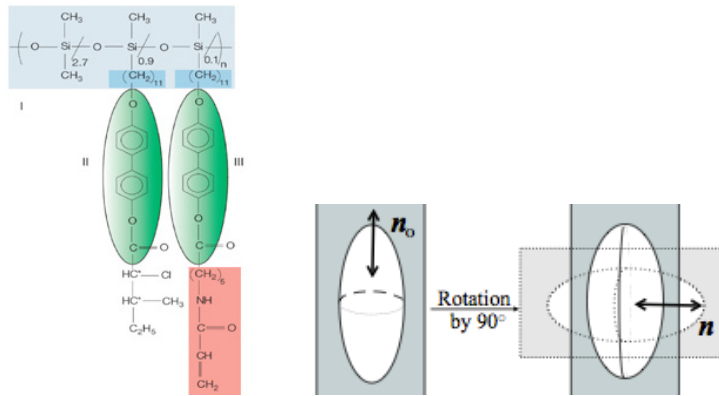


Figure 2.7 The reorientation of liquid crystals bonded to an elastomer network³¹.

2.2 Dielectric Elastomers

Dielectric elastomers (DEs) are electronic EAPs formed from insulating polymer networks with highly deformable mechanical properties and produce large strains induced by applied electrical fields. Dielectric electroactive polymers (D-EAP) are known for their unique properties of high actuation stress (up to 7 Pa)³², high actuation strain (>200%)^{33–39}, high specific energy density (~0.15 J/g)³², high coupling efficiency, fast response time (<3 sec)³⁷, and reliability^{40,41}. They are also lightweight, flexible, easy to process, and inexpensive. They offer tremendous potential for use in emerging technologies such as bio-inspired robots^{42–45}, prosthetic devices^{46,47}, adaptive structures⁴⁸, electroactive fluid pumps^{49,50}, conformable skins, refreshable Braille devices^{51,52}, autofocus lens positioners^{53,54}, speakers, shape and texture systems^{55,56}, active smart textiles⁴⁷, sensors⁵⁷, and energy harvesting systems^{58–68}.

2.2.1 Actuation Mechanism of D-EAPs

D-EAPs consist of a DE film sandwiched between two compliant electrodes. Figure 2.8 illustrates the D-EAPs actuation mechanism. When an electric potential is applied between the compliant electrodes, the attraction between the oppositely charged electrodes and the repulsion of like charges along the same electrode result in a compressive stress ($P_{Maxwell}$) that acts normal (i.e., perpendicularly) to the DE film surface. The normal pressure (primarily Maxwell pressure) serves to compress the membrane in the z -direction and generates strains in the x - and y -directions. The primary actuation mechanism is Maxwell stress produced by the electrostatic forces between the two electrodes^{38,41,69,70}.

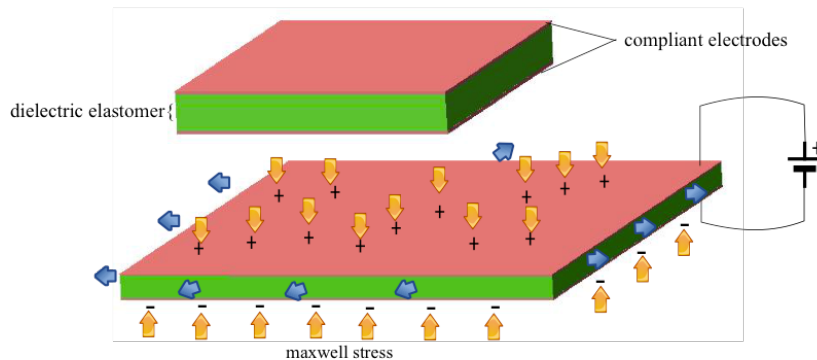


Figure 2.8 Schematic representation of D-EAPs' actuation mechanism.

As Figure 2.8 shows, the actuation mechanism for a D-EAP is comprised of a dielectric elastomer membrane and two compliant electrodes.

The Maxwell pressure is expressed as follows:

$$P_{Maxwell} = \epsilon_0 \epsilon_r E^2 = \epsilon_0 \epsilon_r (v/z)^2 \quad \text{Equation 2.1}$$

where $v/z = E$ is the electric field, ϵ_0 is the permittivity of free space, ϵ_r is the relative dielectric constant of the membrane, v is the voltage, and z is the elastomer membrane thickness.

The voltage required to achieve a target electrostatic pressure can be reduced by decreasing the thickness of the elastomer film. For small strain conditions, the strain in the thickness direction (z) can be expressed as follows:

$$s_z = -p/Y = \frac{\epsilon_0 \epsilon_r (v/z)^2}{Y} \quad \text{Equation 2.2}$$

where Y is the Young's modulus of the elastomer membrane.

The stress and the resulting strain depend critically on the dielectric constant of the membrane and its elastic modulus. The applied voltage and membrane thickness are the design parameters of a DE actuator. Although electric field is a significant parameter, it is subject to severe safety-related limitations in actuator design. The voltage limit is determined by safety issues, and the thickness limits are determined by design and processing constraints. A typical combination of thickness and voltage limits still produces electric fields as high as 10-100 V/ μm , which is a safety concern. Since the Young's modulus of the DE membrane can be controlled to match the stress-strain required for a given application, the dielectric constant of the elastomer membrane is the only parameter to optimize for actuation performance.

Potential methods for improving the dielectric constant of a DE are the same as for general dielectric polymer composites and so include similar drawbacks. In addition to a high dielectric constant, desirable properties of DEs include low viscous component of viscoelasticity and low dielectric loss.

Energy density, defined as maximum energy output per cycle of an unconstrained actuator, is a crucial actuator performance parameter. Energy density is expressed as follows:

$$e_a = ps_z = Y(s_z)^2 \quad \text{Equation 2.3}$$

where e_a is the energy density of the actuator, p is the Maxwell pressure, Y is Young's modulus of the elastomer, and s_z is the actuation strain in the thickness direction.

If a linear stress-strain relation is assumed for both low strains and high strains, the actuation energy density (e_a) can be expressed as follows:

$$e_a = Y[(s_z) - \ln(1 + s_z)] \quad \text{Equation 2.4}$$

by replacing s_z in Equation 2.4 with Equation 2.2. Actuation energy density is given as follows^{32,70}:

$$e_a = Y[(\frac{\epsilon_0 \epsilon_r (v/z)^2}{Y}) - \ln(1 + (\frac{\epsilon_0 \epsilon_r (v/z)^2}{Y}))] \quad \text{Equation 2.5}$$

Equation 2.5 shows the importance of the modulus of elasticity in determining energy density. By fine-tuning mechanical and electrical properties so that viscous loss and dielectric loss are minimized, efficiency of these materials as DEs can be increased. Thus, the

level of actuation achieved can be increased by increasing the permittivity of the elastomer (given by the product of the dielectric constant, k , and the permittivity of free space), of the applied electric field, or of both.

2.2.2 DE Materials

Acrylics (3M VHB series)^{35,37,60,71–76}, silicones^{36,77–81}, poly-butadiene copolymers^{40,82–85}, interpenetrating networks^{86,87}, isoprenes⁸⁸, polyurathenes^{89–92}, and block-copolymers^{82,83,85} are common DE materials. Of these, acrylics and silicones have been most often explored. Although a wide variety of homopolymers have been considered as candidates for D-EAP applications, three dielectric media in particular show technological promise. These include VHB tape (an acrylic adhesive), silicone elastomers, and polyurethanes.

The most common dielectric material investigated for use as a DE is the VHB acrylic pressure-sensitive adhesive film manufactured by 3M. This film is a closed-cell, chemically cross-linked amorphous polyacrylate network, and it exhibits one of the largest actuation strains in this class of materials. For this reason, it is often considered the benchmark for dielectric EAPs. VHB film contains a combination of soft, branched aliphatic groups and light cross-linking of the acrylic polymer chains^{32,93}. The acrylic elastomer is transparent, highly weather-resistant, and thermally stable in the -10 °C to 80 °C temperature range. It is mechanically stable, with a Young's modulus of 1-3 MPa, and can be stretched to 36 times its initial area. The VHB acrylic material has been shown to produce an electromechanical efficiency of around 90% and axial strains of 60-70%. A high blocking stress of 7.2 MPa and an elastic energy density of 3.4 MJ/m³ have also been reported for these films^{33,94,95}.

The actuator preparation of a VHB acrylic film is easier than for other elastomer films because of its double-sided sticky surface. The surface stickiness of acrylic film makes the application of electrodes and prestrain to films simple and easy.

Silicones are polymers with highly flexible Si-O backbones and organic groups that are attached directly to the silicon atom via silicon-carbon bonds. Silicones can have linear, branched, or cross-linked structural forms. There are different types of silicones based on the presence of functional groups: dimethyl silicone elastomers, vinyl silicone elastomers, phenyl silicone elastomers, nitrile silicone elastomers, fluorosilicone elastomers, borosilicones, and silicone carbides. The commercial silicone elastomers are highly cross-linked macromolecules of polydimethylsiloxane (PDMS) that have a high degree of flexibility.

Silicone elastomers have an array of useful properties, including high free volume, a high degree of chemical inertness, high resistance to weathering, good dielectric strength, and low surface tension, in addition to thermal and oxidative stability and an extremely low glass transition temperature (-123 °C). These physical properties, including elastic behavior, remain relatively unchanged over a wide range of temperatures. However, the mechanical properties of pure PDMS are usually poor at room temperature—for example, tensile strength is relatively low for chemically cross-linked PDMS networks. In order to develop useful properties, very high molecular weights or the incorporation of silica filler and a vulcanization process are required. Silicone films can be easily processed using spin-coating or solution-casting methods.

The commercial silicones are formed from three chemical components: polymer, hardener, and silica particles. These three components are formulated in a two-part system, depending on the cross-linking mechanism of silicone. Silica fillers are used in either one or both of these parts as nucleating agents to improve mechanical properties⁹⁶.

Silicone elastomer actuators have the desirable properties of fast response time and high efficiency. The chemistry and molecular weight of the polysiloxanes also influence actuation performance. Operating temperatures of silicones range from -65-240 °C, and the stability of silicone actuators has been demonstrated from -15-150 °C. Silicones are less sensitive to environmental degradation than acrylic elastomers. The most common commercial-grade silicone elastomers are CF 19-21 from NuSil, Dow Corning HS3, Slygard 186, DBJB Enterprises TC-5005, and Wacker Elastosil RT 625^{36,37,97-99}.

Silicones show actuation strains of up to 120%, an efficiency of 80%, and an energy density of 750 kJ/m³. They have a faster response time than acrylics^{32,37,81}, and they also have a dielectric constant of ~3, with a very low dielectric loss of ~0.005 (100 kHz). Silicone D-EAPs can also operate over a wide temperature range.

Silicone elastomers' mechanical behavior varies with the type and amount of added cross-linker. A higher number of methylene groups in the hardener increases the number of reactive sites in the main polymer chain and so decreases the polymer's flexibility⁹⁸. Silicone elastomers are mechanically tunable materials with some amount of silica or hardener in their composition. The actuation behavior of silicone with various hardeners is reported by Zhang et al.⁹⁸ and is displayed in Figure 2.9.

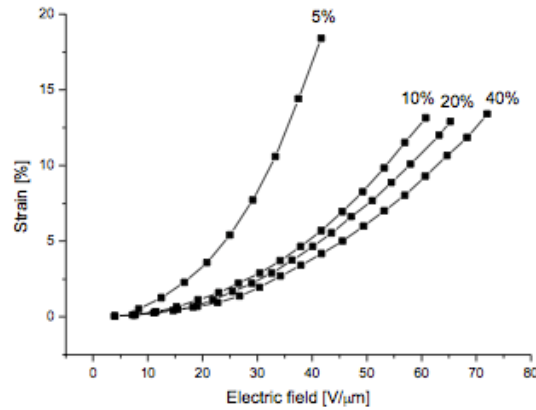


Figure 2.9 Effects of hardener amount on actuation strain for DC3481 silicone elastomer¹⁰⁰.

Thermoplastic polyurethanes (TPUs) are a versatile group of multi-phase segmented polymers that have excellent mechanical and elastic properties, high abrasion, and high chemical resistance. TPUs are physically cross-linked polymers composed of hard and soft segments. The ratio of the hard to soft segments is an important factor of the polymer's mechanical and electrical properties.

TPU elastomer is an electrostrictive polymer composed of a chain of organic units joined by urethane links. These links combine two bi- or higher functional monomers. The actuation stress of PU is high as a result of its high dielectric constant ($\epsilon_{PU} = 8$). However, its actuation stress is not transferred to strain in dielectric elastomer actuator form because of the stiffness of the polymer network. The highest applied electric field shown so far is 5 V/μm, which is quite small due to the material's high dielectric loss, which, in turn, is caused by free ions from residues of the polymerization process¹⁰⁰.

The actuation strain produced by a PU elastomer has both electrostrictive and electrostatic components. Depending on the elastomer's mechanical properties, the electrostrictive coefficient (Q) varies from $150\text{-}450 \times 10^{-18} \text{ m}^2/\text{V}^2$, and the dielectric constant varies from 4-8. The contribution of Maxwell stress is higher at temperatures above room temperature⁹⁰.

Table 2.3 Actuation response of common dielectric elastomers⁸⁵.

Dielectric Elastomer	Elastic Energy Density, J/cm ³	Pressure, MPa	Strain, %	Young's Modulus, MPa	Electric Field, V/ μm	Dielectric Constant	Coupling Efficiency %
Silicone Nusil CF19-2186	0.22	1.36	32	1.0	235	2.8	54
Silicone DC HS3	0.026	0.13	41	0.125	72	2.8	64
Silicone DC Sylgard 186	0.082	0.51	32	0.7	144	2.8	54
Polyurethane Deerfield PT6100S	0.087	1.6	11	17	160	7.0	21
Fluorosilicone DC 730	0.055	0.39	28	0.5	80	6.9	48
Fluoroelastomer Lauren L143HC	0.0046	0.11	8	2.5	32	12.7	15
Isoprene Natural Rubber	0.0059	0.11	11	0.85	67	2.7	21
SEBS161 Copolymer 5-30w% Midblock	0.151	-	Areal 180	0.007-0.163	133	1.7-2	80
SEBS217 Copolymer 5-30w% Midblock	0.139	-	Areal 245	0.002-0.133	98	2-2.2	92

In recent years, triblock copolymers have been employed as thermoplastic dielectric elastomers. They exhibit excellent electromechanical properties, including large actuation strains and high coupling efficiency ($>90\%$)⁸⁸. Block copolymers of thermoplastic elastomers

have attracted attention as dielectric transducers—unlike silicone and acrylic elastomers, they are physically cross-linked structures that exhibit a variety of morphologies. Shankar et al.⁸⁸ found that the actuation performance of triblock copolymer organogel elastomers with swollen midblock-selective solvent exceeded that of an acrylic film. The authors reported actuation areal strains of 250% with an electrical field of 22 V/ μm , with 5 weight percent of midblock polymer composition. Their work shows the benefits of tailoring Young's modulus for better actuation strains, because the dielectric constant of the copolymer gel (2.0-2.2) did not change substantially⁸⁵. Additionally, these elastomer gels present better actuation strain than either acrylic or silicone elastomers under various prestrains¹⁰¹. Table 2.3 reports common dielectric elastomer materials used as D-EAP materials.

2.2.3 D-EAP Electrodes

The performance of a D-EAP depends significantly on electrode quality. An electrode for a D-EAP must maintain two properties: compliance to the elastomer and conductivity. An ideal electrode material should be mechanically compatible with the dielectric elastomer in that it imposes no constraint.

Schlaak et al.¹⁰² summarized the important parameters for electrode material design as follows:

- High compliance
- Low resistance under planar extension
- High surface under large strain to ensure high electrostatic charges
- Good adhesion to the dielectric membrane layer

- Easy manufacturing

After the electrode charging completes, the response time of an actuator depends on the viscoelastic properties of the dielectric membrane. High conductivity is another important property that increases the response speed of an actuator¹⁰³. Conductivities as low as 10^{-3} S/cm could be accepted for electrode materials.

Metallic paints (e.g., silver grease or paint) are one of the most common materials used for DE actuator electrodes due to their ease of application, high compliance, affordability, and strong adhesion to dielectric membranes^{38,40,40,104,105}. Sputtered metal layers have also been studied as compliant electrodes. However, even with patterning enhancements, surface cracks adversely affect conductivity under application of high strains^{106–109}. Self-healing silver sputter electrodes reportedly produce up to 50% areal strains with high reliability⁷⁹. Dry graphite and carbon powders have been used on tacky surfaces (e.g., VHB acrylic tapes), and elastomer composites of these organic fillers with low cross-linking densities show good properties as spray electrodes¹¹⁰. Geometric wrinkling performed on an elastomer surface before electrode application has been shown to improve electrode and actuator performance¹¹¹, and the application of silicone oil to elastomeric composite electrodes has been shown to have an increase on actuator lifetime^{102,112–114}.

Another recently proposed electrode system consists of CNT electrodes with self-repairing properties. Local spots on these electrodes burn out when “shorted”; however, the process is so quick and generates so little heat energy that the dielectric remains intact^{113,115}.

2.2.4 Electromechanical Instability of D-EAPs

Electromechanical instability, also known as pull-in instability, is a type of breakdown that results in a dramatic decrease in polymer thickness and an increase in electric field. Such instability leads to catastrophic failure and has most often been observed in power transmission cables. Electromechanical instability can be mitigated by pre-stretching an elastomer, designing an elastomer of interpenetrating networks, swelling an elastomer with a solvent, or spraying charge on an electrode-free elastomer^{83,86,101,116}.

Vargantwar et al. demonstrated that selectively swollen acrylic triblock copolymers can enhance the actuation of a polymer without any prestrain¹⁰¹. Rontgen's electrode-free charge sprays were demonstrated to act as effective D-EAP electrodes without pull-in instability^{116,117}.

2.2.5 The Effect of Prestrain on D-EAPs

Prestrain is routinely applied to DE films during the fabrication of the DE actuator. The application of prestrain requires homogeneous deformation of the elastomer. A circular fixture is used for prestrain application, depending on the actuator configuration, as depicted in Figure 2.10. The introduction of prestrain significantly increases the maximum strain and pressures that can be generated from a dielectric elastomer actuator because it causes strain-softening of the elastomer film and eliminates the film's electromechanical instabilities^{32,39,87,94,118–121}.

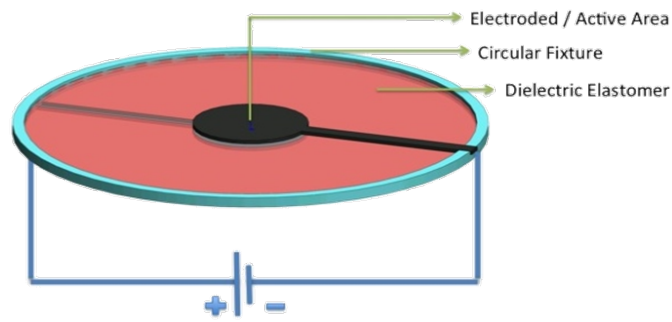


Figure 2.10 A circular actuator with fixture. The elastomer is attached to a circular fixture after a nominal prestrain application.

An elastomer with covalent cross-links can have varying degrees of flexibility. Highly flexible polymer chains undergo large deformations, whereas less flexible ones become fully stretched under a pretension. Fully stretched elastomers behave like rigid structures with minimal deformation, as depicted in Figure 2.11(a). The applied electrical field produces a compressive strain, as depicted in Figure 2.11(b), and the effect of strain-softening can be observed in this structure. The negative effect of strain-softening on actuation can be prevented either by applying a prestrain or by making structural changes in the elastomer material¹²².

The amount of prestrain that is applied to an elastomer also determines the buckling behavior of the elastomer film during actuation. D-EAP buckling is a signal of insufficient prestrain in a dielectric elastomer actuator and indicates that the stress in the thickness direction is not sufficient to exceed the electrode boundary stresses.

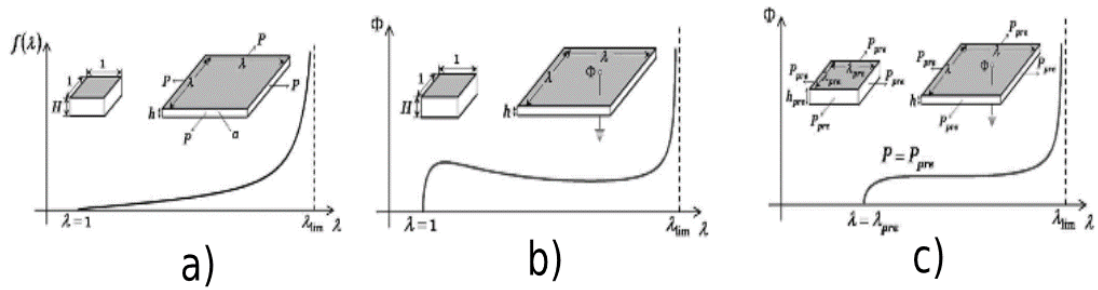


Figure 2.11 Mechanical effects of prestrain on actuation performance: a) mechanical deformation, b) electrical deformation, c) electrical deformation with prestrain¹²².

Pelrine and colleagues demonstrated a dramatic increase in actuation strain, pressure, and energy density of dielectric elastomer films as the result of increasing prestrain in acrylic and silicone elastomers^{32,123}. They reported a biaxial prestrain of 200-400% for acrylic (VHB 4905 by 3M) to achieve optimal actuation. Although biaxial strains do not typically display a preferred actuation direction, uniaxial prestrains direct the actuation primarily in the softer (or lower prestrain) direction³². Higher amounts of prestrain stiffen the polymer, limiting actuation performance. Koh et al. predicted the theoretical required optimal prestrain, taking into account electromechanical instability and strain softening. Their predictions have been empirically supported by actuation experiments using acrylic films¹²².

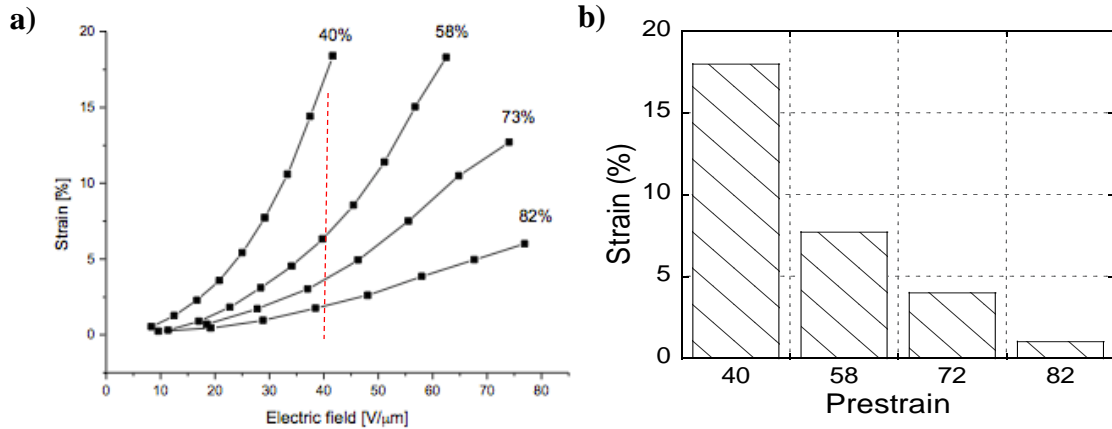


Figure 2.12 Actuation behavior of PDMS elastomers under various strains (a) Strain vs electric field for PDMS actuators. The dotted line drawn perpendicular to 40V/ μm is guide for eye. The numbers at the tops of the plots show the level of prestrain¹⁰⁰. (b) Effect of prestrain levels on electrical breakdown (PDMS elastomer). Strain-prestrain plot was plotted from reference¹⁰⁰.

The application of prestrain thins the film and increases its breakdown strength^{32,94,123} by eliminating electromechanical instabilities. Figure 2.12 shows the influence of unidirectional prestrain on a PDMS elastomer. The increasing prestrain stiffens the film and decreases actuation performance. A nominal prestrain has a positive effect on electrical breakdown of silicone elastomer dielectric actuators. Figure 2.13 plots nominal thickness strain versus prestrain levels¹²⁴.

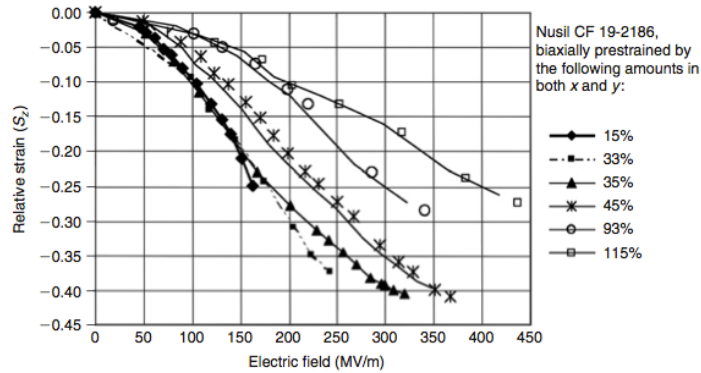


Figure 2.13 Relative actuation performance versus electrical field for various prestrained PDMS films¹²⁶.

Prestrain application to a DE elastomer material also increases the size and weight of the actuator because the application requires a frame¹²⁵. It can also degrade the desired properties of the DE, as the DE undergoes prolonged stress relaxation over long periods of inactivity.

Polymer interpenetrating networks have been used as prestrain-free D-EAP materials due to their locked molecular structure^{126,127}. These elastomers maintain internal prestrain in their free form.

2.2.6 Response Time of D-EAPs

The response time of an actuator depends on two main factors. The first is the conductivity of the electrodes, which can introduce delay into charge and discharge characteristics. The second factor is the viscosity of the elastomer. Figure 2.14 compares acrylic and silicone elastomer response times. Silicone elastomers reach their maximum actuation strain in 3 sec, whereas acrylic elastomers can take up to 3 min to reach maximum strain⁹⁸.

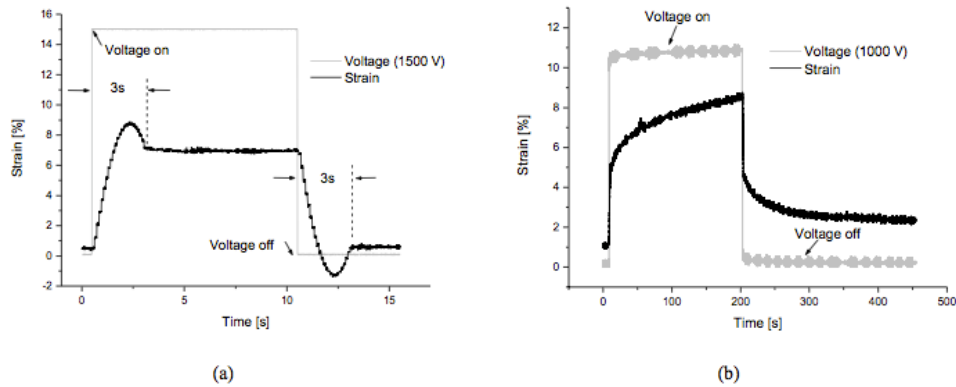


Figure 2.14 Speed response plots of a) PDMS, b) acrylic elastomer actuators¹⁰⁰.

2.2.7 DE-based Energy Harvesting

Energy harvesting using dielectric elastomers is based on converting mechanical work to electrical energy. Dielectric elastomer generators (DEGs) are flexible, lightweight candidates for energy-scavenging systems⁶⁰.

Research on the use of DEGs in energy harvesting has increased recently. McKay et al.⁶⁸ report that initial charges of 2kV can generate up to 0.5kV of output voltages. Jean Mistral et al.⁶¹ and Cohen et al.⁹ report 0.1–0.4mJ/g of energy harvesting from DEGs manufactured using VHB acrylic film.

Several proposed energy-harvesting application areas for elastomers include wind tunnels, human motions⁶¹, ocean waves⁶⁴, highways, and ultrasound energy sources¹²⁸. The energy conversion mechanism of DEGs is similar to that of D-EAPs. DEGs are kept in a deformed state, and free charges are confined to electrodes in their inactive state. The voltage increases in a capacitive system because of the reverse deformation of the elastomer. DEGs are

supported with a circuit to capture the excess charges and keep the system at optimum potential^{59,70}.

2.3 Summary

This review has focused on electroactive polymers and dielectric elastomer actuators. Special attention has been given to dielectric elastomers and dielectric elastomer actuators.

2.4 References

1. Badr, B. M. & Ali, W. G. Applications of Piezoelectric Materials. *Adv. Mater. Res.* **189-193**, 3612–3620 (2011).
2. Heywang, W., Lubitz, K. & Wersing, W. *Piezoelectricity: evolution and future of a technology*. (Springer, 2008).
3. Zhang, P. *Industrial control technology: a handbook for engineers and researchers*. (William Andrew, 2008).
4. Juan, J. S., No, M. L. & Schuh, C. A. Nanoscale shape-memory alloys for ultrahigh mechanical damping. *Nat Nano* **4**, 415–419 (2009).
5. Lagoudas, D. C. *Shape memory alloys: modeling and engineering applications*. (Springer, 2008).
6. Hamilton, R. F. *Investigations into the physical mechanisms that facilitate transformation hysteresis in shape memory alloys*. (ProQuest, UMI Dissertation Publishing, 2011).
7. Carpi, Kornbluh, R., Sommer-Larsen, P., Rossi, D. D. & Alici. Guest editorial introduction to the focused section on electroactive polymer mechatronics. *IEEE/ASME Trans. Mechatron.* **16**, 1–8 (2011).

8. Kim, K. J. & Tadokoro, S. *Electroactive Polymers for Robotic Applications: Artificial Muscles and Sensors*. (Springer Science & Business Media, 2007).
9. Bar-Cohen, Y. *Electroactive polymer (EAP) actuators as artificial muscles*. (SPIE Press, 2004).
10. Tiwari, R. & Garcia, E. The state of understanding of ionic polymer metal composite architecture: a review. *Smart Mater. Struct.* **20**, 083001 (2011).
11. Anand, S. V., Arvind, K., Bharath, P. & Roy Mahapatra, D. Energy harvesting using ionic electro-active polymer thin films with Ag-based electrodes. *Smart Mater. Struct.* **19**, 045026 (2010).
12. Zamani, S. & Nemat-Nasser, S. Controlled actuation of Nafion-based ionic polymer-metal composites (IPMCs) with ethylene glycol as solvent. in *Electroactive Polymer Actuators and Devices* **5385**, 0277–786X/04 (SPIE Press).
13. Kruusamäe, K. *et al.* Self-sensing ionic polymer-metal composite actuating device with patterned surface electrodes. *Polym. Int.* **59**, 300–304 (2010).
14. Kobayashi, T. & Omiya, M. Frequency response of IPMC actuator with palladium electrode. in *Electroactive Polymer Actuators and Devices* **7976**, 797614–797614–7 (SPIE Proceedings, 2011).
15. Xie, X., Bai, H., Shi, G. & Qu, L. Load-tolerant, highly strain-responsive graphene sheets. *J. Mater. Chem.* **21**, 2057 (2011).
16. Pei, Q. & Inganäs, O. Electrochemical applications of the bending beam method; a novel way to study ion transport in electroactive polymers. *Solid State Ion.* **60**, 161–166 (1993).

17. Madden, P. G. A., Madden, J. D. W., Anquetil, P. A., Vandesteeg, N. A. & Hunter, I. W. The relation of conducting polymer actuator material properties to performance. *IEEE J. Ocean. Eng.* **29**, 696–705 (2004).
18. Anquetil, P. A. *et al.* Thiophene-based conducting polymer molecular actuators. in *Proc SPIE* **4695**, 424–434 (2002).
19. Reich, S., Thomsen, C. & Maultzsch, J. *Carbon nanotubes: basic concepts and physical properties.* (Wiley-VCH, 2004).
20. Baughman, R. H. *et al.* Carbon nanotube actuators. *Science* **284**, 1340 (1999).
21. Yun, Y. *et al.* A multi-wall carbon nanotube tower electrochemical actuator. *Nano Lett.* **6**, 689–693 (2006).
22. Baughman, R. H. *et al.* Carbon Nanotube Actuators. *Science* **284**, 1340–1344 (1999).
23. Chen, I.-W. P., Liang, Z., Wang, B. & Zhang, C. Charge-induced asymmetrical displacement of an aligned carbon nanotube buckypaper actuator. *Carbon* **48**, 1064–1069 (2010).
24. Gonnet, P. *et al.* Thermal conductivity of magnetically aligned carbon nanotube buckypapers and nanocomposites. *Curr. Appl. Phys.* **6**, 119–122 (2006).
25. Fukada, E. *Ferroelectric polymers: a special issue of the journal phase transitions.* (Taylor & Francis US, 1989).
26. Nalwa, H. S. *Ferroelectric polymers.* (CRC Press, 1995).
27. Zhang, Q. M., Bharti, V. & Zhao, X. Giant electrostriction and relaxor ferroelectric behavior in electron-irradiated poly(vinylidene fluoride-trifluoroethylene) copolymer. *Science* **280**, 2101–2104 (1998).

28. Yu, Y. & Ikeda, T. Soft actuators based on liquid-crystalline elastomers. *Angew. Chem. Int. Ed.* **45**, 5416–5418 (2006).
29. Ji, Y., Huang, Y. Y., Rungsawang, R. & Terentjev, E. M. Dispersion and alignment of carbon nanotubes in liquid crystalline polymers and elastomers. *Adv. Mater.* **22**, 3436–3440 (2010).
30. Yang, H., Ye, G., Wang, X. & Keller, P. Micron-sized liquid crystalline elastomer actuators. *Soft Matter* **7**, 815 (2011).
31. Warner, M. & Terentjev, E. M. *Liquid crystal elastomers*. (Oxford University Press, USA, 2003).
32. Pelrine, R., Kornbluh, R., Pei, Q. & Joseph, J. High-speed electrically actuated elastomers with strain greater than 100%. *Science* **287**, 836–839 (2000).
33. Ma, W. & Cross, L. E. An experimental investigation of electromechanical response in a dielectric acrylic elastomer. *Appl. Phys. Mater. Sci. Process.* **78**, 1201–1204 (2004).
34. Carpi, F., Mazzoldi, A. & De Rossi, D. High-strain dielectric elastomer for actuation. in *Smart Struct. Mater. 2003 Electroact. Polym. Actuators Devices EAPAD* (ed. Bar-Cohen, Y.) **5051**, 419–422 (SPIE, 2003).
35. Jordi, C., Schmidt, A., Kovacs, G., Michel, S. & Ermanni, P. Performance evaluation of cutting-edge dielectric elastomers for large-scale actuator applications. *Smart Mater. Struct.* **20**, 075003 (2011).
36. Goulbourne, N. C., Mockensturm, E. M. & Frecker, M. I. Electro-elastomers: Large deformation analysis of silicone membranes. *Int. J. Solids Struct.* **44**, 2609–2626 (2007).

37. Michel, S., Zhang, X. Q., Wissler, M., Löwe, C. & Kovacs, G. A comparison between silicone and acrylic elastomers as dielectric materials in electroactive polymer actuators. *Polym. Int.* **59**, 391–399 (2010).
38. O'Halloran, A., O'Malley, F. & McHugh, P. A review on dielectric elastomer actuators, technology, applications, and challenges. *J. Appl. Phys.* **104**, 071101–10 (2008).
39. Zhu, L. H., Zhu, X. L., E, S. J., Hui, A. F. & Cao, J. B. Influence of prestrain on output characteristic of dielectric elastomer film actuators. *Key Eng. Mater.* **455**, 81–86 (2010).
40. Shankar, R., Ghosh, T. K. & Spontak, R. J. Dielectric elastomers as next-generation polymeric actuators. *Soft Matter* **3**, 1116 (2007).
41. Stoyanov, H., Kollosche, M., Risse, S., McCarthy, D. N. & Kofod, G. Elastic block copolymer nanocomposites with controlled interfacial interactions for artificial muscles with direct voltage control. *Soft Matter* **7**, 194 (2011).
42. Anderson, I. A., Ieropoulos, I. A., McKay, T., O'Brien, B. & Melhuish, C. Power for robotic artificial muscles. *Mechatron. IEEE/ASME Trans. On* **16**, 107–111 (2011).
43. Hyouk Ryeol Choi *et al.* Biomimetic soft actuator: design, modeling, control, and applications. *IEEE/ASME Trans. Mechatron.* **10**, 581–593 (2005).
44. Goethals, P. & Leuven, K. U. Tactile feedback for robot assisted minimally invasive surgery: an overview. *Department of Mechanical Engineering KU Leuven, Tech. Rep* (2008).
45. Taya, M. Bio-inspired design of intelligent materials. in *Smart Structures and Materials* **5051**, 54–65 (2003).

46. Biddiss, E. & Chau, T. Dielectric elastomers as actuators for upper limb prosthetics: Challenges and opportunities. *Med. Eng. Phys.* **30**, 403–418 (2008).
47. Carpi, F. & De Rossi, D. Electroactive polymer-based devices for e-textiles in biomedicine. *Inf. Technol. Biomed. IEEE Trans. On* **9**, 295–318 (2005).
48. Prahlad, H. *et al.* Programmable surface deformation: thickness-mode electroactive polymer actuators and their applications. in *Electroactive Polymer Actuators and Devices* (ed. Bar-Cohen, Y.) **5759**, 102–113 (SPIE Proceedings, 2005).
49. Arthur, G. G., McKeon, B. J., Dearing, S. S., Morrison, J. F. & Cui, Z. Manufacture of Micro-sensors and Actuators for Flow Control. *Microelectron. Eng.* **83**, 1205–1208 (2006).
50. Carpi, F., Menon, C. & De Rossi, D. Electroactive elastomeric actuator for all-polymer linear peristaltic pumps. *IEEE/ASME Trans. Mechatron.* **15**, 460–470 (2010).
51. Chakraborti, P. *Development of a Refreshable Prototype Actuator Using Silicone Dielectric Elastomer Actuator (DEA)*. (North Carolina State University, 2010).
52. Mazzone, A., Zhang, R. & Kunz, A. Novel actuators for haptic displays based on electroactive polymers. in *Proc. ACM Symp. Virtual Real. Softw. Technol. - VRST 03* 196 (2003). doi:10.1145/1008653.1008688
53. Choi, S. T., Lee, J. Y., Kwon, J. O., Lee, S. & Kim, W. Varifocal liquid-filled microlens operated by an electroactive polymer actuator. *Opt. Lett.* **36**, 1920–1922 (2011).
54. Tang, H. Smart lens made of dielectric elastomer: simulation study. *Bull. Am. Phys. Soc.* **56**, (2011).

55. Ouyang, G., Wang, K., Henriksen, L., Akram, M. N. & Chen, X. Y. A novel tunable grating fabricated with viscoelastic polymer (PDMS) and conductive polymer (PEDOT). *Sens. Actuators Phys.* **158**, 313–319 (2010).
56. Ouyang, G. M., Wang, K. Y. & Chen, X. Y. Enhanced electro-mechanical performance of TiO₂ nano-particle modified polydimethylsiloxane (PDMS) as electroactive polymers. in *Solid-State Sensors, Actuators and Microsystems Conference* 614–617 (2011).
57. Toth, L. *Design and development of dielectric elastomer transducers with dual actuation and sensory functionality*. (National Library of Canada, 2002).
58. Davies, D. K. Charge generation on dielectric surfaces. *J. Phys. Appl. Phys.* **2**, 1533–1537 (1969).
59. Lo, H. C., McKay, T., O'Brien, B. M., Calius, E. & Anderson, I. Circuit design considerations for regulating energy generated by dielectric elastomer generators. in *SPIE Proceedings* **7946**, 79760C–79760C–8 (2011).
60. Koh, S. J. ., Keplinger, C., Li, T., Bauer, S. & Suo, Z. Dielectric elastomer generators: how much energy can be converted? *Mechatron. IEEE/ASME Trans. On* **16**, 33–41 (2011).
61. Jean-Mistral, C., Basrour, S. & Chaillout, J.-J. Dielectric polymer: scavenging energy from human motion. in *Electroact. Polym. Actuators Devices EAPAD 2008 10 March 2008* **6927**, 692716–1 (SPIE - The International Society for Optical Engineering, 2008).
62. Putson, C. *et al.* Effects of copper filler sizes on the dielectric properties and the energy harvesting capability of nonpercolated polyurethane composites. *J. Appl. Phys.* **109**, 024104 (2011).

63. Guyomar, D. *et al.* Electrostrictive energy conversion in polyurethane nanocomposites. *J. Appl. Phys.* **106**, 014910 (2009).
64. Beeby, S. P., Tudor, M. J. & White, N. M. Energy harvesting vibration sources for microsystems applications. *Meas. Sci. Technol.* **17**, R175–R195 (2006).
65. Cao, J. *et al.* in *Advanced Electrical and Electronics Engineering* (ed. Lee, J.) 201–207 (Springer Berlin Heidelberg, 2011).
66. Ogden, R. & Steigmann, D. *Mechanics and Electrodynamics of Magneto-And Electro-Elastic Materials.* **527**, (Springer Verlag, 2011).
67. Kang, G., Kim, K.-S. & Kim, S. Note: Analysis of the efficiency of a dielectric elastomer generator for energy harvesting. *Rev. Sci. Instrum.* **82**, 046101 (2011).
68. McKay, T. G., O'Brien, B. M., Calius, E. P. & Anderson, I. A. Soft generators using dielectric elastomers. *Appl. Phys. Lett.* **98**, 142903 (2011).
69. Madden, J. D. W. *et al.* Artificial muscle technology: physical principles and naval prospects. *IEEE J. Ocean. Eng.* **29**, 706–728 (2004).
70. Pelrine, R. *et al.* High-field deformation of elastomeric dielectrics for actuators. *Mater. Sci. Eng. C* **11**, 89–100 (2000).
71. Pei, Q. Artificial muscles based on synthetic dielectric elastomers. in *Annual International Conference of the IEEE Engineering in Medicine and Biology Society, 2009. EMBC 2009* 6826–6829 (2009). doi:10.1109/IEMBS.2009.5334480
72. Jan, A. *et al.* Broadening the actuation temperature range for acrylic dielectric elastomers. *ASME Conf. Proc.* **2009**, 283–287 (2009).

73. Kollosche, M., Stoyanov, H., Ragusch, H. & Kofod, G. Dependence on boundary conditions for actuation characteristics of dielectric elastomer actuators. in **7642**, 1–9 (2010).
74. Lochmatter, P. Electromechanical model for static and dynamic activation of elementary dielectric elastomer actuators. in *Proc. SPIE* **61680**,1–13 (2006). doi:10.1117/12.657873
75. Kofod, G., Stoyanov, H. & Gerhard, R. Multilayer coaxial fiber dielectric elastomers for actuation and sensing. *Appl. Phys. A* **102**, 577–581 (2010).
76. Zhao, X. & Suo, Z. Theory of dielectric elastomers capable of giant deformation of actuation. *Phys. Rev. Lett.* **104**, 178302 (2010).
77. Jordan, G. *et al.* Actuated micro-optical submount using a dielectric elastomer actuator. *IEEE/ASME Trans. Mechatron.* **16**, 98–102 (2011).
78. Son, S. & Goulbourne, N. C. Dynamic response of tubular dielectric elastomer transducers. *Int. J. Solids Struct.* **47**, 2672–2679 (2010).
79. Low, S. H. & Lau, G. K. High actuation strain in silicone dielectric elastomer actuators with silver electrodes. **7976**, 797636–797636–11 (2011).
80. Ahnert, K., Abel, M., Kollosche, M., Jørgensen, P. J. & Kofod, G. Soft capacitors for wave energy harvesting. *Journal of Materials Chemistry* **21**, 14492 (2011).
81. Araromi, O. A. *et al.* Spray deposited multilayered dielectric elastomer actuators. *Sens. Actuators Phys.* **167**, 459–467 (2011).
82. Shankar, R., Ghosh, T. K. & Spontak, R. J. Electroactive nanostructured polymers as tunable actuators. *Adv. Mater.* **19**, 2218–2223 (2007).

83. Shankar, R., Ghosh, T. K. & Spontak, R. J. Electromechanical response of nanostructured polymer systems with no mechanical pre-strain. *Macromol. Rapid Commun.* **28**, 1142–1147 (2007).
84. Shankar, R., Ghosh, T. K. & Spontak, R. J. Mechanical and actuation behavior of electroactive nanostructured polymers. *Sens. Actuators Phys.* **151**, 46–52 (2009).
85. Shankar, R., Krishnan, A. K., Ghosh, T. K. & Spontak, R. J. Triblock copolymer organogels as high-performance dielectric elastomers. *Macromolecules* **41**, 6100–6109 (2008).
86. Goulbourne, N. C. A constitutive model of polyacrylate interpenetrating polymer networks for dielectric elastomers. *Int. J. Solids Struct.* **48**, 1085–1091 (2011).
87. Li, B. *et al.* Effect of mechanical pre-stretch on the stabilization of dielectric elastomer actuation. *J. Phys. Appl. Phys.* **44**, 155301 (2011).
88. Puvanattvattana, T. *et al.* Electric field induced stress moduli in polythiophene/polyisoprene elastomer blends. *React. Funct. Polym.* **66**, 1575–1588 (2006).
89. Huang, C., Zhang, Q. M. & Bhattacharya, K. All-organic dielectric-percolative three-component composite materials with high electromechanical response. *Appl. Phys. Lett.* **84**, 4391 (2004).
90. Zhang, Q. M., Su, J., Kim, C. H., Ting, R. & Capps, R. An experimental investigation of electromechanical responses in a polyurethane elastomer. *J. Appl. Phys.* **81**, 2770–2776 (1997).
91. Guillot, F. M., Jarzynski, J. & Balizer, E. Measurement of electrostrictive coefficients of polymer films. *J. Acoust. Soc. Am.* **110**, 2980 (2001).

92. Wang, H. *et al.* The origins of electromechanical response in polyurethane elastomers. in *Proc. Ninth IEEE Int. Symp. Appl. Ferroelectr. 1994ISAF 94* 182–185 (IEEE, 1991). doi:10.1109/ISAF.1994.522333
93. Österbacka, R., An, C. P., Jiang, X. M. & Vardeny, Z. V. Two-dimensional electronic excitations in self-assembled conjugated polymer nanocrystals. *Science* **287**, 839 – 842 (2000).
94. Kofod, G., Sommer-Larsen, P., Kornbluh, R. & Pelrine, R. Actuation response of polyacrylate dielectric elastomers. *J. Intell. Mater. Syst. Struct.* **14**, 787 –793 (2003).
95. Plante, J.-S. & Dubowsky, S. Large-scale failure modes of dielectric elastomer actuators. *Int. J. Solids Struct.* **43**, 7727–7751 (2006).
96. Yim, A. & St. Pierre, L. E. The effect of interfacial energy on heterogeneous nucleation in the crystallization of polydimethylsiloxane. *J. Polym. Sci. [B]* **8**, 241–245 (1970).
97. Gallone, G., Carpi, F., De Rossi, D., Levita, G. & Marchetti, A. Dielectric constant enhancement in a silicone elastomer filled with lead magnesium niobate–lead titanate. *Mater. Sci. Eng. C* **27**, 110–116 (2007).
98. Zhang, X., Wissler, M., Jaehne, B., Breonmann, R. & Kovacs, G. Effects of crosslinking, prestrain, and dielectric filler on the electromechanical response of a new silicone and comparison with acrylic elastomer. in **5385**, 78–86 (2004).
99. Lotters, J. C., Olthuis, W., Veltink, P. H. & Bergveld, P. The mechanical properties of the rubber elastic polymer polydimethylsiloxane for sensor applications. *J. Micromechanics Microengineering* **7**, 145–147 (1997).
100. Kofod, G. Dielectric elastomer actuators. *Tech. Univ. Den. Ph.D. Thesis* (2001).

101. Krishnan, A. S., Vargantwar, P. H., Ghosh, T. K. & Spontak, R. J. Electroactuation of solvated triblock copolymer dielectric elastomers: Decoupling the roles of mechanical prestrain and specimen thickness. *J. Polym. Sci. Part B Polym. Phys.* **49**, 1569–1582 (2011).
102. Schlaak, H. F., Jungmann, M., Matysek, M. & Lotz, P. Novel multilayer electrostatic solid state actuators with elastic dielectric (Invited Paper). in *Electroactive Polymer Actuators and Devices* **5759**, 121–133 (2005).
103. Delille, R. Novel compliant electrodes based on platinum salt reduction. in *Proceedings of SPIE* **6168**, 61681Q–61681Q–11 (2006).
104. Mockensturm, E. M. & Goulbourne, N. Dynamic response of dielectric elastomers. *International Journal of Non-Linear Mechanics* **41**, 388–395 (2006).
105. Pelrine, R., Kornbluh, R. & Kofod, G. High-strain actuator materials based on dielectric elastomers. *Adv. Mater.* **12**, 1223–1225 (2000).
106. Trujillo, R., Mou, J., Phelan, P. E. & Chau, D. S. Investigation of electrostrictive polymers as actuators for mesoscale devices. *Int. J. Adv. Manuf. Technol.* **23**, 176–182 (2004).
107. Urdaneta, M. G., Delille, R. & Smela, E. Stretchable electrodes with high conductivity and photo-patternability. *Adv. Mater.* **19**, 2629–2633 (2007).
108. Lacour, S. P., Wagner, S., Huang, Z. & Suo, Z. Stretchable gold conductors on elastomeric substrates. *Appl. Phys. Lett.* **82**, 2404 (2003).
109. Rosset, S., Niklaus, M., Dubois, P. & Shea, H. R. Large-stroke dielectric elastomer actuators with ion-implanted electrodes. *Microelectromechanical Syst. J. Of* **18**, 1300–1308 (2009).

110. Kujawski, M., Pearse, J. D. & Smela, E. Elastomers filled with exfoliated graphite as compliant electrodes. *Carbon* **48**, 2409–2417 (2010).
111. Watanabe, M., Shirai, H. & Hirai, T. Wrinkled polypyrrole electrode for electroactive polymer actuators. *J. Appl. Phys.* **92**, 4631 (2002).
112. Kujawski, M., Pearse, J. & Smela, E. PDMS/graphite stretchable electrodes for dielectric elastomer actuators. in **7642**, 76420R–76420R–9 (2010).
113. Frackowiak, E., Metenier, K., Bertagna, V. & Beguin, F. Supercapacitor electrodes from multiwalled carbon nanotubes. *Applied Physics Letters* **77**, 2421–2423 (2000).
114. Yuan, W. *et al.* New electrode materials for dielectric elastomer actuators. in *Electroact. Polym. Actuators Devices EAPAD 2007* (ed. Bar-Cohen, Y.) **6524**, 65240N–12 (SPIE, 2007).
115. Yuan, W. *et al.* Self-clearable carbon nanotube electrodes for improved performance of dielectric elastomer actuators. in *Electroactive Polymer Actuators and Devices* **6927**, 69270P–69270P–12 (SPIE Proceedings, 2008).
116. Keplinger, C., Kaltenbrunner, M., Arnold, N. & Bauer, S. Rontgen’s electrode-free elastomer actuators without electromechanical pull-in instability. *Proc. Natl. Acad. Sci.* **107**, 4505–4510 (2010).
117. Li, B., Zhou, J. & Chen, H. Electromechanical stability in charge-controlled dielectric elastomer actuation. *Appl. Phys. Lett.* **99**, 244101 (2011).
118. Wissler, M. & Mazza, E. Modeling of a pre-strained circular actuator made of dielectric elastomers. *Sens. Actuators Phys.* **120**, 184–192 (2005).
119. Palakodeti, R. & Kessler, M. R. Influence of frequency and prestrain on the mechanical efficiency of dielectric electroactive polymer actuators. *Mater. Lett.* **60**, 3437–3440 (2006).

120. Zhao, X. & Suo, Z. Method to analyze electromechanical stability of dielectric elastomers. *Appl. Phys. Lett.* **91**, 061921 (2007).
121. Kofod, G. The static actuation of dielectric elastomer actuators: how does pre-stretch improve actuation? *J. Phys. Appl. Phys.* **41**, 215405 (2008).
122. Koh, S. J. A. *et al.* Mechanisms of large actuation strain in dielectric elastomers. *J. Polym. Sci. Part B Polym. Phys.* **49**, 504–515 (2011).
123. Kornbluh, R. D., Pelrine, R., Pei, Q., Oh, S. & Joseph, J. Ultrahigh strain response of field-actuated elastomeric polymers. in *Smart Struct. Mater. 2000 Electroact. Polym. Actuators Devices EAPAD* (ed. Bar-Cohen, Y.) **3987**, 51–64 (SPIE, 2000).
124. *Dielectric Elastomers as Electromechanical Transducers: Fundamentals, Materials, Devices, Models and Applications of an Emerging Electroactive Polymer Technology.* (Elsevier Science, 2008).
125. Brochu, P. & Pei, Q. Advances in dielectric elastomers for actuators and artificial muscles. *Macromol. Rapid Commun.* **31**, 10–36 (2010).
126. Brochu, P., Niu, X. & Pei, Q. Acrylic interpenetrating polymer network dielectric elastomers for energy harvesting. in *SPIE Proceedings* **7976**, 797606–797606–8 (2011).
127. Ha, S. M., Yuan, W., Pei, Q., Pelrine, R. & Stanford, S. Interpenetrating polymer networks for high-performance electroelastomer artificial muscles. *Adv. Mater.* **18**, 887–891 (2006).
128. Cha, S. *et al.* Porous pvdf as effective sonic wave driven nanogenerators. *Nano Lett.* **11**, 5142–5147 (2011).

CHAPTER 3 Dielectric Composites

Abstract

In this literature review, the dielectric behavior of materials and polymers is discussed, with a focus on the general characteristics of dielectric composites. The dielectric laws and corresponding formulae—which describe homogeneous and composite materials including state-of-the-art nano-engineered dielectric materials—are explored. The effects of fillers—such as ceramics, metals, and organic substances that have exceptional properties on dielectric polymer composites—are discussed with respect to several engineering applications. Dielectric elastomer composites are also reviewed, and the effects of high-dielectric constant materials on actuation performance are discussed. Finally, a set of theories for characterizing the insulating properties of polymer composites and their dielectric constants are described and analyzed.

3.1 Dielectric Properties of Polymers

Dielectrics are insulating materials that do not conduct electricity. When such a material is placed between the electrodes of a parallel-plate capacitor, it brings about an increase in capacitance and exhibits a reversible orientation of molecules and electrons. This behavior is demonstrated under both low and high electrical fields. While low electrical field properties are related to chemical composition, high electrical fields properties are characteristics of dielectric strength. Under low electrical fields, it is possible to measure the dielectric constant, the dissipation factor, and the electrical conductivity of a dielectric. A high electrical field yields information about electric discharge, dielectric breakdown, and arc resistance¹.

3.1.1 Dielectric Constant and Polarization

The dielectric constant (denoted as k or ϵ) of a material is the ratio of the electrical permittivity of the material to the permittivity of vacuum and thus is a dimensionless quantity. The dielectric constant is also the ratio of the two capacitance measurements of parallel plate electrodes with and without insulating material placed between the electrodes. The polarization of the substance between parallel plate capacitors produces a disparity between two capacitance measurements, resulting in a capacitance increase. The relationship between capacitance, substance geometry, and dielectric constant is given in Equation 3.1.

The measure of electric charge storage in a dielectric is known as capacitance, C , and is calculated as follows:

$$C = \frac{\epsilon_0 \epsilon_r A}{t} \quad \text{Equation 3.1}$$

where ϵ_0 is the dielectric constant of the free space (8.854×10^{-12} F/m), A is the area of the electrical conductor, t is the thickness of the dielectric layer, and ϵ_r is the dielectric constant of the medium.

The dielectric constant measurement varies with frequency of alternating current, temperature, and voltage because, as a bulk property, the molecular structure of the material influences its charge storage and polarization under different conditions. The dielectric constant under the equilibrium electric field is known as the static dielectric constant, or low-frequency dielectric constant.

An increase in the frequency of the external electrical field during measurement is followed by a lag attributable to the dielectric relaxations in the medium. The dielectric constant of a medium is proportional to the total relaxations (i.e., polarizations) in the medium:

$$\varepsilon \propto P_{net} \quad \text{Equation 3.2}$$

where P_{net} is the net polarization of the system and ε is the dielectric constant of the medium.

In dielectric materials, unlike in conductors, charges are tightly held with associated protons. An electric field results in polarization that stores energy inside the material. Net polarization in a material results from the cumulative effect of the following five types of polarizations:

- Electronic
- Ionic
- Molecular (dipole)
- Interfacial (space-charge) polarization²⁻⁵
- Hyperpolarization⁶⁻⁸

These five polarization types are represented in Figure 3.1 and are described in more detail below. The equation for net polarization is as follows:

$$P_{net} = P_{electronic} + P_{ionic} + P_{molecular} + P_{interfacial} + P_{hyperpolarization} \quad \text{Equation 3.3}$$

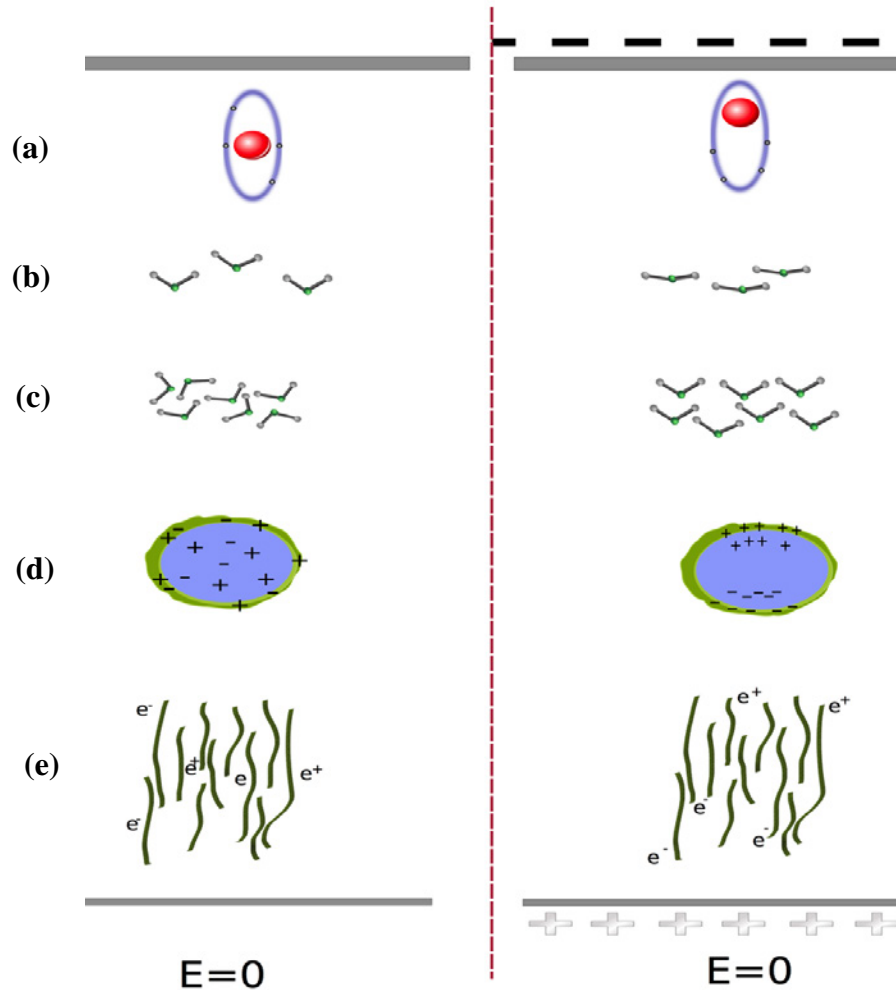


Figure 3.1 Schematic representation of the five types of polarizations: a) $P_{electronic}$, b) P_{ionic} , c) $P_{molecular}$, d) $P_{interfacial}$, e) $P_{hyperelectronic}$

Electronic polarization ($P_{electronic}$) is the displacement of electron clouds relative to the center of the atom under electrical fields. This displacement happens over a remarkably short period of time—about 10^{-15} sec. The dielectric contribution of electronic polarization is small compared to that of other polarization mechanisms, since the movements of the contributing electrons are small. Electronic polarization is calculated as follows:

$$P_{\text{electronic}} = \alpha_{\text{electronic}} E = 4\pi\epsilon_0 r^3 E \quad \text{Equation 3.4}$$

where r is the radius of the electron cloud around an atom^{2,5}.

Ionic polarization (P_{ionic}) is a shift of electrons within ionic substances. Specifically, it is an ionic movement from atoms that have extra charges, such as alkali halides, under electrical fields. These extra charges add up to an electronic polarization, and the movements store energy and increase material capacitance. Ionic polarization occurs around 10^{-15} sec and influences the dielectric constant to a lesser extent than does electronic polarization^{1,2,5,9}.

$$P_{\text{ionic}} = \alpha_{\text{ionic}} E \quad \text{Equation 3.5}$$

Molecular polarization ($P_{\text{molecular}}$), also known as dipolar polarization, occurs in substances that contain permanent dipole movement resulting from the unbalanced sharing of electrons by atoms within a molecule. The rotations of the permanent dipoles enable alignment with the external electric field, causing orientation polarization. Depending on the amount of frictional resistance present, a 10^{-12} - 10^{-15} sec frequency range is characteristic of this type of polarization. Even with zero electrical field conditions, molecular orientations cause local polarization to appear^{2,5}, as represented in Equation 3.6.

$$P_{\text{molecular}} = \alpha_{\text{molecular}} E = \frac{p^2}{3kT} \quad \text{Equation 3.6}$$

Interfacial polarization ($P_{\text{interfacial}}$) is a common phenomenon when materials with phase boundaries and voids are under alternating electrical fields. The accumulated charges at the

interphase of a transitional region create interfacial polarization. Trapped charges move with changes in frequency and depend on the interface bonding and interphase structure. The typical frequency range for this type of polarization is 10^{-3} - 10^3 sec²⁻⁵.

Hyper-electronic polarization ($P_{hyperpolarization}$) is a long-range molecular polarization observed in polymers and biopolymers. This type of polarization has been observed in highly aromatized eka-conjugated polymers (polyacene quinone radical [PAQR] polymers) that carry untied electrons and hole-type carriers. Long-range traveling of untied electrons along the polymer chain is the main cause of this nomadic molecular polarization. Hyper-electronic polarization is of greater magnitude than electronic polarization, and its characteristics include remnant magnetization, metallic conductivity, and unusual pressure sensitivity. Hyper-electronically polarizable materials exhibit high dielectric constants—up to 100,000—which makes them highly desirable for use in developing novel dielectric and optical materials¹⁰.

Hyper-polarization has also been observed in biomacromolecules. One such substance is the highly polarizable biological molecule elastine which is found in the human ear. This molecule is responsible for converting sound vibrations to neuroelectrical signals¹¹. The frequency dependency of each polarization mechanism is shown in Figure 3.2.

The dielectric constant of a non-polar material is proportional to square of its refractive index. However, this relation can rarely be observed experimentally because the two measurements are frequency-dependent and measured in different frequencies.

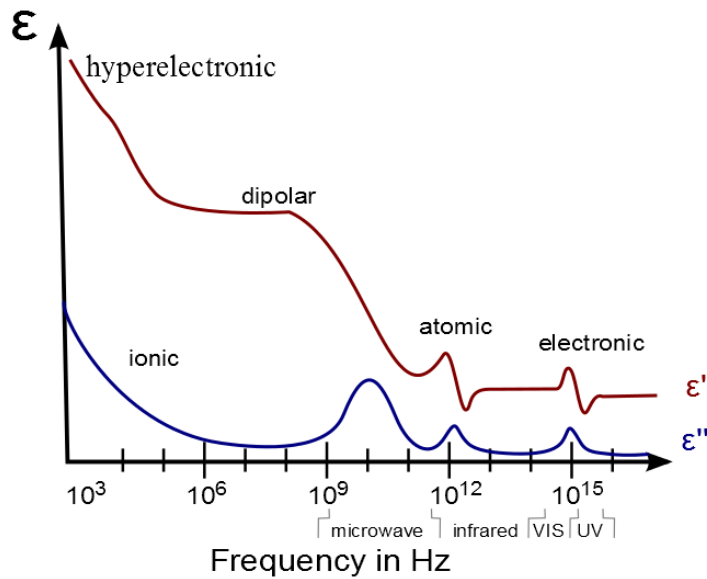


Figure 3.2 Dielectric behavior versus frequency.

3.1.2 Dielectric Loss

Dielectric loss is the imaginary part of the complex dielectric constant, and it provides information about the electrical inefficiency of a dielectric material. The dielectric constant and dielectric loss together form a complex number that indicates the relative actual polarizations and actual losses of a dielectric system.

$$\boldsymbol{\varepsilon} = \boldsymbol{\varepsilon}' - i\boldsymbol{\varepsilon}'' \quad \text{Equation 3.7}$$

The imaginary part of this number is calculated from the response delay of capacitance under an applied electric field. This delay is frequency-dependent and is shown as loss tangent, $\tan(\delta)$, or dissipation, D . The quality factor, Q , is another representation of dissipation in a dielectric system. Q is the inverse of the dissipation factor.

$$D = \frac{\epsilon''}{\epsilon'} = \frac{1}{Q} \quad \text{Equation 3.8}$$

Considering the effect of conductivity, the dielectric constant is expressed as follows:

$$\epsilon = \epsilon' + i \frac{\sigma}{\omega \epsilon_0} \quad \text{Equation 3.9}$$

and the dissipation is expressed as:

$$D = \frac{\epsilon''}{\epsilon'} + \frac{\sigma}{2\pi f \epsilon} = \frac{1}{Q} \quad \text{Equation 3.10}$$

where ϵ' and ϵ'' are the real and imaginary parts of the dielectric permittivity, respectively; σ is the electrical conductivity of the materials; f is the frequency; and Q is the quality factor of the dielectric substance.

Dielectric losses arise from conductivity, molecular relaxations, polarizations, and interfacial polarizations in the material. Conduction loss, attributed to the DC electrical conductivity of the material, represents the flow of the actual charge through the dielectric materials. Interfacial loss originates from the excessively polarized interface induced by the fillers, more specifically from the movement or rotation of the atoms or molecules in an alternating electric field. The losses arising from ionic conductivity and relaxations of polarizations are depicted in Figure 3.2. Any high-dielectric constant material is a candidate for use in most capacitor applications if the dielectric loss has a small value—i.e., 0.01 or lower.

3.1.3 Dielectric Spectroscopy of Polymers

Dielectric spectroscopy is an instrumental method of exploring molecular structure, conformation, and dynamics through inferences from dielectric responses over varying frequencies and temperatures. Dielectric spectroscopy has been used to:

- document the dielectric behavior of well-known polymers,
- relate mechanical, NMR, relaxation, and dielectric properties,
- gather more information about dielectric relaxation of polymers through comparison of results with theoretical values,

In dielectric spectroscopy, applying an alternating electrical field, E_w , results in the polarization, P , of the material. The polarizations inside the material give molecular-level information about the test material based on changes in the electrical field over a wide frequency range.

Since dielectric elastomer transducers are amorphous, the dielectric behavior of amorphous polymers is particularly noteworthy. Amorphous polymers show dielectric loss spectra of α -relaxation, β -relaxation, and normal-mode relaxation. Normal-mode relaxation occurs over frequencies below the α -relaxation peak. It is explained by complete chain motion of the polymer.

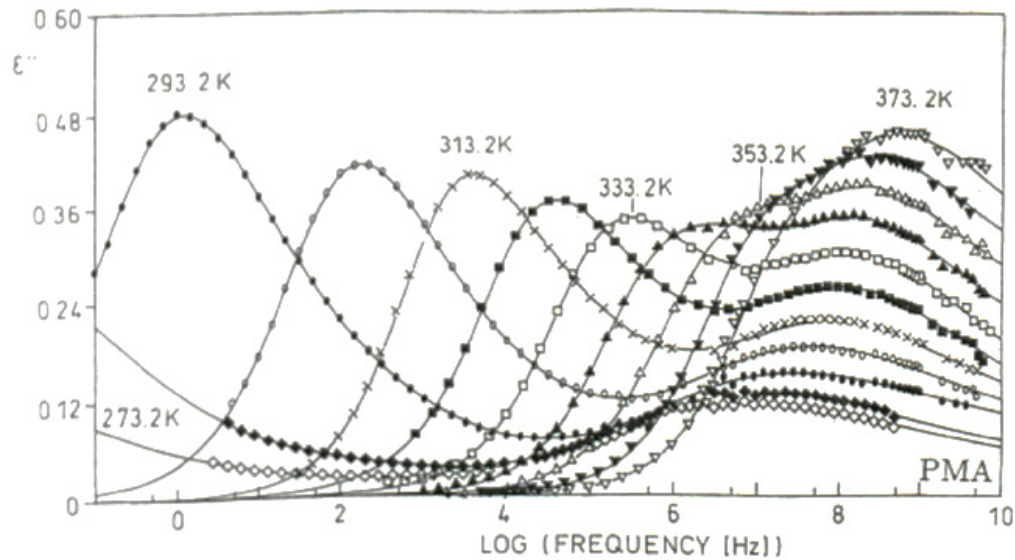


Figure 3.3 Dielectric loss spectra of polymethylacrylate¹².

β , α , and normal-mode relaxation all have unique relaxation rates, relaxation strengths, and loss-peak shapes. β -relaxation is based on local dipole movements, and its relaxation rate shows Arrhenius-like behavior, as shown in Figure 3.3. The β -relaxation loss peak is symmetric and is 4 to 6 decades wide. A temperature increase decreases the width of the β -relaxation loss peak. Although β -relaxation has been observed below temperature T_g , broadband studies also show β -relaxation occurring at temperatures above T_g .

α -relaxation loss refers to the glass transition of material at a dielectric frequency of 10^{-3} Hz and corresponds to the T_g value of differential scanning calorimeter (DSC) measurement. The glass transition temperature depends on micro-Brownian segmental motions of the chains. For bulk polymers, intermolecular interactions also contribute to α -relaxation. The

relaxation rate is described by the Vogel-Fulcher-Tammann (VFT) equation for amorphous polymers. The α -relaxation peak has an asymmetric shape with a width of 2-6 decays, depending on the measurement temperature and cross-linking density of the polymer. Increasing the temperature decreases α -relaxation and merges the α - and β -relaxation peaks.

Dielectric normal-mode relaxation is observed in polymers that have parallel dipole side groups on their polymer backbone. The parallel-placed dipoles in the polymer chain and the chain relaxations contribute to this relaxation. These relaxations provide information about the structure and dynamics of the polymer chains. Dielectric loss data are analyzed with the Cole-Cole, Cole-Davidson, and Fuoss-Kirkwood functions, all of which provide better representations of the origins of molecular-level relaxation than that provided by frequency-dependent raw dielectric data¹²⁻¹⁴.

3.1.4 Dielectric Breakdown

Dielectric strength is an intrinsic property that characterizes any homogeneous, pure material and is measured through the application of high voltage to the dielectric material for a short period. Electrical breakdown is the catastrophic failure of solid or liquid insulators under such high-voltage electrical fields. In a dielectric breakdown test, several breakdown mechanisms can be observed:

3.1.4.1 Erosion Breakdown

There are defects in the forms of voids and cavities within the dielectric material and/or in the boundaries between the electrode and the solid. These voids usually have lower breakdown strengths than the dielectric medium itself. While the field intensity in the cavity

is higher than in the dielectric material, voids reduce the permittivity of the filling medium, causing its dielectric erosion.

3.1.4.2 Streamer Breakdown

In a dielectric system, as an electron enters the conduction band of the dielectric at the cathode, it moves toward the anode under the electrical field. The electron releases energy via electron collisions. In some cases, the free path before a collision is long, and, as a result, an additional electron is produced after collision. Eventually, after many repetitions, a gas-like electron avalanche forms. Streamer theory explains that dielectric breakdown begins after this avalanche reaches a crucial size.

3.1.4.3 Edge Breakdown and Treeing

In insulation systems in which the solid is electrically stressed within another solid or gas material, the weaker medium will influence breakdown voltage to a greater extent than the stronger medium. This breakdown from weaker substance to stronger substance results in the formation of a single discharge channel, leading to the formation of a tree-like structure.

3.1.4.4 Electromechanical Breakdown

The application of high voltage increases the electrostatic attraction and repulsion of surface charges insulator, resulting in stress in the thickness direction of an insulator. Before dielectric breakdown, this stress is in equilibrium with mechanical compressive stress at the outside of a material along the thickness axis. If the electrostatic pressure is higher than the mechanical stress, then electromechanical breakdown will occur. This breakdown works as a constraint, playing a significant role in determining the limits of an electrostatic actuator.

3.1.4.5 Thermal Breakdown and Tracking

Dielectric loss is a significant parameter in selecting the materials for insulation applications. Dielectric losses cause heat production in the medium due to polarization and conductivity. Because heat enhances the conductivity of the medium, dielectric loss ultimately leads to material instability and thermal breakdown.

Tracking is the formation of a conducting path across a surface of insulation as a result of degradation. This degradation takes the form of carbonization and volatilization of the insulating material due to heat created by tiny sparks. Adding suitable fillers to a polymer inhibits carbonization and reduces tracking rates. Polymer structure also affects tracking rates.

For a dielectric material, charge capacity is limited by dielectric breakdown field limits. The maximum electrical field before breakdown determines the breakdown charge capacity, or breakdown Maxwell pressure, for a dielectric elastomer:

$$P_{\text{maxwell}} = \epsilon_0 \epsilon_r (E_{\text{break}})^2 \quad \text{Equation 3.11}$$

where E_{break} is the electrical field at the point of material breakdown. E_{break} is lower for polymer composites than for pure polymers, displaying a substantial decrease in material dielectric strength.

A very rough schematization of dielectric breakdown voltage limits can be calculated if the polymer is assumed to be a purely elastic, homogeneous material at low strains. Under such

conditions, and in the case of Maxwell-stress actuation, the nominal breakdown field of the material is given by the following equation:

$$E_{\text{break}} = \frac{V_{\text{break}}}{d_0} = e^{-1/2} \sqrt{\frac{Y}{2\varepsilon_0\varepsilon'}} \cong 0.6 \sqrt{\frac{Y}{2\varepsilon_0\varepsilon'}} \quad \text{Equation 3.12}$$

where ε' is the dielectric permittivity of the material, Y is its elastic modulus, V_{break} is the breakdown voltage of the sample, and d_0 is its thickness at rest. This equation shows that increasing the dielectric permittivity of a polymer leads to a decrease in its dielectric strength. A local field theory of dielectric media assumes that the local breakdown field of the matrix is the same, with the matrix breakdown field in the composite form¹⁵:

$$\frac{\varepsilon'_m + 2}{3} E_{\text{break},m} = \frac{\varepsilon'_c + 2}{3} E_{\text{break},c} \quad \text{Equation 3.13}$$

However, Equation 3.13 is correct if the polymer is assumed to be homogeneous; polymer composites also follow this relation¹⁶. Moreover, dielectric mixing rules must be taken into account if these equations are to be applied to polymer composites.

3.1.5 Charge Transport in Polymers and Nanocomposites

There are two types of carriers in polymers: electrons (holes) and ions. The free volume amount is important for ionic charge transport in polymers; a decrease has been reported in ionic conductivity under pressure¹⁷, resulting from a decrease in free volume.

Charge transport in an insulating system, J , is measured by current density and depends on electrical field, E , and conductivity, σ :

$$J = E\sigma \quad \text{Equation 3.14}$$

For metals and semiconductors, σ is calculated as follows:

$$\sigma = (ne\mu_n) + (pe\mu_p) \quad \text{Equation 3.15}$$

where e is the elementary charge of a proton (1.602×10^{-19} C); μ_n and μ_p are the mobility of electrons and holes, respectively; n is the concentration of electrons; and p is the concentration of holes.

While well-known equations such as Equation 3.14 and Equation 3.15 fit all materials universally, these equations are also well suited for describing polymers. However, for a polymer, both amorphous and crystalline regions must be accounted for to understand charge transport. In crystalline regions, charge delocalization is possible, and charges are expelled to amorphous regions, where it is possible to observe hole movements¹⁸.

In semi-crystalline polymers, such as polyethylene, transport mechanisms depend on different regions. While crystalline regions show evidence of injections, combinations, and anion electron generation, amorphous regions show evidence of charge-trapping and space charges¹⁸. Various mechanisms of electrical transportation for polymer insulators are summarized in Figure 3.4.

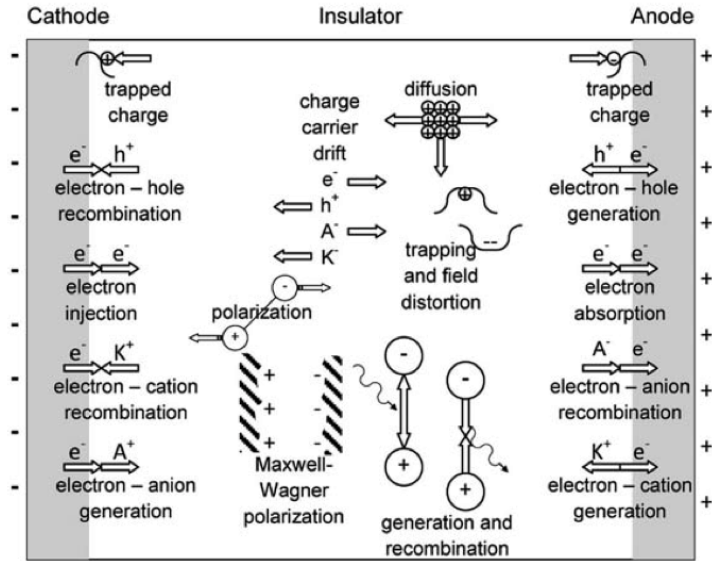


Figure 3.4 A wide variety of charge transports in an insulator¹⁸.

Understanding the distribution of charges along the cross-section of a dielectric medium is extremely important for understanding the high-voltage behavior of polymers and their composites. For a parallel-plate capacitor, electrodes behave like n^+ , while the insulator has more holes and is considered p^- . As holes and electrons combine, the excess electrons produce a space charge, called a “homocharge,” that gathers around the cathode. The anode has a large quantity of negative space charges due to hole injection, which causes field enhancement at this electrode. This negative field enhancement is known as “heterocharge” (see Figure 3.5).

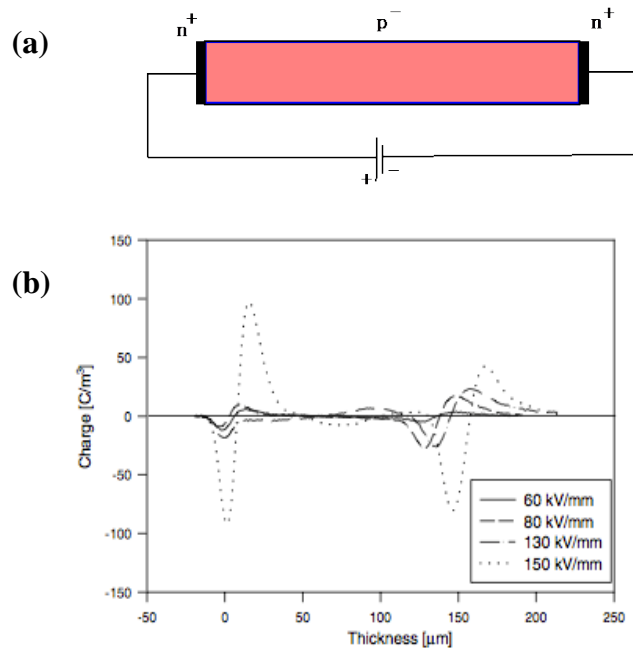


Figure 3.5 a) Schematic representation of p^- and n^+ regions of an insulating polymer; b) the accumulation of heterocharges and homocharges over an insulator in the first 10 sec of voltage application under various electrical fields. Right: cathode; left: anode¹⁹.

The Stern layer consists of the atom layers responsible for charge accumulation on electrode surfaces and particle surfaces (see Figure 3.6). This structure has a significant impact on dielectric measurements and mechanisms because of electrode polarization and electric field distribution^{18–20}.

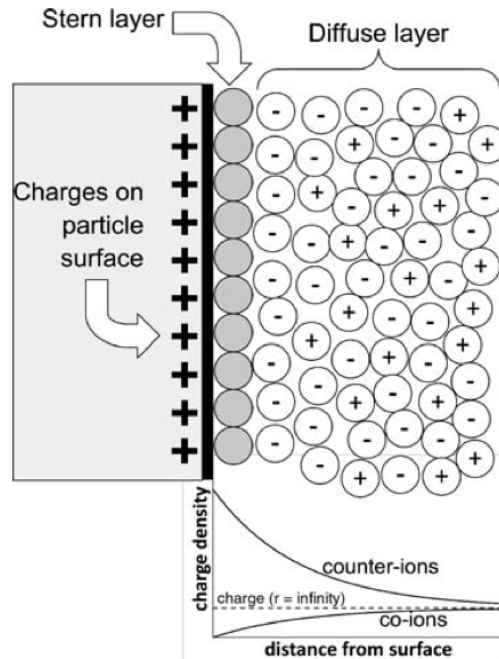


Figure 3.6 Stern diffuse double layer produced by nanoparticles on a charged surface within a dielectric composite¹⁸.

3.2 Dielectric Constant Enhancement

One of the major challenges in the development of dielectric elastomer actuators is the high electrical field requirement—actuating these elastomer films requires voltages of up to 400 V/ μm . This high electrical field requirement is typically addressed by lowering the electrical field in a number of ways, one of which is to use dielectric fillers to increase the dielectric constant so as to reduce the required field for a certain strain. Other common methods used to increase the dielectric constant of a medium include making use of the interfacial polarization and Coloumb Blockade. These methods are discussed in later sections.

3.2.1 Interfacial Polarization

Interfacial polarizations arise around the fillers or defects in a dielectric. Dielectric fillers with dimensions below 200nm have different properties than do those with larger size fillers. (This difference is reviewed further in Sections 4.3.1 and 4.3.2.) The scaling law that applies to comparable quantities does not represent the nanodielectric composites. Since interfaces dominate dielectric behavior at nano-size, they become extremely important for nanodielectrics⁴.

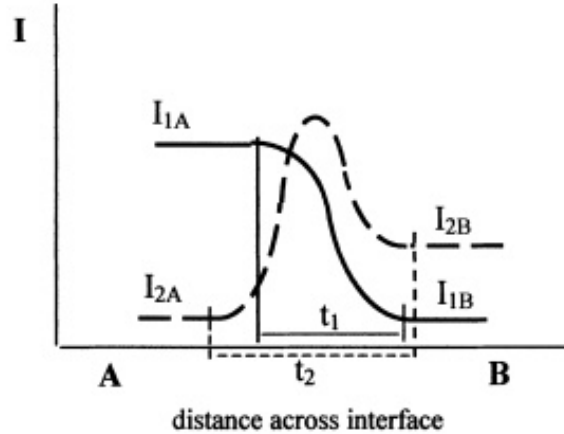


Figure 3.7 Effect of particle interface size (in nm) on intensity of physical properties⁴.

Over a gradient between two materials, interface properties can have a gradually changing impact, or the interface can have characteristics distinct from those of the two materials themselves. This behavior is shown in Figure 3.7 Intensity, I_1 , shows the behavior of properties like concentration of materials and energy density. These properties show a gradual change throughout the interphase. I_2 type properties, such as metal-dielectric contact

and electron concentration (depicted in Figure 3.8), electron hole concentration, mechanical stress, and interfacial surface energy show a peak behavior throughout the transition between the two materials.

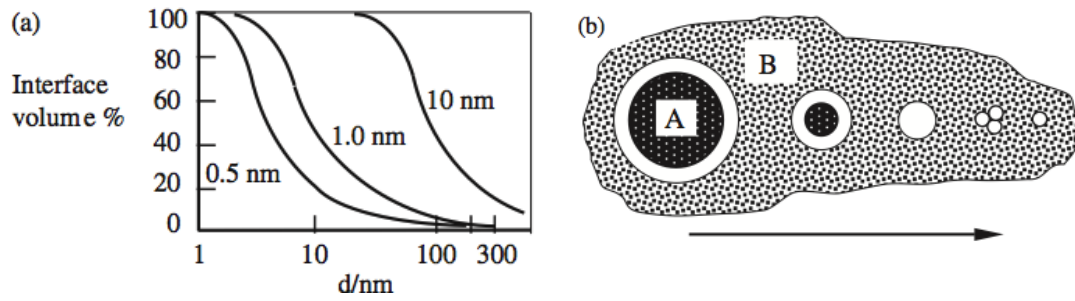


Figure 3.8 Increase of interface volume (a) Relationship between filler diameter versus interface volume, representation of relationship given in plot. (b) In image A is filler B is matrix⁴.

These interface properties become meaningful when long-range forces are around 10nm. The influence of the interface can be controlled by a reduction in particle size and an increase in volumetric concentration. The surface conductivity of the particle interfaces also influences the dielectric constant, ϵ , by producing dipoles at low frequencies^{21,22}.

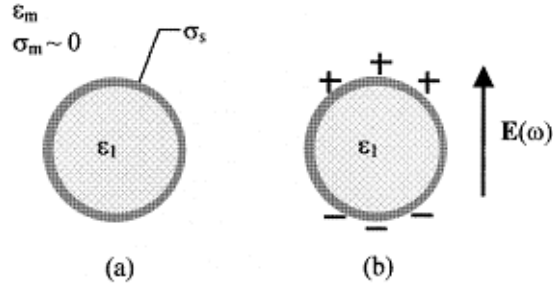


Figure 3.9 The O'Konski model assumes a conductive interface layer on a particle: (a) $E = 0$, (b) $E \neq 0$.

The O'Konski model⁴ explains the induced dipoles along the surface of a particle and the interphase polarizations between the dielectric filler and the polymer matrix. The long-range movement of charges around the filler results in accumulation of like charges around the particle, the whole charge distribution in media become heterogeneous under varying electrical fields. Figure 3.9(b) depicts the distribution of surface charges varying with electrical field.

3.2.2 Coulomb Blockade (CB) Effect of Metal Nanoparticles

The Coulomb blockade is the increase in resistance at low-bias voltages in a metal-polymer composite. The metal nanoparticles in a matrix can present a blockade to electrons because of an island-sea arrangement, observed as a single electron tunnel junction. The dielectric loss of the conductive filler-polymer composite shows evidence of single-electron tunneling inside a polymer matrix^{23,24}. These conductive nanoparticles behave like an infinite number of series capacitors inside the polymer matrix (see Figure 3.10 for a representation of this model). Furthermore, these particles increase the capacitance and resistance of the polymer

composite due to electron blockades. Lu et al.²⁵ report that silver nanoparticles, in situ-synthesized in an epoxy resin, show lower dielectric loss than a pristine polymer with lower concentrations due to the effect of the Coulomb blockade.

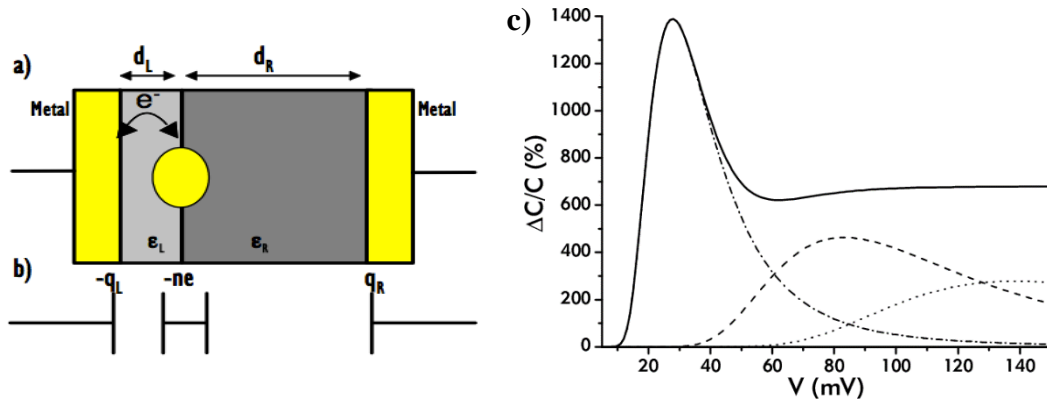


Figure 3.10 a) Schematic representation of a Coulomb blockade; b) model of the structure as two capacitors in a series; c) capacitance performance versus voltage results computed theoretically²⁶.

3.3 Dielectric Polymer Nanocomposites

Nanodielectrics are dielectric materials consisting of more than one species, at least one of which is less than 100nm dimensions in size^{21,22,26–28}. Nanodielectrics differ from other dielectric composites in the following ways²⁹:

- They have higher dielectric constants.
- They display a linear increase in breakdown with increasing filler concentration.
- They display a higher endurance strength than that of their matrix and fillers.

Because of their relatively high energy density, low cost, high reliability, high electric breakdown field, and low dielectric loss, dielectric polymer nanocomposites are of interest in many applications, including electrical energy storage, electronic packaging, high energy-density applications^{30,31}, and electrical insulation.

The preferred process for working with high-*k* dielectric composite fillers is to convert them into nanodielectrics by introducing nanoparticles. These dielectric composites can help achieve thinner dielectric films, which result in higher capacitances. Therefore, more nanoparticles of ceramic, metallic, or even organic semiconductors have recently been introduced into the preparation of high-*k* dielectric materials³²⁻³⁹.

Polymer nanocomposites can be processed using any one of four known methods:

- In situ polymerization
- Melt blending
- The solvent casting method
- The sol-gel method

The in situ polymerization and melt blending methods are the most commonly used techniques for manufacturing thermosetting and thermoplastic polymers and nanoparticles.

3.3.1 Polymer Nanocomposites

The main advantage of in situ polymerization of composites is that it enables grafting of nanofillers onto polymer chains or side groups. This technique is particularly useful for the preparation of insoluble and thermally unstable polymers, which cannot be processed through

solution or melt methods. Depending on the polymer's required molecular weight and molecular weight distribution, chain transfer, radical, anionic, and ring-opening metathesis polymerizations can be used for in situ polymerization processing.

Melt blending is a method for processing thermoplastic polymers through high temperatures. The main advantages of this technique are fast processing times and simplicity. Amorphous polymers can be processed above their glass transition temperature, and semi-crystalline polymers show softening behavior above their melting temperatures.

Melt blending is a method for processing thermoplastic polymers through high temperatures. The main advantages of this technique are fast processing times and simplicity. Amorphous polymers can be processed above their glass transition temperature, and semi-crystalline polymers show softening behavior above their melting temperatures.

The solvent casting method is all solution-processing method. It follows these processing steps:

- Dispersion of particles in either a solvent or a polymer solution through energetic agitation.
- Mixing of nanoparticles and polymers in a solution through energetic agitation
- Controlled evaporation of a solvent, which leaves a composite film

3.3.2 Ferroelectric Ceramic/Polymer Composites

High- k ceramics have been widely investigated as fillers for polymer composites in various dielectric applications, such as embedded capacitors, dielectric elastomers, and energy

storage. A ceramic dielectric filler is classified as belonging to one of three different categories depending on its permittivity:

- Low permittivity (ϵ up to 15)
- Medium permittivity (ϵ between 15 and 500)
- High permittivity (ϵ between 500 and 20,000)

BaTiO₃ is an example of a high-permittivity material. TiO₂ lies in the medium range, while silicates are in the low-permittivity range³⁰. Incorporation of ceramic fillers into a polymer matrix increases the composite dielectric constant, which is calculated from the ratio of the polymer matrix volume to the ceramic filler volume. The composite dielectric constant therefore lies somewhere between the polymer dielectric constant and the ceramic dielectric constant. This method of incorporating ceramic fillers into a polymer matrix combines the advantages of polymer properties and polymer processing with the advanced dielectric properties of ceramics such as lead titanium oxide (PbTiO₃), lead zirconate titanate (Pb(Zr,Ti)O₃), PMN-PT (Pb(Mg_{1/3}Nb_{2/3}O₃) ± PbTiO₃), lead magnesium niobate-lead titanate (PMN-PT), barium titanate (BaTiO₃), and titanium dioxide (TiO₂). Although both filler and matrix components have unique properties, combining matrix and filler in a composite and retaining the properties of each in their entirety is challenging.

Incorporation of ceramic fillers into a polymer matrix increases the composite dielectric constant, which is calculated from the ratio of the polymer matrix volume to the ceramic filler volume. The composite dielectric constant therefore lies somewhere between the polymer dielectric constant and the ceramic dielectric constant. This method of incorporating

ceramic fillers into a polymer matrix combines the advantages of polymer properties and polymer processing with the advanced dielectric properties of ceramics such as lead titanium oxide (PbTiO_3), lead zirconate titanate ($\text{Pb}(\text{Zr,Ti})\text{O}_3$), PMN-PT ($\text{Pb}(\text{Mg}_{1/3}\text{Nb}_{2/3}\text{O}_3) \pm \text{PbTiO}_3$), lead magnesium niobate-lead titanate (PMN-PT), barium titanate (BaTiO_3), and titanium dioxide (TiO_2). Although both filler and matrix components have unique properties, combining matrix and filler in a composite and retaining the properties of each in their entirety is challenging.

In its early phase, polymer dielectric research focused on incorporating micron-sized ceramics into polymer matrices. Larger ceramic fillers exhibit considerably higher permittivity than nanoparticles due to the effect of the crystal structure of ceramic fillers. Additionally, the polymer morphology is not affected for larger ceramic-polymer composites: End-chain or side-chain structure is not hindered by ceramic fillers⁴⁰⁻⁴².

Because of their highly polar crystal structure, barium titanate (BaTiO_3) fillers allow for the production of reasonably high-dielectric constant composites. Particle size affects the cooperative movements of dipoles and can change the alteration of particle crystal structures from tetragonal to cubic or pseudocubic. The particle's size affects the crystal structure of the ceramic. Thus, this change in size results in the phonon softening of a particle, which contributes to the spontaneous polarization of the material⁴¹. This crystal structure modification is because of BaTiO_3 's low permittivity.

Kakimoto et al.⁴⁰ used barium titanate to study the effect of particle size on dielectric composites. Their results show that the dielectric constants of BaTiO_3 suspensions from large

BaTiO₃ fillers (>300nm) do not increase, while the dielectric constant of suspensions does increase with smaller particle sizes, of 70-200nm. The dielectric constant of BaTiO₃ is reported to be around 1,500 for BaTiO₃ suspensions at 70nm, so this particle size of 70nm is the optimum particle size for BaTiO₃ because it has the highest dielectric constant for nanoparticles^{40,42}.

Increasing the amount of ceramic filler in a polymer composite is an effective method for obtaining a high-*k* composite. A drawback of this method, however, is the loss of the unique and desirable properties of pure polymers, such as low modulus and low flexibility. Poor dispersion of particles, poor adhesion at the particle/matrix interface, and trapped air in the composite may cause undesirable problems in polymer composites⁴³.

However, due to their crystal structures and sizes, not all nanoparticles show the cumulative effect of polarization shown by micron-sized particles. The nanofillers have a higher ratio of surface area to volume than other fillers, and they display an increase in dielectric constant. Ceramic nanofillers lead to improved homogeneous internal charge distribution within a composite material and increased material dielectric strength^{20,44}. Ceramic nanofillers also affect polymer cohesive energy density and free volume.

Nelson et al.⁴⁵ studied 23-nm and micron-sized TiO₂ fillers in an epoxy-based matrix. A pulsed electroacoustic measurement method was developed to determine the inner charge distribution of a polymer composite. In inner charge distribution experiments, researchers observed that the theory of interfacial polarization did not explain the organization of TiO₂ in composites. Extremely small TiO₂ particles move together with the polymer host under an

electrical field. A 10% loading was suggested for nanoparticles to provide optimally improve in a composite's mechanical and electrical properties²⁰.

Nanoparticle dispersion and the adhesion between the nanoparticles and the polymer matrix were increased using several techniques, including in situ polymerization of particles in the matrix and surface functionalization of the nanoparticles⁴⁶⁻⁴⁸. Core-shell structures, as shown in Figure 3.11, were obtained by applying electrostatic forces to the surfaces of barium titanate nanoparticles⁴⁹. Core-shell nanoparticles were also used, and the matrix was prepared through in situ polymerization. These techniques improved the polymer composites by increasing the dielectric constant of these films; their mechanical properties and dielectric loss values were comparable to those of neat polymers⁵⁰.

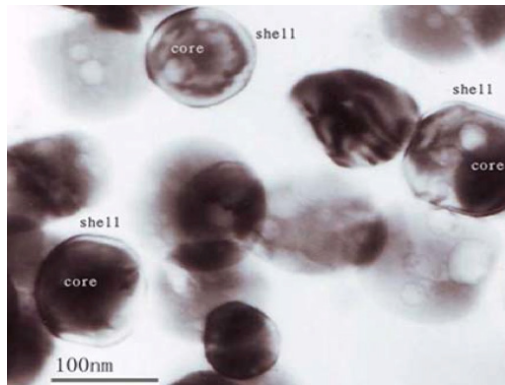


Figure 3.11 TEM image of BaTiO₃/PI composite film made through in situ polymerization with BaTiO₃⁵¹.

Imperfections in the dielectric and mechanical properties of polymer-ceramic composites occur due to a lack of interfacial bonding between the ceramic particles and the polymer

matrix. Therefore, the formation of chelation bonds at the interfaces of the polymer and the ferroelectric ceramics can improve interfacial adhesion and interfacial charge transfer and thereby enhance the electric properties of composites. Yao et al.⁵¹ report a novel method for developing an ultra-high-dielectric constant material with polarizations arising from interface charges and losses due to interfacial polarization. The increase of dielectric constant was due to conductivity and was accompanied by an exponential increase in loss. Yao et al.⁵¹ also present spectroscopic evidence of decreasing loss with increasing temperature as proof of interfacial polarizations along the interface of PZT-VAMA-PVDF.

0-3 composites are random polymer composites of hard particles connected in zero dimensions and of a soft polymer matrix fully connected in three dimensions. A 0-3 piezoelectric composite is made up of piezoelectric ceramic particles dispersed throughout a polymer matrix⁵². The dielectric constant of the polymer matrix has a dominant effect on the dielectric constant of 0-3 (random) composites. For example, a 0-3 composite composed of $\text{CaCu}_3\text{Ti}_4\text{O}_{12}$ ($\epsilon = 20,000$) and P(VDF-TrFE) shows a high dielectric constant of 610 at 100 Hz at room temperature. This composite has been reported to have a dielectric constant only 3% greater than that of filler⁵¹. Ceramic-polymer composites were shown to require a high loading level of ceramic fillers to achieve high dielectric constants⁹.

Nanoclay silicate montmorillonite nanoparticles have been used to enhance the dielectric constant of epoxy resin. Isomorphous substitution within the epoxy layers creates intrinsic surface-negative charges, which cause orders-of-magnitude increases in the nanocomposite's

dielectric constant. These intrinsic charges have been reported to also improve ionic conductivity⁵³.

Bimodal distribution of ceramic nanoparticles within a matrix is a recognized way of increasing the dielectric constant of polymer composites. Tummala et al.⁵⁴ report that a bimodal distribution of ceramic-epoxy composites yields a dielectric constant of 135 due to the packing improvement.

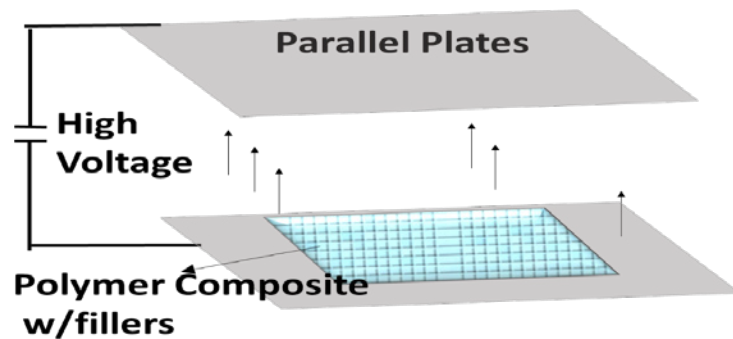


Figure 3.12 Electrical field alignment of fillers in a polymer composite.

Changing the spatial distribution of fillers in the polymer matrix can enhance the dielectric properties of 0-3 composites. The application of an electric field to a polymer composite in its pre-cured form, as shown in Figure 3.12, aligns nanoparticles according to field. These composites are termed 1-3 composites when particles are aligned in the z -direction. Tomer et al.⁵⁵ investigated the effect of electrical field alignment of nanoparticles on the dielectric constant of a composite material. In a 1-3 dielectric composite, orientation in the z -direction increases the dielectric constant and decreases the dielectric loss. The application of an

electric field in the x - y plane results in the alignment of nanoparticles parallel to this plane. The electrical field-aligned composites have slightly higher dielectric constants and lower dielectric losses than 0-3 composites⁵⁵.

3.3.3 Metal Filler-Polymer Composites

The use of conductive fillers is an effective method for producing high- k materials. Conductive fillers have been investigated for use in applications such as embedded capacitors, supercapacitors, dielectric elastomers, antennas, sensors, and energy generators. The adhesion strength between filler and matrix and the consequent balance in mechanical properties cause this class of fillers to be preferred over polymer/ceramic composites.

Various types of metallic fillers, along with other conductive fillers, have been introduced for the purpose of increasing the dielectric constant of polymer composites. Metal nanoparticles such as nickel, cobalt, silver, aluminum, and steel—as well as organic conductive materials such as carbon nanotubes, polyanilines, and polythiophenes—have been extensively investigated as percolative dielectric materials. They have also been combined to form multiphase percolative composite systems. Organic conductive fillers are discussed in the next section of this review.

Composites containing metallic fillers exhibit extremely high dielectric constants, observed in the vicinity of the critical filler concentration, which is known as the percolation threshold. For polymer-conductive filler composites, the formation of conducting paths is explained by

percolation theory. The dielectric constant of a percolative composite system is expressed as follows:

$$\epsilon_r = \frac{\epsilon_D}{f - f_c} \quad \text{Equation 3.16}$$

where ϵ_D is the dielectric constant of a polymer matrix, ϵ_r is the relative dielectric constant of the insulating matrix, f is the percolation threshold concentration, and f_c is the concentration of actual filler.

The increase in dielectric constant for a percolative filler is presented by the power law:

$$\epsilon_r = \left| \frac{\epsilon_D}{f - f_c} \right|^{-q} \quad \text{Equation 3.17}$$

where q is the critical exponent of the dielectric constant. Bergman and Imry^{56,57} derived formula in Equation 3.17, which describes the behavior of this power law in the vicinity of the percolation threshold:

$$\epsilon(w, p_c) w^{-y}, \sigma(w, p_c) wx \quad \text{Equation 3.18}$$

where $x + y = 1$. Expression given in Equation 3.18 models the effects of metal clusters on the dielectric constant and on conductivity, since polarization effects and electronic diffusion vary inside clusters.

While the real part of the dielectric constant benefits from conductive fillers, the imaginary

part also increases dramatically due to conductive paths established inside the material. High proximity and high contact of these metal fillers increase the dielectric constant and dielectric loss. Above the percolation threshold, the composite will be a conductive one. This drawback, the formation of percolation paths, has been addressed primarily through manipulating the filler size and shape, tailoring the Ligand Shell metal core, and 3-1 dimensional aligning of the metal nanoparticles⁵⁸.

As discussed earlier, space charge, interphase polarization, and Coulomb blockade effects arise from this kind of polymer-filler integration. Exploiting this polarization in different size regimes is practical. Dang et al.⁵⁹ used 5- μm Ni particles to engineer a PVDF matrix as a composite in the vicinity of a 0.18 percolation threshold. A large dielectric constant of more than 400 and increased conductivities ranging from 10^{-9} S/m to 10^{-3} S/m were reported where filler loadings were below percolation thresholds.

A nanoparticle supercapacitor polymer network is a polymer composite with a high dielectric constant and high electrical resistance. It consists of metal nanoparticles in a polymer matrix and shows a Coulomb blockade effect, the single-electron charging effect observed in “island-sea” type structures, in which tunneling is isolated in localized electron regions. An extremely small filler size increases resistance at the percolation threshold. Whereas filler size and concentration increase a composite’s dielectric constant, the Coulomb blockade effect decreases its dielectric loss. As seen in Figure 3.13, the effects of silver concentration on dielectric constant and dielectric loss are significant in epoxy composites²³.

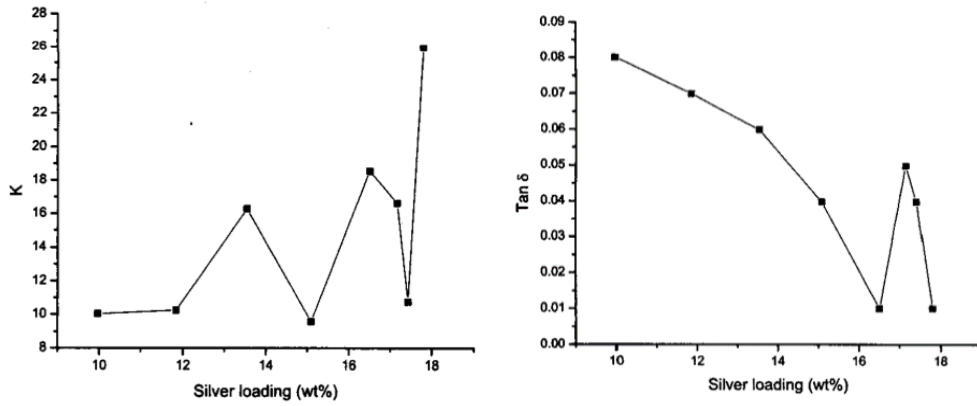


Figure 3.13 Dielectric behavior of silver (20 nm) epoxy nanocomposites²⁵.

The dielectric behavior of nanocomposites at concentrations below the percolation threshold has been studied using a PVDF polymer matrix and steel fiber fillers with a diameter of 30 μm and a length of 500 μm . An increase in effective tunneling distances with one-dimensional fillers was observed at low concentrations. The increase in dielectric constant below percolation follows the power law of classical scaling theory, at 9.4 vol% of steel-fiber filler⁶⁰, with a boundary-level capacitance effect due to interface polarization. Dielectric loss and electrical conductivity were observed to increase according to the power law at the percolation threshold for metal fillers^{61,199}.

$$\varepsilon_c \propto (f_c - f_{filler})^{-s}, f_c > f_{filler} \quad \text{Equation 3.19}$$

Interphase polarization was also calculated for filler surface area. For example, consistent dielectric constants and dielectric losses over a high-frequency sweep (up to 10 MHz) indicated a dipolar polarization in the system in polyimide (PI)-alumina nanocomposites. A

dipolar polarization in the interphase has been associated with particle surface area. PI-alumina composite (in which alumina filler size is 10nm) exhibited an increase in dielectric constant from 3.5 to 15 at 20 wt% concentration, primarily due to interphase polarizations. This increase was verified through filler surface area calculation⁶².

The Gor'kov-Eliashberg effect, also known as the strand theory of metal nanoparticles, has been observed in metallic nanowires under the application of electric fields. Percolation effects increase the dielectric constants of composites tremendously under electrostatic alignment, with the use of nanorods and nanowires of gold, silver, and polypyrroles. An extremely high dielectric constant of 10^5 was observed⁶³; this can be explained by strand theory. Ultrafine metal particles were elongated to form metal filaments in the direction of the electric field. According to strand theory:

$$\varepsilon \approx (q_s l_0)^2 \quad \text{Equation 3.20}$$

where q_s is the Fermi-Thomas screening wave vector and l_0 is the strand length of the fillers. An application of bias voltage brings about the heating and alignment of the wires and forms an assembly of ultrafine metal particles.

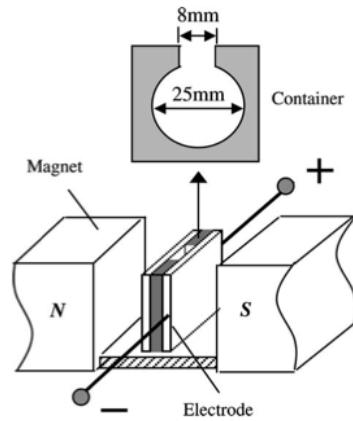


Figure 3.14 Curing of composite samples under external magnetic and electrical fields³⁵.

The simultaneous application of electric and magnetic fields to a polymer composite in the course of matrix curing, as depicted in Figure 3.14, forms one- to three-dimensional composites for metal nanoparticles. The DC resistivity, dielectric constant, and dielectric loss of a composite are controlled through alignment of the fillers along the x - and y -axes. This alignment increases the percolation threshold by decreasing the conductivity along the z -axis.

Phase velocity (v), electromagnetic radiation over the medium, is influenced by both the permittivity (ϵ) and permeability (μ) of the medium, as follows⁶⁴:

$$v = \sqrt{\frac{1}{\epsilon\mu}} \quad \text{Equation 3.21}$$

Zhang et al.³³ studied filler anisotropy to improve anisotropy in the z -direction, with Ni-C core-shell fillers under magnetic and electrical fields. The authors reported a decrease of

three to four orders of magnitude in the resistivity of aligned composites. Increased dielectric constants and dielectric losses were also reported at up to 10 wt% filler content. The electrical field ($E = 2 \text{ kV/mm}$) and magnetic field ($B = 0.8 \text{ T}$) had a synergistic effect, working together to maximize the conductivity. As a result, the decrease in inter-particle distance caused electron hopping. These results are represented in Figure 3.15³³.

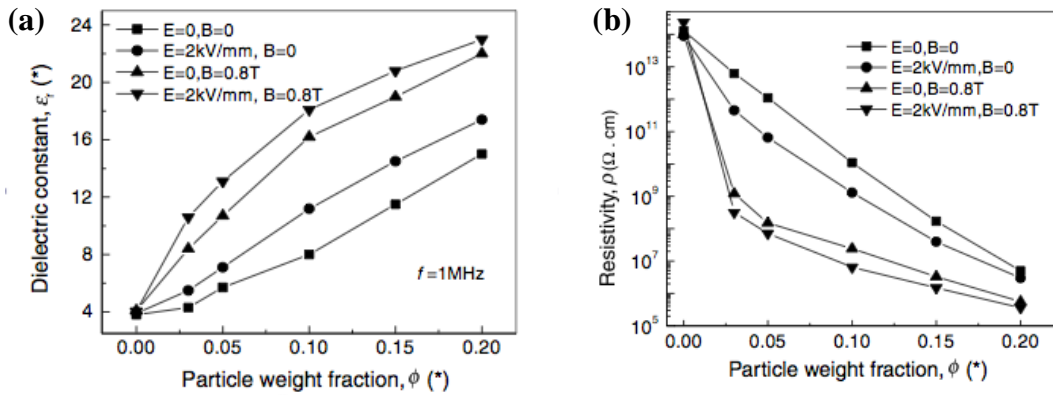


Figure 3.15 Effect of Ni-C core-shell particle weight fraction and external fields on dielectric constant and resistivity³⁵.

A recent study used a polar matrix and a nonpolar matrix (PVDF and LDPE, respectively) to investigate the effect of matrix properties on the composite dielectric constant. An unexpected difference of two orders of magnitude in effective dielectric constant was found along with comparable conductivity between the two matrix materials. These results demonstrate that a polar matrix with a high dielectric constant creates an extremely high-dielectric constant composite⁶⁴.

3.3.4 Organic Filler-Polymer Composites

In recent years, research investigating nanoelectronics and molecular electronics has increased significantly. Researchers have shown a preference for using all-organic materials in developing organic electronics. The primary goal in this field is to create thin, light, flexible, and inexpensive organic electronics for use in sensors, displays, and solar cell technologies. Many organic nanometer-scale materials are widely used as fillers for polymer composites to manipulate the dielectric constant. Such materials include carbon black⁶⁵, carbon nanotubes⁶⁶⁻⁷⁰, fullerenes, conductive polymers, graphite, semiconductor nanoparticles, nanowires⁷¹⁻⁷⁵, and organic metallocenes.

Similar to metallic fillers, conductive organic fillers produce high-dielectric constant nanocomposites with critical concentrations below the percolation threshold. For most of these organic fillers, an increase in dielectric constant is accompanied by the adverse effects of decreased dielectric strength and increased dielectric loss. As an example, an increase in the diameter of carbon black filler improves the dielectric constant of a polymer nanocomposite but decreases its dielectric strength. Also, a high concentration of carbon black increases dielectric permittivity but has a significant detrimental effect on both dielectric strength and dielectric loss⁷⁶. Carbon black-filled (19 wt%) polyurethane composites exhibit k values as high as 4400⁷⁷.

CNTs have also been investigated for use as polymer composite fillers in dielectric materials. The percolation threshold of a carbon nanotube filler is less than that of a carbon black filler because of the nanotubes' low length-to-width ratio and high conductivity^{67-69,78}. A

composite of 1.6 vol% multiwall carbon-nanotubes and poly-vinylidene fluoride has been reported as having an approximate dielectric constant of 300 and a dielectric loss of around 0.4⁶⁸.

Conducting and semiconducting polymers, such as polyaniline (PANI)⁷⁹⁻⁸², polythiophene⁷⁵, and polypyrrole⁸³, are frequently studied as conductive fillers in engineering dielectric composites. Polyaniline has attracted special attention because of its high polymerization yield, controllable electrical conductivity, good environmental stability, and relatively low cost. Polyaniline in partially crystalline form shows a dielectric constant of up to 10^4 ⁸⁴.

Processing method is very important for nanocomposites. The dielectric behavior of composites produced through the in situ polymerization method is entirely different from that of composites produced through simple mixing. In situ processing of composites yields dielectric constants of up to 1000, while simple mixing yields dielectric constants of less than 10. In situ formation gives the best homogeneity and dispersion and improves dielectric properties with the help of interface polarization, electrode polarization, and ionic conductivity. However, simple mixing of species can also decrease dielectric loss through decrease of conductivity⁸⁵. In situ processing can be used to form undoped polyaniline, a process that relies on the use of alkali constituents, and to transform conductive PANI emeraldine salt into a nonconductive PANI emeraldine base. An acidic processing environment was suggested by Lu et al.⁸⁶ for PANI because the increase in the dielectric constant of these blends depends on the conductivity of PANI.

In summary, all organic percolative composites of polymers can produce extremely high dielectric constants, resulting in high capacitances. Dielectric modulus calculations have also been used to study the origins of these extremely high capacitances, which result from electrode polarization^{87,88}. The main advantage of calculating the electric modulus is suppression of the effects of electrode polarization. The complex electric modulus is calculated from the imaginary and real parts of the dielectric constant over a range of frequencies by combining the two formulae in Equation 3.22 and Equation 3.23 as $M'(w) + iM''(w)$ ^{89,179}:

$$M'(w) = \frac{\varepsilon'(w)}{\varepsilon'(w)^2 + \varepsilon''(w)^2} \quad \text{Equation 3.22}$$

and

$$M''(w) = \frac{\varepsilon''(w)}{\varepsilon'(w)^2 + \varepsilon''(w)^2} \quad \text{Equation 3.23}$$

The conductivity of PANI-polymer composites ranges from 10^{-9} to 10^{-3} S/cm, with around 4 to 10 wt% filler content depending on the polymer matrix and filler content³⁸. As seen in Table 3.1, a dramatic increase in dielectric constant and loss in the vicinity of conductive percolation has been reported for these composites. In addition, Lu et al.⁸⁹ report extremely high dielectric constants—up to 2980—which is explained by the presence of Maxwell-Wagner polarization and higher charges carried by conductive fillers.

A relatively new approach to increasing the dielectric constant while sustaining low dielectric loss has been to coat conducting nanofillers with an insulating layer^{36,70,90,91}. Yang et al. showed that coating multi-walled carbon nanotubes (MWCNT) with an insulating layer and dispersing them in polystyrene increased the dielectric constant to more than 40, with a loss tangent below 0.06 at room temperature⁷⁰.

Table 3.1 Dielectric behavior of PANI/epoxy composites³⁸.

PANI content	8 wt%	15 wt%	20 wt%	25 wt%
ϵ'	10	192	916	2980
ϵ''	0.08	0.48	0.55	0.48

Carbon nanotubes (CNT) were functionalized with Poly(styrene-*b*-(ethylene-*co*-butylene)-*b*-styrene) (SEBS) and employed as high-dielectric constant fillers using a click coupling method. These core-shell-structured CNTs were then dispersed to form CNT-SEBS composites. These hetero structures have enhanced mechanical and dielectric properties⁹².

Another possible use of interface manipulation is in the formation of a conductive interface between two insulating polymers. An interface of polar and nonpolar perovskites forms a two-dimensional electron cloud between two crystal surfaces, and this formation results in conductivity. Although the mechanism of this phenomenon has not yet been agreed upon⁹³,

the phenomenon is observed in polar groups containing interphases due to the dipole moments of these groups⁹⁴. Polymers such as 3-(2-pyridyldithio) propionyl hydrazide (PDPH) were used to test interphase conductivity¹⁶⁵, since PDPH has high dipole moments. The conductivities of these interphases as reported by Lu et al.⁹⁵ are shown in Figure 3.16. According to their results, these polymer interfaces are desirable for use in many electronic applications, including in improving the dielectric behavior of polymeric materials.

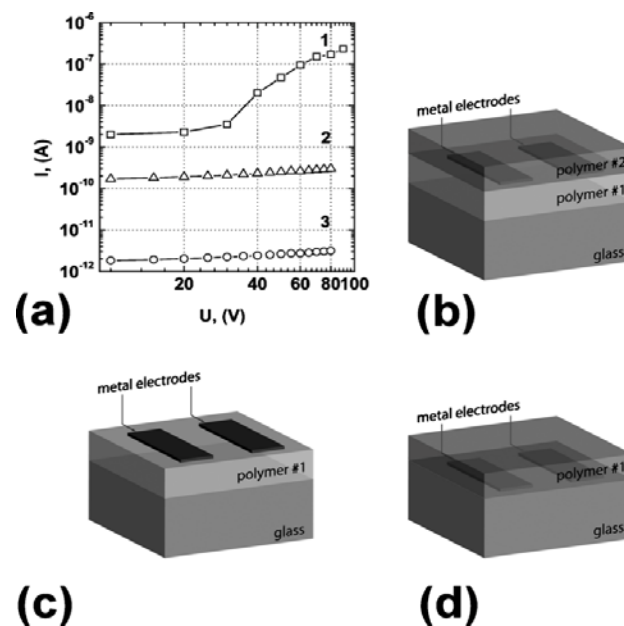


Figure 3.16 Surface conductivity of PDPH polymer: (a) V-I characteristics; (b) sample with two polymer layers (1st line in plot (a)); (c) sample with one polymer layer, where the electrodes are on the surface of the polymer (2nd in the plot (a)); (d) sample with one polymer layer, where the electrodes are under the polymer film (3rd in the plot (a))⁹⁷.

3.4 High-Dielectric Constant Elastomer Composites

The most common dielectric elastomers are silicone, acrylic, and polyurethane. There are a number of methods for increasing the permittivity of these materials, including incorporating ceramic fillers, metal fillers, and organic fillers. High- k elastomer composites were discussed in the section above in the context of actuator electromechanical properties.

3.4.1 Ceramic Fillers

Ceramic nanoparticles have been manipulated to enhance dielectric behavior of a dielectric electroactive polymers (D-EAP). Zhang et al.⁹⁶ report that the use of powder-sized (10- μm) TiO_2 with 30% concentration almost doubled the permittivity, transverse strain, and stress performance of a PDMS composite actuator⁹⁶. Particle size is very important in determining dielectric behavior: Smaller (15-nm) TiO_2 particles are reported as increasing the dielectric constant by 350%, in contrast to the 170% increase obtained using 300-nm particles in styrene-*b*-(ethylene-co-butylene)-*b*-styrene (SEBS) co-polymer. The ceramic filler of TiO_2 increases the Young's modulus by around 200% for nanoparticle fillers and 500% for micro-particle composites of SEBS⁴⁴. Barium titanate fillers produced the same level of increase in PDMS at lower concentrations. The same trend has been observed with niobate-lead titanate (PMN-PT) and elastomers, which produce lower stiffening than do micron-sized particles due to the nanofillers' spherical shape⁹⁷. Ceramic fillers affect cross-linking density above concentrations of 20%⁹⁸.

The use of surfactants on TiO_2 to increase dispersion decreases the dielectric performance of a composite, suggesting that the surface phase is the main contributor to dielectric constant

enhancement⁴⁴. The coating of TiO₂ nanoparticles, with silicone oil specifically, enhances a composite's dielectric properties (dielectric constant and loss) as well as its mechanical properties. More specifically, the layer of silicone oil at the surface of the TiO₂ reduces the composite's dielectric loss by limiting Maxwell-Wagner polarizations and decreases its elastic modulus due to surface interactions¹⁸. Incorporation of ceramic filler increases a composite's electrical breakdown^{48,49,99}; however, when ceramic filler is incorporated into a D-EAP, electrical breakdown decreases^{44,97,100}.

The host-guest type of ceramic fillers (TiO₂-silicone oil) was developed to address the low-dielectric strength problem¹⁸. Polyethylene glycol (PEG, a surfactant), when administered to TiO₂ as a filler with 30% concentration, has been reported to decrease actuation response time from 9 μ s to 3 μ s¹⁰¹. Drying ceramic fillers increases the rate of electrical breakdown^{98,102,103}. The contribution of ceramic fillers to critical electrical field improvements and elastomer actuation stabilities has been verified both theoretically and experimentally¹⁰⁴.

Nguyen et al.¹⁰⁵ studied the role of cross-link density and plasticizer (dioctyl phthalate, or DOP) in dielectric enhancement as well as in the variation of the elastic modulus using TiO₂ loadings on a NBR polymer composite. In their experiments, the elastic modulus of the synthetic elastomer decreased when the content of the DOP increased because the plasticizer weakened the carbon chain's connection in the elastomer. The elastic modulus first increased when the TiO₂ content increased from 0 to 20 phr (parts per hundred rubber) but then decreased when the TiO₂ content increased from 20 to 40 phr. The authors concluded that

DOP negatively affects dielectric loss and breakdown due to an increase in small molecular polarizations¹⁰⁵.

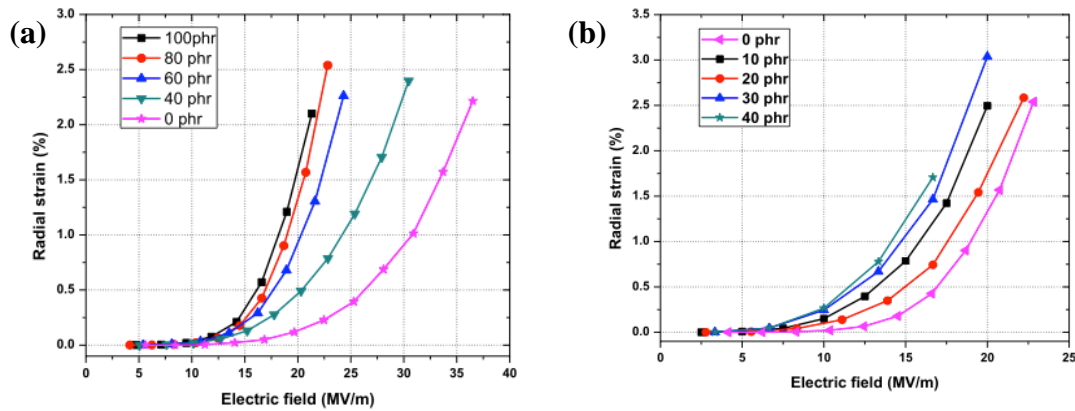


Figure 3.17 Actuation performances of NBR elastomer composite with the addition of varying a) DOP, b) TiO₂ concentrations¹⁰⁷.

The presence of DOP fillers in the NBR matrix decreases electrical breakdown limits. As seen in Figure 3.17(b), TiO₂ fillers enhance radial strain and working electric field until a concentration of 30 phr is reached¹⁰⁵.

3.4.2 All-Organic Composites

Experimentally, an exceptionally large increase in permittivity has been observed in the vicinity of the percolation threshold for conductive fillers in polymers. This percolation effect was described in previous sections. Cameron et al.⁷⁷ studied graphite fillers in polyurethane polymer networks to understand the percolation behavior of graphite in actuators. Their results showed a 25-fold reduction in electrical field, with approximately 18 vol% loadings below the percolation threshold. These composites exhibited an increase in

actuation strain for low electric fields. Their conductivity exponentially increased with applied field, and this increasing conductivity resulted in failures due to overheating of the elastomer composites⁷⁷. Although percolated networks of organic conductive fillers possess drawbacks, encasing the conductive polymer within an insulating shell (Core-shell, PANI-divinyl benzene^{106,107}) minimizes these disadvantages. This method was shown to increase electrical breakdown strength and increase the actuation strain from 4.8% to 10% at 50 V/ μm by 15 wt% filler concentration¹⁰⁶.

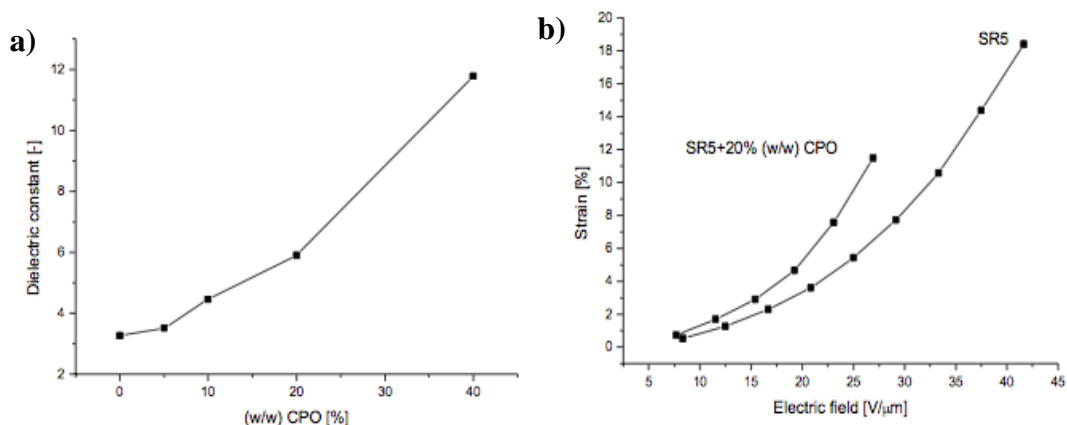


Figure 3.18 Dielectric constant vs. actuation strain for CPO-PDMS elastomer composites¹⁰⁹. a) Dielectric constant-CuPc weight concentration- plot b) Strain-electric field plot.

The metal complexes of phthalocyanines have excellent dielectric properties. For instance, the oligomer copper-phthalocyanine (CuPc; see Figure 3.19 for chemical structure) has a high dielectric constant of 10,000 due to long-range electron delocalization. It also has a high dielectric loss due to long-range intermolecular electron hopping. A high dielectric constant

of 400¹⁰⁸ with a PVDF matrix and a dielectric constant of 11 with a PDMS (SR5)¹⁰⁹ matrix has been observed from 40 wt% loading of CPO-polymer composites at low frequencies (as shown in Figure 3.18). PDMS-based composites exhibit lower actuation rates than that of virgin PDMS due to early breakdown. The increase of PVDF-CPO composite actuator strain is reported to be 2% in the thickness direction^{109,110}. According to Zhang et al.¹⁰⁹, non-uniform field distribution in heterogeneous media has been shown to increase the strain responses of actuators as well as cause conformation changes and molecular reorientation in CPO under large external fields.

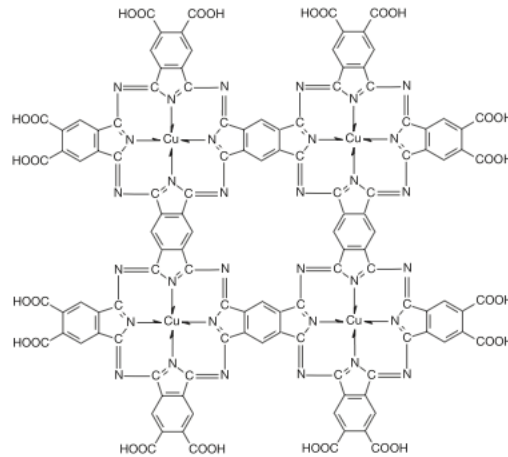


Figure 3.19 Schematic of oligomer copper-phthalocyanine (CuPc).

Guiffard et al.¹¹¹ studied the effects of charge trapping on the electrode surface as well as space-charge polarizations using high-dielectric constant organic fillers. Thin films of these composites exhibit a higher actuation strain, as depicted in Figure 3.20. This result is explained by the electric field distribution originating from space charges and being injected

into polymer surfaces through the electrodes. These injected charges also increase Maxwell stress and electrostriction pressures. Another study concerning the PANI/P(VDF-TrFE-CTFE) composite demonstrated a 25% total strain originating from heterogeneous field distribution¹¹².

The polymer form of CuPc (poly(CuPc)) has a higher—almost tenfold—impact on the stiffening of PDMS elastomer composite due to filler-matrix interactions. This stiffening decreases the actuation performance of the high-dielectric constant material¹¹³. A composite of a low-modulus matrix and a low-percolative filler—e.g., Dow Corning HS IV (0.23 MPa) and high-aspect ratio SWCNT—has been reported to increase actuation performance¹¹⁴.

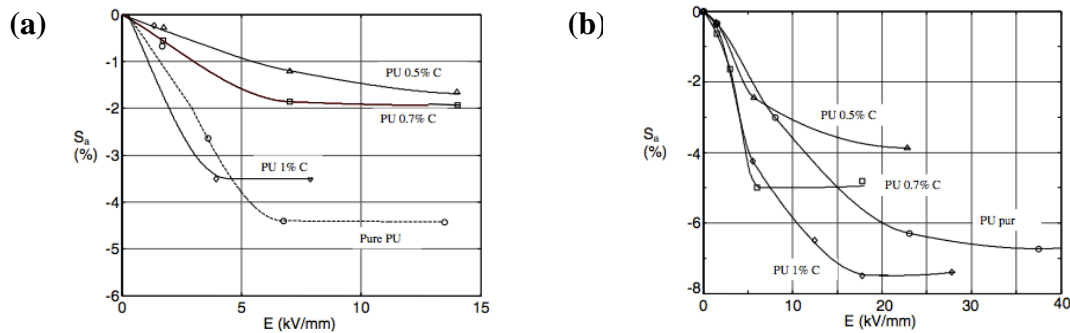


Figure 3.20 Actuation response of a) thick, b) thin samples of polyurethane-carbon black elastomer composites¹¹³.

Huang et al. report that a three-component PANI-CPO-PU composite produced 10% thickness strain, four times higher than that produced by CPO-CPO and eight times higher than that produced by pure polyurethane¹¹⁵. The effective elastic modulus of the composite

materials and the uneven distribution of electric field over the samples are two main reasons for the high actuation generation of a three-component system.

Risse et al.¹¹⁶ synthesized a dielectric elastomer actuator material from dipole (N-Allyl-N-methyl-4-nitroanilin) grafted PDMS. This material has been reported to cause an increase in dielectric constant from 3.3 to 6.0 and a decrease in modulus from 1.7 MPa to 0.3 MPa, depending on composition of dipoles. Because electrical breakdown decreases with the addition of dipoles (130 V/ μm to 50 V/ μm), the end use of this composite actuator material is limited to low electrical field applications.

Polymer blending is another method of making unique polymer structures with desirable dielectric properties. Polymer blending has received attention recently as a method for studying D-EAP materials. In a study of polymer blending on polyurethane and PDMS materials, Gallone et al.⁹⁷ compared silicone, polyurethane, and blends they created using both inorganic and organic fillers in order to understand the transducing mechanisms of dielectric electroactive polymers. Interestingly, the incorporation of PU polymer in silicone at a 40% concentration ratio caused a relatively high dielectric constant of 15 at low frequency measurements due to Maxwell-Wagner interphase polarization of blend species. Accompanying this increase was a substantial increase in dielectric loss, which was due to increases from ionic conductivity. The ionic conductivity increased because of monomer species that remained during the PU polymerization⁹⁷.

In Gallone et al.'s experiments, an entirely organic poly(methylmethacrylate)/b-poly(n-butylacrylate)/b-poly(methyl methacrylate) triblock co-polymer was produced with micro-phase separations in various solvents. The use of solvent-altered domains resulted in the production of a controllable elastic modulus and dielectric constant. The toluene-processed films showed radial strains as high as 10% under 4-KV/mm electric fields as well as corresponding enhancements in dielectric and mechanical properties¹¹⁷.

The dielectric properties, elastic moduli, and electromechanical responses of silicone dielectric elastomers have been composited with carbon black (CB) and BaTiO₃. When compared with single filler/rubber composites, these three-component nanocomposites have been shown to exhibit complex behavior, possibly due to the interactions between the two kinds of fillers. The increase in concentration of CB (BaTiO₃) would play a destructive role in the network structure formed by fillers. In this three-component composite, the BaTiO₃ particles were reported to have high dielectric permittivity, which the electrical networks created by the CB particles contributed to¹¹⁸. A maximum electromechanical strain of ca. 8 % was achieved at mass fractions of $m_{CB} = 0.03$ and $m_{BT} = 0.06$ for this composite at ca. 30 V/ μ m. The resultant electromechanical strain may be attributable to the large dielectric permittivity in the three-component nanocomposites.

Rudykh et al.¹¹⁹ found that the positioning and dimensions of micro-structured composites significantly affected actuator performance, with the use of block-copolymers for the fabrication of elastomers. Finite-element analysis demonstrated that a tenfold increase in the coupling efficiency of a composite dielectric elastomer actuator is achievable using the

angular lamination method (see Figure 3.21 for model design) to fabricate the dielectric elastomer actuator materials. The proposed laminates can consist of acrylic and polyaniline polymers¹¹⁹.

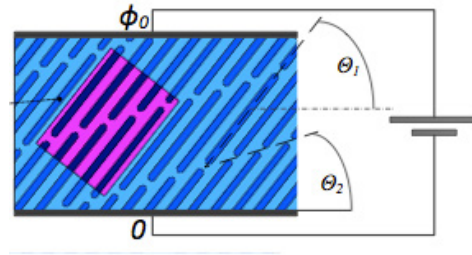


Figure 3.21 Representation of periodic layered-design EAPs for FE analysis¹²¹.

3.4.3 Polymer Synthesis for Dielectric Elastomers

In recent studies, modifying elastomer polymers and cross-linkers at the molecular level has been shown to enhance the permittivity of a silicone matrix for dielectric electroactive polymers. Kussmaul et al.¹²⁰ studied functional cross-linkers with different chemical groups. A trifunctional vinyl cross-linker was modified to produce various cross-linkers with particular functionalities depending on chemical structure. Incorporating these functional cross-linkers created polydimethylsiloxane (PDMS) networks with better mechanical and physical properties. For example, a 0.25 weight percent of the push-pull dipole ethynyl-4-nitrobenzene increased the dielectric permittivity of PDMS by 35% due to the cross-linker's dipolar nature. The authors¹²⁰, through fluorescence microscopy tests, also demonstrated the functionalization of polymer networks by fluorine-based cross-linkers and the wide dispersion of cross-linkers throughout the PDMS network.

A similar modification is main-chain dipole attachment. In this process, a push-pull dipole is synthesized to be compatible with the silicone cross-linking chemistry, allowing for direct grafting to the cross-linker molecules in a one-step film formation process. This method prevents agglomeration and yields elastomer films that are homogeneous down to the molecular level. The dipole-to-silicone network grafting reaction was confirmed by Kussmaul et al.^{120,121} using Fourier-transform infrared spectroscopy (FTIR). The chemical, thermal, mechanical, and electrical properties of films with dipole contents ranging from 0 wt% to 13.4 wt% were thoroughly characterized in this study. Dipole grafting modified the permittivity and stiffness of PDMS, resulting in a sixfold increase in actuation strain compared to the actuation strain of neat polymers observed in a comparable electrical field^{120,121}.

3.5 Dielectric Mixing Theories

Simple mixing equations predict the dielectric constant of a polymer composite from the behaviors of the pure polymer matrix and the filler, given volume fractions of each component. Several equations describe the effective dielectric constant of a mixture; empirical equations include the Maxwell Garnett (MG) equation, the Bruggeman equation, the Hanai-Bruggeman equation, and the empirical Lichtenecker mixture equation^{2,122–125}.

Lichtenecker's logarithmic mixture formula describes a practical approach for determining the dielectric constant of a homogenous material¹²³. This empirical formula for multiphase composites is as follows:

$$|\varepsilon_{\text{eff}}| = (1-f)|\varepsilon_1| + f|\varepsilon_2|, \quad \frac{\varepsilon_{\text{eff}}'}{\varepsilon_{\text{eff}}''} = \frac{\varepsilon_1''}{\varepsilon_1'} + \frac{\varepsilon_2''}{\varepsilon_2'}, \quad \ln \varepsilon_{\text{eff}} = \sum_i f_i \ln \varepsilon_i \quad \text{Equation 3.24}$$

where ε_{eff} is the relative dielectric constant of the composite and ε_i is the component dielectric constant. The Lichtenecker model also includes parallel series mixing models and cubic models for use in extreme cases¹²². Maxwell-Wagner-Sillars polarization occurs at the boundaries of distinctive materials at meso and macro scales, causing a higher charge separation relative to pure materials. This charge separation can be estimated from atomic and molecular contribution models, and it results in a higher dielectric loss². The Sillars equation is:

$$\varepsilon_c = \varepsilon_m \left[1 + \frac{3v_f(\varepsilon_f - \varepsilon_m)}{2\varepsilon_m + \varepsilon_f} \right] \quad \text{Equation 3.25}$$

Finally, the Maxwell-Garnett equation is as follows:

$$\varepsilon_c = \varepsilon_m \left(1 + \frac{3v_f(\varepsilon_f - \varepsilon_m)}{(1 - v_f)(\varepsilon_f - \varepsilon_m) + 3\varepsilon_m} \right) \quad \text{Equation 3.26}$$

Nonhomogeneous materials including suspensions or colloids, phase-separated polymers, blends, and polymer composites are considered Maxwell-Wagner-Sillars materials. The dielectric constant of such a material is predicted using Equation 3.26. However, this equation is not useful for predicting the dielectric constant of materials when there is disparity among the components' dielectric constants or in conditions where filler loading

levels are too high^{2,126}. The Maxwell-Wagner formula was altered to create a universal formula, shown in Equation 3.27 below, by the addition of factor ν , which describes the effect of filler geometry on mixing nature¹²⁷.

$$\frac{\epsilon_{eff} - \epsilon_0}{\epsilon_{eff} + 2\epsilon_0 + \nu(\epsilon_{eff} - \epsilon_0)} = f \frac{\epsilon - \epsilon_0}{\epsilon + 2\epsilon_0 + \nu(\epsilon_{eff} - \epsilon_0)} \quad \text{Equation 3.27}$$

A ν of 0 returns this formula to the Maxwell-Wagner-Sillars formula and the Lorentz-Lorenz polarizations formula.

Consistently, $\nu = 2$ gives the Bottcher equation (Equation 3.29) or the Bruggeman mixing formula for lamellae and disc fillers (Equation 3.28). $\nu = 3$ gives a quasi-crystalline approximation derived by Gyorffy, Korringa, and Mills^{126,127}.

The Bruggeman equation is as follows:

$$\frac{\epsilon_f - \epsilon_c}{\epsilon_c^{1/3}} = \frac{(1 - \nu_f)(\epsilon_f - \epsilon_m)}{\epsilon_c^{1/3}} \quad \text{Equation 3.28}$$

The Bottcher equation is as follows:

$$\frac{\epsilon_c - \epsilon_m}{3\epsilon_c} = \nu_f \frac{\epsilon_f - \epsilon_m}{2\epsilon_c + \epsilon_f} \quad \text{Equation 3.29}$$

The preceding mixture models assume the fillers are shaped like individual spheres and do not take into account interactions between these spheres. However, the electric field that

arises from the interaction of fillers becomes significant with increasing filler concentration. The Jayasundere and Smith model takes into consideration inter-particle interaction effects on dielectric behavior, a consideration which is especially important for random composites¹²⁸. This model has been widely used to model ceramic-polymer mixtures^{129–132}.

The Jayasundere and Smith equation is as follows:

$$\epsilon_c = \frac{\epsilon_m v_m + \epsilon_f v_f \frac{3\epsilon_m}{(2\epsilon_m + \epsilon_f)} \left[1 + 3v_f \frac{(\epsilon_f - \epsilon_m)}{2\epsilon_m + \epsilon_f} \right]}{v_m + v_f \frac{3\epsilon_m}{(2\epsilon_m + \epsilon_f)} \left[1 + 3v_f \frac{(\epsilon_f - \epsilon_m)}{2\epsilon_m + \epsilon_f} \right]} \quad \text{Equation 3.30}$$

The Jayasundere-Smith equation is especially applicable to low-volume fractions. For high-volume concentration of ceramic fillers, the Effective Medium Theory (EMT) mixing rules have been especially useful. These rules can be applied to insulating fillers with volume fractions of up to 0.5 in order to determine both dielectric constant and dielectric loss, with 10% maximum deviation^{128,133–135}. EMT has also been used to understand percolated composites. The theoretical calculations are reported to be consistent with experimental results^{3,136}. The EMT equations are as follows:

$$\frac{\epsilon'_i - \epsilon'}{(\epsilon')^{1/3}} = \frac{(1 - \phi)(\epsilon'_i - \epsilon'_m)}{(\epsilon'_m)^{1/3}} \quad \text{Equation 3.31}$$

$$\varepsilon'' = \frac{(\varepsilon'_i - \varepsilon')(\varepsilon'_i + 2\varepsilon'_m)\varepsilon'\varepsilon''_m}{(\varepsilon'_i - \varepsilon'_m)(\varepsilon'_i + 2\varepsilon')\varepsilon'_m} + \frac{3(\varepsilon' - \varepsilon'_m)\varepsilon'\varepsilon''_i}{(\varepsilon'_i - \varepsilon'_m)(\varepsilon'_i + 2\varepsilon')}$$

Equation 3.32

Vo et al.¹³⁷ considered the particle interphase on dielectric constant calculations. Their model, shown in Figure 3.22, also incorporated particle overlaps and high weight concentrations and closely fits the experimental data^{137,138}.

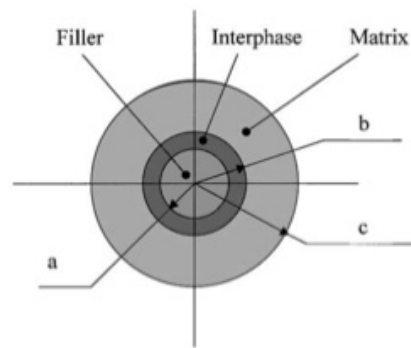


Figure 3.22 The geometry for modelling core-shell filled composites for their dielectric behavior: (a) particle, (b) interphase, and (c) matrix parts in dielectric composites¹³⁹.

Ab initio simulations are considered to be another precise method for modeling and calculating the dielectric constants of materials and composites^{47,57,139}. These simulations have led to several significant inferences about nanodielectrics. According to Liping et al.¹⁴⁰, polymer-metal oxide interphases do not show a large gap, and delocalization occurs within only a few atomic layers confined to the metal-oxide side. The effective permittivity depends on the chain packing density of polymers. The nanofiller-induced free volume in nanocomposites could be a dominant factor in reducing the effective permittivity of

nanocomposites¹⁴⁰.

3.6 Concluding Remarks

This review has focused on dielectric elastomers and their dielectric properties. Special attention was given to polymer nanocomposites with high dielectric constants as well as to the principles of dielectrics and dielectric behavior enhancements.

There is great demand for novel materials for use in dielectric elastomer applications, in which high k , low dielectric loss, and ease of processing are key features. A number of materials, such as ceramics, metals, and organic compounds, were reviewed for their ability to increase dielectric constants.

The dielectric constants of ceramic-polymer composites are not dependent on frequency and temperature. However, their dielectric permittivity is often low, even if a high loading of ceramic particles is incorporated. Moreover, their breakdown strength is weak if the ceramic particles are not surface-treated.

Metal-polymer composites follow the percolation threshold for their dielectric behavior. A dramatic increase was reported in the dielectric constant below the percolation threshold of these composites. These metal fillers were reported to decrease actuation performance tremendously due to low dielectric strength of composites. However, it is worth noting that they have presented an actuation strain increase under low electric fields.

Matrix-filler interactions and filler size are extremely important for the electrical and dielectric properties of metal- and ceramic-filled polymer composites. Polar matrices have

reportedly caused a higher increase in dielectric constant than nonpolar matrices in their composites.

Interphasic regions are crucial to the dielectric properties of materials. As particle size decreases, interphase volume increases logarithmically. It is worth exploring the synergy between different types of fillers and the potential of using core-shell fillers in order to attain high- k polymer composites with other excellent mechanical properties.

Considering nano-dielectric phenomena is important when designing high-dielectric constant materials. Inclusion of a core-shell structured filler is another important way to promote dispersion of the filler throughout the polymer and the interfacial interactions between them. A core-shell filler also increases filler-polymer compatibility, which improves the mechanical properties of the composite and increases the dispersion of filler material in the polymer matrix. Improved dispersion also increases the specific surface area of the filler. The use of a core-shell structured filler, either metal or ceramic, instead of an unstructured filler increases the dielectric constant of a composite and decreases its dielectric loss.

Uniform dispersion of nanoparticles throughout a nanocomposite is essential to achieving improved dielectric properties and reproducibility since nanoparticle agglomeration leads to undesirable electrical and mechanical material properties. Dispersion may also minimize defects or voids in the composite, which can degrade breakdown strength and therefore overall energy density.

In general, the above-mentioned properties are also applicable to elastomer composites.

Dielectric elastomer actuators generally require softer elastomer composites than do other polymer composite applications. Most elastomers exhibit a decrease in hardness due to a lower average molecular weight and a lesser degree of cross-linking. It is possible to optimize the elastomer's mechanical properties after achieving a satisfactory dielectric constant.

The application of this knowledge to dielectric elastomer networks results in improved dielectric constant and thus improved actuation performance. The mechanical properties of D-EAPs also affect actuation performance, including Young's modulus. This improvement in dielectric constant has been observed to take the form of higher actuation strain and higher blocking force performance. All organic and custom-synthesized elastomers have also been revived as D-EAP materials. These materials possess a higher dielectric strength than do their composite counterparts. Blends, conductive polymers, and dipole-grafted elastomer networks have been proposed as D-EAP materials.

3.7 References

1. Van Krevelen, D. W. & Te Nijenhuis, K. in *Properties of Polymers (Fourth Edition)* (eds. by, D. W. V. K. & Nijenhuis, K. T.) 319–354 (Elsevier, 2009). at <<http://www.sciencedirect.com/science/article/pii/B978008054819700011X>>
2. Das-Gupta, D. K. in *Encyclopedia of RF and Microwave Engineering* (John Wiley & Sons, Inc., 2005). at <[doi/10.1002/0471654507.eme072/abstract](https://doi.org/10.1002/0471654507.eme072/abstract)>
3. Liu, X., Wu, Y., Wang, X., Li, R. & Zhang, Z. Effect of interphase on effective permittivity of composites. *J. Phys. Appl. Phys.* **44**, 115402 (2011).

4. Lewis, T. J. Interfaces are the dominant feature of dielectrics at the nanometric level. *Dielectr. Electr. Insul. IEEE Trans. On* **11**, 739–753 (2004).
5. Griffiths, D. J. *Introduction to Electrodynamics*. (Addison Wesley, 1999).
6. Clays, K. *et al.* Enhancement of the molecular hyperpolarizability by a supramolecular amylose-dye inclusion complex, studied by hyper-Rayleigh scattering with fluorescence suppression. *Chem. Phys. Lett.* **293**, 337–342 (1998).
7. Hartman, R. D. & Pohl, H. A. Hyperelectronic polarization in macromolecular solids. *J. Polym. Sci. Part A-1 Polym. Chem.* **6**, 1135–1152 (1968).
8. Guo, M. *Investigations of novel high dielectric materials and new mechanisms*. (University of Michigan, 2009).
9. Shan, X. *High dielectric constant 0-3 ceramic-polymer composites*. (Auburn University, 2009).
10. Pohl, H. Giant polarization in high polymers. *J. Electron. Mater.* **15**, 201–203 (1986).
11. Urry, D. W. *et al.* Elastin: a representative ideal protein elastomer. *Philos. Trans. R. Soc. Lond. B. Biol. Sci.* **357**, 169–184 (2002).
12. Kremer, F. & Schönhals, A. *Broadband Dielectric Spectroscopy*. (Springer, 2002).
13. Runt, J. P. & Fitzgerald, J. J. *Dielectric spectroscopy of polymeric materials: fundamentals and applications*. (An American Chemical Society Publication, 1997).
14. Hedvig, P. *Dielectric spectroscopy of polymers*. (John Wiley & Sons Inc, 1977).
15. Blythe, A. R. & Bloor, D. *Electrical properties of polymers*. (Cambridge University Press, 2005).

16. Dang, Z.-M. *et al.* Fundamentals, processes and applications of high-permittivity polymer–matrix composites. *Prog. Mater. Sci.* **57**, 660–723 (2012).
17. Ieda, M. Electrical Conduction and Carrier Traps in Polymeric Materials. *IEEE Trans. Electr. Insul.* **EI-19**, 162–178 (1984).
18. Stoyanov, H., Kollosche, M., Risse, S., McCarthy, D. N. & Kofod, G. Elastic block copolymer nanocomposites with controlled interfacial interactions for artificial muscles with direct voltage control. *Soft Matter* **7**, 194 (2011).
19. Lewis, T. J. A Model for Nano-composite Polymer Dielectrics under Electrical Stress. in *IEEE International Conference on Solid Dielectrics, 2007. ICSD '07* 11–14 (2007). doi:10.1109/ICSD.2007.4290740
20. Nelson, J. K. & Fothergill, J. C. Internal charge behaviour of nanocomposites. *Nanotechnology* **15**, 586–595 (2004).
21. Nelson, J. K. Overview of nanodielectrics: Insulating materials of the future. in *Electrical Insulation Conference and Electrical Manufacturing Expo, 2007* 229–235 (2007). doi:10.1109/EEIC.2007.4562626
22. Frechette, M. F., Trudeau, M. L., Alamdar, H. D. & Boily, S. Introductory remarks on nanodielectrics. *Dielectr. Electr. Insul. IEEE Trans. On* **11**, 808–818 (2004).
23. Li, Y., Pothukuchi, S. & Wong, C. P. Development of a novel polymer-metal nanocomposite obtained through the route of in situ reduction and its dielectric properties [capacitor applications]. in *Electronic Components and Technology Conference, 2004. Proceedings. 54th* **1**, 507–513 Vol.1 (2004).
24. Seneor, P. *et al.* Principle of a variable capacitor based on coulomb blockade of nanometric-size clusters. *Europhys. Lett. EPL* **65**, 699–704 (2004).

25. Lu, J., Moon, K.-S., Xu, J. & Wong, C. P. Synthesis and dielectric properties of novel high-K polymer composites containing in-situ formed silver nanoparticles for embedded capacitor applications. *J. Mater. Chem.* **16**, 1543 (2006).
26. Tanaka, T. Dielectric nanocomposites with insulating properties. *Dielectr. Electr. Insul. IEEE Trans. On* **12**, 914–928 (2005).
27. Danikas, M. G. & Tanaka, T. Nanocomposites-a review of electrical treeing and breakdown. *Electr. Insul. Mag. IEEE* **25**, 19–25 (2009).
28. Fréchette, M. F. & Reed, C. W. On molecular dielectrics in their role in shaping and controlling nanodielectrics. in *Electrical Insulation and Dielectric Phenomena, 2006 IEEE Conference on* 333–337 (2006).
29. Smith, R. C., Liang, C., Landry, M., Nelson, J. K. & Schadler, L. S. The mechanisms leading to the useful electrical properties of polymer nanodielectrics. *IEEE Trans. Dielectr. Electr. Insul.* **15**, 187–196 (2008).
30. Nalwa, H. S. *Handbook of low and high dielectric constant materials and their applications. volume 1: materials and processing. volume 2: phenomena, properties and applications.* (Academic Press, 1999).
31. Chu, B. *et al.* A dielectric polymer with high electric energy density and fast discharge speed. *Science* **313**, 334–336 (2006).
32. Zhang, Z. *et al.* New silicone dielectric elastomers with a high dielectric constant. in *Modeling, Signal Processing, and Control for Smart Structures.* **6926** (SPIE, 2008).
33. Zhang, B., Xie, C., Hu, J., Wang, H. & Gui, Y. Novel 1-3 metal nanoparticle/polymer composites induced by hybrid external fields. *Compos. Sci. Technol.* **66**, 1558–1563 (2006).

34. Bai, Y., Cheng, Z.-Y., Bharti, V., Xu, H. S. & Zhang, Q. M. High-dielectric-constant ceramic-powder polymer composites. *Appl. Phys. Lett.* **76**, 3804 (2000).
35. Li, J. *et al.* Nanocomposites of ferroelectric polymers with TiO₂ nanoparticles exhibiting significantly enhanced electrical energy density. *Adv. Mater.* **21**, 217–221 (2009).
36. Yuan, J.-K. *et al.* High dielectric permittivity and low percolation threshold in polymer composites based on SiC-carbon nanotubes micro/nano hybrid. *Appl. Phys. Lett.* **98**, 032901 (2011).
37. Saha, S. K., DaSilva, M., Hang, Q., Sands, T. & Janes, D. B. A nanocapacitor with giant dielectric permittivity. *Nanotechnology* **17**, 2284–2288 (2006).
38. Tabellout, M., Fatyeyeva, K., Baillif, P.-Y., Bardeau, J.-F. & Pud, A. A. The influence of the polymer matrix on the dielectric and electrical properties of conductive polymer composites based on polyaniline. *J. Non-Cryst. Solids* **351**, 2835–2841 (2005).
39. Shen, Y., Lin, Y., Li, M. & Nan, C.-W. High dielectric performance of polymer composite films induced by a percolating interparticle barrier layer. *Adv. Mater.* **19**, 1418–1422 (2007).
40. Kakimoto, M. *et al.* Polymer-ceramic nanocomposites based on new concepts for embedded capacitor. *Mater. Sci. Eng. B* **132**, 74–78 (2006).
41. Uchino, K., Eiji Sadanaga & Terukiyo Hirose. Dependence of the crystal structure on particle size in barium titanate. *J. Am. Ceram. Soc.* **72**, 1555–1558 (1989).
42. Leonard, M. R. & Safari, A. Crystallite and grain size effects in BaTiO₃. in *Applications of Ferroelectrics, 1996. ISAF '96., Proceedings of the Tenth IEEE International Symposium on* **2**, 1003–1005 vol.2 (1996).

43. Brochu, P. & Pei, Q. Advances in dielectric elastomers for actuators and artificial muscles. *Macromol. Rapid Commun.* **31**, 10–36 (2010).
44. Mc Carthy, D. N., Risse, S., Katekomol, P. & Kofod, G. The effect of dispersion on the increased relative permittivity of TiO₂/SEBS composites. *J. Phys. Appl. Phys.* **42**, 145406 (2009).
45. Nelson, J. K. *Dielectric polymer nanocomposites*. (Springer, 2009).
46. He, Q., Wu, L., Gu, G. & You, B. Preparation and characterization of Acrylic/Nano-TiO₂ composite latex. *High Perform. Polym.* **14**, 383–396 (2002).
47. Moya, J. S., Lopez-Esteban, S. & Pecharromás, C. The challenge of ceramic/metal microcomposites and nanocomposites. *Prog. Mater. Sci.* **52**, 1017–1090 (2007).
48. Scolan, E. & Sanchez, C. Synthesis and characterization of surface-protected nanocrystalline titania particles. *Chem. Mater.* **10**, 3217–3223 (1998).
49. Dang, Z. M., Song, H. T., Lin, Y. Q. & Ma, L. J. High and low dielectric permittivity polymer-based nanohybrid dielectric films. in *Journal of Physics: Conference Series* **152**, 012047 (2009).
50. Dang, Z.-M. *et al.* Advanced calcium copper titanate/polyimide functional hybrid films with high dielectric permittivity. *Adv. Mater.* **21**, 2077–2082 (2009).
51. Yao, J. *et al.* Enhancement of dielectric constant and piezoelectric coefficient of ceramic–polymer composites by interface chelation. *J. Mater. Chem.* **19**, 2817 (2009).
52. Hossack, J. A. & Auld, B. A. Improved modeling of 0:3 composite materials. in *Ultrasonics Symposium, 1995. Proceedings., 1995 IEEE* **2**, 945–949 vol.2 (1995).

53. Williams, E. P. M. *et al.* Dielectric nanocapacitance effect of thermoset polymeric matrix nanocomposites. *J. Polym. Sci. Part B Polym. Phys.* **42**, 1–4 (2004).
54. Windlass, H., Raj, P. M., Balaraman, D., Bhattacharya, S. K. & Tummala, R. R. Colloidal processing of polymer ceramic nanocomposite integral capacitors. *Electron. Packag. Manuf. IEEE Trans. On* **26**, 100–105 (2003).
55. Tomer, V., Randall, C. A., Polizos, G., Kostelnick, J. & Manias, E. High- and low-field dielectric characteristics of dielectrophoretically aligned ceramic/polymer nanocomposites. *J. Appl. Phys.* **103**, 034115–7 (2008).
56. Bergman, D. J. & Imry, Y. Critical behavior of the complex dielectric constant near the percolation threshold of a heterogeneous material. *Phys. Rev. Lett.* **39**, 1222 (1977).
57. Bergman, D. J. The dielectric constant of a composite material--A problem in classical physics. *Phys. Rep.* **43**, 377–407 (1978).
58. Nicolais, L. & Carotenuto, G. *Metal-polymer nanocomposites*. (John Wiley and Sons, 2005).
59. Dang, Z. -M, Lin, Y. -H & Nan, C. -W. Novel ferroelectric polymer composites with high dielectric constants. *Adv. Mater.* **15**, 1625–1629 (2003).
60. Li, Y.-J., Xu, M., Feng, J.-Q. & Dang, Z.-M. Dielectric behavior of a metal-polymer composite with low percolation threshold. *Appl. Phys. Lett.* **89**, 072902 (2006).
61. Panda, M., Srinivas, V. & Thakur, A. K. On the question of percolation threshold in polyvinylidene fluoride/nanocrystalline nickel composites. *Appl. Phys. Lett.* **92**, 132905 (2008).

62. Murugaraj, P., Mainwaring, D. & Mora-Huertas, N. Dielectric enhancement in polymer-nanoparticle composites through interphase polarizability. *J. Appl. Phys.* **98**, 054304 (2005).
63. Saha, S. K. Nanodielectrics with giant permittivity. *Bull. Mater. Sci.* **31**, 473–477 (2008).
64. Panda, M., Srinivas, V. & Thakur, A. K. Role of polymer matrix in large enhancement of dielectric constant in polymer-metal composites. *Appl. Phys. Lett.* **99**, 042905 (2011).
65. Annadurai, P., Mallick, A. K. & Tripathy, D. K. Studies on microwave shielding materials based on ferrite- and carbon black-filled EPDM rubber in the X-band frequency. *J. Appl. Polym. Sci.* **83**, 145–150 (2002).
66. Yu, C., Masarapu, C., Rong, J., Wei, B. & Jiang, H. Stretchable supercapacitors based on buckled single-walled carbon-nanotube macrofilms. *Adv. Mater.* **21**, 4793–4797 (2009).
67. Baughman, R. H., Zakhidov, A. A. & de Heer, W. A. Carbon nanotubes—the route toward applications. *Science* **297**, 787 (2002).
68. Wang, L. & Dang, Z.-M. Carbon nanotube composites with high dielectric constant at low percolation threshold. *Appl. Phys. Lett.* **87**, 042903 (2005).
69. Breuer, O. & Sundararaj, U. Big returns from small fibers: A review of polymer/carbon nanotube composites. *Polym. Compos.* **25**, 630–645 (2004).
70. Yang, Y., Gupta, M. C., Dudley, K. L. & Lawrence, R. W. Novel carbon nanotube–polystyrene foam composites for electromagnetic interference shielding. *Nano Lett.* **5**, 2131–2134 (2005).

71. Shimomura, T., Akai, T., Abe, T. & Ito, K. Atomic force microscopy observation of insulated molecular wire formed by conducting polymer and molecular nanotube. *J. Chem. Phys.* **116**, 1753 (2002).
72. Shimomura, T. *et al.* Conductivity measurement of insulated molecular wire formed by molecular nanotube and polyaniline. *Synth. Met.* **153**, 497–500 (2005).
73. Cacialli, F. *et al.* Cyclodextrin-threaded conjugated polyrotaxanes as insulated molecular wires with reduced interstrand interactions. *Nat Mater* **1**, 160–164 (2002).
74. Grigoras, M. & Stafie, L. Electrically insulated molecular wires. *Supramol. Chem.* **22**, 237–248 (2010).
75. Qiu, L. *et al.* Organic thin-film transistors based on polythiophene nanowires embedded in insulating polymer. *Adv. Mater.* **21**, 1349–1353 (2009).
76. Nelson, P. N. & Hervig, H. C. High dielectric constant materials for primary voltage cable terminations. *IEEE Trans. Power Appar. Syst.* **103**, 3211–3216 (1984).
77. Cameron, C. G., Underhill, R. S., Rawji, M. & Szabo, J. P. Conductive filler: elastomer composites for Maxwell stress actuator applications. in **5385**, 51–59 (2004).
78. Kerr, C. J., Huang, Y. Y., Marshall, J. E. & Terentjev, E. M. Effect of filament aspect ratio on the dielectric response of multiwalled carbon nanotube composites. *J. Appl. Phys.* **109**, 094109 (2011).
79. Soares, B. G., Leyva, M. E., Barra, G. M. O. & Khastgir, D. Dielectric behavior of polyaniline synthesized by different techniques. *Eur. Polym. J.* **42**, 676–686 (2006).
80. Joo, J. *et al.* Microwave dielectric response of mesoscopic metallic regions and the intrinsic metallic state of polyaniline. *Phys. Rev. B* **49**, 2977 (1994).

81. Meng, C., Liu, C., Chen, L., Hu, C. & Fan, S. Highly flexible and all-solid-state paperlike polymer supercapacitors. *Nano Lett.* **10**, 4025–4031 (2010).
82. Yan, X. Z. & Goodson, T. High dielectric hyperbranched polyaniline materials. *J. Phys. Chem. B* **110**, 14667–14672 (2006).
83. Deligöz, H. & Tieke, B. Conducting composites of polyurethane resin and polypyrrole: solvent-free preparation, electrical, and mechanical properties. *Macromol. Mater. Eng.* **291**, 793–801 (2006).
84. Joo, J. *et al.* Charge transport of the mesoscopic metallic state in partially crystalline polyanilines. *Phys. Rev. B* **57**, 9567 (1998).
85. Chwang, C.-P., Liu, C.-D., Huang, S.-W., Chao, D.-Y. & Lee, S.-N. Synthesis and characterization of high dielectric constant polyaniline/polyurethane blends. *Synth. Met.* **142**, 275–281 (2004).
86. Lu, J., Moon, K.-S., Kim, B.-K. & Wong, C. P. High dielectric constant polyaniline/epoxy composites via in situ polymerization for embedded capacitor applications. *Polymer* **48**, 1510–1516 (2007).
87. Dutta, P., Biswas, S. & De, S. K. Dielectric relaxation in polyaniline-polyvinyl alcohol composites. *Mater. Res. Bull.* **37**, 193–200 (2002).
88. Yu, S., Hing, P. & Hu, X. Dielectric properties of polystyrene–aluminum-nitride composites. *J. Appl. Phys.* **88**, 398 (2000).
89. Korzhenko, A. A. *et al.* Dielectric relaxation properties of poly(ethylene-terephthalate)-polyaniline composite films. *Synth. Met.* **98**, 157–160 (1998).
90. Kim, J.-B., Yi, J.-W. & Nam, J.-E. Dielectric polymer matrix composite films of CNT coated with anatase TiO₂. *Thin Solid Films* **519**, 5050–5055 (2011).

91. Yuen, S.-M. *et al.* Preparation, morphology, mechanical and electrical properties of TiO₂ coated multiwalled carbon nanotube/epoxy composites. *Compos. Part Appl. Sci. Manuf.* **39**, 119–125 (2008).
92. Yadav, S. K., Mahapatra, S. S., Cho, J. W. & Lee, J. Y. Functionalization of multiwalled carbon nanotubes with poly(styrene-*b*-(ethylene-co-butylene)-*b*-styrene) by click coupling. *J. Phys. Chem. C* **114**, 11395–11400 (2010).
93. Chambers, S. A. Understanding the mechanism of conductivity at the LaAlO₃/SrTiO₃(001) interface. *Surf. Sci.* **605**, 1133–1140 (2011).
94. Popović, Z. S., Satpathy, S. & Martin, R. M. Origin of the two-dimensional electron gas carrier density at the LaAlO₃ on SrTiO₃ interface. *Phys. Rev. Lett.* **101**, 256801 (2008).
95. Gadiev, R. M. *et al.* The conducting polymer/polymer interface. *Appl. Phys. Lett.* **98**, 173305 (2011).
96. Carpi, F. & Rossi, D. D. Improvement of electromechanical actuating performances of a silicone dielectric elastomer by dispersion of titanium dioxide powder. *IEEE Trans. Dielectr. Electr. Insul.* **12**, 835–843 (2005).
97. Gallone, G., Carpi, F., De Rossi, D., Levita, G. & Marchetti, A. Dielectric constant enhancement in a silicone elastomer filled with lead magnesium niobate–lead titanate. *Mater. Sci. Eng. C* **27**, 110–116 (2007).
98. Böse, H., Uhl, D., Flittner, K. & Schlaak, H. Dielectric elastomer actuators with enhanced permittivity and strain. in **7976**, 79762J–79762J–13 (2011).
99. Das-Gupta, D. K. & Doughty, K. Polymer-ceramic composite materials with high dielectric constants. *Thin Solid Films* **158**, 93–105 (1988).

100. Tangboriboon, N., Sirivat, A., Kunanuruksapong, R. & Wongkasemjit, S. Electrorheological properties of novel piezoelectric lead zirconate titanate $\text{Pb}(\text{Zr}_{0.5}\text{Ti}_{0.5})\text{O}_3$ -acrylic rubber composites. *Mater. Sci. Eng. C* **29**, 1913–1918 (2009).
101. Ouyang, G. M., Wang, K. Y. & Chen, X. Y. Enhanced electro-mechanical performance of TiO_2 nano-particle modified polydimethylsiloxane (PDMS) as electroactive polymers. in *Solid-State Sensors, Actuators and Microsystems Conference (TRANSDUCERS), 2011 16th International* 614–617 (2011). doi:10.1109/TRANSDUCERS.2011.5969778
102. Andres Perez, N., Sylvestre, A., Auge, J. L., Do, M. T. & Rowe, S. Dielectric spectroscopy in Silicone Rubber Incorporating Nanofillers. in *2006 IEEE Conference on Electrical Insulation and Dielectric Phenomena* 453–456 (2006). doi:10.1109/CEIDP.2006.311967
103. Steeman, P. A. M., Maurer, F. H. J. & van Es, M. A. Dielectric monitoring of water absorption in glass-bead-filled high-density polyethylene. *Polymer* **32**, 523–530 (1991).
104. Liu, L., Liu, Y., Zhang, Z., Li, B. & Leng, J. Electromechanical stability of electroactive silicone filled with high permittivity particles undergoing large deformation. *Smart Mater. Struct.* **19**, 115025 (2010).
105. Nguyen, H. C. *et al.* The effects of additives on the actuating performances of a dielectric elastomer actuator. *Smart Mater. Struct.* **18**, 015006 (2009).
106. Molberg, M. *et al.* High Breakdown Field Dielectric Elastomer Actuators Using Encapsulated Polyaniline as High Dielectric Constant Filler. *Adv. Funct. Mater.* **20**, 3280–3291 (2010).

107. Opris, D. M., Crespy, D., Lowe, C., Molberg, M. & Nuesch, F. Phthalocyanine and encapsulated polyaniline nanoparticles as fillers for dielectric elastomers. in *Electroactive Polymer Actuators and Devices (EAPAD) 2009* **7287**, 72870L–8 (SPIE, 2009).
108. Zhang, Q. M. *et al.* An all-organic composite actuator material with a high dielectric constant. *Nature* **419**, 284–287 (2002).
109. Zhang, X., Wissler, M., Jaehne, B., Breonnimann, R. & Kovacs, G. Effects of crosslinking, prestrain, and dielectric filler on the electromechanical response of a new silicone and comparison with acrylic elastomer. in **5385**, 78–86 (2004).
110. Huang, C., Ren, K., Zhang, S., Xia, F. & Zhang, Q. M. High dielectric constant polymer nano-composites actuator materials. in *2005 12th International Symposium on Electrets, 2005. ISE-12* 91–94 (IEEE, 2005). doi:10.1109/ISE.2005.1612326
111. Guiffard, B., Seveyrat, L., Sebald, G. & Guyomar, D. Enhanced electric field-induced strain in non-percolative carbon nanopowder/polyurethane composites. *J. Phys. Appl. Phys.* **39**, 3053–3057 (2006).
112. Huang, C. & Zhang, Q. Enhanced dielectric and electromechanical responses in high dielectric constant all-polymer percolative composites. *Adv. Funct. Mater.* **14**, 501–506 (2004).
113. Szabo, J. P. *et al.* Elastomeric composites with high dielectric constant for use in Maxwell stress actuators. in *Smart Structures and Materials 2003: Electroactive Polymer Actuators and Devices (EAPAD)* **5051**, 180–190 (SPIE, 2003).
114. Underhill, R. S. & Michalchuk, B. W. Carbon nanotube-elastomer composites for use in dielectric polymer actuators. in *International Conference on MEMS, NANO and Smart Systems* 369–370 (2005). doi:10.1109/ICMENS.2005.32

115. Huang, C., Zhang, Q. M. & Bhattacharya, K. All-organic dielectric-percolative three-component composite materials with high electromechanical response. *Appl. Phys. Lett.* **84**, 4391 (2004).
116. Risse, S., Kussmaul, B., Krüger, H., Waché, R. & Kofod, G. DEA material enhancement with dipole grafted PDMS networks. in *Electroactive Polymer Actuators and Devices* (eds. Bar-Cohen, Y. & Carpi, F.) **7976**, 79760N–79760N–7 (SPIE, 2011).
117. Jang, Y., Kato, T., Ueki, T. & Hirai, T. Performance of PMMA-PnBA-PMMA dielectric film actuator with controllable phase morphology. *Sens. Actuators Phys.* **168**, 300–306 (2011).
118. Zhao, H., Xia, Y.-J., Dang, Z.-M., Zha, J.-W. & Hu, G.-H. Composition dependence of dielectric properties, elastic modulus, and electroactivity in (carbon black-BaTiO₃)/silicone rubber nanocomposites. *J. Appl. Polym. Sci.* **127**, 4440–4445 (2013).
119. Rudykh, S., Lewinstein, A., Uner, G. & deBotton, G. Giant enhancement of the electromechanical coupling in soft heterogeneous dielectrics. *Appl. Phys. Lett.* **102**, 151905 (2013).
120. Kussmaul, B., Risse, S., Wegener, M., Kofod, G. & Krüger, H. Novel DEA materials by chemical grafting of silicone networks on molecular level. in *Proc. of SPIE Vol 8340*, 83400Y–1 (2012).
121. Kussmaul, B., Risse, S., Wegener, M., Kofod, G. & Krüger, H. Matrix stiffness dependent electro-mechanical response of dipole grafted silicones. *Smart Mater. Struct.* **21**, 064005 (2012).
122. Montgomery, C. *Technique of microwave measurements*. (McGraw-Hill Book Co., 1947).

123. Simpkin, R. Derivation of Lichtenecker's logarithmic mixture formula from Maxwell's equations. *IEEE Trans. Microw. Theory Tech.* **58**, 545–550 (2010).
124. Wagner, K. W. Erklärung der dielektrischen Nachwirkungsvorgänge auf Grund Maxwellscher Vorstellungen. *Arch. Für Elektrotechnik* **2**, 371–387 (1914).
125. Carpi, F., Rossi, D. D., Kornbluh, R., Pelrine, R. E. & Sommer-Larsen, P. *Dielectric Elastomers as Electromechanical Transducers: Fundamentals, Materials, Devices, Models and Applications of an Emerging Electroactive Polymer Technology*. (Elsevier, 2011).
126. Sihvola, A. H. & Pekonen, O. P. M. Effective medium formulae for bi-anisotropic mixtures. *J. Phys. Appl. Phys.* **29**, 514–521 (1996).
127. Sihvola, A. H. Self-consistency aspects of dielectric mixing theories. *IEEE Trans. Geosci. Remote Sens.* **27**, 403–415 (1989).
128. Jayasundere, N. & Smith, B. V. Dielectric constant for binary piezoelectric 0-3 composites. *J. Appl. Phys.* **73**, 2462 (1993).
129. Cho, S.-D., Lee, S.-Y., Hyun, J.-G. & Paik, K.-W. Comparison of theoretical predictions and experimental values of the dielectric constant of epoxy/BaTiO₃ composite embedded capacitor films. *J. Mater. Sci. Mater. Electron.* **16**, 77–84 (2005).
130. Joseph, T., Uma, S., Philip, J. & Sebastian, M. T. Electrical and thermal properties of PTFE-Sr₂ZnSi₂O₇ composites. *J. Mater. Sci. Mater. Electron.* **22**, 1000–1009 (2010).
131. Xu, J., Bhattacharya, S., Pramanik, P. & Wong, C. P. High dielectric constant polymer-ceramic (Epoxy varnish-barium titanate) nanocomposites at moderate filler loadings for embedded capacitors. *J. Electron. Mater.* **35**, 2009–2015 (2006).

132. Solomon, S. $\text{SmAlO}_3+\text{Ba}(\text{Zn}_{1/2}\text{Nb}_{2/3})\text{O}_3$: microwave ceramic composite. *J. Mater. Sci. Mater. Electron.* **22**, 1203–1207 (2011).
133. Yang Rao, Jianmin Qu, Marinis, T. & Wong, C. P. A precise numerical prediction of effective dielectric constant for polymer-ceramic composite based on effective-medium theory. *IEEE Trans. Compon. Packag. Technol.* **23**, 680–683 (2000).
134. Poon, Y. M. & Shin, F. G. A simple explicit formula for the effective dielectric constant of binary 0-3 composites. *J. Mater. Sci.* **39**, 1277–1281 (2004).
135. Hu, Y., Zhang, Y., Liu, H. & Zhou, D. Microwave dielectric properties of PTFE/ CaTiO_3 polymer ceramic composites. *Ceram. Int.* **37**, 1609–1613 (2011).
136. Webman, I. Effective-medium approximation for diffusion on a random lattice. *Phys. Rev. Lett.* **47**, 1496 (1981).
137. Vo, H. T. & Shi, F. G. Towards model-based engineering of optoelectronic packaging materials: dielectric constant modeling. *Microelectron. J.* **33**, 409–415 (2002).
138. Todd, M. G. & Shi, F. G. Validation of a novel dielectric constant simulation model and the determination of its physical parameters. *Microelectron. J.* **33**, 627–632 (2002).
139. Sareni, B., Krähenbühl, L., Beroual, A. & Brosseau, C. Ab Initio simulation approach for calculating the effective dielectric constant of composite materials. *J. Electrostat.* **40-41**, 489–494 (1997).
140. Yu, L. First principles studies of interface dielectric properties of polymer/metal-oxide nanocomposites. (North Carolina State University, 2009).

CHAPTER 4 Synthesis and Phase Behavior of PDMS/PU Blends

Abstract

This paper first reviews the phase behavior of polymers and interpenetrating networks, focusing on the synthesis and development of elastomer materials from polymer blends consisting of polydimethylsiloxane (PDMS) and polyurethane (PU). PDMS and PU were blended reactively for this study. The polymers' physical and chemical characteristics, as well as the interactions between the blend species, were investigated.

All synthesis materials, production methods, and characterization methods are explained in detail below. The characteristics of the blend materials, such as their chemical structures and mechanical properties, are discussed. In this study, various compositions were characterized using DMA, DSC, FTIR, SEM, and dielectric spectroscopy. The blend systems studied in this work display two glass transition temperatures (T_g) and indicate macro phase separation. The blends exhibited increased dielectric constants and mechanical properties with respect to pure PDMS elastomers.

4.1 Introduction

The processes of polymer mixing, alloying, and blending involve combining species of molecules into a single final product. A number of polymers can possibly form boundless combinations of self-organized polymer blends with outstanding specific properties, such as engineered band gaps¹, pattern ability^{2,3}, and high energy density (dielectric constant)⁴. Due to these properties, polymer blends have found applications in such areas as

nanolithography^{2,3,5} and the manufacturing of photovoltaic devices⁶, transistors⁷, supercapacitors⁴, and optoelectronic devices⁸.

A polymer mixture formation with one polymer synthesized or cross-linked in the presence of the other is called an interpenetrated polymer network (IPN)⁹. The process of making an IPN is known as reactive blending, and the resulting blends differ from other polymer blends and mixtures in two ways: Creep and flow are hindered, and continuity of one of the phases is required.

IPNs are classified as either sequential or simultaneous according to their network formation order¹⁰. Sequential IPNs are formed through in situ polymerization in already crosslinked and swollen elastomer networks. Simultaneous IPNs are those in which the monomers or pre-polymers and crosslinking agents for the synthesis of both networks are mixed together. The reactions are carried out simultaneously. The crosslinking reaction should proceed according to different mechanisms to avoid chemical interaction between macromolecules of the two networks.

IPNs can be prepared in several ways. Firstly, they can be prepared as an in situ synthesis of distinctive polymer species that are not forming a copolymer network in the same environment. Secondly, they can be prepared through a process in which polymer species are blended with each other and crosslinks are formed among the same polymer species. Finally, the third method is a combination of the first two methods: the formation of an IPN through synthesis of a species inside the second polymer species, resulting in what is known as

known as a semi-IPN. Semi-IPN formation begins with linear polymer chains that are then cured as blend formation proceeds.

In these formations, the crosslinks that create IPNs can be either chemical or physical. Along with chemical crosslinks, physical intermolecular polar interactions, and donor–acceptor interactions, crosslinks originating from other molecular configurations—including crystals, ion clusters, and hard blocks of block copolymers—play a very important role in network formation¹¹.

In situ IPNs are more stable than polymer blends because of the curing process through which they are created^{12–14}. In situ IPNs have a phase-separated morphology that depends on the fraction of each species present, on thermodynamic interactions, and on reaction kinetics and the rate of forming networks. The thermodynamics of mixing the two components determine the morphologies of curing blend systems. Micro heterogeneous phase separation of blends follows curing to form the final structure. The curing of polymers can also result in an imposed compatibility as compared to usual blends, and the resulting materials exhibit good dimensional stability over time^{15,16}.

The dynamics of in situ IPN phase formation follow thermodynamic rules and are consistent with chemical crosslinking reactions at the same time. Rosenberg et al.¹⁷ studied the phase behavior of in situ IPNs used as curing systems. The growth of the chain fragment molecular mass renders species incompatible after a certain conversion degree. This incompatibility among species is reported to begin in the early stages of a reaction (1 to 8 percent conversion) as molecular weight increases. The transition from compatibility to

incompatibility proceeds during the reaction as the molecules grow. After critical conversion, polymers follow the semi-IPN phase diagram. The phases, which correspond to the moment at which the elastic forces of the networks fix the phase separation, are called quasi-equilibrium phases¹⁵.

The phase behavior of semi-IPN blends depends on the compatibility, or thermodynamic interaction, between components; the kinetics of the curing reaction; the composition; the mobility of the polymer chain; and the polymerization degree at time of gelation. These system phases separate in concentrations smaller than those at which IPNs phase-separate. In studying highly compatible blends of PMMA and PEO, in situ IPNs, and their semi IPN formations Filip et al.¹⁸ observed a decrease in miscibility in semi-IPNs in comparison with blends and reported that IPNs with a PEO concentration of 60 percent appeared transparent, although semi-IPNs are transparent below 10 percent PEO content concentration.

The phase behavior of polymer blends determines blend and IPN properties. The thermodynamic interactions discovered by Helmholtz¹⁹ control these blends' self-assembled phase behavior, and a balance between the free energy of the system and the enthalpic and entropic factors together governs their phase dynamics²⁰ (see Equation 4.1).

$$\Delta G = \Delta H - T\Delta S \quad \text{Equation 4.1}$$

Flory, Huggins, Scott, and Magat²¹⁻²⁵ established a qualitative model, shown in Equation 4.2, that assumes the lattice is incompressible (i.e., not dependent on T and P). The free energy of a blend system, ΔG_m , determines the phase separation dynamics of the polymer blend. Equilibrium polymer-polymer phase behavior is controlled by molecular architecture, choice

of monomers, composition, and degree of polymerization. The incorporation of polymer architecture into the general equation as symbols ϕ , N , and χ provides the basis for determining the mixture of free energy, as shown in Equation 4.2²⁶:

$$\frac{\Delta G_m}{k_B T} = \frac{\phi_A}{N_A} \ln \phi_A + \frac{(1 - \phi_A)}{N_B} \ln(1 - \phi_A) + \phi_A(1 - \phi_A)\chi \quad \text{Equation 4.2}$$

In the above equation, χ is the Flory-Huggins²¹⁻²⁵ interaction parameter, a temperature-sensitive parameter that contributes substantially to enthalpic level; k_B is the Boltzmann constant; N is the polymer repeat; and ϕ is the volume fraction in a random section of a polymer chain on an incompressible lattice ($\phi_A + \phi_B = 1$)¹⁶.

The term on the left-hand side accounts for free energy, and ΔG_m represents free energy per segment. The first two terms on the right-hand side account for entropy of mixing, ΔS_m , which increases with mixing. Larger chains, higher N , show less mixing configurations decrease ΔS_m . The last term on the right-hand side represents the enthalpy of mixing, and the value of the segmental interaction parameter in this term, χ , affects ΔG_m . The parameter χ is a combination of the enthalpy and excess entropy of a particular system and is determined experimentally. This model in Equation 4.2 was further modified to include compressibility (T, P)^{27-29,29} and van der Waals³⁰ interaction effects on the χ parameter and to reveal the effects of pressure on upper critical and lower critical solution transitions (UCST and LCST).

Nucleation-growth and spinodal decomposition in the cloud-point conversion are two phase separation mechanisms for blends as well as IPNs. The nucleation and growth mechanism of a system is driven by the thermodynamic stability of the system. It is mainly dependent on

the concentration dependence of the Gibbs free energy. If $\partial^2 G / \partial \phi_2^2 > 0$, the system is unstable, and instability manifests as large concentration fluctuations. On the other hand, if $\partial^2 G / \partial \phi_2^2 < 0$, the system produces small fluctuations, resulting in a more heterogeneous phase formation with smaller domain size²⁶.

In these formations, the crosslinks that form IPNs can be either chemical or physical. Along with chemical crosslinks, other aspects of chemical substances' interaction—including physical intermolecular polar interactions, donor-acceptor interactions, crosslinks originating from crystals, ion clusters, and hard blocks of block copolymers—play a very important role in network formation¹¹. In network systems capable of forming physical crosslinks, the contribution of physical crosslinks to the effective network density is significant.

In situ IPNs are more stable than polymer blends because of their curing process¹²⁻¹⁴. They have a phase-separated morphology that depends on the fraction of each species, the thermodynamic interactions within the IPN, and its reaction kinetics and rate of forming networks. The phase behavior of curing systems and IPNs is determined by the processes of phase separation that take place during IPN formation. Micro heterogeneous phase separation of blends follows curing to form the final IPN structure. The curing of polymers can result in an increased compatibility over blends, and exhibit good dimensional stability over time^{15,16}.

In general, the phase behavior of semi-IPN curing systems depends on the compatibility, or thermodynamic interaction, among components as well as the curing reaction kinetics, composition, mobility of the polymer chain, and polymerization degree at the time of

gelation. Semi-IPN curing systems were reported to phase-separate at lower concentrations than IPNs.

Polymer blends, including IPNs, have been examined using small-angle X-ray, dynamic mechanical analysis (DMA), transmission electron microscopy (TEM), scanning electron microscopy (SEM), dielectric relaxation spectroscopy¹⁵, and optical imaging^{16,26,31}. The homogeneity of these systems can be observed directly from small-angle X-ray scattering. Transmission electron microscopy, along with the staining of polymers, is used to reveal blend morphology³². DMA is an indirect mechanical method of studying these systems to understand their interphases. The curve of tensile loss factor, $\tan(\delta)$, versus temperature displays a single temperature peak between the neat polymers of blends. The curve of tensile loss versus temperature exhibits two peaks, indicating the immiscible polymer compositions²⁰. Time-resolved light scattering and optical microscopy have been widely used to study the phase-separation kinetics of heterogeneous systems because the material's light transmittance decreases and the blend transforms from translucent to opaque³³.

Even the phase formation of a curing system is difficult to predict theoretically. Phase formation has been studied through consideration of thermodynamic interactions, crosslinking degree of network formations, and interfacial tension for sequential IPN formation¹⁰.

Although IPNs and semi-IPNs are not in a state of thermodynamic equilibrium, miscibility and compatibility are forced because each IPN or semi-IPN is considered to be in a quasi-equilibrium position. Two-phase heterogeneous IPN systems display a degree of

interpenetration in the interface of the constituent species due to the reactive bonding of the phases during IPN formation^{15,17,34,35}.

The use of higher temperatures accelerates the curing mechanism for curing systems. A curing system formed from PS and PDMS has been proven to reinforce the physical properties of the system because of resulting changes in the crystal structures of elastomers³⁶. Even though the effect of temperature on IPN formation can be determined based on the phase diagram of the curing system, the effect of temperature on miscibility is not yet fully understood.

At high pressures, the onset point of phase separation moves toward higher conversion of polymerization, and the mixture remains homogeneous at high molecular weight levels. Synthesis pressure also affects rate of phase separation by reducing the mobility of the polymer chains with reduced free volume¹⁸. This pressure's effect on the mixture's interaction parameter is not known quantitatively, but compatibility is generally assumed to increase at high pressure. The combined effects of increased compatibility and reduced rate of phase separation alter the degree to which the two components mix according to competition between the entropy and the standard Flory-Huggins term. Two possibilities exist for UCST:

(1) Case I UCST: Due to competition between the processes represented by the entropy and standard Flory-Huggins terms in Equation 4.2, the pressure has a destabilizing effect.

(2) Case II UCST: Due to differences in the energy parameters of each of the components³⁰, the pressure has a stabilizing effect.

The number of crosslinks and the amount of inter-network grafting³⁷ are important factors in the degree of phase separation^{34,35,38–41}. Crosslinking increases component molecular weights and changes the chain entropy and free energy, possibly driving the system from an initially homogeneous, one-phase region to a two-phase region⁴². Grafting collagen (cellulose acetate butyrate) to PDMS appears to enhance PDMS's thermomechanical and biomedical properties³⁷. The higher relative formation rate of the two partner networks can also increase phase behavior³⁶.

Polymer end groups also enhance the miscibility and phase behavior of blends in the cases of polar and nonpolar mixing systems. Experiments with α,ω -trimethylsilyl PDMS (PDMS–CH₃), α,ω -propylamino PDMS (PDMS–NH₂), and α,ω -propylcarboxy PDMS (PDMS–COOH) showed different cloud point curves for each upon mixture with polystyrene. The incorporation of amine end groups into PDMS shows an increased compatibility in comparison with PDMS–CH₃. The calculated binary interaction parameters show an increasing trend as polarity increases⁴³, suggesting that the repulsive nature of the interactions within the PDMS backbone results in increased compatibility of polymers. The strategy of using compatible chain end groups for low molecular weight polymers has been adopted to formation of copolymers of immiscible polymers⁴⁴.

Another method of improving the compatibility of two polymers is to use compatibilizer, which are usually block or graft copolymers. Compatibilizer segments, which include monomers of the polymers that are being blended, can reduce interfacial tension between polymer species⁴⁵. Zu et al.² report that an interfacial tension reduction of 82% was achieved

by employing a diblock polymer of the same species for the interphase region. Weight concentration of polymer and copolymer mixing order largely determined the amount of reduction. Compatibilization results from entropic inhibition of phase separation into micelles. The micelle formation at the copolymer interface and possible saturation limits the compatibility of the polymers blends⁴⁶. Wignall et al.⁴⁷ have shown that phase separation can be triggered by differences in the topologies of the two phases in polyolefin blends as well as in polysiloxane blends.

Polydimethylsiloxane (PDMS) exhibits poor mechanical properties because of the weak intermolecular interactions among its polymer chains. In order to enhance the mechanical properties of PDMS elastomers, filler compounds⁴⁸⁻⁵⁰, copolymers^{51,52}, and blending methods^{32,53,54} have been utilized. PDMS is also incompatible with other polymers because of its low solubility parameter and exceptional flexibility⁵⁵. These properties make PDMS a difficult polymer to use in non-equilibrium IPN architectures. PDMS form phase-separated morphologies with polymers such as polyurethane⁵⁶, polymethylmethacrylate⁵⁷, polystyrene⁵³, polybutadiene⁵³, polycarbonate⁵⁸, and epoxy⁵⁹. As noted, the majority of blends of commercial polymers are phase-separated; however, phase-separated blends often display useful mechanical and electrical properties that make them suitable for certain applications.

Dielectric elastomers have been employed to produce field-induced actuators from soft materials. Their performance is a result of the physical and chemical properties of materials. Polymer blends^{60,61} and elastomer formulations^{62,63} have been preferred to polymer-ceramic

and polymer-metal nanocomposites⁶⁴⁻⁶⁶ for preparation of all organic elastomer actuator materials^{61,67,68}. The mechanical properties of nanocomposites restrict their use in dielectric elastomers. Loading these composites with large amounts of ceramic filler causes high dielectric constants, which regrettably leads to an unacceptable degree of stiffness^{66,69} and an undesirably low composite electrical breakdown field. Conductive fillers, on the other hand, form conductive paths in the elastomer, resulting in high dielectric loss and low dielectric strength. Ultimately, this increase in stiffness or conductivity results in early electrical breakdown of the actuator material for both filler types^{70,71}. These polymer-polymer systems, including polymer blends and elastomer formulations, offer lower overall stiffness and higher dielectric breakdown strength.

In this work, dynamic, mechanical, and thermal behaviors of neat and reactive immiscible blends of PU and PDMS have been investigated with two different chain end groups. Interesting characteristics of PDMS, such as good insulation and the ability to maintain elastomeric behavior over a wide range of temperatures, were a primary reason for selecting a PDMS network as the matrix. However, due to the low dielectric behavior and low mechanical properties of neat PDMS networks, a PU polymer-blending approach was adopted to reduce these common problems.

4.2 Materials and Experimental Methods

4.2.1 Materials

Silicone (PDMS) and polyurethane (PU) materials were used as matrices and fillers, respectively, for blend preparation. Two routes of elastomer formulation were adopted for

blend matrix preparation and were used to form Type I and II blend elastomers. The Type I PDMS was commercially available Sylgard 186 (Dow Corning, NY), and the Type II matrix was formulated in our lab. Thermoplastic poly(ether-urethane) (Elastollan 1180A, BASF) is a thermoplastic elastomer sold in commercial pellet form. Elastollan 1180A, a relatively high-dielectric constant polymer ($\epsilon = 7.8$ at 100 Hz), was used as dielectric filler in this work. Tetrahydrofuran (Fisher Sci, USA), an excellent blending solvent, was used during the process of blend preparation.

4.2.1.1 Matrix Materials

Chemical crosslinking of siloxanes can be accomplished through four types of common commercial reactions⁷²: 1) peroxide-induced free radical reactions, 2) condensation reactions, 3) hydro-silylation addition reactions, and 4) hydride silane/silanol reactions. In our experiments, we used a hydro-silylation addition reaction for the Type I elastomer because of this PDMS's commercial availability and excellent electrical and mechanical properties.

In developing matrix elastomers with a formulated dielectric matrix (referred to here as "Type II elastomers"), increased interphase compatibility of the matrix and filler was needed. To achieve this, we employed a condensation (i.e., alkoxy-cure) reaction that entailed linking hydroxyl-terminated siloxanes in the presence of a tin catalyst and developing crosslinking through an isocyanate functional crosslinker (3-isocyanatopropyltriethoxy-silane)^{37,51,52,73-77}. These reactions were also reportedly observed with graft blending⁷⁸. The hydroxyl-terminated PDMS is compatible with PU in terms of network formation properties because its polar end groups bring its solubility parameter close to that of PU.

Materials for Blends with the Type I Elastomer

The Type I elastomer used in this research is an addition-cure elastomer produced by Dow Corning Co. under the name Sylgard 186. It is a two-part elastomer consisting of a hydride functional silicone polymer and a vinyl-terminated crosslinker. It is formed using an addition polymerization reaction initiated by a platinum catalyst.

The two parts of a Type I elastomer are known as Parts A and B. Part A consists of a vinyl functional silicone fluid with a platinum catalyst and includes silica nanoparticles as reinforcement fillers. Part B consists of a hydride functional crosslinker and inhibitor. A platinum complex participates in a reaction that forms ethylene bridges between species. The reaction rate depends on heat and lasts 24 hours. Ethylene bridges create elastomer networks between the hydride functional crosslinker and the vinyl functional polymer. Consequently, an elastomer with an ethyl-bridged elastomer network produces no byproduct in the closed elastomer environment except H₂ gas, which solubilizes in the polymer and quickly outgasses to the environment with no observable bubbles. This reaction mechanism is pictured below in Figure 4.1(a)-(c), and Table 4.1 provides the material information.

Materials for Blends with the Type II Elastomer

Our method for producing Type II elastomers with a hydroxyl-terminated PDMS based network DMS S42 (Gelest, PA) was catalyzed with tin (45 ppm). Polymerization took place at room temperature in a moist environment. The Type II elastomer is an alkoxy condensation system consisting of a hydroxyl functional polymer and an isocyanate functional crosslinker. Alkoxy condensation systems involve hydroxyl functional polymers

and alkoxy-functional crosslinking compounds. The alkoxy functional crosslinker undergoes a hydrolysis step that results in a hydroxyl group, which then participates in a condensation reaction with another hydroxyl group attached to the polymer. This reaction can proceed without the assistance of the tin catalyst, but the catalyst amount increases the reaction rate⁴⁰.

In producing Type II elastomers, we incorporated an isocyanate to increase the functionality of the crosslinker and utilized an alkoxy mechanism to increase interphase adhesion between polymer species. PU has a polar structure and a hydroxyl end group similar to the hydroxyl-terminated PDMS polymer network. This was expected to increase compatibility to a minuscule degree⁴³. The isocyanate mono-functional group in the crosslinker was introduced to increase the possible chemical interaction of PDMS polymers with PU elastomers during network formation. This crosslinker can establish links with both PU and PDMS hydroxyl end groups⁴⁹. The isocyanate single-function group in the crosslinker is also reactive to the PU elastomer side groups^{51,52,73-77}. This procedure results in a tetra-functional network in which the siloxane backbones join the PU elastomers together in the interphase regions of the blends. This formulation of end group included structure for Type II elastomers is depicted in Figure 4.2.

The polymer networks were prepared from the hydroxyl-terminated PDMS (Gelest, PA) using tin as a catalyst. They were cured at room temperature. An example formulation of a Type II elastomer is as follows:

10 g of PDMS fluid DMS S42 ($M_w = 77.000$),

5 μ l crosslinker (Gelest, PA),

45 μ l of tin catalyst.

All solvents were obtained from Sigma-Aldrich and used as received.

The formulation above was used for all blend compositions. The formulation of elastomers is given in Table 4.1, and Figure 4.1(d), (e), and (f) depict the reaction mechanism for the Type II elastomer.

Table 4.1 PDMS matrix elastomer composition comparison of types I and type II for blend materials formulation.

Material	PDMS Name	PDMS Polymer Properties	Crosslinker	Catalyst	Reaction Mechanism	Reinforcement Filler
PDMS Type I	Sylgard 186 base, Dow Corning	Hydride e.g.	Vinyl functional cross-linker	Platinum (Sigma Aldrich)	Two-part addition polymerization	Fumed silica
PDMS Type II	DMS S42, Gelest	Hydroxyl e.g.	3- iocyanatopropyl triethoxy-silane	Tin (Sigma Aldrich)	Condensation reaction (alkoxy)	None

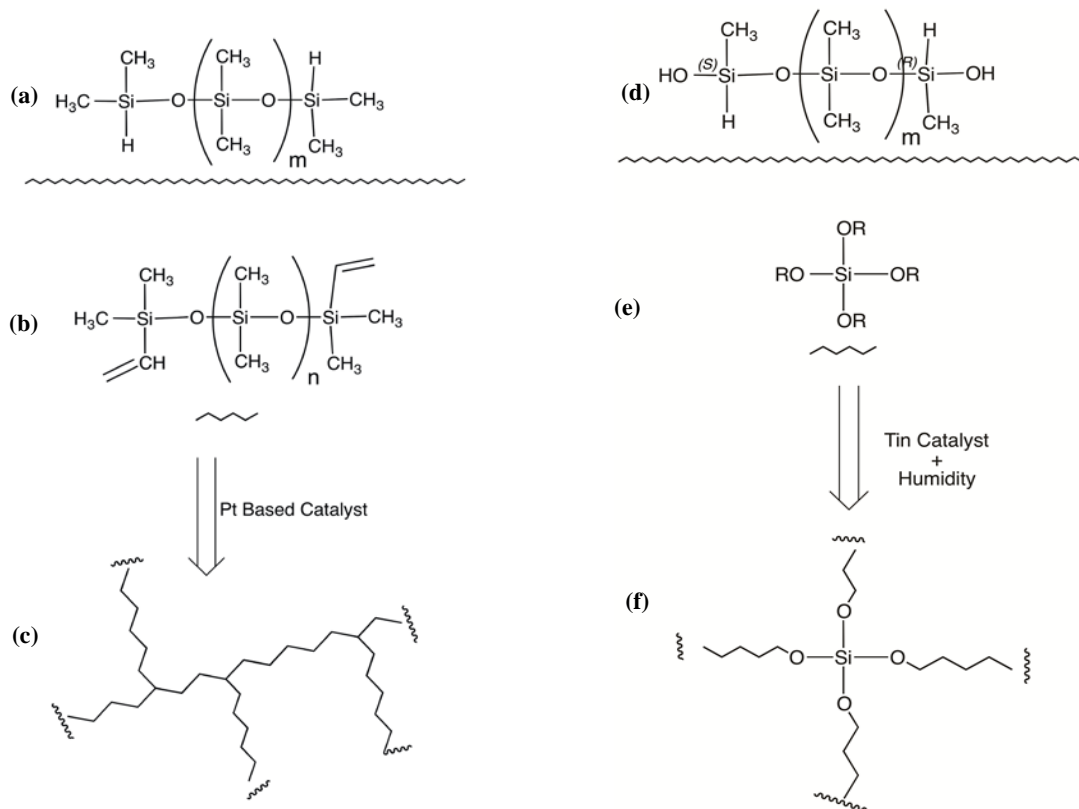


Figure 4.1 Chemical Formulation PDMS elastomer networks, Type I (a,b,c) and Type II (d,e,f). Polymer (a) is a hydride functional PDMS fluid, crosslinker (b) is a multi-functional crosslinker, (c) is a PDMS elastomer network, (d) is hydroxyl functional PDMS fluid, crosslinker (e) is a multi-functional crosslinker, and (f) is the PDMS elastomer network. The catalyst is tin, and the reaction takes place in a humid environment.

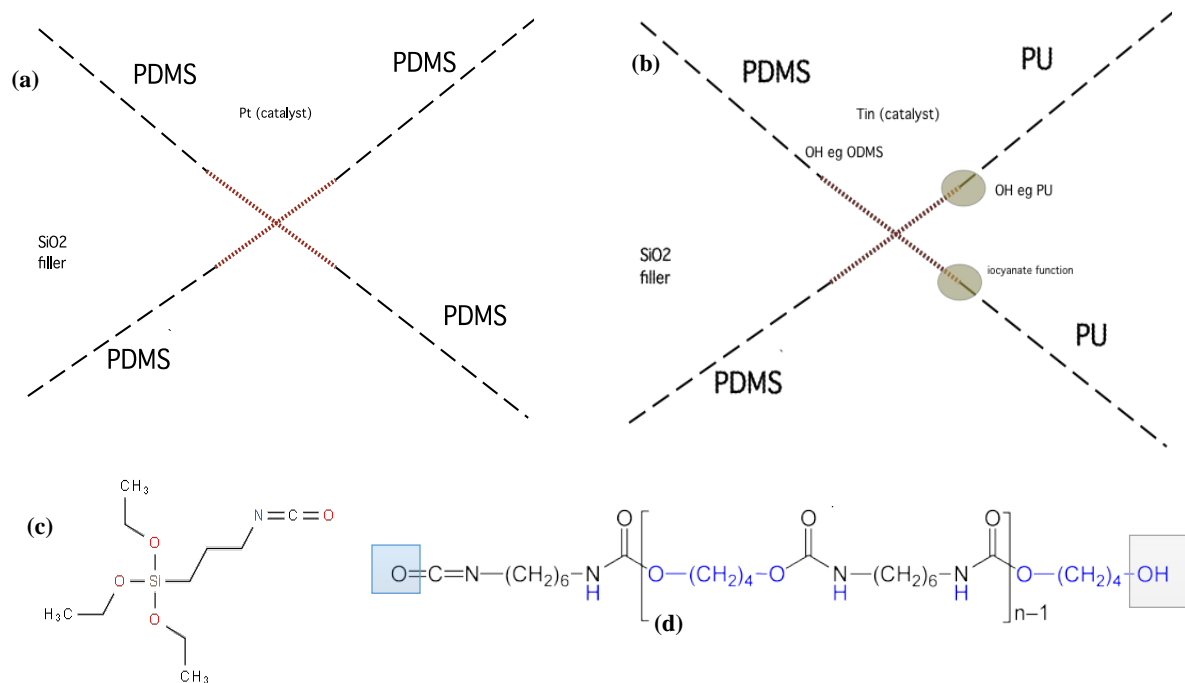


Figure 4.2 Possible routes of interaction between PDMS and PU elastomers: (a) schematic of network formation of Type I elastomer; (b) schematic of network formation of Type II elastomer; (c) chemical structure of 3-iodocyanatopropyltriethoxy-silane crosslinker; (d) chemical structure of polyurethane elastomer with end groups shaded.

4.2.2 Polymer Blend Preparation

In the blending of PDMS and PU, the large solubility differences between the two materials make selecting the right co-solvent crucial. Specifically, the mechanical properties of the blend elastomers are dependent on the blending co-solvents selected. PDMS is a non-polar polymer with a low solubility parameter and is not soluble in polar solvents such as DMF, NMP, and DMAc, which are good solvents for polyurethane. PDMS instead prefers solvents such as THF, 2-ethoxyethyl ether (EEE), dioxane, and toluene.

We prepared the blends by simply mixing PDMS and PU in THF. The PDMS and PU polymers were both dissolved in co-solvent THF in separate containers. The PDMS base part was mixed with the THF solvent at room temperature for three hours. PU pellets were dissolved in the THF solvent for 12 hours at 50 °C. The PDMS and PU solutions were mixed using a magnetic stirrer. The crosslinker and catalyst of the PDMS matrix were added to the final polymer mixture, and this mixture was processed using a high-shear mixer for one minute. The sequence of magnetic stirring and planetary high-shear mixing was performed so as to prevent premature curing of the PDMS system for the Type II elastomer matrix. The mixture was then poured on Teflon substrates for film formation for mechanical and dielectric characterization. These blends were also separately thinned to a thickness of 100 μm using a spin-coater for electromechanical characterization. The samples were then dried in an oven, first at room temperature and later at 80 °C sequentially for 12 hours for solvent evaporation and PDMS curing. The samples were then collected and prepared for characterization. Figure 4.3 summarizes this process.

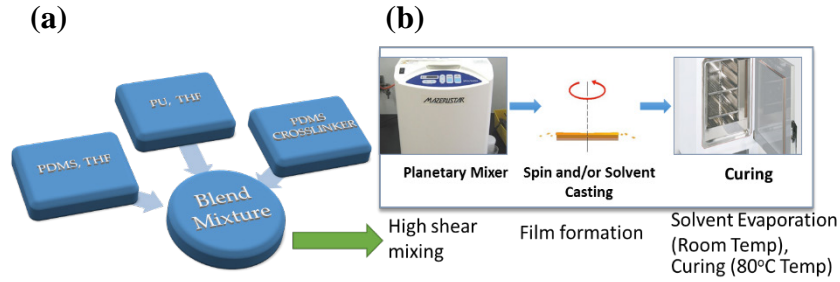


Figure 4.3 Schematic of blend elastomer preparation: (a) mixing PU/THF and PDMS/THF mixture and addition of the PDMS crosslinking agent to the mixture for film formation, (b) use of planetary mixer for overall mixing and curing film preparation.

4.2.3 Compatibility Estimation

An estimate of the polymer-polymer interaction (χ) was calculated as in Equation 4.3:

$$\chi = \beta + \frac{V}{RT} |\delta_1 - \delta_2| \quad \text{Equation 4.3}$$

where β is the lattice constant, which was set to 0.34; R is the gas constant; T is the absolute temperature; and δ_1 and δ_2 are the independent PU and PDMS solubilities, respectively. These solubility parameters were calculated theoretically from the polymers' cohesive energy densities⁷⁹, applying the group contributions method that takes into account PU's hard and soft segment ratio, along with the data from the thermodynamic tabulations of Fedors⁸⁰. In our calculations, we took into consideration the PDMS end groups and PU hard-to-soft segmental ratio using Equation 4.4 to calculate our solubility parameter:

$$\delta_p = \rho \left| \frac{\sum F_i}{M} \right| = \frac{\sum F_i}{V} \quad \text{Equation 4.4}$$

where V is molar volume, ρ is the polymer density; F is the molecular attraction constant; and M is the molecular weight of the repeating unit. For PU, $p = 1$; for PDMS, $p = 2$.

4.2.4 Dynamic Mechanical Property Characterization

Dynamic mechanical analysis (DMA) measurements were carried out on the blends and on the homopolymers of PU and PDMS, with frequency and temperature sweeps processed separately. These analyses were conducted according to the ASTM Standard Guide (ASTM D5026) using a tensile test fixture and rectangular geometry for each sample. The frequency sweep experiments were performed over a range of 0.01 Hz to 100 Hz on a dynamic mechanical analyzer RSA3 (TA Instruments, New Castle, DE) at room temperature for the three different materials: PDMS, PU, and the blends. The gauge lengths of the specimens were 25 mm over a cross-section of about 0.5 mm². A control on the position with a prestrain of 0.5 mm (corresponding to a strain of ± 0.02) with a preload of 0.05 N was observed for frequency tests. Thus, the samples were always in tension, even at the low points of the cycles. Dynamic testing equipment software, Orchestrator (TA Instruments), calculated the phase angle ϕ between the applied displacement and the measured force and used the specimen shape to convert the stiffness and the phase information to provide the values of E' , the storage modulus; E'' , the loss modulus; and $\tan(\delta)$, the tangent of the phase angle.

The frequency response of the blends and their constituent polymers, E' and E'' with the logarithmic frequency sweep, has been studied between $10 \cdot 10^{-1}$ and $10 \cdot 10^3$ rad/sec to understand the frequency-related dynamic behavior of blends.

To understand the viscoelastic response of the composites, a DMA with a temperature sweep was conducted using a dynamic mechanical analyzer from TA Instruments (Q800). The tests were performed in tension mode over a temperature range of (-125)-200 °C, with a heating rate of 3 °C/min at a frequency of 1 Hz and a strain amplitude of 0.1%. Strain sweeps were performed to ensure measurements were carried out within the limits of the linear response of the materials, and all data acquired were subject to this limitation. The gauge length was 15 mm, and the specimen width was 6 mm. Dynamic elastic (E') and loss (E'') moduli were recorded while the sample was heated. The glass transition temperatures (T_g) of the samples were determined from the peaks of $\tan(\delta)$. The DMTA data were analyzed using TA Instruments Universal Analysis 2000 software.

4.2.5 Differential Scanning Calorimeter (DSC) Analysis

Thermal analyses of the blend elastomers were conducted using a TA Instruments Differential Scanning Calorimeter (DSCs-Q2000) over a temperature range of -100-300 °C with a heating rate of 10 °C/min under a nitrogen atmosphere. Two heating and cooling scan cycles were performed within the operating range. The thermal history of the blended samples was removed with the first cycle, and the melting temperature (T_m), the crystallinity temperature (T_c), and enthalpy of fusion (ΔH) were determined from the second cycle. The PDMS exhibited crystallization peaks in the DSC experiments. PDMS crystallinity was calculated as the ratio of ΔH from this study to the ΔH at 100% crystallinity. The percent crystallinity values of the polymers in the homoelastomers and blends were calculated using Equation 4.5⁸¹. The ΔH at 100% crystallinity of PDMS was defined as 37.43 J/g for the enthalpy of fusion of PDMS⁴⁸.

$$X = \frac{\Delta H_f - \Delta H_c}{w \times \Delta H_f^0} \times 100 \quad \text{Equation 4.5}$$

4.2.6 Fourier-Transform Infrared Spectroscopy (FTIR) Analysis

FTIR was performed on pure PDMS, pure PU, and the blend samples with 20% PU concentration using a Perkin-Elmer Spectrum 100 spectrometer. A background scan and eight subsequent measurement scans were performed for each sample. A diamond tip was used in the spectrometer for better penetration of the elastomer. The 100 μm -thick samples were examined under atmospheric pressure at a resolution of 4 cm^{-1} . The data were collected over a range of 400-4000 cm^{-1} and analyzed using OPUS 4.0 (Bruker Optics) software.

4.2.7 Morphological Property Characterization

The representative specimens of the blends were prepared for scanning with electron microscopy (SEM) imaging. The blend elastomers were cross-fractured in liquid nitrogen, and the samples were then coated with approximately 15nm of a gold/palladium (Au/Pd) mixture. SEM imaging was performed using secondary electrons of a high-resolution field-emission SEM (JSM-6400F, JEOL) operated at an accelerating voltage of 10 kV and a magnification of 500x to 5000x to determine blend morphology. The images were analyzed using the imageJ software package (developed by the NIH) to determine the PU species size in the blends.

4.3 Results

4.3.1 Compatibility Estimation

The solubility parameters of the polymers were calculated using the values in Table 4.2. $\delta_{\text{Type I PDMS-CH}_3}$ was calculated to be $17.2 \text{ (J/cm}^3\text{)}^{1/2}$; $\delta_{\text{Type II PDMS-OH}}$ was calculated to be $17.5 \text{ (J/cm}^3\text{)}^{1/2}$; and δ_{PU} was calculated to be $33.1 \text{ (J/cm}^3\text{)}^{1/2}$ ⁴³. Since the solubility parameters of the two components differ by $15.3 \text{ (J/cm}^3\text{)}^{1/2}$ and $15.6 \text{ (J/cm}^3\text{)}^{1/2}$ for Types I and II (as calculated by subtracting the PU and PDMS solubility parameters), respectively, these two polymers are heterogeneous except under extreme conditions. These calculated results for estimating results are consistent with the previous work of Yilgor et al.⁴⁴ and similar to experimental results obtained by Vlad et al.⁵⁶. However we can say the effect of end groups are negligible on polymer compatibility.

Table 4.2 E_{coh} (internal energy) and V_g (internal molar volume) of polymer constitutes⁷⁹.

Index Units	Constitution	E_{coh} (J/mol)	V_i (cm ³ /mol)
1	-COOH	27630	28.5
2	-CO-	17370	10.8
3	-CH ₂ -	4937	16.1
4	-NH-	8370	4.5
5	>C ₆ H ₅	31940	33.4
6	-CH ₃	4707	33.5
7	(-Si-O) -2CH ₃	243	0.99
8	-OH	29790	10
9	=CH ₂	4310	28.5

4.3.2 Dynamic Mechanical Analysis (DMA)

The dynamic properties of PDMS and PU and their blends were analyzed under both changing frequency (DMFA) and changing temperature (DMTA). The storage modulus and mechanical loss factor, $\tan(\delta)$, for the homopolymers and blends are given in Figure 4.5 and Figure 4.6, respectively. Figure 4.4 shows the frequency response of polymer dynamic mechanical properties.

A frequency sweep under isothermal conditions and a temperature sweep at constant frequency were performed because the temperature sweep provides important information about phase interactions whereas the frequency sweep gives information about the mechanical and damping properties of blends. The PDMS-PU system was measured at an increasing frequency of 0.1-100 rad/sec at constant room temperature. These data, plotted in Figure 4.4, showed a stable storage modulus for all elastomers. The modulus of 0.4 MPa for Type II PDMS increased up to 1.5 MPa for Type II blends. A loss modulus between 0.05 and 0.15 was also observed for the blends (see Figure 4.4). The slight increase in loss modulus over the increasing frequency is typical for polymers and polymer blends. Over the frequency interval, the modulus of each sample was constant while the loss tangent increased slightly. Indeed, it is well known that the modulus of PU and PDMS homopolymers increases with increasing both physical and chemical crosslink density⁸². The storage modulus of the 20 wt% PU/Type I PDMS blends was found to be higher than that of the 40 wt% PU/Type I PDMS blends, while the Type II blend elastomers showed an increase in storage modulus for both compositions. Overall damping properties were lower for Type II elastomers than for Type I elastomers (see Figure 4.4(d) and Figure 4.4(b), respectively).

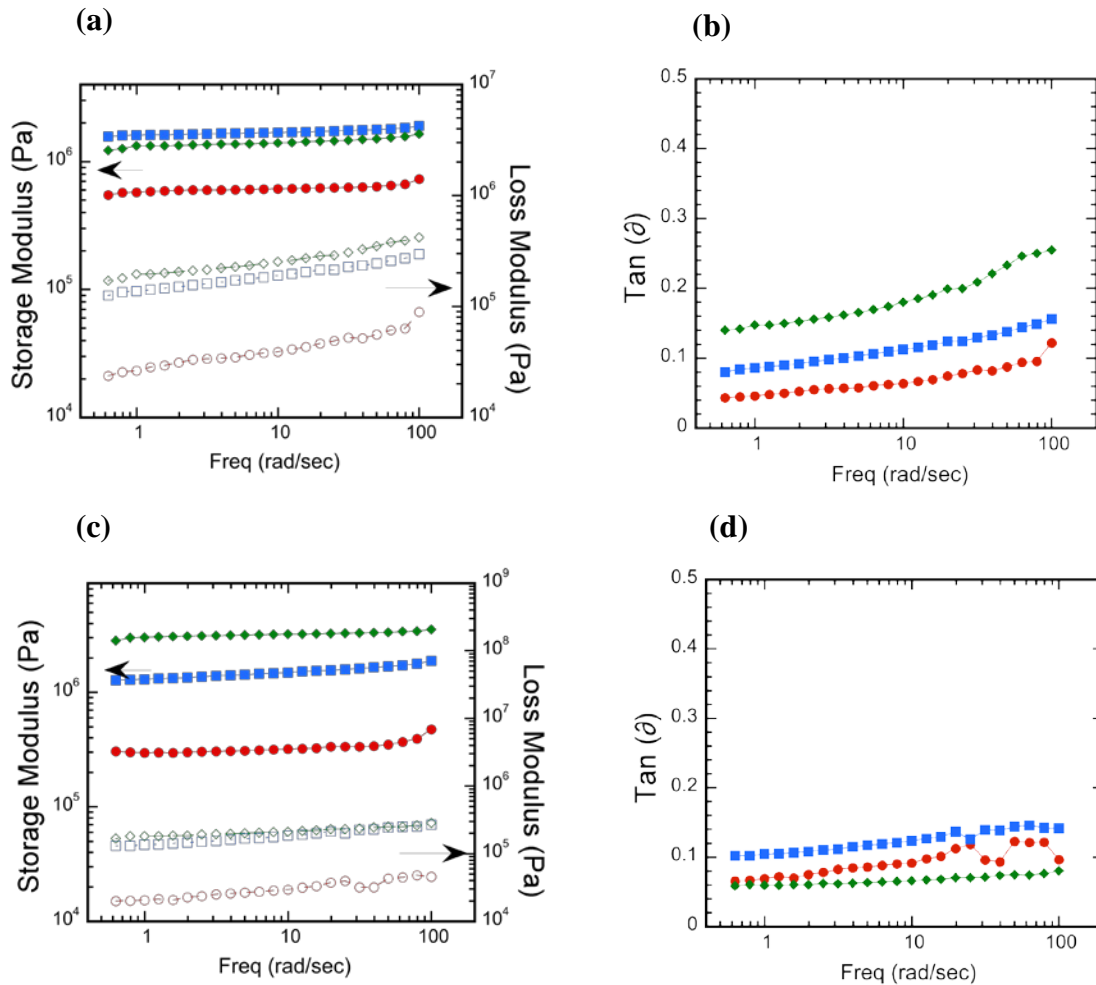


Figure 4.4 DMFA Analysis of Type I PDMS and Type II PDMS and blend: (a) Storage modulus and loss modulus with varying frequency of Type I elastomers, (b) $\tan(\delta)$ of blends for varying frequency of Type I elastomers, (c) storage modulus and loss modulus with varying frequency for Type II elastomers, (d) $\tan(\delta)$ of blends for varying frequency Type II elastomers. Symbols are as follows: (●) represents pure PDMS; (■) represents 10/90 PU/PDMS blends; and (◆) represents 20/80 PU/PDMS blends. Open symbols correspond to the loss modulus of the samples.

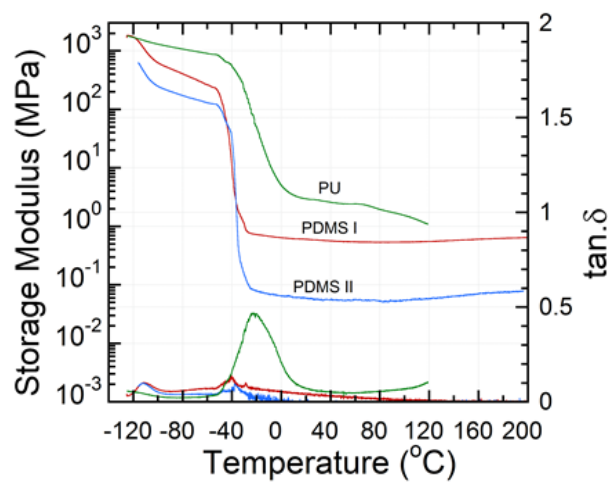


Figure 4.5 DMTA Analysis of homopolymers of PU, Type I PDMS, and Type II PDMS. Storage modulus and $\tan(\delta)$ were plotted from $-130\text{ }^{\circ}\text{C}$ to $200\text{ }^{\circ}\text{C}$. PU sample breaks at ca. $120\text{ }^{\circ}\text{C}$. Red line (—) represents the Type I PDMS; blue line (—) represents the Type II PDMS; green line (—) represents PU elastomer.

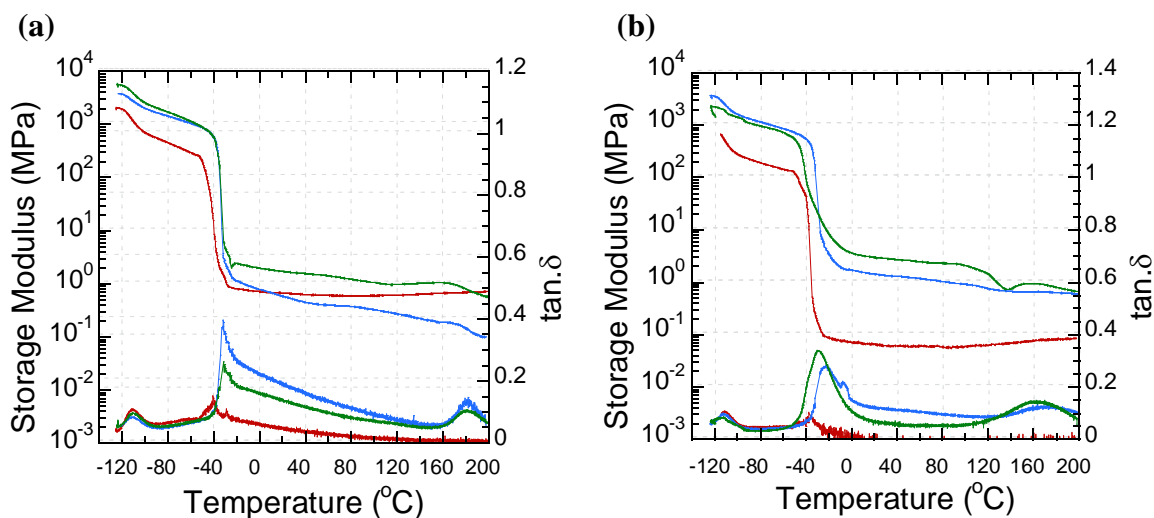


Figure 4.6 DMA Analysis of Type I elastomer and its blends. Red line (—) represents pure PDMS; blue line (—) represents the 10 PU wt% concentration blend sample; green line (—) represents the 20 PU wt% concentration blend sample: (a) storage modulus and loss modulus with varying temperature from -130 °C to 200 °C for PDMS elastomer Type I and blends with 10 and 20 wt% PU concentrations; (b) storage modulus and loss modulus with varying temperature from -130 °C to 200 °C for PDMS elastomer Type II and blends with 10 and 20 wt% PU concentrations.

Dynamic mechanical temperature data for the homonetworks are shown in Figure 4.5, and data for the blended networks are shown in Figure 4.6. As would be expected due to the glassy state of the polymer, the storage modulus (the left hand side of each panel in Figures 4.5 and 4.6) is high at low temperatures for both blends and homopolymers. As temperature increases, the storage modulus decreases by two orders of magnitude due to the polymer's rubbery behavior. The loss tangent (the bottom plots in Figures 4.5 and 4.6) reaches its maximum near the glass transition temperature (T_g). In the data for the PDMS samples, presented in Figure 4.6, the first of the three peaks corresponds to the usual glass transition

temperature. As can be seen, PDMS Type I and II elastomers exhibit glass transition temperatures of -111 °C and -112 °C, respectively. The T_g of blends remains unchanged as PU wt% vary, indicating that the PDMS chains participating in the glass transition do not change with silica content. For the PU homopolymer, a sharp peak in E'' with a maximum between -30 °C and -15 °C (see Figure 4.5) is assigned to the glass transition of PU, with a loss tangent peak occurring at -20.1 °C.

For PDMS elastomers, a second T_g (T_{g2}) has been observed at 60 °C to 100 °C above the polymer's T_g (i.e., $T_{g2} \in [T_g + 60 \text{ °C}, T_g + 100 \text{ °C}]$). This T_{g2} was observed in polymer composites with high-surface area microfillers and nanofillers such as carbon black, silica^{83,84}, and ionomers⁸⁵. The second T_g , T_{g2} , was -40.5 °C for Type I PDMS and -37.8 °C for Type II PDMS. In literature this second peak was attributed to the T_g of the polymer layer surrounding the particles⁸⁵. A greater number of silica particles decreased the size and maximum temperature of this peak⁸⁶. Our experiments for Type I PDMS with silica fillers found similar behavior but a smaller T_{g2} (see Figure 4.5 for Type II PDMS), even without silica fillers. Robertson et al.⁸⁷ focused on the reasons for the existence of the second loss tangent peak in polymer-particle composites. According to the authors, this second peak is not the glass transition response of an immobilized polymer shell but rather is associated with the suppression of flow relaxation (chain diffusion) of the polymer chains due to incomplete terminal relaxation. Partially crosslinked unfilled polymer systems have also been reported to produce the same higher-temperature $\tan(\delta)$ peak (T_{g2}). However, according to report by Robertson et al.⁸⁷, since we observe second relaxation peak on Type I and Type II

elastomers, we can infer that there exist a small number of uncrosslinked chain end groups that result in a second relaxation peak.

We observed a small shift in T_g to a temperature of approximately $-31\text{ }^\circ\text{C}$ for the blends of both types and for all concentrations. These blend T_g s surpassed the observed second T_g of PDMS polymers and showed a higher blend T_g for all compositions. All T_g measurements for these samples are displayed in Table 4.3. Additionally, the loss modulus followed the same trend as the storage modulus: plateauing as temperature increased at the same points at which storage modulus decreased sharply before leveling off. These points correspond to the polymers' transition from a glassy state to a rubbery state.

Table 4.3 Glass transition temperature (T_g) of polymer blends and their pure polymer constitutes. The temperature data was calculated from the $\tan(\delta)$ peaks in Figure 4.6.

Polymer Composition (wt %)	T_g ($^{\circ}\text{C}$)	T_{g2} ($^{\circ}\text{C}$)	$T_{g\text{-blends}}$ ($^{\circ}\text{C}$)
PU	-20.4		
Type I PDMS	-111.3	-40.5	
Type I +10% PU	-110.0		-30.5
Type I + 20% PU	-111.2		-31.4
Type I + 40% PU	-110.2		-30.1
Type II PDMS	-112.1	-37.8	
Type II + 10% PU	-112.2		-30.1
Type II+ 20% PU	-112.3		-30.2
Type II + 40% PU	-112.4		-29.0

A significant improvement in the physical properties of Type II PDMS and its blends was achieved by incorporating the polyurethane polymer. The elastic modulus of this network was significantly improved, from 0.2 MPa to 1 MPa. Storage and loss tangent versus temperature data for the blends are plotted in Figure 4.6. The curves in both plates ((a) for Type I and (b) for Type II) show the shifted T_g at approximately -31°C for the PU and at -111°C for both the Type I and Type II PDMS. Since the temperatures of the transitions in

the blend are identical to those in the homonetworks, the two polymers are incompatible, and the blend is phase-separated.

4.3.3 Differential Scanning Calorimetry (DSC) Analysis

DSC analyses of the blends, PU, and PDMS are provided in Figure 4.7. These plots were created from the measurements taken during the second heating cycle, which ran from -90 °C to 260 °C. A PDMS elastomer generally exhibits four DSC peaks during the second heating cycle: (1) the glass transition, (2) an exothermic crystalline formation (cold crystallization), (3) the endothermic melting of one crystalline form, and (4) the other crystalline form of the polymer⁸⁸. Aranguren et al.⁴⁸ report that this crystallization during the heating cycle displays peak dependencies on cooling and heating rates. In our experiments, we observed a single endothermic crystallization peak for both PDMS types and their blends. A single crystallization peak, without a cold-crystallization peak, is proof of an existing one-crystal form, with quite perfectly formed crystals⁸⁹. A cold crystallization has generally been observed in linear PDMS networks⁸⁸. Cold-crystallization peaks were absent in the measurements we obtained during the second heating run (see Figure 4.7), indicating that the samples were cured.

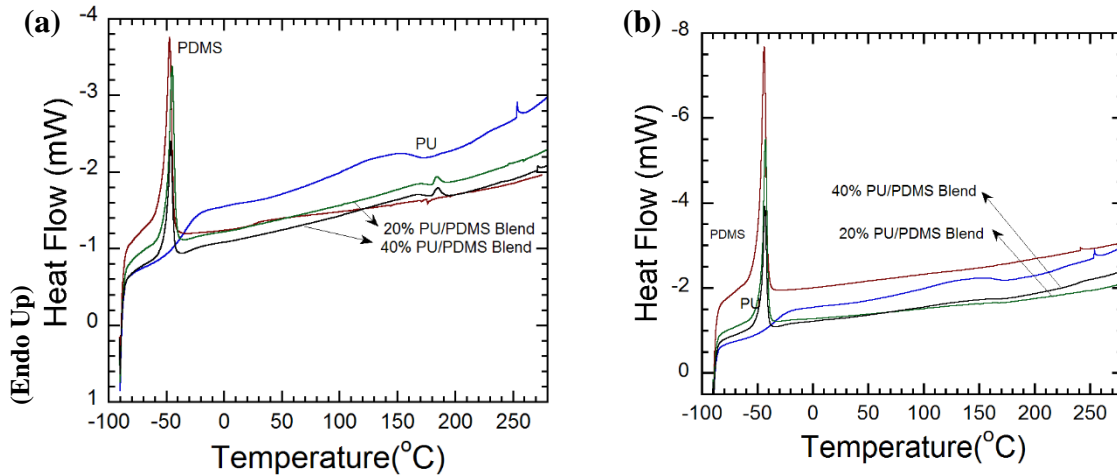


Figure 4.7 DSC Analysis of Types I and II elastomer and their blends. Red (—) represents pure PDMS; blue line (—) represents PU polymer; green line (—) represents 20 PU wt% concentration blend sample; and black line (—) represents 40 PU wt% concentration blend sample: (a) storage modulus and loss modulus with varying temperature from -120 °C to 200 °C for PDMS elastomer Type I and its blends with 20 wt% and 40 wt% concentrations; (b) storage modulus and loss modulus with varying temperature from -120 °C to 200 °C for PDMS elastomer Type II and its blends with 20 and 40 wt% concentrations.

Table 4.4 Crystallinity and crystallinity peak temperatures of elastomers with different PDMS/PU ratios in casting solutions. These calculations are based on the data presented in Figure 4.7

Polymer Type	ΔH_m (J/g)	X_c (%)	Overall ΔX_c (%)	PDMS phase ΔX_c (%)	X_c Peak (°C)
PU	15,4				-22.4
Type I neat PDMS		41	-	-	-40.5
Type I +10% PU			%-11	%-1	-30.5
Type I + 20% PU	12.1	32	%-22	%-2	-31.4
Type I + 40% PU	7.8	21	%-50	%-2	-30.1
Type II neat PDMS	23.3	62	-		-37.8
Type II+ 10% PU					-30.1
Type II+ 20% PU	18.4	49	%-31	%-0.5	-30.2
Type II + 40% PU	12.9	35	%-43	%-1	-29.0

The noticeable peaks in Figure 4.7 represent endothermic melting of a single crystalline form. These thermograms show a single large peak around -50 °C, attributed to the crystallization of PDMS networks and indicating a complete chemically crosslinked polymer network⁹⁰. Such single large peaks present in thermograms indicate a complete chemically crosslinked polymer network⁸⁷, with peaks around -50 °C related to crystallization of PDMS networks.

Incorporating silica fillers did not significantly affect the main T_g of cured and uncured PDMS networks or the segmental mobility of polymer chains. However, ΔC_p is reported to be around 1/4 of that of the uncured polymer³⁸ with around 0.140 J/g°C for cured PDMS samples. The literature reports an increase in heterogeneous nucleation crystallization and a

decrease in general crystallization with incorporation of silica fillers. This different results reported in the literature is reported to be a result of differences in silica filler interface chemistry⁴⁸.

In our DSC results, provided in Figure 4.7, there were fewer crystals in the PDMS with silica fillers because the presence of silica fillers is only in Type I PDMS, it has lower heat of fusion, and less amount of crystals. The crystals in Type II elastomers showed internal stresses increased by the crystal formation occurring during heating cycles.

In general, the heat of fusion is reported to decrease with increasing silica concentration and crosslinking density, because crosslinking decreases both the extent and the stability of the crystal phase⁴⁸. Silica decreases the measured heat, but it also interferes with the crystallization process and affects ΔH_{fs} values because the polymer loops and chain ends cannot crystallize when attached to solid surfaces due to topological constraints. As a result, the bound elastomer reaches a lower degree of crystallization than the pure polymer. This effect is similarly observed in our results: The Type I blends showed a smaller crystallization peak for each composition and smaller ΔH_{fs} values in pure form. It can be concluded from the DSC data reported in Figure 4.7(a)-(b) that the Type II blends had a higher number of crystals than the Type I blends.

In DCS of PU and PDMS, polymers were shown to be disrupted over a 250-450 °C temperature range, depending on hard and soft segment degradation⁹¹⁻⁹³. In our experiments, PU endotherms were around 260 °C (see Figure 4.7(a)-(b)). There was a fluctuation in heat of fusion at about 200 °C.

The calculated crystallinity of each composition is listed in Table 4.4. The data show that the crystallinity of PDMS was reduced negligibly by the incorporation of PU. The depressed crystallization in the PDMS/PU blends was attributed to the higher compatibility between PDMS and PU chains in another study⁹⁴. However in our work, crystallinity in the PDMS phase showed a decrease around 1-2% for Type I blends and around 1% for Type II blends. This results suggests that the PDMS polymer crystal structure is not slightly to not affected by PU phase.

The crystalline melting temperatures of the blends were not significantly different from those displayed by the pure PDMS sample. The crystalline fusion enthalpies of the blends decreased with PU content, as shown in Table 4.4. Because these peaks at around -50 °C (shown in Figure 4.7(a)-(b)) represent an overlap of second-segmental PDMS movement and of PU T_g , a complete evaluation of these samples was not possible. However, we were able to obtain more information in this temperature region from our DMA data: the polymer blends maintained their pristine individual polymer characteristics.

The DSC curves of the PDMS-PU blend are a simple superposition of the DSC curves of the respective pure polymers, indicating an absence of significant interactions between PU and PDMS. The PU was observed to exhibit two T_g temperatures, one originating from soft segments and the other from hard segments. A T_g of -20.1 °C for the PU elastomer in DSC was observed. The glass transition of PU at -20 °C could be clearly observed in DMA, as discussed earlier, but became unobservable as PDMS endothermic crystallization at -41 °C became dominant in both type of blends.

PDMS blends have been reported to phase-mix with soft segments of other polymers⁹⁵. However, we observed a phase separation for both types of blends and all compositions. The lower glass transition temperature of the blends, around 1 °C, resembled that of PDMS, indicating little to no mixing of the PU soft segments into the PDMS domain. Crystallization changes in the PDMS phase of the blends, provided in Table 4.4, confirm this result.

4.3.4 FTIR Analysis

FTIR band assignments for PU and PDMS are provided in Table 4.5. FTIR data plots for the Type I PDMS, Type II PDMS, PU, and blends are provided in Figure 4.8 and Figure 4.9.

The FTIR spectra of the ether-based PU are shown in Figure 4.8. Generally, the chemical composition of the polyurethane is based on the hard-segment (urethane-group) crystalline domain and the soft-segment (polyether or polyester) amorphous phase⁹⁶. FTIR spectra of PU display the following peaks: The hard segments of PU was at 1729 cm⁻¹ urethane (non-hydrogen-bonded) and 1701 cm⁻¹ urethane (hydrogen-bonded) The amide II and amide III bands for polyurethanes appeared at 1537 cm⁻¹ and 1230 cm⁻¹, respectively. The hydrogen-bonded urethane N-H stretch occurred at 3326 cm⁻¹. The bands at 2963 cm⁻¹, 2903 cm⁻¹, and 2875 cm⁻¹ were linked to symmetric and asymmetric –CH₂– and –CH₃ groups, while the bands at 1597 cm⁻¹ and 1413 cm⁻¹ were ascribed to the aromatic carbon-carbon double bonding⁹⁷.

The presence of the urethane structure can be verified by the FTIR peaks at 1530 cm⁻¹, which were due to NH bending; at 1703 cm⁻¹, due to the carbonyl stretching; and at 3320 cm⁻¹, due to the NH stretching from the urethane linkage. Additionally, polyether urethane was

identified by the band at 1082 cm^{-1} , which represents the ether (C–O–C) linkage⁹⁸, and by the peak at 1220 cm^{-1} .

Table 4.5 FTIR assignments of PU and PDMS polymers^{96–99}.

PU Assignments	PDMS Assignments
3326 ν (N–H) (H-bonded)	2960 ν (C–H) in CH ₃
2940 ν_a (C–H) in CH ₂	1260 δ (C–H) in Si-CH ₃
2855 ν_s (C–H) in CH ₂	1080 ν_a (Si–O–Si) in Si-O-Si
1729 ν (C=O) urethane non-bonded	1016 ν_s (Si–O–Si) in Si-O-Si
1701 ν (C=O) urethane H-bonded	790 ρ (C–H) in Si-CH ₃
1597 ν (C–C) aromatic ring	
1530 ν (C–N) + δ (N–H) amide II	
1414 ν (C–C) aromatic ring	
1313 ν (C–N) + δ (N–H)	
1220 ν (C–N) + δ (N–H) amide III	
1115 ν_a (C–O–C) aliphatic ether	
1082 ν (C–O–C) in hard segment (O=C–O–C) urethane linkage	

ν =stretching mode, ν_a =asymmetric stretching, ν_s =symmetric stretching, δ = in-plane

bending or scissoring, ρ =in-plane bending or rocking,

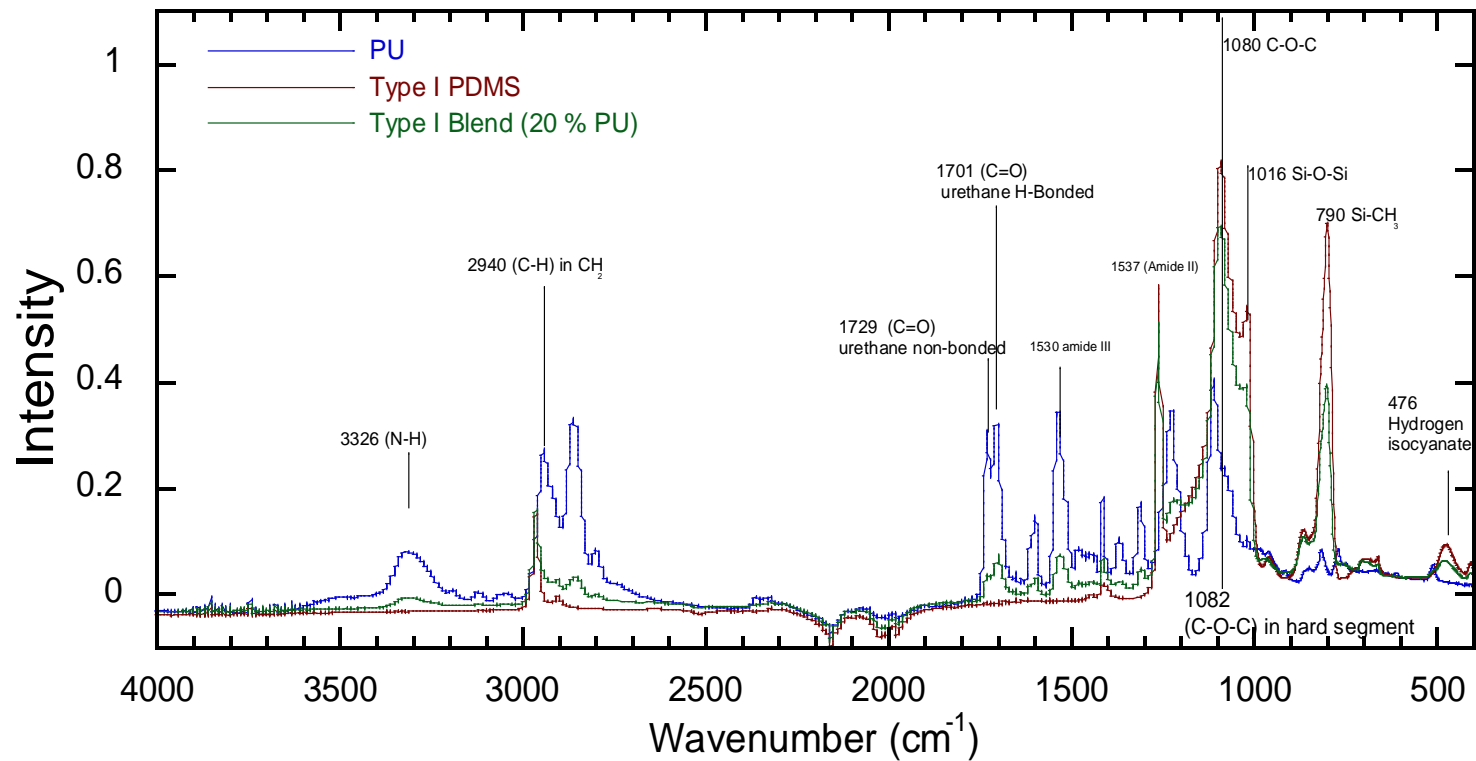


Figure 4.8 FTIR Spectrum for Type I PDMS, PU, and its blends: red (—) represents pure PDMS; blue (—) represents pure PU; green (—) represents 20 PU wt% concentration Type II blend.

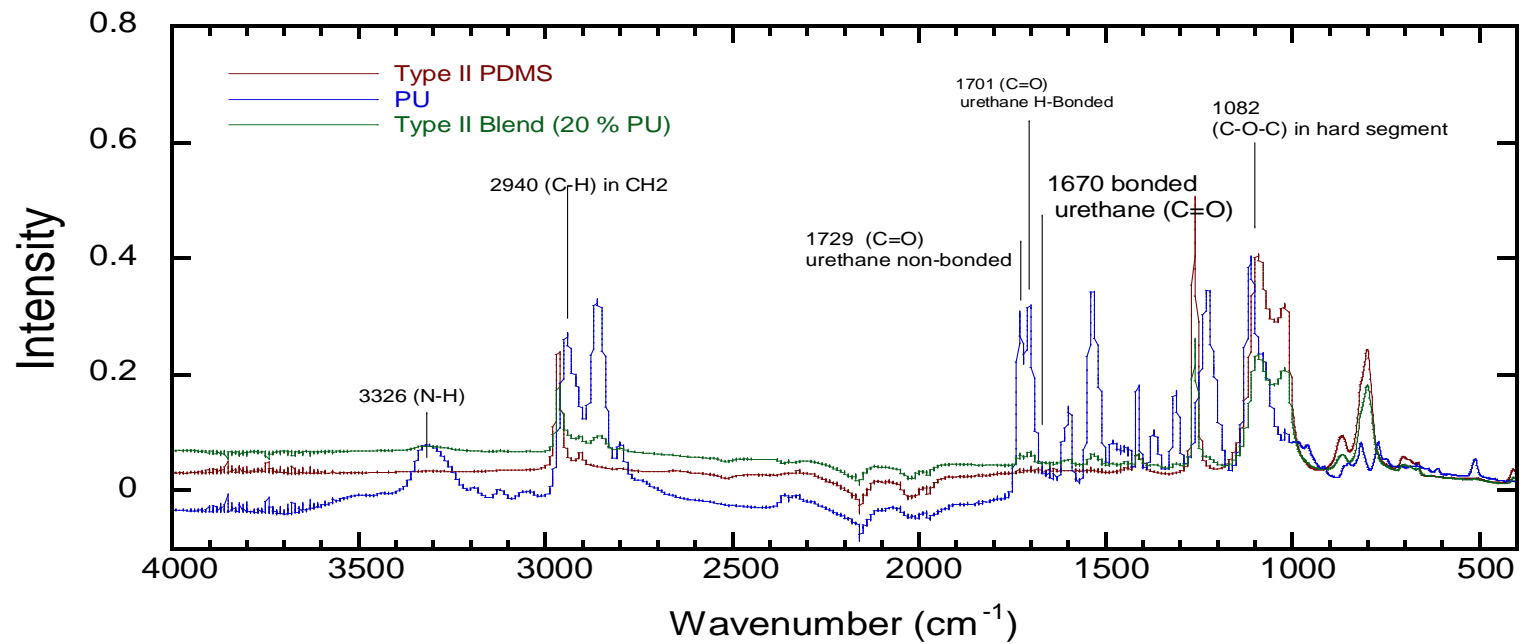


Figure 4.9 FTIR Spectrum for Type II PDMS, PU, and its blends: red (—) represents pure PDMS; blue (—) represents pure PU; green (—) represents 20 PU wt% concentration Type II blend.

Two types of PDMS are depicted separately in Figure 4.8 and Figure 4.9 for Type I and Type II blends, respectively. In Figure 4.8, the intensive bands at 1016 cm^{-1} and 1080 cm^{-1} correspond to the Si–O–Si and C–O–C groups. The absorption band at around 790 cm^{-1} is attributable to the Si–CH₃ linkage. The CH₃ bending and rocking peaks are apparent at 1260 and 801 cm^{-1} , respectively.

Type I elastomers exhibited peaks near 960 cm^{-1} and 470 cm^{-1} these peaks were attributed in literature to PDMS-containing vinyl end groups present in the elastomer after the hydrosilylation reaction¹⁰⁰. These peaks also confirm the crosslinking of Type I PDMS and its blends.

FTIR of Type II PDMS elastomers, plotted in Figure 4.9, did not exhibit a peak pattern differing substantially from that of Type I elastomers in Figure 4.8, confirming that the final chemical structures of Type II and Type I elastomers are similar, with the exception of the vinyl double bonds observed in Type I elastomers. In Type I blends, carbonyls that were not involved in hydrogen bonding are apparent near 1732 cm^{-1} , and those associated with poorly ordered hydrogen bonding can be observed at 1720 cm^{-1} . In Type I elastomer blend systems, we also observed non-hydrogen bonded carbonyls at 1729 cm^{-1} and poorly hydrogen-bonded carbonyl groups near 1701 cm^{-1} . All peaks associated with hydrogen bonding carbonyl groups were found to be negligible in Type II elastomer blends.

Silanol groups, generally recognized as hydration sites, are expected to give rise to strong absorption bands in infrared spectra, mainly in the range of $3800\text{--}3200\text{ cm}^{-1}$. Hydrogen bonding shifts the OH wave number to a lower value and broadens the absorption band¹⁰¹. As

shown in Figure 4.9, Type II blends exhibited flattened PU hydration sites due to the absence of hydrogen bonding between PU and Type II PDMS networks.

The FTIR data for Type II PDMS and its blends shown in Figure 4.9 did not display a peak at 2270 cm^{-1} , which represents -NCO groups of crosslinker, which could be consumed in network formation.

In general, the FTIR spectrum of blends in Figure 4.8 and Figure 4.9 was similar to those of constituting PDMS. Confirming the chemical interaction of PU and PDMS species using FTIR spectroscopy was not possible.

4.3.5 Morphological Characterization

We used SEM to discover the morphological properties of the elastomer blends. The SEM images are provided in Figure 4.10 through Figure 4.13. The blend morphologies of the Type I and Type II blend samples show the uniform distribution of the spherical PU phases throughout the PDMS matrix, as also shown in Figure 4.10(a). In general, the domains of immiscible polymer blends are round in shape, which serves to minimize interfacial area.

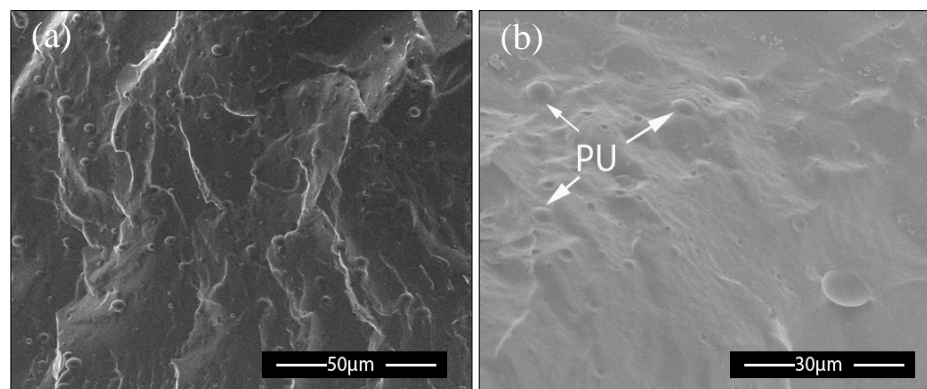


Figure 4.10 Morphological views of PU/PDMS blend elastomers with (a) representative 10% PU filler concentration and (b) spherical PU distributed throughout the PDMS matrix. (image taken from 10 wt% PU / Type I PDMS blends.)

As we examined the blend images, we observed that the density of spherical PU fillers distributed throughout each sample increased as PU concentration increased. We compared 10%, 20%, and 40 wt% PU/PDMS blends to understand the PU filler size in PDMS (see Figure 4.11).

We also noticed an increase in average filler size with the increase in filler weight concentration(Figure 4.11) The distribution of the fillers was also analyzed for a large number of samples through image analysis to fully explore the relationship between PU concentration and PU filler size; in short, filler size increased with the increase in filler concentration. In terms of morphology, fillers were spherical for low-concentration (10-20%) blends but became ovoid as filler concentration increased to 40%. This change in shape may be owing to result of solvent removal process. These results are reported in Figure 4.11(a)-(d). In Figure 4.11(a), we observe spherical PU fillers, each measuring less than 1 μm in diameter for 2 wt% concentration. Figure 4.11(b) reveals spherical PU fillers from 10 wt%

concentration blends with an average diameter of 2.5 μm . Figure 4.11 (c) shows the 20 wt% concentration fillers with an average diameter of 4.5 μm , and Figure 4.11(d) shows the blend having 40 wt% PU concentration with an average diameter of 8 μm fillers.

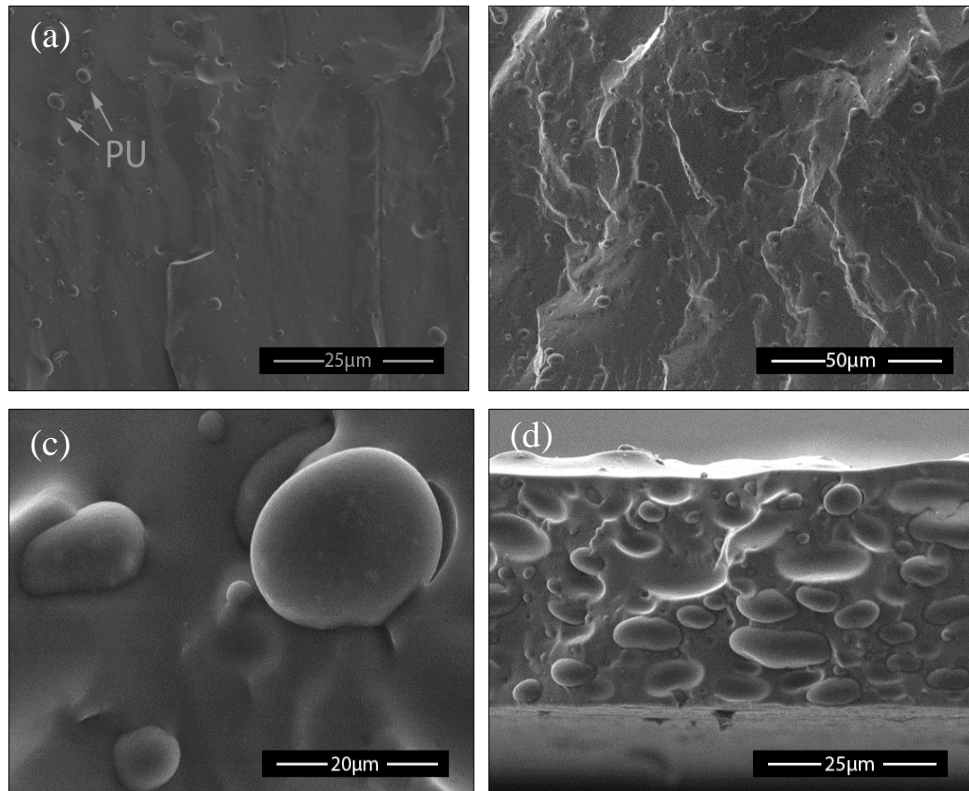


Figure 4.11 Representative morphological electron microscope images of PU/PDMS blend elastomers with (a) a film cross-section of 2% PU filler concentration; (b) spherical 10% PU fillers distributed throughout the PDMS matrix; (c) spherical 20% PU fillers distributed throughout the PDMS matrix; (d) spherical and ovoid 40% PU fillers distributed throughout the PDMS matrix.

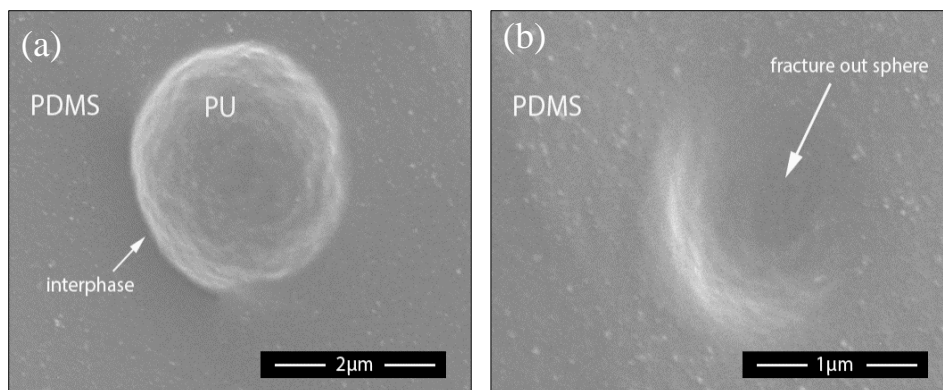


Figure 4.12 Morphological cross-sections of blend Type I elastomers. Images (a) and (b) show the dispersion of spherical PU elastomer fillers throughout the PDMS matrix; this points to the separation of spherical PU fillers from the PDMS matrix. These images were taken after a fracture of blends occurred in liquid nitrogen. The interphases between the species are pointed out in the images above.

The cross-section in Figure 4.12(a) shows the interfaces of the PU and PDMS in a blend. This representative image of a spherically shaped single filler was taken from 10 wt% blend Type I shows the PDMS matrix separation from PU fillers during the fracture tearing of samples. The blend samples were fractured after being soaked in liquid nitrogen; Figure 4.12(b) shows the PU filler fractured out from the PDMS matrix.

Increasing weight concentration of PU in the Type I and Type II blends was found to correspond with denser distribution of the spherical PU fillers. Average filler size also increased with increased filler concentration. The increase in PU weight concentration affected the elastomers' surface morphology, as shown in Figure 4.11(a)-(d). The cross

sections of the blends were also analyzed using ImageJ software to determine the average filler size. These data are plotted in Figure 4.14.

The Type II blends were also characterized using SEM microscopy. In contrast to what the Type I blends showed in the interphase images, the Type II blends, displayed in Figure 4.13(a), exhibited the matrix diffused with the spherical shapes of the PU elastomer phase. Figure 4.13(b) shows the PU and PDMS interface in Type II blends.

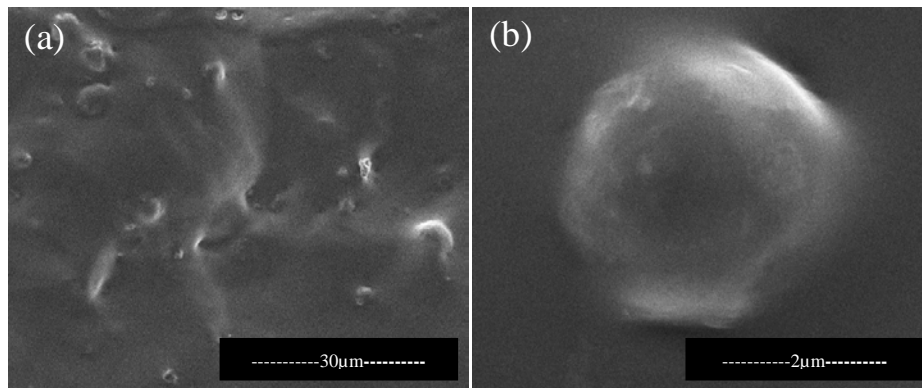


Figure 4.13 Morphology of blend elastomers with 2 wt% PU concentration: (a) cross-sectional view of Type II elastomer blends and (b) spherical PU filler edges diffused to PDMS.

According to the SEM results, the PU phases were relatively uniformly dispersed throughout the PDMS matrix at low weight concentrations. However, at a high weight PU concentration, the filler dimensions increased and the uniformity of PU size decreased. A plot of these effects is provided in Figure 4.14⁹. Klemperer et al.⁹ observed similar results related to the phase behavior of blends with respect to PU concentration.

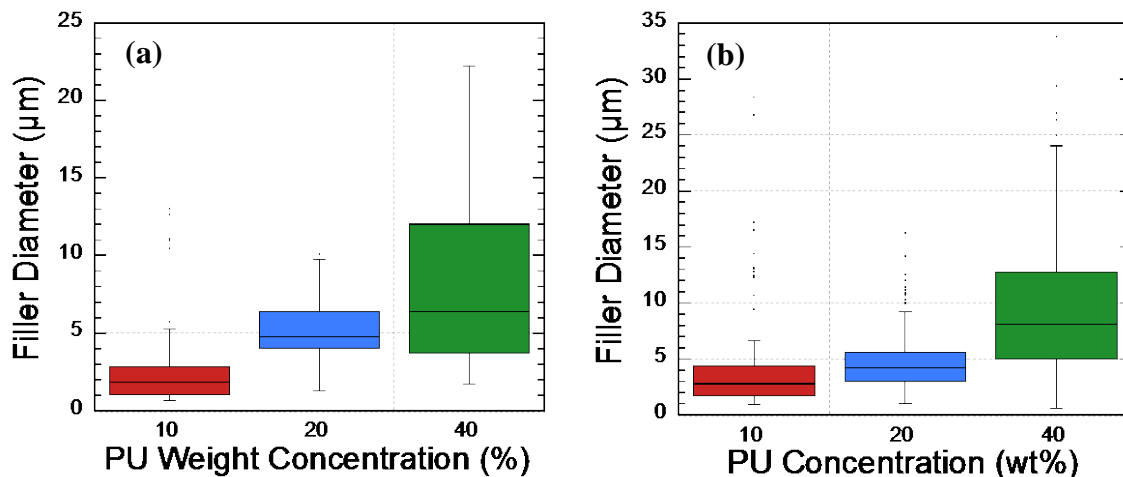


Figure 4.14 Analysis of morphological cross-sectional images of blends for both Type I and Type II elastomers. SEM images were analyzed for filler dimensions: (a) Type I distribution of size of filler diameter blends and (b) Type II distribution of approximate filler size diameter blends.

4.3.6 Dielectric Characterization

The dielectric constant (effective permittivity) of Type I blends are given in Figure 4.15. In this figure, all blends of PU and PDMS showed a significant increase in dielectric constant with the increasing wt % of PU in blends. This improvement was greater in blends with low PU weight concentrations than in elastomers with high PU weight concentrations. Specifically, the increase in dielectric constant for the blends with a PU load of 5 wt% was higher than for the blends with weights of 20% and 40%. This difference can be explained by superior dispersion of PU throughout the PDMS at lower PU weight concentrations.

In the plots of the PU filler size data provided in Figure 4.14, lower weight concentrations showed smaller filler sizes. The relationship between filler size and the increase in dielectric constant can be a proof of interfacial polarization between the PU and PDMS polymers.

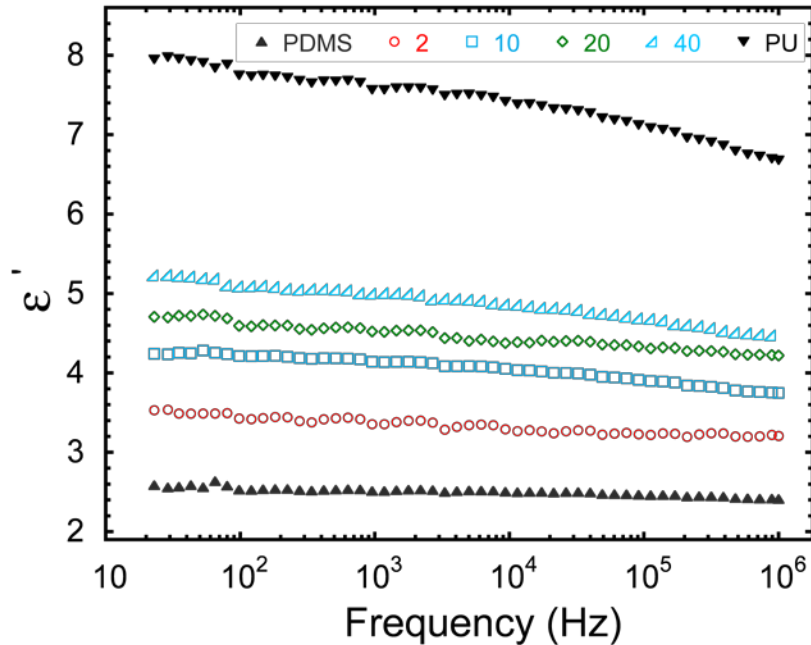


Figure 4.15 The dielectric constant (effective permittivity, ϵ') as a function of frequency for Type I blends. (▼)PU, (△) 40 wt% PU, (◇) 20 wt% PU, (□) 10 wt% PU, (○) 2 wt% PU, (▲)PDMS.

The dielectric constants of the PU elastomer and blend composites showed a slight decrease from low frequency to high frequency. This decrease can be attributed to the increase in dielectric loss of blends in high frequencies (plotted in Figure 4.16). This comparison was found to be even more consistent for 40% PU blends and can be attributed to the higher dielectric loss in these samples.

The elastomer blends containing PU and the pure PU displayed higher dielectric dissipation than the pure PDMS at high frequencies. The same trend was observed for dielectric constant. The dielectric dissipation for all blends decreased as frequency increased.

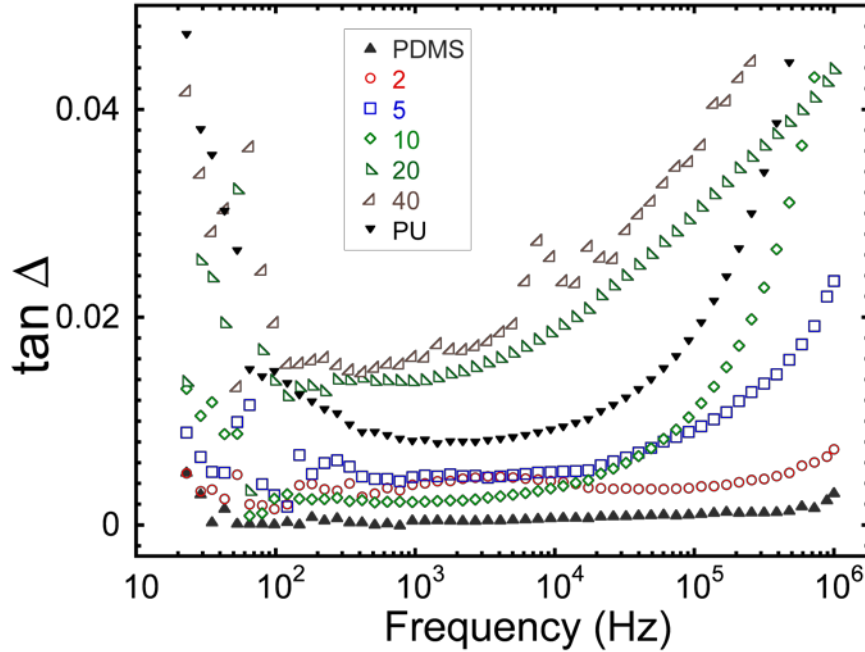


Figure 4.16 Dielectric loss, ($\tan \Delta$) as a function of frequency for the Type II blends. (\blacktriangledown)PU, (\triangle) 40 wt% PU, (\diamond) 20 wt% PU, (\square) 10 wt% PU, (\circ) 2 wt% PU/PDMS blends, (\blacktriangle)PDMS.

In literature⁶⁰, the PU-PDMS composites and the pure PU elastomer showed higher dielectric loss values than the PDMS elastomer. The dielectric loss of PU elastomers has been reported to increase due to α -relaxation and ionic conductivity¹⁰². The dielectric $\tan(\Delta)$ versus frequency behavior versus frequency that we plotted in Figure 4.16 for PU is comparable to that described in the literature¹⁰². For high concentrations blends exhibited higher dielectric losses than the pure PDMS elastomer. In fact, all of the polymer blends exhibited low

dielectric loss, a highly desirable quality for dielectric composites. The $\tan(\Delta)$ values reported in Figure 4.16 were less than 0.06 for all elastomer compositions at frequencies 20 to 10^6 Hz. Their low losses and high dielectric constants relative to pure PDMS make these materials good candidates for use as actuators in dielectric insulation applications.

4.3.7 Evaluation of Dielectric Properties

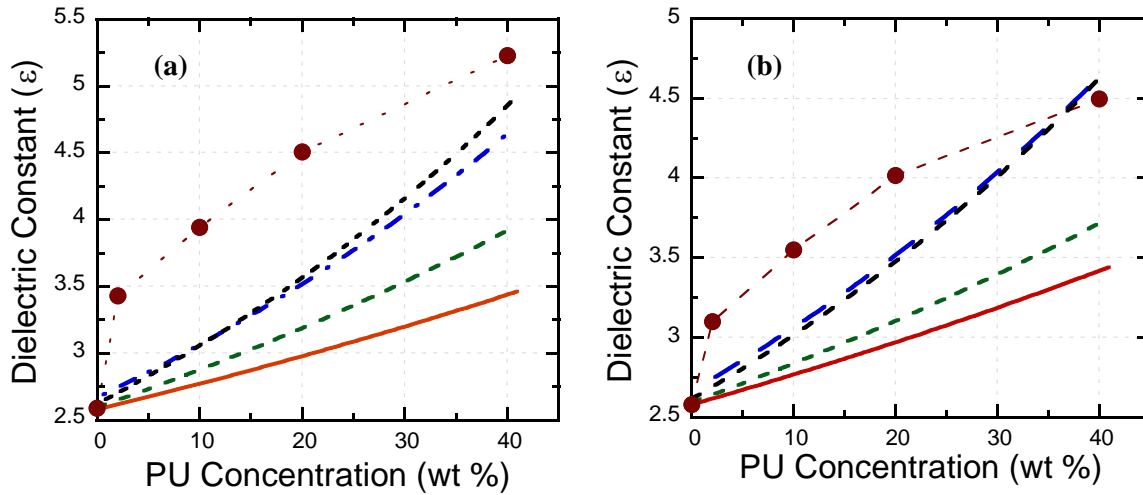


Figure 4.17 Effective permittivity as a function of weight fraction of polyurethane (a) at a low-frequency measurement (100 Hz) and (b) at a high-frequency measurement (10^6 Hz). The dashed lines represent the theoretically predicted results based on weight concentration. Dashed lines represent (—) series, (---) logarithmic, (-·-) parallel, and (--) Maxwell Garnet theoretical prediction of mixing for dielectric constant, in order from bottom to top. Data connected with dots serve guide to eye.

Figure 4.17 is a plot of dielectric constant versus PU wt% at frequencies of (a) 100 Hz and (b) 10^6 Hz. We also superimposed the theoretical rule of mixture curves over the experimental measurement points of the blends to explore the underlying mechanisms of the

blends' dielectric constant. Greater improvement in blend composite dielectric behavior was observed for low-frequency blend compositions than for high-frequency compositions. The values of the low-frequency dielectric constant for both high and low frequencies dielectric constants did not follow any of the theoretical predictions while values were even higher than the Maxwell Garnet model predictions.

Because improvement of effective permittivity was prominent in low-frequency regions, we can infer that the interphase properties of these blends had a positive impact on dielectric properties.

4.4 Conclusions

The mechanical and elastomeric properties of silicone networks are improved through the synthesis of semi-interpenetrating networks of poly (dimethylsiloxane)/polyurethane. The miscibility of two polymers was studied with the goal of improving the mechanical and dielectric properties of their blends. Two types of PDMS elastomers with varying chemical structures and crosslinking mechanisms were investigated for their dynamic mechanical, thermal, dielectric, and chemical properties. Type I PDMS blends had decreased mechanical properties as compared to pure Type I PDMS, while Type II blends displayed increased mechanical properties as compared to pure Type II PDMS. The effects of Type II formulation on a blend's electromechanical properties will be discussed in Chapter 5.

The homopolymers of PDMS and PU were transparent, whereas all of the blended IPNs of the PDMS-PU systems were opaque, indicating phase separation. The miscibility calculations and the results of the dynamic mechanical analysis confirmed the

incompatibility and immiscibility of these two polymers. The blended semi-IPNs of the PDMS-PU systems formed phase-separated polymer pairs because they displayed two T_g s similar to the glass transition temperatures of both homopolymers. PDMS-PU semi-IPN blends showed an increase of up to 5.2 at low-frequency measurements and 4.5 at high-frequency measurements. These blends therefore have an advantage over pure PDMS elastomers in terms of dielectric constant.

The promise of blending approach lies in the fact that the increase in dielectric constant did not significantly increase the dielectric loss and stiffness of the blend elastomers. The high shear mixing were the keys to creating a blend film with a higher dielectric constant and low loss. Although, the dielectric loss of the blends increased; satisfactory results were achieved to evaluating them as dielectric elastomer actuator materials. These results will be presented in Chapter 5.

4.5 References

1. Wong, F. *et al.* Changing molecular band offsets in polymer blends of (P3HT/P(VDF-TrFE)) poly(3-hexylthiophene) and poly(vinylidene fluoride with trifluoroethylene) due to ferroelectric poling. *RSC Adv.* **4**, 3020–3027 (2013).
2. Zhu, S. *et al.* Confinement-induced miscibility in polymer blends. *Nature* **400**, 49–51 (1999).
3. Jacobs, H. O. & Whitesides, G. M. Submicrometer patterning of charge in thin-film electrets. *Science* **291**, 1763–1766 (2001).
4. Dang, Z.-M., Yuan, J.-K., Yao, S.-H. & Liao, R.-J. Flexible nanodielectric materials with high permittivity for power energy storage. *Adv. Mater.* **25**, 6334–6365 (2013).

5. Ding, Y., Garland, S., Howland, M., Revzin, A. & Pan, T. Universal nanopatternable interfacial bonding. *Adv. Mater.* **23**, 5551–5556 (2011).
6. Li, G. *et al.* High-efficiency solution processable polymer photovoltaic cells by self-organization of polymer blends. *Nat. Mater.* **4**, 864–868 (2005).
7. Hamilton, R. *et al.* High-performance polymer-small molecule blend organic transistors. *Adv. Mater.* **21**, 1166–1171 (2009).
8. Wolfer, P. *et al.* Solution structure: defining polymer film morphology and optoelectronic device performance. *J. Mater. Chem. C* **2**, 71–77 (2013).
9. Klemperer, D. *Advances in Interpenetrating Polymer Networks*. (CRC Press, 1994).
10. Sperling, L. H. & Mishra, V. The current status of interpenetrating polymer networks. *Polym. Adv. Technol.* **7**, 197–208 (1996).
11. Siegfried, D. L., Thomas, D. A. & Sperling, L. H. A reexamination of polystyrene/polystyrene homo interpenetrating polymer networks: aspects of relative network continuity and internetwork coupling. *Macromolecules* **12**, 586–589 (1979).
12. Lipatov, Y. S. & Alekseeva, T. T. in *Phase-Separated Interpenetr. Polym. Netw.* 1–227 (Springer Berlin Heidelberg, 2007).
13. Fichet, O., Vidal, F., Darras, V., Boileau, S. & Teyssié, D. in *Silicon Based Polym.* (eds. Ganachaud, D. F., Boileau, D. S. & Boury, P. B.) 19–28 (Springer Netherlands, 2008).
14. Lee, D. S. & Kim, S. C. Polyurethane interpenetrating polymer networks (IPN's) synthesized under high pressure. 3. Morphology and Tg behavior of polyurethane-polystyrene semi-IPN's and linear blends. *Macromolecules* **17**, 2222–2227 (1984).

15. Sánchez, M. S. *et al.* Forced compatibility in poly(methyl acrylate)/poly(methyl methacrylate) sequential interpenetrating polymer networks. *Polymer* **42**, 10071–10075 (2001).
16. Xiao, H., Ping, Z. H., Xie, J. W. & Yu, T. Y. The synthesis and morphology of semi-interpenetrating polymer networks based on polyurethane–polydimethylsiloxane system. *J. Polym. Sci. Part Polym. Chem.* **28**, 585–594 (1990).
17. Rozenberg, B. A. & Sigalov, G. M. *Heterophase network polymers: synthesis, characterization, and properties*. (CRC Press, 2004).
18. Du Prez, F. E., Tan, P. & Goethals, E. J. Poly(ethylene oxide)/poly(methyl methacrylate) (semi-)interpenetrating polymer networks: Synthesis and phase diagrams. *Polym. Adv. Technol.* **7**, 257–264 (1996).
19. Atkins, P. W. *The laws of thermodynamics*. (Oxford University Press, 2010).
20. Utracki L. A. in *Interpenetr. Polym. Netw.* **239**, 77–123 (American Chemical Society, 1994).
21. Huggins, M. L. Some properties of solutions of long-chain compounds. *J. Phys. Chem.* **46**, 151–158 (1942).
22. Huggins, M. L. Theory of solutions of high polymers. *J. Am. Chem. Soc.* **64**, 1712–1719 (1942).
23. Huggins, M. L. Thermodynamic properties of solutions of long-chain compounds. *Ann. N. Y. Acad. Sci.* **43**, 1–32 (1942).
24. Flory, P. J. *Principles of polymer chemistry*. (Cornell University Press, 1953).

25. Scott, R. L. & Magat, M. The thermodynamics of high-polymer solutions: i. the free energy of mixing of solvents and polymers of heterogeneous distribution. *J. Chem. Phys.* **13**, 172–177 (1945).
26. Bates, F. S. Polymer-polymer phase behavior. *Science* **251**, 898–905 (1991).
27. Eichinger, B. E. & Flory, P. J. Thermodynamics of polymer solutions. Part 4.— Polyisobutylene and n-pentane. *Trans. Faraday Soc.* **64**, 2066–2072 (1968).
28. Flory, P. J. Statistical thermodynamics of liquid mixtures. *J. Am. Chem. Soc.* **87**, 1833–1838 (1965).
29. Flory, P. J., Orwoll, R. A. & Vrij, A. Statistical thermodynamics of chain molecule liquids. i. an equation of state for normal paraffin hydrocarbons. *J. Am. Chem. Soc.* **86**, 3507–3514 (1964).
30. Masnada, E. M., Julien, G. & Long, D. R. Miscibility maps for polymer blends: Effects of temperature, pressure, and molecular weight. *Journal of Polymer Science Part B: Polymer Physics* **52**, 419–443 (2013).
31. Alekseeva, T. T. *Phase-Separated Interpenetrating Polymer Networks*. (Springer, 2007).
32. Majumdar, P. & Webster, D. C. Surface microtopography in siloxane–polyurethane thermosets: the influence of siloxane and extent of reaction. *Polymer* **48**, 7499–7509 (2007).
33. Kulkarni, A. S. & Beaucage, G. Reaction induced phase-separation controlled by molecular topology. *Polymer* **46**, 4454–4464 (2005).
34. Briber, R. M. & Bauer, B. J. Effect of crosslinks on the phase separation behavior of a miscible polymer blend. *Macromolecules* **21**, 3296–3303 (1988).

35. Nevissas, V., Widmaier, J. M. & Meyer, G. C. Effect of crosslink density and internetwork grafting on the transparency of polyurethane/polystyrene interpenetrating polymer networks. *J. Appl. Polym. Sci.* **36**, 1467–1473 (1988).
36. Faghihi, F., Morshedian, J., Razavi-Nouri, M. & Ehsani, M. Dynamic rheological and mechanical behaviour of poly(dimethylsiloxane)/low density polyethylene immiscible blends: interfacial modification via reactive blending. *Iran. Polym. J.* **17**, 755–765 (2008).
37. Rezaei, S. M. & Mohd Ishak, Z. A. The biocompatibility and hydrophilicity evaluation of collagen grafted poly(dimethylsiloxane) and poly (2-hydroxyethylmethacrylate) blends. *Polym. Test.* **30**, 69–75 (2011).
38. Zhou, P. *et al.* Interpenetrating polymer networks of poly (dimethyl siloxane–urethane) and poly (methyl methacrylate). *J. Polym. Sci. Part Polym. Chem.* **31**, 2481–2491 (1993).
39. Derouiche, A., Bettachy, A., Benhamou, M. & Daoud, M. Kinetics of microphase separation in crosslinked polymer blends. *Macromolecules* **25**, 7188–7191 (1992).
40. Cho, S. H., Andersson, H. M., White, S. R., Sottos, N. R. & Braun, P. V. Polydimethylsiloxane-based self-healing materials. *Adv. Mater.* **18**, 997–1000 (2006).
41. Inoue, T. Reaction-induced phase decomposition in polymer blends. *Prog. Polym. Sci.* **20**, 119–153 (1995).
42. Olabis, O. *Polymer-polymer miscibility*. (Elsevier, 2012).
43. Lee, M. H., Fleischer, C. A., Morales, A. R., Koberstein, J. T. & Koningsveld, R. The effect of end groups on thermodynamics of immiscible polymer blends. 2. Cloud point curves. *Polymer* **42**, 9163–9172 (2001).

44. Yılıgör, E. & Yılıgör, İ. Hydrogen bonding: a critical parameter in designing silicone copolymers. *Polymer* **42**, 7953–7959 (2001).
45. Fang, L. *et al.* Precise pattern replication of polymer blends into nonuniform geometries via reducing interfacial tension between two polymers. *Langmuir* **28**, 10238–10245 (2012).
46. Hu, W., Koberstein, J. T., Lingelser, J. P. & Gallot, Y. Interfacial tension reduction in polystyrene/poly(dimethylsiloxane) blends by the addition of poly(styrene-*b*-dimethylsiloxane). *Macromolecules* **28**, 5209–5214 (1995).
47. Wignall, G. D., Alamo, R. G., Londono, J. D., Mandelkern, L. & Stehling, F. C. Small-angle neutron scattering investigations of liquid–liquid phase separation in heterogeneous linear low-density polyethylene. *Macromolecules* **29**, 5332–5335 (1996).
48. Aranguren, M. I. Crystallization of polydimethylsiloxane: effect of silica filler and curing. *Polymer* **39**, 4897–4903 (1998).
49. Hassanajili, S., Khademi, M. & Keshavarz, P. Influence of various types of silica nanoparticles on permeation properties of polyurethane/silica mixed matrix membranes. *J. Membr. Sci.* **453**, 369–383 (2014).
50. Dewimille, L., Bresson, B. & Bokobza, L. Synthesis, structure and morphology of poly(dimethylsiloxane) networks filled with in situ generated silica particles. *Polymer* **46**, 4135–4143 (2005).
51. Joki-Korpela, F. & Pakkanen, T. T. Incorporation of polydimethylsiloxane into polyurethanes and characterization of copolymers. *Eur. Polym. J.* **47**, 1694–1708 (2011).

52. Bai, H.-C., Tao, L., Pang, Y.-J., Zhou, Y.-J. & Chen, J. Synthesis and characterization of hydroxypropyl terminated polydimethylsiloxane-polyurethane copolymers. *J. Appl. Polym. Sci.* **129**, 2152–2160 (2013).
53. Hamurcu, E. E. & Baysal, B. M. Interpenetrating polymer networks of poly(dimethylsiloxane) with polystyrene, polybutadiene and poly(glycerylpropoxytriacylate). *Macromol. Chem. Phys.* **196**, 1261–1276 (1995).
54. Kim, P.-S., Lee, S.-W., Park, J.-W., Park, C.-H. & Kim, H. J. Kinetic and characterization of UV-curable silicone urethane methacrylate in semi-IPN-structured acrylic PSAs. *J. Adhes. Sci. Technol.* **27**, 1866–1872 (2013).
55. Lucas, P. & Robin, J.-J. in *Funct. Mater. Biomater.* 111–147 (Springer Berlin Heidelberg, 2007). at <http://link.springer.com/chapter/10.1007/12_2007_115>
56. Vlad, S., Vlad, A. & Oprea, S. Interpenetrating polymer networks based on polyurethane and polysiloxane. *Eur. Polym. J.* **38**, 829–835 (2002).
57. Turner, J. S. & Cheng, Y.-L. Morphology of PDMS–PMAA IPN membranes. *Macromolecules* **36**, 1962–1966 (2003).
58. Boileau Sylvie, Bouteiller Laurent, Khalifa Riadh Ben, Liang Yi & Teyssié Dominique. in *Silicones Silicone-Modif. Mater.* **729**, 383–394 (American Chemical Society, 2000).
59. Yang, S. *et al.* Thermally resistant UV-curable epoxy–siloxane hybrid materials for light emitting diode (LED) encapsulation. *J. Mater. Chem.* **22**, 8874–8880 (2012).
60. Gallone, G., Galantini, F. & Carpi, F. Perspectives for new dielectric elastomers with improved electromechanical actuation performance: composites versus blends. *Polym. Int.* **59**, 400–406 (2010).

61. Chwang, C.-P., Liu, C.-D., Huang, S.-W., Chao, D.-Y. & Lee, S.-N. Synthesis and characterization of high dielectric constant polyaniline/polyurethane blends. *Synth. Met.* **142**, 275–281 (2004).
62. Kussmaul, B., Risse, S., Wegener, M., Kofod, G. & Krüger, H. Novel DEA materials by chemical grafting of silicone networks on molecular level. in *Proc SPIE Vol 8340*, 83400Y–1 (2012).
63. Skova, A. L., Bejenariua, A., Bøgelundb, J., Benslimanec, M. & Egedea, A. D. Influence of micro-and nanofillers on electro-mechanical performance of silicone EAPs. in *Proc SPIE Vol 8340*, 83400M–1 (2012).
64. Xu, J., Bhattacharya, S., Pramanik, P. & Wong, C. P. High dielectric constant polymer-ceramic (Epoxy varnish-barium titanate) nanocomposites at moderate filler loadings for embedded capacitors. *J. Electron. Mater.* **35**, 2009–2015 (2006).
65. Meng-Meng, L. *et al.* Dielectric properties of electrospun titanium compound/polymer composite nanofibres. *Chin. Phys. B* **19**, 028102 (2010).
66. Li Li *et al.* Novel polymer-ceramic nanocomposite based on new concepts for embedded capacitor application (I). *Compon. Packag. Technol. IEEE Trans. On* **28**, 754–759 (2005).
67. Carpi, F., Gallone, G., Galantini, F. & De Rossi, D. Silicone-poly(hexylthiophene) blends as elastomers with enhanced electromechanical transduction properties. *Adv. Funct. Mater.* **18**, 235–241 (2008).
68. Carpi, F., Gallone, G., Galantini, F. & De Rossi, D. Enhancement of the electromechanical transduction properties of a silicone elastomer by blending with a conjugated polymer. in *SPIE Proceedings* (ed. Bar-Cohen, Y.) **6927**, 692707–692707–11 (2008).

69. Carpi, F. & Rossi, D. D. Improvement of electromechanical actuating performances of a silicone dielectric elastomer by dispersion of titanium dioxide powder. *IEEE Trans. Dielectr. Electr. Insul.* **12**, 835–843 (2005).
70. Ouyang, G. M., Wang, K. Y. & Chen, X. Y. Enhanced electro-mechanical performance of TiO₂ nano-particle modified polydimethylsiloxane (PDMS) as electroactive polymers. in *16th Int.Solid-State Sens. Actuators Microsyst. Conf. 2011* 614–617 (2011).
71. Anquetil, P. A. *et al.* Thiophene-based conducting polymer molecular actuators. in *Proc SPIE* **4695**, 424–434 (2002).
72. Muzafarov, A. *Silicon polymers*. (Springer, 2010).
73. Tsige, M. *et al.* Interactions and structure of poly(dimethylsiloxane) at silicon dioxide surfaces: Electronic structure and molecular dynamics studies. *J. Chem. Phys.* **118**, 5132 (2003).
74. Karabela, M. M. & Sideridou, I. D. Effect of the structure of silane coupling agent on sorption characteristics of solvents by dental resin-nanocomposites. *Dent. Mater.* **24**, 1631–1639 (2008).
75. Seeni Meera, K. M., Murali Sankar, R., Jaisankar, S. N. & Mandal, A. B. Physicochemical studies on polyurethane/siloxane cross-linked films for hydrophobic surfaces by the sol–gel process. *J. Phys. Chem. B* **117**, 2682–2694 (2013).
76. Park, S., Kim, J. S., Chang, Y., Lee, S. C. & Kim, C. A covalently interconnected phosphazene–silicate network: synthesis and surface functionalization. *J. Inorg. Organomet. Polym.* **8**, 205–214 (1998).

77. Tingaut, P., Weigenand, O., Militz, H., Jéso, B. D. & Sèbe, G. Functionalisation of wood by reaction with 3-isocyanatopropyltriethoxysilane: Grafting and hydrolysis of the triethoxysilane end groups. *Holzforschung* **59**, 397–404 (2005).
78. Park, J. H., Park, K. D. & Bae, Y. H. PDMS-based polyurethanes with MPEG grafts: synthesis, characterization and platelet adhesion study. *Biomaterials* **20**, 943–953 (1999).
79. Van Krevelen, D. W. & Te Nijenhuis, K. in *Properties of Polymers (Fourth Edition)* (eds. by, D. W. V. K. & Nijenhuis, K. T.) 319–354 (Elsevier, 2009).
80. Fedors, R. F. A method for estimating both the solubility parameters and molar volumes of liquids. *Polym. Eng. Sci.* **14**, 147–154 (1974).
81. Mehta, A., Gaur, U. & Wunderlich, B. Equilibrium melting parameters of poly(ethylene terephthalate). *J. Polym. Sci. Polym. Phys. Ed.* **16**, 289–296 (1978).
82. Sekkar, V., Bhagawan, S. S., Prabhakaran, N., Rama Rao, M. & Ninan, K. N. Polyurethanes based on hydroxyl terminated polybutadiene: modelling of network parameters and correlation with mechanical properties. *Polymer* **41**, 6773–6786 (2000).
83. Robertson, C. G., Lin, C. J., Rackaitis, M. & Roland, C. M. Influence of particle size and polymer–filler coupling on viscoelastic glass transition of particle-reinforced polymers. *Macromolecules* **41**, 2727–2731 (2008).
84. Berriot, J., Montes, H., Lequeux, F., Long, D. & Sotta, P. Evidence for the shift of the glass transition near the particles in silica-filled elastomers. *Macromolecules* **35**, 9756–9762 (2002).

85. Tsagaropoulos, G. & Eisenberg, A. Direct observation of two glass transitions in silica-filled polymers. Implications to the morphology of random ionomers. *Macromolecules* **28**, 396–398 (1995).
86. Tsagaropoulos, G. & Eisenberg, A. Dynamic mechanical study of the factors affecting the two glass transition behavior of filled polymers. similarities and differences with random ionomers. *Macromolecules* **28**, 6067–6077 (1995).
87. Robertson, C. G. & Rackaitis, M. Further consideration of viscoelastic two glass transition behavior of nanoparticle-filled polymers. *Macromolecules* **44**, 1177–1181 (2011).
88. Clarson, S. J., Dodgson, K. & Semlyen, J. A. Studies of cyclic and linear poly(dimethylsiloxanes): 19. Glass transition temperatures and crystallization behaviour. *Polymer* **26**, 930–934 (1985).
89. Zhang, D., Liu, Y., Shi, Y. & Huang, G. Effect of polyhedral oligomeric silsesquioxane (POSS) on crystallization behaviors of POSS/polydimethylsiloxane rubber nanocomposites. *RSC Adv.* **4**, 6275 (2014).
90. Dollase, T., Spiess, H. W., Gottlieb, M. & Yerushalmi-Rozen, R. Crystallization of PDMS: The effect of physical and chemical crosslinks. *EPL Europhys. Lett.* **60**, 390 (2002).
91. Grassie, N. & Macfarlane, I. G. The thermal degradation of polysiloxanes—I. Poly(dimethylsiloxane). *Eur. Polym. J.* **14**, 875–884 (1978).
92. Grassie, N. & Zulfiqar, M. Thermal degradation of the polyurethane from 1,4-butanediol and methylene bis(4-phenyl isocyanate). *J. Polym. Sci. Polym. Chem. Ed.* **16**, 1563–1574 (1978).

93. Hwang, H.-D. & Kim, H.-J. Enhanced thermal and surface properties of waterborne UV-curable polycarbonate-based polyurethane (meth)acrylate dispersion by incorporation of polydimethylsiloxane. *React. Funct. Polym.* **71**, 655–665 (2011).
94. Lue, S. J., Ou, J. S., Kuo, C. H., Chen, H. Y. & Yang, T.-H. Pervaporative separation of azeotropic methanol/toluene mixtures in polyurethane–poly(dimethylsiloxane) (PU–PDMS) blend membranes: Correlation with sorption and diffusion behaviors in a binary solution system. *J. Membr. Sci.* **347**, 108–115 (2010).
95. Patrício, P. S. O., de Sales, J. A., Silva, G. G., Windmüller, D. & Machado, J. C. Effect of blend composition on microstructure, morphology, and gas permeability in PU/PMMA blends. *J. Membr. Sci.* **271**, 177–185 (2006).
96. Moroi, G. Preparation and characterization of polyesterurethane/copper metallopolymers. *React. Funct. Polym.* **68**, 268–283 (2008).
97. Kuan, H.-C. *et al.* Synthesis, thermal, mechanical and rheological properties of multiwall carbon nanotube/waterborne polyurethane nanocomposite. *Compos. Sci. Technol.* **65**, 1703–1710 (2005).
98. Mrad, O. *et al.* A comparison of plasma and electron beam-sterilization of PU catheters. *Radiat. Phys. Chem.* **79**, 93–103 (2010).
99. Wang, F. Polydimethylsiloxane modification of segmented thermoplastic polyurethanes and polyureas. (Thesis, Virginia Polytechnic Institute and State University, 1998).
100. Esteves, A. C. C. *et al.* Influence of cross-linker concentration on the cross-linking of PDMS and the network structures formed. *Polymer* **50**, 3955–3966 (2009).

101. Bistričić, L., Baranović, G., Leskovac, M. & Bajsić, E. G. Hydrogen bonding and mechanical properties of thin films of polyether-based polyurethane–silica nanocomposites. *Eur. Polym. J.* **46**, 1975–1987 (2010).
102. Tsonos, C., Apekis, L., Zois, C. & Tsonos, G. Microphase separation in ion-containing polyurethanes studied by dielectric measurements. *Acta Mater.* **52**, 1319–1326 (2004).

CHAPTER 5 Electromechanical Response of Blends of PU and PDMS

Abstract

Chapter 4 described the blending of a thermoplastic polyurethane (PU) polymer with two types of cross-linked polydimethylsiloxane (PDMS) elastomers. The characteristics of these blend materials, such as their chemical structures and mechanical properties, were also discussed in Chapter 4. In this chapter, electromechanical properties of the actuators prepared from these blends are presented.

Results showed that the blending of a high- k PU into the PDMS dielectric elastomer Type I increased the elastomer's dielectric constant and decreased its dielectric breakdown strength. This process also sharply reduced the elastomer's elastic modulus, which contributed to its large strain at low electric fields. The largest actuated strain found for the Type I elastomer blends, 16%, was obtained at an electric field of 60 V/ μm with 30% actuator prestrain.

However, an increase in a material's dielectric constant is a natural corollary to a decrease in its dielectric strength, and this results in decreased actuation strain and energy density of the actuator. This is believed to be due to such blend properties as phase incompatibilities in the interphase morphologies. These incompatibilities in Type I blends resulted in low electrical breakdown and decreased mechanical properties in the form of low actuation strength and low electromechanical energy density.

We used another type of PDMS elastomer matrix, which we called Type II, to overcome the interphase-related problems of dielectric strength and mechanical properties of blends. This new blend of PU and Type II PDMS, with its increased actuation strain and energy density,

has great potential as a dielectric elastomer actuator material. In contrast to the Type I blends, the Type II blends exhibited higher actuation strain due to their low Young's modulus and high electrical breakdown. The largest actuated strain found for the Type II elastomer blends, 27%, was obtained at an electric field of 90 V/ μm with 30% actuator prestrain.

5.1 Introduction

Electroactive polymers (EAPs), one of the most promising groups of responsive materials due to their high actuation performance, convert electrical energy to mechanical energy¹⁻⁴. EAPs can change shape or size in response to external electrical stimulation. In contrast to other actuator materials, these polymers have mechanical and electrical properties that enable easy processing and tunability⁵⁻⁸. While all electroactive polymers have these advantages, the subset of dielectric elastomer materials and actuators are superior in cost, weight, shock tolerance, ease of processing, scalability, and energy density.

Lightweight dielectric electroactive polymers (D-EAP) are one of the most promising kinds of EAPs because of their particularly high actuation strain and ease of processing. These properties may enable new performance improvements in bio-inspired robots⁹⁻¹², prosthetic devices^{4,13}, adaptive structures¹⁴, fluid pumps^{15,16}, refreshable braille actuators^{17,18}, autofocus lens positioners^{19,20}, speakers²¹, shape and texture systems^{22,23}, smart textiles¹³, and energy-harvesting systems²⁴⁻²⁸.

In its simplest form, a D-EAP consists of a dielectric elastomer film placed between two compliant electrodes to form a parallel plate capacitor, as shown in Figure 5.1(b). When an electrical potential is applied to the electrodes, electrostatic attraction between the two

electrode surfaces causes deformation of the elastomer, which in turn creates a significant change in the lateral plane of the dielectric elastomer film. In addition, the repulsion of like charges on the individual electrodes leads to planar stretching of the film. The resulting pressure in the thickness direction of the dielectric elastomer film—also known as the Maxwell pressure—is calculated as follows:

$$P_{\text{Maxwell}} = \epsilon\epsilon_0 E^2 = \epsilon\epsilon_0 (v/z)^2 \quad \text{Equation 5.1}$$

where E is the electric field, ϵ_0 is the permittivity of free space, ϵ_r is the relative dielectric constant of the membrane, V is the voltage, and z is the elastomer membrane thickness. The direction of the actuation strain is a function of the electrostatic pressure and the material's modulus in the thickness direction and is calculated as follows²⁹:

$$s_z = -\frac{P_{\text{Maxwell}}}{Y} = -\frac{\epsilon_0\epsilon_r(v/z)^2}{Y} \quad \text{Equation 5.2}$$

where s_z is the thickness strain and Y is the Young's modulus of the elastomer.

Much of the research investigating D-EAPs has been devoted to producing materials that can convert electrical to mechanical energy efficiently (i.e., with minimal energy loss). The fundamental properties of an actuator material are its relative dielectric constant (ϵ_r) and Young's modulus (Y) and the conductivity of the compliant electrodes. These properties can be modified through polymer compositing that vary the amounts and kinds of fillers used and thereby enable the desired interactions between composites.

In actuation of D-EAPs, both the dielectric constant and the electrical breakdown strength of a material are of considerable importance. Increasing the electric field (E) by increasing the material's dielectric constant (ϵ_r) results in an increase in electrostatic pressure (P_{Maxwell}).

Unfortunately, increasing the electric field is not desirable due to corresponding safety issues. Therefore, the best approach to better actuator performance is to increase the dielectric constant of the dielectric elastomer material. However, a material's electrical breakdown strength (E_b) is just as significant as its dielectric constant; the dielectric strength of a composite determines ultimate actuation performance.

Applying initial prestrain is also an acceptable method for improving the electromechanical performance of a D-EAP. While nominal prestrain is needed to evaluate D-EAP actuation behavior, it also limits the material's behavior by increasing hysteresis and thereby producing a bulky actuator assembly.

Elastomer-based composites and blends have been effective in the development of high-dielectric constant materials for actuator applications. Three principal materials exist that can increase the dielectric constant of a polymer composite:

- High-dielectric constant ceramic fillers (e.g., TiO_2)³⁰⁻³²
- Conductive fillers (e.g., carbonaceous particles)³³⁻³⁷
- Polymer blends and elastomer formulation³⁸⁻⁴⁰

The first two methods have disadvantages for D-EAP applications. High volumes of ceramic filler lead to unacceptable degrees of stiffness and low breakdown of an elastomer's electric field^{32,41}. Conductive fillers form conductive paths in the elastomer, resulting in high dielectric loss and low dielectric strength. Using either type of filler causes early electrical breakdown of the actuator material^{23,42}.

D-EAP elastomers have produced commercially available materials in combination with the above-mentioned fillers. Recently, dielectric elastomers have been formulated for dielectric elastomer actuators to engineer an optimum material, one with a tunable dielectric constant and tunable mechanical properties. These formulations have aided in the molecular-level design of dielectric elastomers, taking into account the polymer-polar side groups for dielectric enhancement as well as specific cross-linkers and fillers^{43,44}.

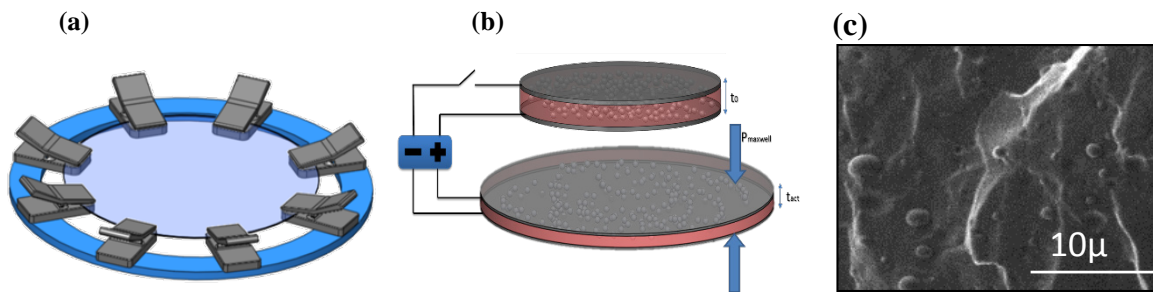


Figure 5.1 A circular actuator preparation from elastomers: (a) application of prestrain to a DE, (b) operation principle for D-EAP actuators, (c) fractured cross-section electron microscope image of a 5 wt% composition blend elastomer. PU fillers are 1-2 um in size and spherical in shape.

Finally, the third method, polymer blending³⁸⁻⁴⁰, has also been used in the fabrication of D-EAP. Polyurethane (PU) has been used as high- k filler in ground form⁴⁵ as well as in situ synthesized form in polydimethylsiloxane (PDMS) to improve the electromechanical properties of the composites. PU has been demonstrated to increase the dielectric constant of PDMS from 3 to 13, but these materials exhibited high dielectric loss⁴⁵. Interpenetrating polymer networks (IPNs) of acrylic elastomer and 1,6-hexanediol diacrylate were

synthesized by Goulbourne et al.⁴⁶ to demonstrate that prestrain of an actuator can be preserved in the IPN structure. Recently, Krishna et al.⁶ reported the development of a PU fiber-acrylic elastomer composite with high actuation stress and energy density.

In this research, a polymer/polymer blend with a high dielectric constant was formulated without compromising dielectric loss or dielectric strength, thus demonstrating that the electromechanical actuation response can be tailored to the application. This can be accomplished by increasing the blend elastomer's dielectric permittivity through simple polymer blending to fabricate a reliable material. In our study, we used a simple mixture of widely used D-EAP materials PDMS and PU.

In Chapter 4, we reported on the chemical and physical properties of PU and PDMS blends. In this chapter, we describe the dielectric, mechanical, and electromechanical properties of actuators prepared from these blends.

5.2 Theoretical Background

Maxwell pressure, coupling efficiency, and energy density are critical parameters for evaluating actuator performance. We calculated these parameters from the dielectric constants of the actuator materials and the actuation strains determined from the actuation videos.

The actuation response of a D-EAP film is due to the Maxwell pressure ($P_{Maxwell}$) perpendicular to the film surface generated upon electrical stimulation⁴⁷:

$$P_{Maxwell} = \frac{1}{A} \frac{dU}{dz} \quad \text{Equation 5.3}$$

Here, the $P_{Maxwell}$ is electrostatic pressure along the thickness direction, and z is the thickness of the blend elastomer.

$$U = \frac{Q^2}{2C} = \frac{Q^2}{\epsilon\epsilon_0 A_{xy}} \quad \text{Equation 5.4}$$

In Equation 5.4, U is the electrostatic potential of the capacitor, Q^2 is the charge on the plates, A_{xy} is the lateral surface area undergoing compression, C is the capacitance of the D-EAP actuator assembly ($C = \epsilon_r \epsilon_0 A_{xy}/z$), ϵ_0 is the permittivity of free space, and ϵ_r is the dielectric constant of the elastomer.

For materials with ideal elasticity, dU/dz is equal to the mechanical work that can be performed by an actuator. The deformation of an elastomer during actuation is constant volume deformation:

$$dV = zdA_{xy} + A_{xy}dz = 0 \quad \text{Equation 5.5}$$

Assuming the electrostatic energy completely transforms into Maxwell pressure,

$$P_{Maxwell} = \frac{Q^2}{\epsilon\epsilon_0 A_{xy}} \quad \text{Equation 5.6}$$

And the Maxwell pressure, as calculated as in Equation 5.6, can be simplified as follows:

$$P_{Maxwell} = \epsilon\epsilon_0 E^2 \quad \text{Equation 5.7}$$

Equation 5.7 is an abbreviated form of Equation 5.6 using $E = Q/(\epsilon_0 \epsilon A_{xy})$.

Based on assumptions and Equations 5.3 through 5.7, such actuator properties of elastomers as Maxwell pressure, coupling efficiency, and energy density—key parameters for actuator evaluation—were derived in literature^{29,47,48}.

The coupling efficiency (K^2) of an actuator is defined as the ratio of electrical energy converted to mechanical work relative to the applied electrical energy. For elastomers capable of isochoric deformation with negligible viscous losses, K^2 is calculated as follows²⁹:

$$K^2 = -2s_z - s_z^2 \quad \text{Equation 5.8}$$

where s_z is elastomer thickness strain. The energy density (E) of an elastomer is calculated as follows²⁹:

$$E = Y[s_z - \ln(1 + s_z)] \quad \text{Equation 5.9}$$

where Y is the compressive Young's modulus and s_z is, again, the thickness strain of the elastomer.

The thickness direction strain (s_z) is a factor of electrostatic pressure and modulus of actuator ($P_m = -Ys_z$) for small deformations ($s_z < 20\%$). Since the deformation during the actuation is linearly elastic, Hooke's law of compression can be used to directly relate s_z to the applied electric field.

$$s_z = -\epsilon\epsilon_0 \frac{E^2}{Y} \quad \text{Equation 5.10}$$

In Equation 5.10, Y depends on actuator prestrain and actuation strain; the deformation in the thickness direction (s_z) is calculated using the constant-volume equation after obtaining the

actuator areal deformation measurement. The in-plane strains and thickness of an ideal elastomer are related to one another as follows:

$$(1 + s_x)(1 + s_y)(1 + s_z) = 1 \quad \text{Equation 5.11}$$

Additionally, if we assume that the actuation-induced deformation is isotropic and that $s_x = s_y = s_{xy}$, we can calculate the actuation strain from the lateral radial strain (as observed during actuation) as follows:

$$s_z = (1 + s_{xy})^{-2} - 1 \quad \text{Equation 5.12}$$

Thus, we used the thickness-direction actuation strain (s_z) to calculate the actuator performance for blend elastomers.

The electromechanical sensitivity, β , gives information about general dependencies of actuation strain under a specified electrical field. β was obtained by using Equation 5.13⁴⁹ as follows:

$$s_z = \frac{E^2}{-\epsilon\epsilon_0 Y} = \beta E^2 \quad \text{Equation 5.13}$$

5.3 Materials and Methods

Detailed information on these were presented in Chapter 4. Nevertheless, in order to put the information presented in this chapter in context we mention a brief summary here.

5.3.1 Materials

We used two polymers for blend preparation: polyurethane (PU) and polydimethylsiloxane (PDMS). As matrix materials, we used two types of PDMS, referred to as Type I and Type

II. We used commercially available PDMS Sylgard 186 with a hydro-silylation addition reaction for the Type I elastomer due to its excellent electrical and mechanical properties. For the Type II PDMS, we formulated hydride silane/silanol-based PDMS. For the PU we used thermoplastic poly(ether-urethane) (Elastollan 1180A, BASF), which is available in commercial pellet form and has a relatively high dielectric constant ($\epsilon = 7.8$ at 100 Hz). Tetrahydrofuran (Fisher Sciences, USA) was used as a blending solvent.

Sylgard 186, the Type I PDMS, is a two-part elastomer consisting of a hydride-functional silicone polymer (part A) and a vinyl-terminated cross-linker (part B). A platinum complex participates in the reaction, which forms ethylene bridges between polymer and cross-linker through an additional polymerization reaction. Consequently, there was no byproduct in the elastomer except H_2 gas, which solubilizes in the polymer and so quickly outgasses to the environment, leaving no observable bubbles. The rate of this reaction depends on applied heat. Chapter 4, Section 2 described the reaction mechanism of this curing system.

The Type II elastomer used was an alkoxy condensation system consisting of a hydroxyl-functional polymer (DMS S42, Gelest Co, PA) and an isocyanate-functional cross-linker. Polymerization took place at room temperature atmospheric humidity. The alkoxy-functional cross-linker underwent a hydrolysis step, which left a hydroxyl group. This hydroxyl group then participated in a condensation reaction with another hydroxyl group attached to the polymer.

The isocyanate mono-functional group in the cross-linker also served to increase the possible chemical interaction of the PDMS polymers with the PU elastomers during network

formation—the cross-linker can establish links with both PU hydroxyl end groups and PDMS hydroxyl end groups⁵⁰. The isocyanate single-function group in the cross-linker is also reactive with the PU elastomer side groups^{51–57}, and this procedure results in a tetra-functional network in which the siloxane backbones join the PU elastomers within the interphase regions of blends. Additionally, the hydroxyl chain end groups of PDMS polymer networks are thermodynamically more attractive to PU because of PU's polar structure. This behavior is expected to increase the miscibility of PDMS⁵⁸.

Type II PDMS cures at room temperature. The formulation of Type II PDMS is as follows: 10 g PDMS fluid (DMS S42; Mw = 77,000 g/mol); 5 μ l cross-linker (Gelest, PA); 45 μ l tin catalyst. This formulation was used for all Type II blend compositions.

For the matrix elastomers we formulated, we needed to increase the interphase compatibility of the matrix and filler. To achieve this, we employed a condensation (i.e., alkoxy-cure) reaction, which entailed linking hydroxyl-terminated siloxanes in the presence of a tin catalyst and an isocyanate functional cross-linker (3-isocyanatopropyltriethoxy-silane)^{51–57,59}.

5.3.2 Blend Preparation

The PDMS and PU polymers were dissolved separately in THF as a co-solvent. The PDMS base part was mixed with the THF at room temperature for three hours, and the PU pellets were dissolved in the THF for 12 hours at 50 °C. The PDMS mixture and the PU mixture were combined and mixed using a magnetic stirrer. The cross-linker and catalyst of the PDMS matrix were added to this final polymer mixture, which was then processed using a high-shear mixer for 1 minute. (The magnetic stirring and high-shear mixing sequence were

used in order to prevent premature curing of the PDMS.) The mixture was then poured onto Teflon substrates to form a film for mechanical and dielectric characterization. These blend mixtures were also separately thinned down to a thickness of 100-200 μm using a spin-coater for electromechanical characterization. The samples were dried in an oven at room temperature for 12 hours to enable solvent evaporation and were cured at 80 °C for 12 hours to facilitate network formation. The samples were then prepared for characterization. Figure 5.2 shows the experimental order of blending the PU and PDMS elastomers.

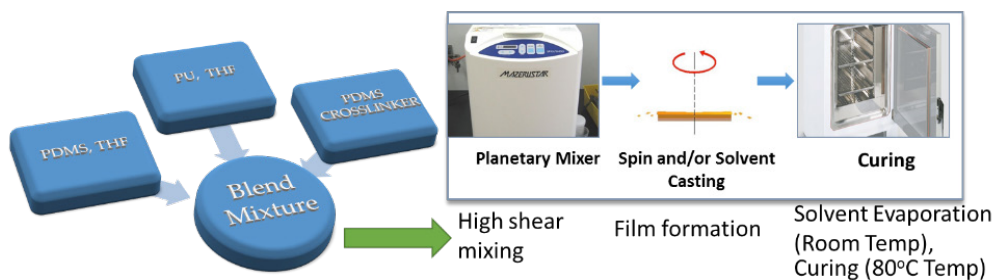


Figure 5.2 Scheme of blend elastomer preparation. Mixing of the PU/THF and PDMS/THF mixtures and addition of the PDMS crosslinking agent to the mixture for film formation.

5.3.3 Dielectric Characterization

The dielectric behavior of the films was measured using an LCR meter (GW Instek LCR-8101G) equipped with a parallel plate dielectric test fixture (Agilent 16451B). The LCR meter was connected to a computer to perform the dielectric measurement over a frequency range of 20 to 10^6 Hz at room temperature, which allowed us to measure sample impedance,

capacitance, and resistance. The capacitance (C) and dielectric dissipation data for the samples were collected, and the real (effective) dielectric constant (ϵ) was calculated from the capacitance and thickness (t) of the sample using the following equation:

$$\epsilon = Ct/A \quad \text{Equation 5.14}$$

where A is electrode area. The real part of the relative dielectric constant was calculated from capacitance values, and the dissipation factor was recorded from the the LCR meter.

5.3.4 Mechanical Characterization

Mechanical characterization of the composite elastomer films was performed using a uniaxial tensile load frame (MTS-30G). The films were cut into 10 mm-by-50 mm rectangular strips. The initial moduli of the blends were obtained from the initial region (5 percent strain) of stress-strain data. The test rate was set to 5 mm/min, and gauge length was set to 25 mm.

5.3.5 Electromechanical Characterization

The electromechanical behavior of the blend samples was evaluated using a circular actuator test. The actuators were prepared from these films as depicted in Figure 5.1(a).

The films were cut into 6 cm-diameter circles, which were then placed on the circular fixtures under uniform pretension (30%) using equally spaced plastic grips with rubber tips. These grips were assembled around the perimeter of a circular fixture with lock strip tapes (3M). We created a circular active area at the center of each test specimen by applying compliant silver paste electrodes (Chemtronics CircuitWorks, Kennesaw, GA) on both sides of the specimen to form a D-EAP, as shown in Figure 5.1(b). The electrodes were connected

to a high-voltage power supply (Bertan 225-30R, Spellman High Voltage Electronics Corp., Hauppauge, NY) that was programmed through an automated-voltage trigger. The voltage was increased by 500 V/s until the specimen underwent dielectric breakdown. As the voltage increased, video of the electrode area (the active area) was recorded using a digital video camera (DMK 23FM021, Imaging Source, NC). The resulting video was analyzed frame by frame with ImageJ software (developed by the NIH) to determine the actuation strains at given electrical potentials.

5.4 Results and Discussion

In Chapter 4, we discussed the properties of the elastomer blends along with their synthesis and development from the incompatible polymer species PDMS and polyurethane. The PU and PDMS were blended in the preparation of dielectric elastomer actuator materials. We used DMA, DSC, FTIR, SEM, and dielectric spectroscopy to study the physical and chemical characteristics of the polymer, as well as the interactions between the blend species, for various compositions of PDMS-PU blends. The blends studied here displayed two glass transition temperatures (T_{gs}), indicating micro-phase separation. The blends also exhibited increased dielectric constants and improved mechanical properties as compared to pure PDMS.

5.4.1 Mechanical Properties

We also tested the blend elastomers' mechanical properties since they play a major role in actuator performance assessment. Theoretically, the thickness strain of an actuator is s_z , a function of both the material's dielectric constant and its compression modulus. An ideal

elastomer is incompressible and has a Poisson's ratio of 0.5, and so its electric field-induced strains are small, with free boundary conditions.

One of the most important mechanical properties of a dielectric elastomer actuator is its Young's modulus. During the actuation of an elastomer, the Maxwell pressure generates an in-plane extension, the magnitude of which depends on the elastomer's mechanical properties. The tensile behaviors (i.e., the stress-strain relationships) of the Type I and Type II PDMS and PU films were plotted in Figure 5.3.

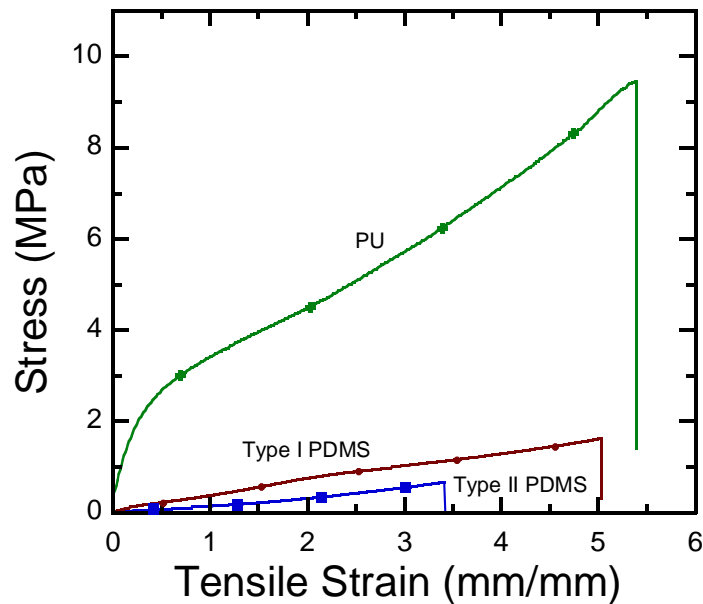


Figure 5.3 Mechanical properties of PU and PDMS samples: Stress-strain curve for pristine PU and PDMS elastomers: The red dot (•) Type I PDMS elastomer; blue square (■) Type II PDMS elastomer; and green plus (+) represents PU elastomer.

The initial modulus values were determined from the initial portion (0–5%) of the stress-strain curve. The modulus values were 0.6 MPa for the Type I PDMS, 0.18 MPa for the Type II PDMS, and 4.7 MPa for the PU.

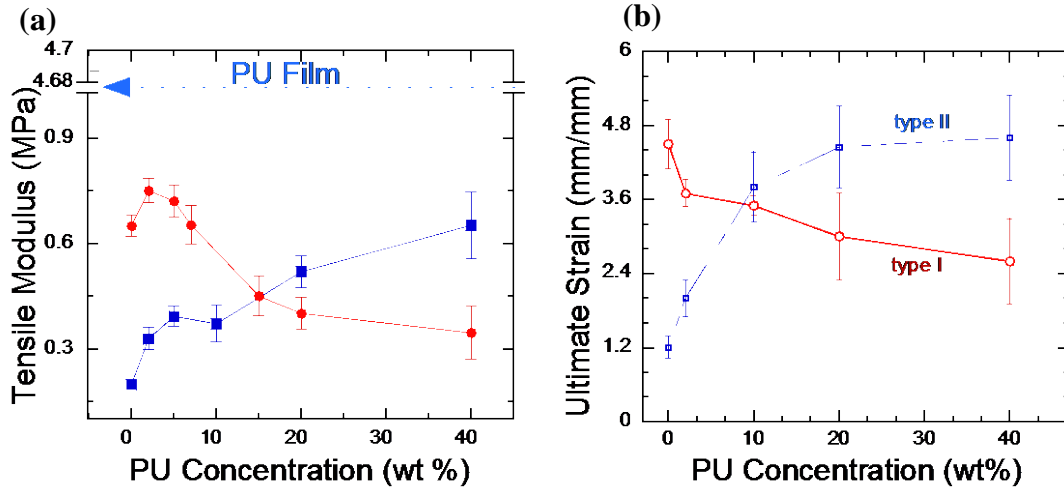


Figure 5.4 Mechanical properties of blends. (a) Young’s modulus (filled symbols) of the blend elastomer versus PU weight concentration. The open red circles (●) represent the Type I blend elastomers’ tensile modulus; the filled blue squares (■) represent the Type II blend elastomers’ tensile modulus. (b) Ultimate strain (open symbols) values for blend elastomers. The open red circles (○) represent the Type I blend elastomers’ tensile strain; the open blue squares (□) represent the Type II blend elastomers’ tensile strain.

The mechanical properties of the PU/PDMS blends were expected to improve as the PU concentration increased due to PU’s high modulus. In this research, as plotted in Figure 5.4, we observed a predicted increase in stiffness up to 10 wt% concentration of PU. In the Type I blends, an increase in PU concentration did not significantly increase the blend’s mechanical properties with respect to modulus and maximum stress. Moreover, these properties

decreased for 10 wt% PU concentration. Furthermore, blends with a 40 wt% concentration of PU became weaker and exhibited a lower modulus (0.4 MPa) than the PDMS elastomer. These results, plotted in Figure 5.4(a), indicated an increase in Young's modulus for Type I blends circa 10 wt% PU concentration. For the PU concentrations above 10 wt%, the blends' Type I mechanical properties; Young's modulus and maximum strength decreased. The Type II blends also showed a significant reduction in ultimate strain, from around 4.5 MPa to 2.3 MPa, with increasing PU weight concentration. Ultimate tensile stress decreased from 4.5 MPa to 0.9 MPa.

Type II PDMS exhibited a lower initial modulus and failure strain than Type I PDMS. The mechanical properties of the Type II blends increased along with modulus and ultimate tensile strain. Type II blends showed an increase from ca. 0.2 MPa to 0.6 MPa with increasing PU weight concentration. Type II elastomer ultimate tensile strain also increased from 3.3 to 4.5 with increasing PU weight concentration.

The results of these experiments, presented in Chapter 4, suggested no significant degree of interphase mixing between PU and PDMS. Figure 5.4(a) and (b) plot Young's modulus versus PU concentration and ultimate tensile strain versus PU concentration, respectively. The results make it clear that the mechanical strength and Young's modulus of the Type I blends decreased while the mechanical properties of the Type II blends increased with an increase in PU wt% concentration. The results given in this chapter are concordant with the results reported in Chapter 4, revealing that the Type I blends are immiscible and experience

lower interfacial adhesion. Type II blends also showed little to no phase mixing, and their mechanical properties increased with the increase in PU content.

For Type I blends, the ultimate strain decreased with higher levels of PU content. This decrease in both strength and modulus was a result of polymer phase separation and interphase incompatibility between the polymer species. In Type I blends, the incompatibility became more significant as the concentration of PU increased.

As shown in Figure 5.4, the Young's moduli of the Type II PDMS and the Type II blends were 0.18 MPa and 0.8 MPa, respectively, for 40 wt% concentration of PU. The tensile properties of the Type II blends increased with the increasing PU concentration. The ultimate strain of the Type II PDMS increased with increasing PU weight concentration, as shown in Figure 5.4(b).

These increases in modulus and ultimate strain can be attributed to the phase properties of the Type II blends and the interaction of the blend's two species. However, there was no evidence of phase mixing for Type I or Type II.

5.4.2 Electromechanical Properties

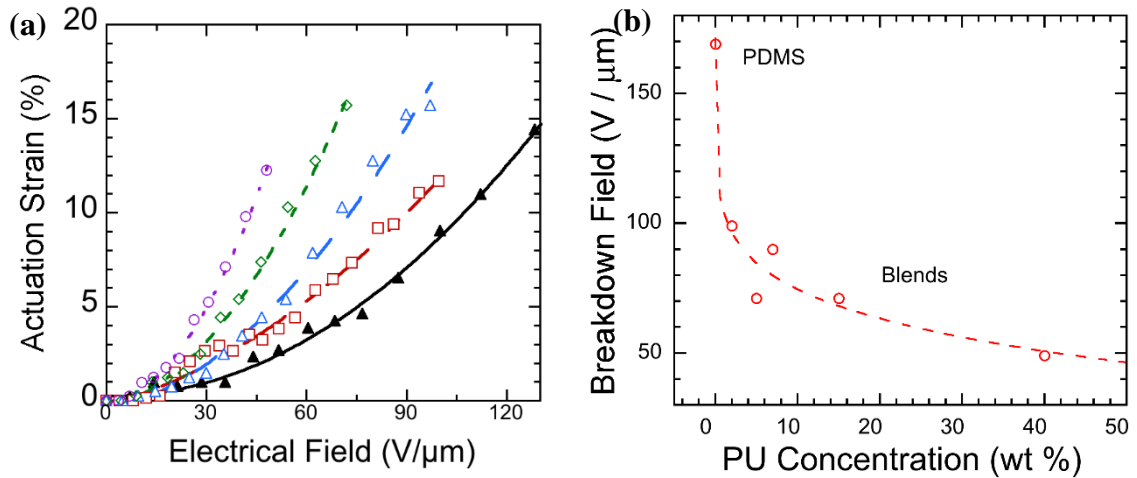


Figure 5.5 The dependence of actuation strain on electric field or the the Type I blend elastomers for various filler concentrations (wt%): (a) actuation strain versus electrical field for films of Type I PDMS (\blacktriangle), Type I blends of 2 wt% PU (\square), 10 wt% (\triangle), 20 wt% (\diamond), 40 wt% PU compositions (\circ). Type I PDMS (\blacktriangle) reached to a maximum actuation strain of ~ 25 at ~ 180 V/ μm , which was excluded from the plot. Lines are guides for eye. (b) Electromechanical breakdown field versus PU weight percentage for Type I blends. All lines serve as guide for eye.

Figure 5.5(a) displays the actuation strains (s_x) of the Type I blends as a function of actual electrical field. The actuation strains of the blends were higher than that of the neat Type I elastomer at all electrical fields. The control Type I PDMS (Sylgard 186, Dow Corning, NY) exhibited outstanding dielectric strength (actual electrical field at actuator electrical breakdown was circa 180 V/ μm). This high dielectric strength eventually resulted in a higher actuation strain of $\sim 24\%$. However, the pure Type I PDMS did not exhibit a high actuation strain at low electric fields.

The dielectric strengths for the Type I blends are plotted in Figure 5.5(b) as a function of blend composition. The dielectric strengths of the blends of all concentrations were lower than that of the Type I PDMS. The Type I blends with 2 weight percentage PU showed a decrease in dielectric strength of almost 40% compared to the control sample. The dielectric strength of these materials decreased to 100 V/ μm with the incorporation of PU elastomer filler. The decrease in electrical breakdown strength can be explained by the reduction in mechanical modulus⁶⁰.

The dielectric strength of the Type I blends with 40 wt% PU was less than 60% of that of the Type I PDMS control sample. The dielectric strength of the blend elastomers decreased as the weight concentration of the incorporated PU increased. The decreased dielectric strength of the Type I blends limited the actuation performance of these actuators and resulted in a lower actuation strain.

To facilitate comparison of the actuation response of various blend compositions, we plotted the actuation strain as a function of PU content at an arbitrary electric field, 60 V/ μm , as shown in Figure 5.6(a). We compared this to a curve of dielectric constant versus composition for the Type II blends and Type I PDMS (see Figure 5.6 (b)). The dielectric constant increased with the increase in weight concentration; therefore, the actuation strain improved for all blend elastomers as compared to the PDMS elastomer.

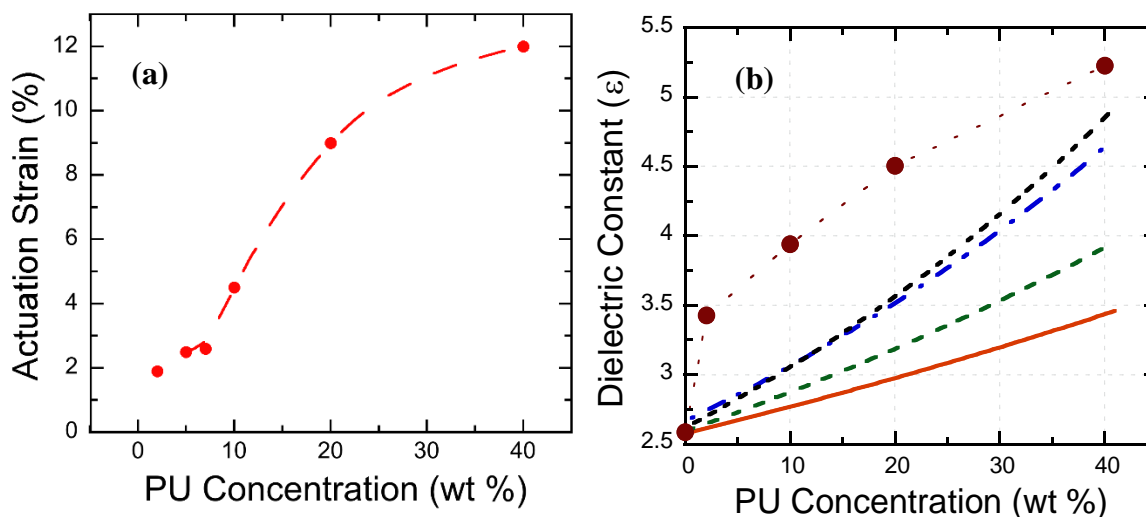


Figure 5.6 Dielectric strength of the Type I blend elastomers and the Type I PDMS elastomer. The dielectric breakdown electrical fields were plotted from electromechanical actuation tests of the elastomers. The dashed lines serve to connect data points. (b) Dielectric constant of blends versus PU weight concentration. Dashed lines represent (—) series, (---) logarithmic, (- - -) parallel, and (---) Maxwell Garnet theoretical prediction of mixing for dielectric constant, in order from bottom to top.

The improvement in actuation strain was a result not only of the increase in dielectric constant but also of the decrease in Young's modulus. The effect of elastomer modulus on actuation response for the Type I blends with high PU composition ratios can be attributed primarily to the blends' decrease in stiffness (see Figure 5.4).

To understand the electromechanical properties of these elastomers, we compared the effective dielectric constants of the elastomer blends at 100 Hz to the corresponding linear actuation strains, s_x , at an electric field of 60 V/ μm . The relationship between dielectric constant and actuation strain is explored in Figure 5.6. While actuation strain increased

because of the increasing dielectric constant of the blends, the increase in actuation strain of the Type I blends were higher than increase their dielectric constant. Because of the decrease in modulus and increase in dielectric constant with the increasing concentration of PU, the Type I blends showed improved actuation strains. This behavior can be explained by the dominant behavior of the material's Young's modulus over Maxwell pressure⁶¹.

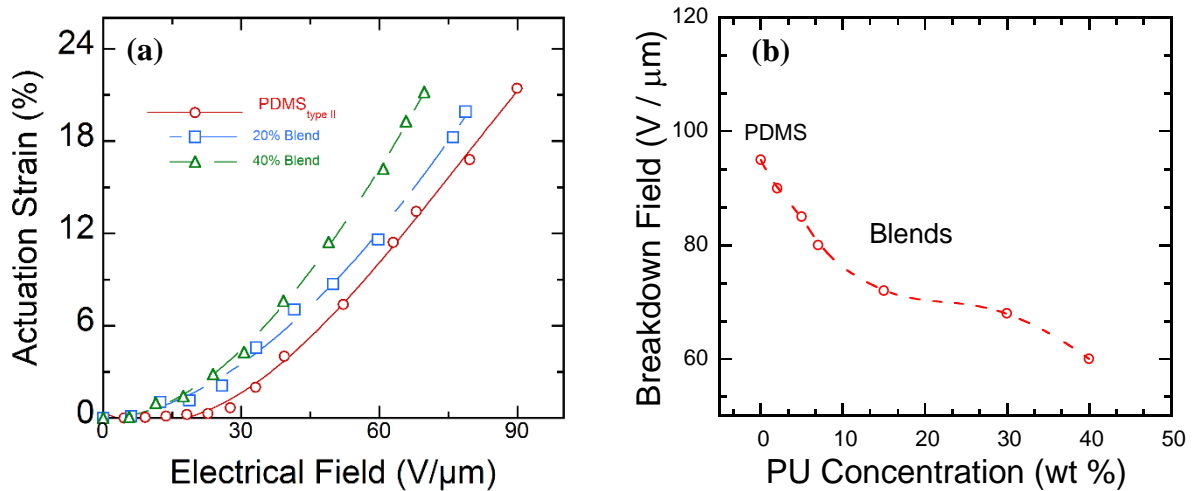


Figure 5.7 The dependence of actuation strain for the Type II blend elastomers at various filler concentrations: (a) actuation strain versus electrical field for concentrations (Pure Type II, 20 wt% and 40 wt%) (b) electromechanical breakdown field versus PU weight percentage for the Type II blends for 50 V/μm.

Figure 5.7(a) plots actuation strain, versus actual electrical field for the Type II blends and the PDMS control sample. The Type II PDMS control sample (DMS S42, Gelest) exhibited weak electromechanical properties in the form of low dielectric strength (95 V/μm) and low actuation strain as compared to the Type I control sample, which exhibited high dielectric strength. High dielectric strength of an elastomer eventually results in higher actuation strain.

For all blend concentrations, the dielectric strength was lower than that of PDMS. The dielectric strength of the Type II blends also decreased as the PU weight concentration increased. However, this dielectric strength decrease rate in Type II blends is lower than Type I blends.

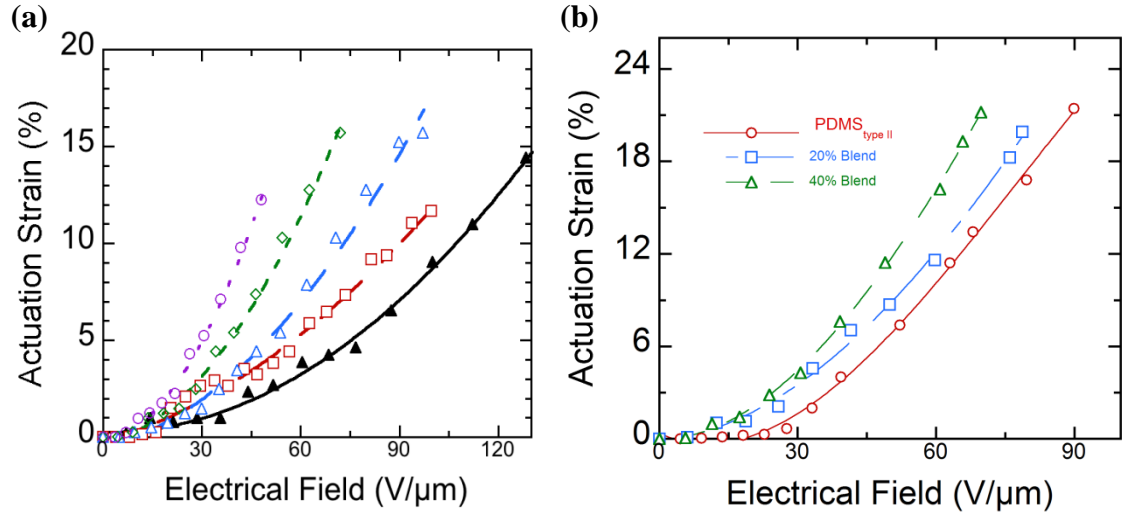


Figure 5.8 Actuation strain versus electrical field for (a) Type I and (b) Type II blends. (a) Type I PDMS (\blacktriangle), (\square) Type I blends of 2 wt% PU, (\triangle) 10 wt%, (\diamond) 20 wt%, (\circ) 40 wt% PU concentrations. (b) Pure Type II PDMS, 20 wt% and 40 wt% PU concentrations.

Compared to the pure PDMS, all PU/PDMS blends showed lower dielectric strength. Blends with 2 wt% concentration of PU of Type I blends, breakdown strength decreased by around 50%. Therefore, the dielectric strength of these materials decreased with the incorporation of more PU elastomer filler.

In conclusion, the incorporation of the PU elastomer was beneficial to the Type II blends: the electrical breakdown fields of these blends were higher than those of the Type I blends. The

dielectric strength data for the Type I blends and the Type II blends are compared in Figure 5.9. By way of comparison at 60 V/ μm electrical field, actuation strain as a function of weight percentage of PU content is shown in Figure 5.11(a) and (b).

Similar to what was observed with Type I blends, mechanical properties has effect on actuation performance of Type II blends. The high PU concentration Type II blends displayed an increase in actuation strain attributable to an increase in dielectric strength and a decrease in stiffness of the polymer blends.

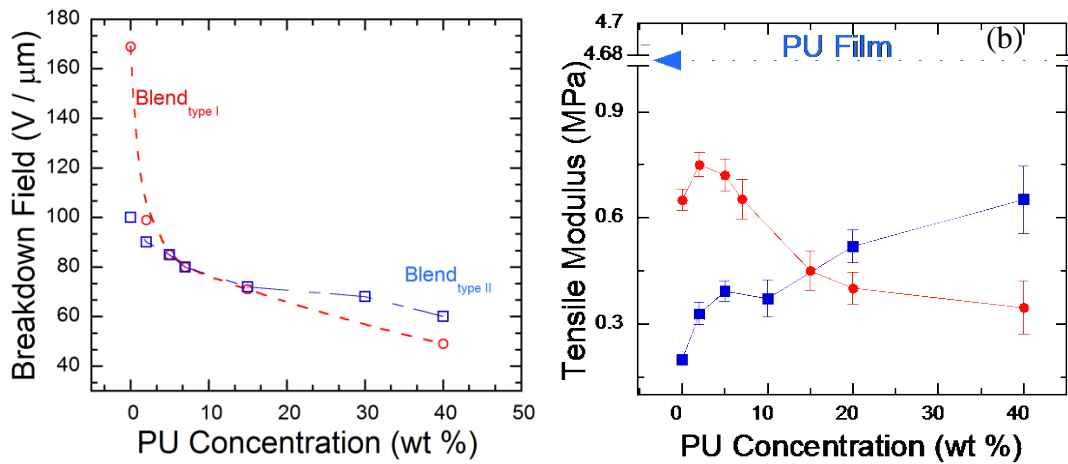


Figure 5.9 (a) Dielectric strength of the blends and the PDMS elastomer. The dielectric breakdown electrical fields were plotted from the ultimate electromechanical actuations of the elastomers. Red open dots (\circ) represent the Type I blends' tensile strains; blue open squares (\square) represent the Type II blends' tensile strains. (b) Young's modulus of the blends elastomer versus PU weight concentration. Red filled dots (\bullet) represent the Type I blends' tensile modulus; blue filled squares (\blacksquare) represent the Type II blends' tensile modulus.

In Figure 5.10, we analyze the electromechanical properties of these elastomers by comparing the effective permittivity of composites at 100 Hz to the linear actuation strain, s_x , at a $60 \text{ V}/\mu\text{m}$ voltage. The dielectric constant increased with the increase in weight concentration; therefore, actuation strain improved for all blend elastomers relative to the PDMS elastomer.

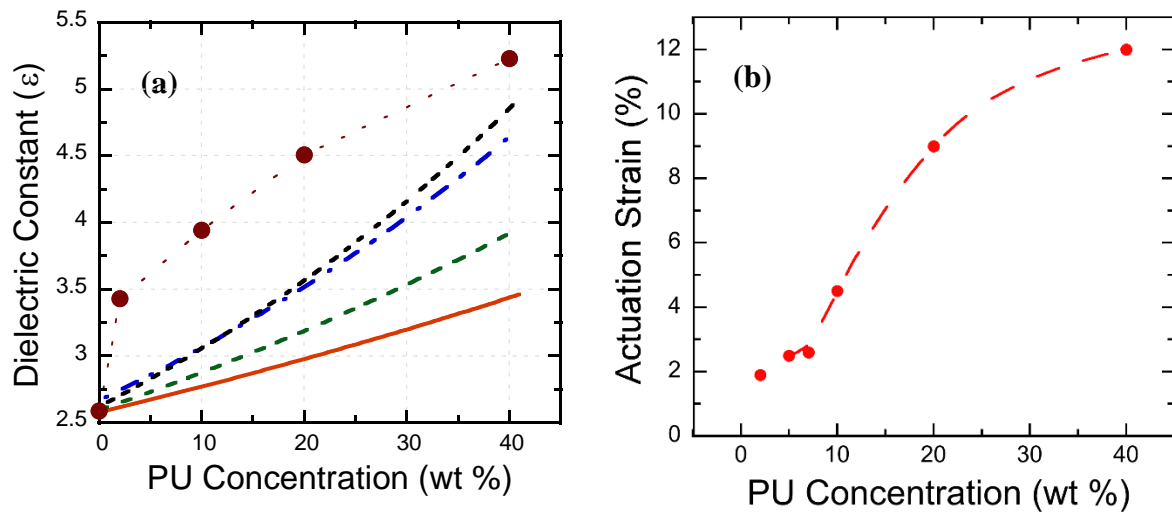


Figure 5.10 Dielectric strength of the blend elastomers and the PDMS elastomer: (a) dielectric constant versus PU weight percentage in the Type I blends (Dashed lines represent (—) series, (---) logarithmic, (- - -) parallel, and (---) Maxwell Garnet theoretical prediction of mixing for dielectric constant, in order from bottom to top. Data connected with dots serve guide to eye.) and b) actuation strain at $60 \text{ V}/\mu\text{m}$ as a function of PU weight concentration. Breakdown electrical fields were plotted based on electromechanical actuation tests of elastomers. The solid and dashed lines serve to connect the data.

The relationship between relative permittivity and actuation strain is shown in Figure 5.10. We compared the effective dielectric constants of the elastomer blends at 100 Hz with the

corresponding linear actuation strains, s_x , at $60 \text{ V}/\mu\text{m}$ to understand these elastomers' electromechanical properties. The increase in the blends' dielectric constant also resulted in increased actuation strain, as can be seen in Figure 5.10(b), the actuation responses of the Type II blends increased from circa 9.5% to 14%.

In summary, it was found that polarization response and energy density were enhanced in Type I and Type II blends containing PU (5 and 40 weight %). This enhancement is related to the interface effect between the two polymers that comprised the blends. Their breakdown field also decreased by about $90 \text{ V}/\mu\text{m}$, nearly 50%, due to the decrease in elastic modulus brought about by blend interphase properties. The Type II blends showed a decrease in electrical breakdown compared to the Type I blends. These results are summarized in Figure 5.9(b).

5.4.3 Actuator Performance

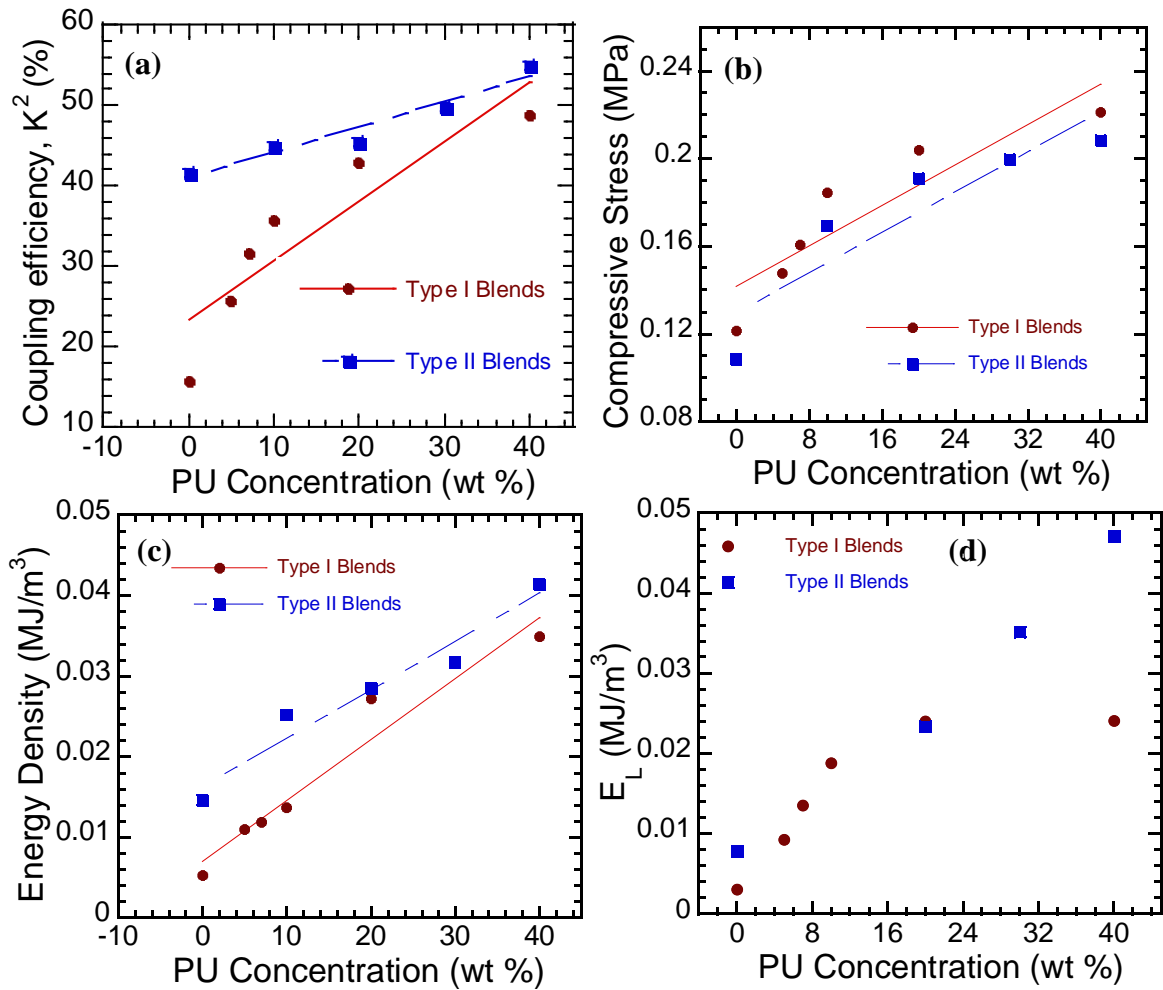


Figure 5.11 The actuator performance of blends: (a) electromechanical coupling efficiency (K^2), (b) compressive (Maxwell) stress, (c) electromechanical energy density given by $-P_{\text{Maxwell}}(1+s_z)/2$ on a unit volume basis, and (d) elastic energy density (E_L) displayed in terms of PU weight concentration. In all cases, the magnitude of the electric field is $60 \text{ V}/\mu\text{m}$. The solid and dashed lines are linear fits to the data; these serve as guides for the eye.

An important metric of D-EAP actuators is electromechanical coupling efficiency (K^2), related to energy conversion efficiency. This measure is plotted as a function of PU weight concentration (wt%) in Figure 5.11(a) for pure Type I and Type II PDMS/PU blends at 60 V/ μm . The pure PDMS sample exhibited a K^2 of 15.82%. The K^2 for the Type I blends increased at a high rate, to 37.12% at 10 wt% concentration. At 40 wt%, K^2 for the Type I blends was 44.96%. The K^2 for the Type II pure PDMS was 41.62%, and the K^2 for the Type II blends showed no significant change from this value, and dropped 10 wt%, before beginning to rise a low rate at 20 wt%. From this value of K^2 , 46.78%, it rose slightly to 54.86 at 40 wt%.

Compressive stress, plotted in Figure 5.11(b), displayed a similar pattern as the electromechanical coupling efficiency for both the Type I and Type II elastomers. The pure PDMS exhibited a compressive stress of 0.121 MPa. Like K^2 , it rose steeply to 0.184 at 10 wt% and then began to level off to reach 0.221 MPa at 40 wt%. Unlike Type II's K^2 , however, Type II's compressive stress follows a similar pattern to Type I's compressive stress. Type II pure PDMS exhibited a measure of 0.1084 MPa. From this level, it rose steeply to 0.170858 at 10 wt% and then continued to increase as a function of wt% but at a decreasing rate to end at 0.209453 at 40 wt%.

The energy densities of the blends are reported in Figure 5.11(c). The pure Type I PDMS exhibited an energy density of 0.00523 MJ/m³; this increased to 0.010937 MJ/m³ in the 5 wt% PU blend. Not until the incorporated PU was at 20 wt% did the energy density increase sharply from 0.021 MJ/m³ at 10 wt% to 0.027 MJ/m³ before ending at 0.330 MJ/m³ at 40

wt%. The pure Type II PDMS exhibited an energy density of 0.014 MJ/m³. Type II's energy density exhibited sharp increases at 10 wt% (0.019 MJ/m³) and 40 wt% (0.041 MJ/m³) and exhibited much lower rates of increase between these two concentration levels.

Finally, we analyzed the elastic energy density (E_L) of the blends. The pure Type I PDMS exhibited an E_L of 0.003045 MJ/m³. With the incorporation of PU, E_L increased at a high rate until it reached 0.0188 MJ/m³ at 10 wt% PU, at which point it leveled off. It continued to increase but at a much lower rate; finally, at 40 wt%, E_L was 0.024 MJ/m³, up from 0.024033 MJ/m³ at 20 wt%. The pure Type II PDMS exhibited an E_L of 0.007 MJ/m³. At 2 wt%, this value increased by almost 100% by 0.013MJ/m³, leveled off at 10 wt%, and then increased at a to 0.047 MJ/m³ at 40 wt%.

Electromechanical sensitivity, β , was calculated using Equation 5.13. The Type I and Type II blends were compared to their corresponding Type I and Type II PMDS control samples using the following formula:

$$\beta_r = \beta_{Blend} / \beta_{PDMS} \quad \text{Equation 5.15}$$

where β_r is the ratio of electromechanical sensitivity of a blend to that of the pure PDMS material (Type I, 0.003; Type II, 0.008), a relative electromechanical sensitivity of the blends. The Type I blends showed dramatic increase in relative sensitivities. The 5 wt%, 7 wt%, 10 wt%, and 40 wt% blends were 3.0, 4.5, 6.0, and 7.9 times the β_{PDMS} , respectively. Type II's relative differences were not as dramatic but were nonetheless significant. The 5 wt%, 7

wt%, 10 wt%, and 40 wt% blends were 1.8, 1.4, 3.0, 4.5, and 6.0 times that of the pure PDMS's β_{PDMS} , respectively.

In sum, the dielectric constant is as important as the initial Young's modulus of an actuator material in terms of effect on a dielectric elastomer's actuator performance. In a similar experiment by Zhao et al.⁶², plasticized PDMS/TiO₂ composite, the actuation response of high concentration PU-PDMS blends was attributed to both a decrease in polymer stiffness and an increase in dielectric constant.

In our experiments, the increased breakdown strength was due to the decrease in Young's modulus and the decrease in matrix filler interactions.

5.5 Conclusions

In this chapter, the electromechanical properties of the PU/PDMS blend elastomers were reported. When the high-permittivity PU polymer was blended with the PDMS, the enhanced dielectric constant improved actuation strain. Polymer blend elastomer showed an increased dielectric constant. However, the dielectric strength of the blend elastomers was low due to an incompatible blend formation.

These problems were studied through a different formulation of elastomer matrix. The electromechanical properties of this second type of elastomer were also evaluated. Although direct comparison of Type I and Type II was not entirely possible, we concluded that the Type II elastomer formulation showed higher actuation strain and coupling efficiency due to increased dielectric strength.

In conclusion, the electromechanical properties discussed thus far establish that the PU/PDMS films are a better alternative than pure PDMS elastomers for D-EAP applications. The method presented demonstrate that actuation strain of D-EAP actuators can be greatly and conveniently enhanced through blending of a polymer that increases dielectric constant. PU/PDMS composites exhibited higher actuation strain, energy density, and coupling efficiency at relatively low electric fields when compared to control PDMS samples. Therefore, PU/PDMS composites are suitable for low-electric field, energy-efficient actuation, including use in micro-robotic systems, biomedical devices (e.g., active braille and steerable catheters), and smart prosthetics.

5.6 References

1. Bar-Cohen, Y. *Electroactive polymer (EAP) actuators as artificial muscles*. (SPIE Press, 2004).
2. Brochu, P. & Pei, Q. Advances in dielectric elastomers for actuators and artificial muscles. *Macromol. Rapid Commun.* **31**, 10–36 (2010).
3. O'Halloran, A., O'Malley, F. & McHugh, P. A review on dielectric elastomer actuators, technology, applications, and challenges. *J. Appl. Phys.* **104**, 071101–10 (2008).
4. Biddiss, E. & Chau, T. Dielectric elastomers as actuators for upper limb prosthetics: Challenges and opportunities. *Med. Eng. Phys.* **30**, 403–418 (2008).
5. Shankar, R., Ghosh, T. K. & Spontak, R. J. Electroactive nanostructured polymers as tunable actuators. *Adv. Mater.* **19**, 2218–2223 (2007).

6. Subramani, K. B., Cakmak, E., Spontak, R. J. & Ghosh, T. K. Enhanced electroactive response of unidirectional elastomeric composites with high-dielectric-constant fibers. *Adv. Mater.* **26**, 2949–2953 (2014).
7. Shankar, R., Krishnan, A. K., Ghosh, T. K. & Spontak, R. J. Triblock copolymer organogels as high-performance dielectric elastomers. *Macromolecules* **41**, 6100–6109 (2008).
8. Vargantwar, P. H., Shankar, R., Krishnan, A. S., Ghosh, T. K. & Spontak, R. J. Exceptional versatility of solvated block copolymer/ionomer networks as electroactive polymers. *Soft Matter* **7**, 1651 (2011).
9. Anderson, I. A., Ieropoulos, I. A., McKay, T., O'Brien, B. & Melhuish, C. Power for robotic artificial muscles. *Mechatron. IEEE/ASME Trans. On* **16**, 107–111 (2011).
10. Hyouk Ryeol Choi *et al.* Biomimetic soft actuator: design, modeling, control, and applications. *IEEE/ASME Trans. Mechatron.* **10**, 581–593 (2005).
11. Goethals, P. & Leuven, K. U. Tactile feedback for robot assisted minimally invasive surgery: an overview. *Dep. Mech. Eng. KU Leuven Tech Rep* (2008).
12. Taya, M. Bio-inspired design of intelligent materials. in *Proceedings of SPIE* **5051**, 54–65 (2003).
13. Carpi, F. & De Rossi, D. Electroactive polymer-based devices for e-textiles in biomedicine. *Inf. Technol. Biomed. IEEE Trans. On* **9**, 295–318 (2005).
14. Prahlad, H. *et al.* Programmable surface deformation: thickness-mode electroactive polymer actuators and their applications. in *Electroactive Polymer Actuators and Devices* (ed. Bar-Cohen, Y.) **5759**, 102–113 (SPIE Proceedings, 2005).

15. Arthur, G. G., McKeon, B. J., Dearing, S. S., Morrison, J. F. & Cui, Z. Manufacture of Micro-sensors and Actuators for Flow Control. *Microelectron Eng* **83**, 1205–1208 (2006).
16. Carpi, F., Menon, C. & De Rossi, D. Electroactive elastomeric actuator for all-polymer linear peristaltic pumps. *IEEE/ASME Trans. Mechatron.* **15**, 460–470 (2010).
17. Chakraborti, P. *et al.* A compact dielectric elastomer tubular actuator for refreshable Braille displays. *Sens. Actuators Phys.* **179**, 151–157 (2012).
18. Mazzone, A., Zhang, R. & Kunz, A. Novel Actuators for Haptic Displays Based on Electroactive Polymers. in *Proceedings of the ACM Symposium on Virtual Reality Software and Technology* 196–204 (ACM, 2003). doi:10.1145/1008653.1008688
19. Choi, S. T., Lee, J. Y., Kwon, J. O., Lee, S. & Kim, W. Varifocal liquid-filled microlens operated by an electroactive polymer actuator. *Opt. Lett.* **36**, 1920–1922 (2011).
20. Tang, H. Smart lens made of dielectric elastomer: simulation study. *Bull. Am. Phys. Soc.* **56**, (2011).
21. Heydt, R., Kornbluh, R., Eckerle, J. & Pelrine, R. Sound radiation properties of dielectric elastomer electroactive polymer loudspeakers. in **6168**, 61681M–61681M–8 (2006).
22. Ouyang, G., Wang, K., Henriksen, L., Akram, M. N. & Chen, X. Y. A novel tunable grating fabricated with viscoelastic polymer (PDMS) and conductive polymer (PEDOT). *Sens. Actuators Phys.* **158**, 313–319 (2010).

23. Ouyang, G. M., Wang, K. Y. & Chen, X. Y. Enhanced electro-mechanical performance of TiO₂ nano-particle modified polydimethylsiloxane (PDMS) as electroactive polymers. in *Solid-State Sensors, Actuators and Microsystems Conference* 614–617 (2011).
24. Davies, D. K. Charge generation on dielectric surfaces. *J. Phys. Appl. Phys.* **2**, 1533–1537 (1969).
25. Lo, H. C., Mckay, T., O'Brien, B. M., Calius, E. & Anderson, I. Circuit design considerations for regulating energy generated by dielectric elastomer generators. in 79760C–79760C–8 (2011). doi:10.1117/12.880723
26. Koh, S. J. ., Keplinger, C., Li, T., Bauer, S. & Suo, Z. Dielectric elastomer generators: how much energy can be converted? *Mechatron. IEEE/ASME Trans. On* **16**, 33–41 (2011).
27. Jean-Mistral, C., Basrour, S. & Chaillout, J.-J. Dielectric polymer: scavenging energy from human motion. in *Electroactive Polymer Actuators and Devices (EAPAD) 2008, 10 March 2008* **6927**, 692716–1 (SPIE - The International Society for Optical Engineering, 2008).
28. Kang, G., Kim, K.-S. & Kim, S. Note: Analysis of the efficiency of a dielectric elastomer generator for energy harvesting. *Rev. Sci. Instrum.* **82**, 046101 (2011).
29. *Dielectric Elastomers as Electromechanical Transducers: Fundamentals, Materials, Devices, Models and Applications of an Emerging Electroactive Polymer Technology.* (Elsevier Science, 2008).
30. Xu, J., Bhattacharya, S., Pramanik, P. & Wong, C. P. High dielectric constant polymer-ceramic (Epoxy varnish-barium titanate) nanocomposites at moderate filler loadings for embedded capacitors. *J. Electron. Mater.* **35**, 2009–2015 (2006).

31. Meng-Meng, L. *et al.* Dielectric properties of electrospun titanium compound/polymer composite nanofibres. *Chin. Phys. B* **19**, 028102 (2010).
32. Li Li *et al.* Novel polymer-ceramic nanocomposite based on new concepts for embedded capacitor application (I). *Compon. Packag. Technol. IEEE Trans. On* **28**, 754–759 (2005).
33. Saha, S. K., DaSilva, M., Hang, Q., Sands, T. & Janes, D. B. A nanocapacitor with giant dielectric permittivity. *Nanotechnology* **17**, 2284–2288 (2006).
34. Gangopadhyay, R. & De, A. Conducting Polymer Nanocomposites: A Brief Overview. *Chem. Mater.* **12**, 608–622 (2000).
35. Ferroelectric polymer/silver nanocomposites with high dielectric constant and high thermal conductivity. *Appl. Phys. Lett.* **95**, 242901–242901–3 (2009).
36. Xu, J. & Wong, C. P. Effect of the polymer matrices on the dielectric behavior of a percolative high-k polymer composite for embedded capacitor applications. *J. Electron. Mater.* **35**, 1087–1094 (2006).
37. Yadav, S. K., Mahapatra, S. S., Cho, J. W., Park, H. C. & Lee, J. Y. Enhanced mechanical and dielectric properties of poly(vinylidene fluoride)/polyurethane/multi-walled carbon nanotube nanocomposites. *Fibers Polym.* **10**, 756–760 (2010).
38. Carpi, F., Gallone, G., Galantini, F. & De Rossi, D. Silicone-poly(hexylthiophene) blends as elastomers with enhanced electromechanical transduction properties. *Adv. Funct. Mater.* **18**, 235–241 (2008).
39. Carpi, F., Gallone, G., Galantini, F. & De Rossi, D. Enhancement of the electromechanical transduction properties of a silicone elastomer by blending with a conjugated polymer. in *SPIE Proceedings* (ed. Bar-Cohen, Y.) **6927**, 692707–692707–11 (2008).

40. Chwang, C.-P., Liu, C.-D., Huang, S.-W., Chao, D.-Y. & Lee, S.-N. Synthesis and characterization of high dielectric constant polyaniline/polyurethane blends. *Synth. Met.* **142**, 275–281 (2004).
41. Carpi, F. & Rossi, D. D. Improvement of electromechanical actuating performances of a silicone dielectric elastomer by dispersion of titanium dioxide powder. *IEEE Trans. Dielectr. Electr. Insul.* **12**, 835–843 (2005).
42. Anquetil, P. A. *et al.* Thiophene-based conducting polymer molecular actuators. in *Proc. SPIE* **4695**, 424–434 (2002).
43. Madsen, F. B., Dimitrov, I., Daugaard, A. E., Hvilsted, S. & Skov, A. L. Novel cross-linkers for PDMS networks for controlled and well distributed grafting of functionalities by click chemistry. *Polym. Chem.* **4**, 1700 (2013).
44. Ma, W., Wu, L., Zhang, D. & Wang, S. Preparation and properties of 3-aminopropyltriethoxysilane functionalized graphene/polyurethane nanocomposite coatings. *Colloid Polym. Sci.* **291**, 2765–2773 (2013).
45. Gallone, G., Galantini, F. & Carpi, F. Perspectives for new dielectric elastomers with improved electromechanical actuation performance: composites versus blends. *Polym. Int.* **59**, 400–406 (2010).
46. Goulbourne, N. C. A constitutive model of polyacrylate interpenetrating polymer networks for dielectric elastomers. *Int. J. Solids Struct.* **48**, 1085–1091 (2011).
47. Pelrine, R. *et al.* High-field deformation of elastomeric dielectrics for actuators. *Mater. Sci. Eng. C* **11**, 89–100 (2000).
48. Pelrine, R., Kornbluh, R., Pei, Q. & Joseph, J. High-speed electrically actuated elastomers with strain greater than 100%. *Science* **287**, 836–839 (2000).

49. Pelrine, R. E., Kornbluh, R. D. & Joseph, J. P. Electrostriction of polymer dielectrics with compliant electrodes as a means of actuation. *Sens. Actuators Phys.* **64**, 77–85 (1998).
50. Hassanajili, S., Khademi, M. & Keshavarz, P. Influence of various types of silica nanoparticles on permeation properties of polyurethane/silica mixed matrix membranes. *J. Membr. Sci.* **453**, 369–383 (2014).
51. Bai, H.-C., Tao, L., Pang, Y.-J., Zhou, Y.-J. & Chen, J. Synthesis and characterization of hydroxypropyl terminated polydimethylsiloxane-polyurethane copolymers. *J. Appl. Polym. Sci.* **129**, 2152–2160 (2013).
52. Joki-Korpela, F. & Pakkanen, T. T. Incorporation of polydimethylsiloxane into polyurethanes and characterization of copolymers. *Eur. Polym. J.* **47**, 1694–1708 (2011).
53. Tsiges, M. *et al.* Interactions and structure of poly(dimethylsiloxane) at silicon dioxide surfaces: Electronic structure and molecular dynamics studies. *J. Chem. Phys.* **118**, 5132 (2003).
54. Karabela, M. M. & Sideridou, I. D. Effect of the structure of silane coupling agent on sorption characteristics of solvents by dental resin-nanocomposites. *Dent. Mater.* **24**, 1631–1639 (2008).
55. Seeni Meera, K. M., Murali Sankar, R., Jaisankar, S. N. & Mandal, A. B. Physicochemical studies on polyurethane/siloxane cross-linked films for hydrophobic surfaces by the sol-gel process. *J. Phys. Chem. B* **117**, 2682–2694 (2013).
56. Park, S., Kim, J. S., Chang, Y., Lee, S. C. & Kim, C. A covalently interconnected phosphazene-silicate network: synthesis and surface functionalization. *J. Inorg. Organomet. Polym.* **8**, 205–214 (1998).

57. Tingaut, P., Weigenand, O., Militz, H., Jéso, B. D. & Sèbe, G. Functionalisation of wood by reaction with 3-isocyanatopropyltriethoxysilane: Grafting and hydrolysis of the triethoxysilane end groups. *Holzforschung* **59**, 397–404 (2005).
58. Lee, M. H., Fleischer, C. A., Morales, A. R., Koberstein, J. T. & Koningsveld, R. The effect of end groups on thermodynamics of immiscible polymer blends. 2. Cloud point curves. *Polymer* **42**, 9163–9172 (2001).
59. Rezaei, S. M. & Mohd Ishak, Z. A. The biocompatibility and hydrophilicity evaluation of collagen grafted poly(dimethylsiloxane) and poly (2-hydroxyethylmethacrylate) blends. *Polym. Test.* **30**, 69–75 (2011).
60. Kollosche, M. & Kofod, G. Electrical failure in blends of chemically identical, soft thermoplastic elastomers with different elastic stiffness. *Appl. Phys. Lett.* **96**, 071904 (2010).
61. Ouyang, G., Wang, K. & Chen, X. Y. TiO₂ nanoparticles modified polydimethylsiloxane with fast response time and increased dielectric constant. *J. Micromechanics Microengineering* **22**, 074002 (2012).
62. Zhao, H., Wang, D.-R., Zha, J.-W., Zhao, J. & Dang, Z.-M. Increased electroaction through a molecular flexibility tuning process in TiO₂-polydimethylsilicone nanocomposites. *J. Mater. Chem. A* **1**, 3140 (2013).

CHAPTER 6 Electromechanical Response of PU-PDMS Composite Films

Abstract

Chapters 4 and 5 discussed the process of blending a thermoplastic polyurethane (PU) polymer with two types of cross-linked polydimethylsiloxane (PDMS) elastomers as well as the electromechanical properties of the blends. In this chapter, we will describe the fabrication of a solution-cast PDMS film reinforced with electrospun PU nanofibers. As reported in previous chapters, microscopic analysis showed uniform distribution of PU fibers throughout the PDMS matrix without any dominant voids and with good filler-matrix interface. Moreover, the fiber nanocomposites exhibited a significant increase in dielectric constant with increasing concentration of PU fiber filler.

The maximum linear actuation strain for these composites was 26%, with 1.25 wt% filler concentration. Additionally, the coupling efficiency was improved 45% for PDMS for 3.75 wt% PU fiber filler concentration at a 50 V/ μm electric field.

6.1 Introduction

Electroactive polymers (EAPs) change their shape in response to electric stimulation¹⁻⁸. Moreover, EAPs are easy to process and lightweight, so they are considered excellent material for such specialized applications as muscle-like actuators, biomimetic grippers, and steerable catheters¹⁻⁸. They have also been used in optical lenses, loudspeakers, haptic displays, vibration damping systems, and pumps^{1,2,5-11}.

An important class of EAPs, dielectric electroactive polymer (D-EAP), are superior to rigid and striction-limited shape memory alloys, electroactive ceramics, and other electroactive

polymers because of their higher actuation strain and response speed and lower power density and power usage and also they are especially resilient to damage.

The actuation mechanism of a dielectric elastomer depends mainly on the electrostatic compression pressure (P_{Maxwell}) between the compliant electrodes placed in parallel along the elastomer's thickness direction (z), as demonstrated in Figure 6.1(a). An elastomer film is stretched and compressed by a voltage applied across these electrodes. The increasing charge density increases the compression among negative charges in the two sides of the elastomer as like charges on the elastomer surface move further from each other. These charges generate the compression forces that are transferred to the elastomer in the lateral direction. Thus, the lateral direction actuation is a result of electrical input, and this actuation requires an elastomer film exhibiting a low modulus and high dielectric constant.

The utility of dielectric elastomer (DE) materials in most practical applications is limited by the need to apply unacceptably high electric fields in order to obtain the desired actuation performance. The most desirable route to overcome this limitation is to improve the dielectric properties of the DE materials so as to increase the necessary stress/strain levels. Incorporating high-permittivity materials into elastomers to form blends or composites has been the most promising and facile route to improving the dielectric constant of potential DE materials. The dielectric responses of elastomer composites containing ceramic or metal particles and organic fillers have been investigated extensively.

In general, polymer-polymer systems are preferable to ceramic composites for D-EAP applications because their constituents are likely to be more compatible. However, miscibility and compatibility issues between two polymer species as well as the problems inherent in formulating good elastomers are drawbacks to this approach.

The advantages PDMS include a broad usable temperature range; low chemical reactivity; resistance to oxygen, ozone, and solar radiation; and good electric insulation¹². However, it has the disadvantages of a low dielectric constant and low fracture resistance.

All-organic polymer composites have been produced using several methods. Electrospinning is one method used to construct three-dimensional surfaces through drawing of polymeric solutions under high electric fields. Electrospun nanofibers have been investigated for use in nanoscale devices^{13,14} because of their small uniform dimensions.

Electrospun fiber composites have also been produced for use in dielectric applications. In general, the dielectric constants of electrospun fibers are very low because of their highly porous structure. Dielectric constants of 1.5 to 2 have been reported for nanofiber mats with 80% porosity. Polymers exhibiting a high dielectric constant produce a fiber mat with a high dielectric constant. A PVDF polymer with $\epsilon = 6.8$ was shown to have a minimum dielectric constant of 2.04 because of its porous structure of 79%¹⁵.

An increase in fiber diameter increases the density of the electrospun fiber mat and therefore its dielectric constant¹⁵. Removing air from the composite has also been shown to prevent a decrease in the dielectric constant. (This was accomplished through filling voids with another polymer or sintering the fiber mat and pelleting it under high pressures¹⁶.) Appropriate

wetting and infusion of the fiber web is extremely important because inclusion of air in the polymer composite decreases its dielectric constant and degrades its mechanical properties. Composites of carbon nanotube-polymer produced through electrospinning have reported to exhibited a dielectric constant of approximately 60^{17,18}. The advantage of electrospinning for these composites having low dielectric loss with circa 0.05 even 25 vol% carbon nanotube loadings.

Investigation of spinability of fillers such as carbon nanotubes, ceramics and metals for electrospun fibers were investigated widely for various applications^{19,20}. For dielectric explorations, Khan et al. encapsulated carbon nanotubes and NiZn ferrite to polyvinylpyrrolidone (PVP) and polyacrylonitrile fiber mats. Dielectric measurements show significant an increase up to 8 from 3 for both composite fiber mats depending on filler concentrations^{21,22}. A rotational direction polarization and space charge polarization are responsible for high dielectric constants up to 32 for polar polymer matrices²³. The carbonblack encapsulation experiment on electrospun mats show a decrease in single electrospun fiber conductivity because of different charge transfer mechanisms of filler and polymers²⁴. The control of conductivity and dielectric loss is also suggested using ceramic fillers²⁵.

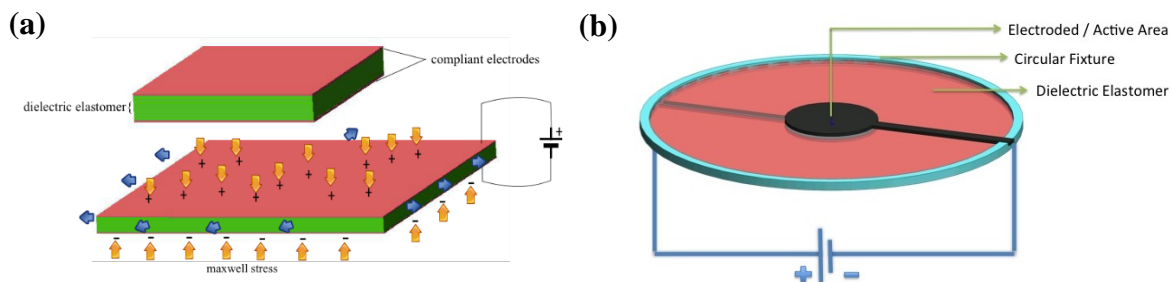


Figure 6.1 (a) A dielectric elastomer actuator and its actuation mechanism ; (b) DE circular actuator configuration.

In this work, we incorporated electrospun fibers into an elastomeric matrix to enhance the elastomer's dielectric behavior. The resulting electrospun fiber composites showed improved dielectric and electromechanical behavior as compared to the neat elastomer.

6.2 Materials and Methods

In this work, PDMS elastomer was used as the polymer matrix, and PU electrospun fiber web was used as the filler.

6.2.1 Materials

6.2.1.1 Polyurethane Nanofibers

The polyurethane (PU) was commercial product Deerfield PT6110. PU film was cut into small pieces and dissolved in a DMF/Chloroform (volume 50/50) solvent mixture for 6 hours. This polymer mixture was then transferred to an electrospinning syringe whose silver-coated needle was connected to a high-voltage power supply (Gamma, Model ES30N, FL). Then, an aluminum foil plate (for the collection of the resulting electrospun fiber) was grounded. A syringe infusion (Gennie Scientific, Model 100, CT) controlled the polymer

solution's feed rate through the syringe. After several trials, a feed rate of 80 $\mu\text{L}/\text{min}$ was determined to be optimal for fiber formation. A fibrous membrane of varying thickness was deposited onto the collector plate as a result of electrospinning the PU solution under a high voltage (24 kV) with the DMF/Chloroform solvent blend. A period of 10 to 40 minutes was selected to spin varying amounts of nanofiber webs.

The electrospun nanofibers were dried at room temperature for 12 hours. The nanofiber webs were deposited Au/Pd and then characterized using SEM microscopy (Phenom scanning electron microscope), which allowed us to observe the nanofibrous structures.

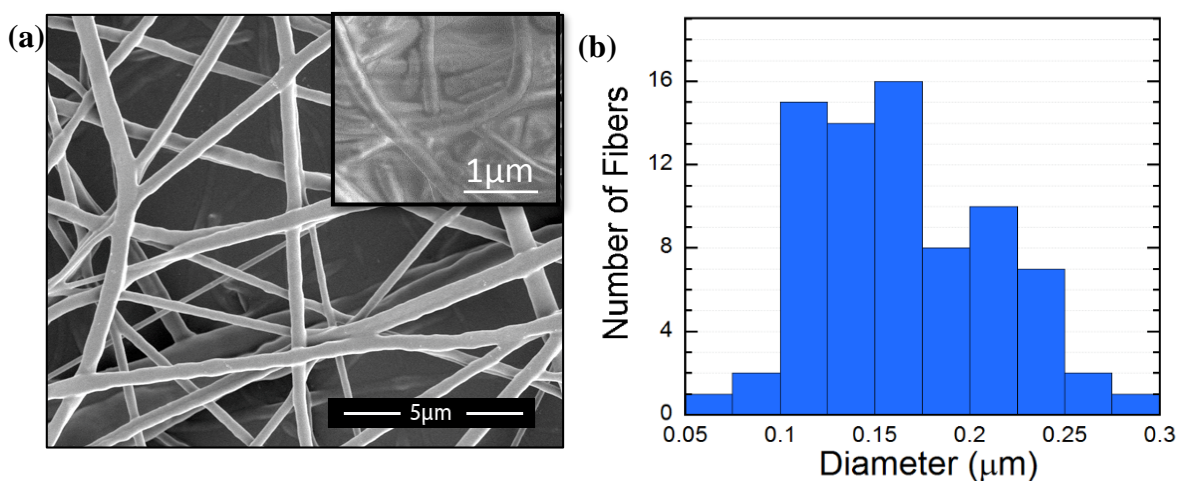


Figure 6.2 Analysis of an electrospun PU fiber web: (a) an SEM image of fibers (the nanofibers after mixing in to hexane solvent is shown in the inset image) and (b) analysis of fiber diameter distribution. Fibers had an average diameter of 125 nm.

Figure 6.2(a) is a representative image of an electrospun PU elastomer fiber web. As determined through scanning electron microscopy (SEM), the fibrous membrane consisted of

smooth fibers with a well-controlled average diameter of 125nm and a mean pore size of about 0.65 μm . The distribution of fiber diameter is plotted in Figure 6.2(b). The PU nanofiber webs were also mixed into hexane to test their endurance, and the nanofibers were collected and imaged to observe the effect of the hexane on their morphology. The inset image of Figure 6.2(a) illustrates the effect of the hexane on nanofibers. This and the other nanofiber images were analyzed using ImageJ software (developed by the National Institutes of Health, MA).

6.2.1.2 Matrix Materials

Chemically cross-linked PDMS was used as the matrix material in composite preparation. For this we used two types of elastomers, as Chapters 4 and 5 described in detail.

6.2.2 Composite Preparation

The elastomer composites were prepared through infusion of PDMS into PU nanofibers, which had been created through electrospinning. The preparation steps were as follows: Following the electrospinning process, the nanofiber web samples were placed in petri dishes without being separated from the aluminum foil film. The PDMS matrix was diluted with hexane as the solvent (at a 4:1 hexane:PDMS weight ratio) using a magnetic bar stirrer. A cross-linker and catalyst were then added to the PDMS solution to initiate elastomer network formation. This mixture was then poured into PU electrospun nanofiber webs that had been placed on petri dish molds 6 cm in diameter. Each petri dish substrate of PU nanofiber was filled with 2 mg of PDMS matrix, as shown in Figure 6.4(b). Filler concentration in the resulting PDMS elastomer composite fiber was approximately 1.25% to 5% weight. The

PDMS-infused nanofiber web composites were kept in sealed petri dishes at room temperature for three days to allow for curing at a controlled evaporation rate. They were then removed from the aluminum substrates. Their electrical, mechanical, electromechanical, and morphological properties were then characterized. Figure 6.3 provides a flowchart of the steps described above, and Figure 6.4 depicts them graphically.

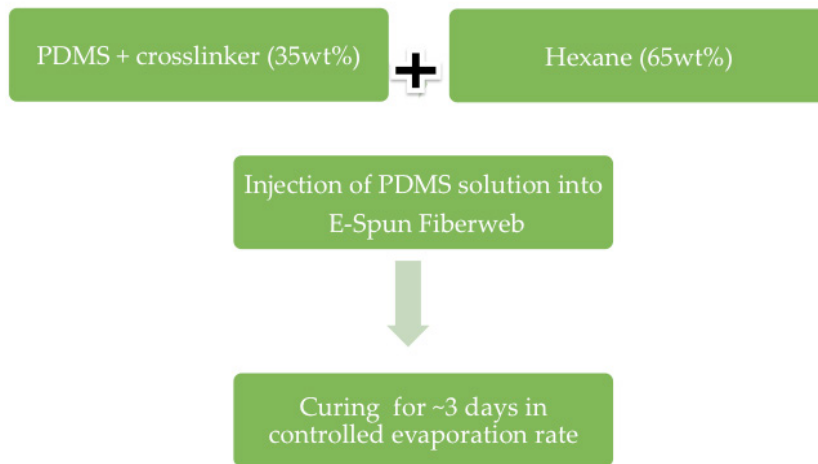


Figure 6.3 Preparation steps of the nanofiber composite elastomer films.

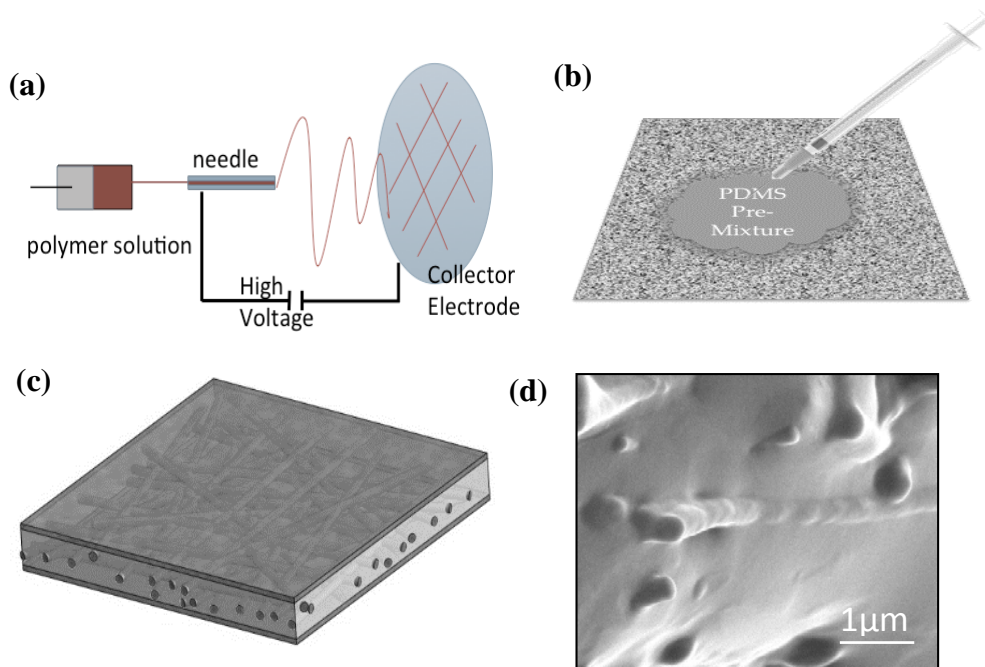


Figure 6.4 Preparation of nanofiber composite: (a) electrospinning of PU, (b) infusion of PDMS into PU fiber webs, (c) 3D schematic of final composite structure, and (d) cross-section image of elastomer composite; nanofibers and part of fibers are an apparent in the image.

6.1.1 Dielectric Characterization

The dielectric behavior of the composites was measured using an LCR meter (GW Instek LCR-8101G). A 12 mm-diameter parallel plate capacitor was created by applying silver paste electrodes (Chemtronics Circuit Works, Kennesaw, GA) to each side of the composites. The LCR meter was programmed to take capacitance measurements over a frequency range of 20 Hz to 10^6 Hz at room temperature, and the resulting impedance, capacitance, and resistance of the samples were reported at each frequency. The capacitance and dissipation

data for the blend samples were collected, and their dielectric constants were calculated using the following equation and the capacitance and thickness values:

$$\varepsilon = Ct/A \quad \text{Equation 6.1}$$

where C is capacitance, t is elastomer thickness, and A is electrode area. The real part of the relative dielectric constant was calculated from the capacitance measurement, and the dissipation factor was directly collected from the equipment.

6.2.3 Mechanical Characterization

The mechanical properties of the electrospun nanofiber composite elastomer films were analyzed through uniaxial tensile tests performed with a universal tensile tester MTS-30G (Instron, PA). The rectangular (10 mm by 50 mm) composite film strips were placed in instrument grips equipped with compressed air. The test speed was set to 5 mm/min, and the gauge length was set to 25 mm. The initial moduli of the composites were obtained from the initial region of stress-strain data.

6.2.4 Electromechanical Characterization

We tested the electromechanical properties of the matrix-infused electrospun fiber composite elastomers by constructing a circular actuator. The actuation strain and electrical breakdown properties of the composites were recorded as represented in Figure 6.1(b). The following procedure was used to prepare the actuator. A uniform prestrain of 30% was applied to the elastomer composites and held using a circular fixture. A circular active area was created at the center of each test specimen by applying compliant silver paste electrodes (Chemtronics CircuitWorks, Kennesaw, GA) on both sides of the specimen. The electrodes were extended

to copper leads with silver paste, and corner leads were connected to a high-voltage power supply (Bertan 225-30R, Spellman High Voltage Electronics Corp., Hauppauge, NY). The voltage trigger was controlled by LabVIEW computer software (National Instruments). The voltage was increased by 500 V/s until the specimen underwent dielectric breakdown. As the voltage was increased, video of the active area was also recorded using the same software and a FireWire video camera (DMK 23FM021, Imaging Source, NC). The video was analyzed frame by frame with ImageJ software (developed by the National Institutes of Health, MA). The radial dimension change of the active area was calculated from the relative pixel changes in the video.

6.2.5 Morphological Characterization

SEM imaging was utilized to understand the morphological properties of the nanofiber composite films. These films were cross-fractured in liquid nitrogen and then coated with 15nm of Au/Pd. A field-emission scanning electron microscope (FESEM), JEOL JSM-6400F, was operated at an accelerating voltage of 10 kV for morphological characterization.

6.3 Results and Discussion

This work was completed in two steps. The first step focused on the development of composites of matrix-infused nanofiber elastomers from a commercially available silicone matrix. The second step focused on the development of an elastomer matrix to improve actuator performance. The positive results reported were due to improvements in the interfaces between the nanofibers and the matrix, as evidenced by the mechanical and electrical properties of the PU nanofiber and PDMS composite films.

6.3.1 Morphology

PU nanofibers possess a high surface area-to-volume ratio. Because of this, when we incorporated them into our solution-cast silicone film, they exhibited a high surface area for adhesion, which had the potential to improve the composite's overall mechanical properties. The SEM images displayed in Figure 6.5(a-b) show fiber-reinforced film composites with nanofibers embedded in the silicone matrix. Both sides of the nanofibers are covered by the PDMS matrix, further indicating the successful incorporation of nanofibers into the silicone.

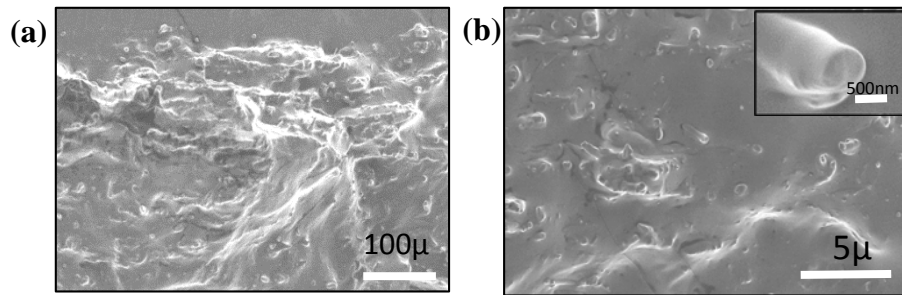


Figure 6.5 Cross-sectional view of the PU-PDMS nanofiber composite: (a) low-magnification view of a composite film's cross-section and (b) high-magnification image of composite films. Inset image shows a single PU electrospun fiber edge.

6.3.2 Dielectric Properties

Dielectric constant data and $\tan(\Delta)$ dissipation factor data were plotted for pure PDMS, pure PU, and the PU/PDMS nanofiber films (see Figure 6.6). All matrix-infused electrospun fiber composite elastomers showed significant improvement in dielectric constant with small amounts of nanofiber filler (maximum of 5 wt%).

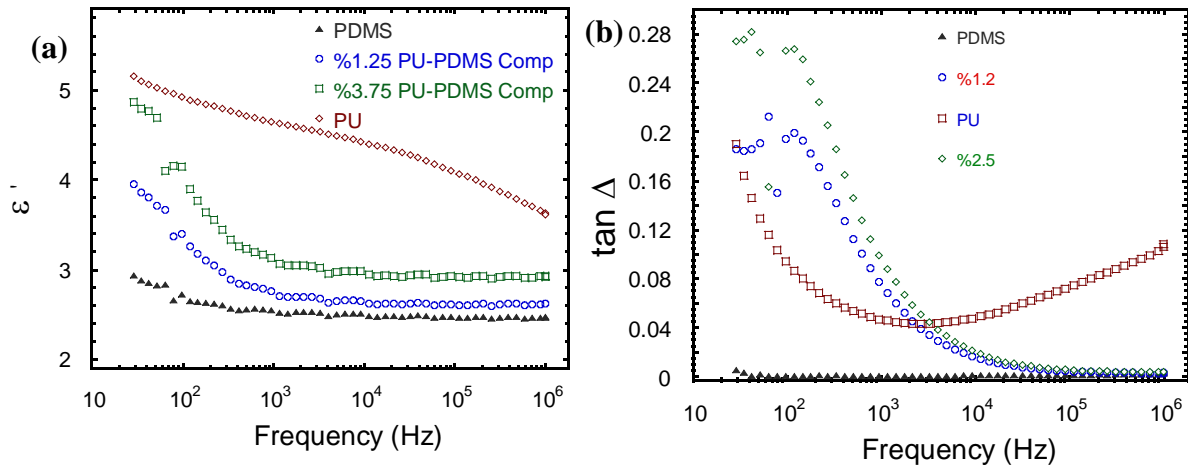


Figure 6.6 Dielectric properties of fiber-infused composites: (a) effective permittivity as a function of frequency; (b) dielectric loss factor, $\tan(\Delta)$, as a function of PU fibers.

As can be seen in the dielectric constant versus frequency plot in Figure 6.6(b), the composites' dielectric constants increased in both the high- and low-frequency regions. However, dielectric measurements taken at low frequencies were higher than those taken at high frequencies for all samples. At low frequencies, the dielectric constants of the composite elastomer films were found to be quite high for all weight concentrations. This can be explained by these materials' interfacial relaxation mechanism. The increase in interfacial area of the filler also increases the polarizations in the composites^{28,29}.

The composite and pure PU elastomer samples displayed higher dielectric dissipation than the neat PDMS at high frequencies. In the composites, dielectric constant decreased as frequency increased. Elastomer composites containing PU and the pure PU elastomer had higher dielectric losses than the pure PDMS elastomer at high frequencies; this behavior affected dielectric constant of composites and resulted in the dielectric constant decrease at

high frequencies. The increase in $\tan(\Delta)$ was high, especially for low-frequency dielectric measurements.

Since the improvement in effective permittivity was greater in the low-frequency region, we can infer that the interphase properties of these composites have a positive effect on dielectric properties. The results in the dielectric loss of the composites for low frequency was also high.

6.3.3 Mechanical Properties

The mechanical properties of nanofiber composites play a major role in actuation strain and in the energy density characteristics of fiber composite films. The mechanical properties of the neat and composite samples used in this study were also characterized and are shown in Table 6.1.

Table 6.1 Mechanical properties of the neat and composite film samples.

Sample	Tensile strength (MPa)	Strain at break (%)	Tensile modulus (MPa)	Tensile strength (MPa)	Strain at break (%)	Tensile modulus (MPa)
Neat PU web	5.8 ± 1.5	510 ± 125	2.29 ± 0.24			
Type	Type I			Type II		
Neat PDMS (control)	3.6 ± 0.7	500 ± 60	0.65 ± 0.11	2.2 ± 0.7	350 ± 52	0.18 ± 0.11
1.25 PU/PDMS type I composite	7.5 ± 1.2	660 ± 40	0.78 ± 0.21	6.5 ± 1.3	550 ± 40	0.45 ± 0.14
2.5 PU/PDMS type I composite	8.1 ± 1.2	720 ± 40	0.92 ± 0.15	7.1 ± 0.9	580 ± 40	0.65 ± 0.22
3.75 PU/PDMS type I composite	8.2 ± 1.2	740 ± 50	1.05 ± 0.25	7.5 ± 1.3	600 ± 50	0.85 ± 0.15

Inclusion of PU in the composites resulted in a significant increase in tensile strength compared to that of pure PDMS. As determined from stress-strain behavior, the initial modulus values for Type I and Type II neat PDMS were 0.65 MPa and 0.18 MPa, respectively. When PU was included at 1.25 wt%, these values increased to 0.78 MPa and 0.45 MPa. At the highest percentage weight of PU, 3.75 %, these values were 1.05 MPa and 0.95 MPa, respectively. Therefore, tensile modulus showed a significant increase as percentage of PU increased.

The Type I and Type II elastomer silicone films (e.g., neat PDMS) exhibited falling rate curves until failure occurred, with average tensile strengths of 3.6 ± 0.7 MPa and 2.2 ± 0.7 MPa, respectively. When PU was introduced, these increased, ranging from 7.5 ± 1.2 MPa

and 6.5 ± 1.3 MPa at 1.25 percentage weight to 8.2 ± 1.2 MPa and 7.5 ± 1.3 MPa at 3.75 percentage weight for Types I and II, respectively.

Likewise, as shown in Table 6.1, tensile strain increased with the introduction of PU into the composite. The PU fiber-reinforced silicone films showed linear curves from 0-300% strain; the curves then leveled off until failure. Pure Type I and Type II PDMS exhibited tensile strains of 500 ± 60 % and 350 ± 52 %, respectively. As percentage weight of PU in the PDMS blends increased and ranged from 1.25 to 3.75, Type I and Type II tensile strains ranged from $660 \pm 40\%$ to $740 \pm 50\%$ and $550 \pm 40\%$ to $600 \pm 50\%$, respectively.

The results of our study therefore confirm that the mechanical properties of the Type I and Type II silicone films improve significantly with the addition of PU nanofibers as nanofillers.

6.3.4 Electromechanical Properties

The previous section looked at the improvement in the mechanical properties of films that produced from nanofiber composites of PU and PDMS. This section will report the effects on the blends' electromechanical properties, summarized in Figure 6.7.

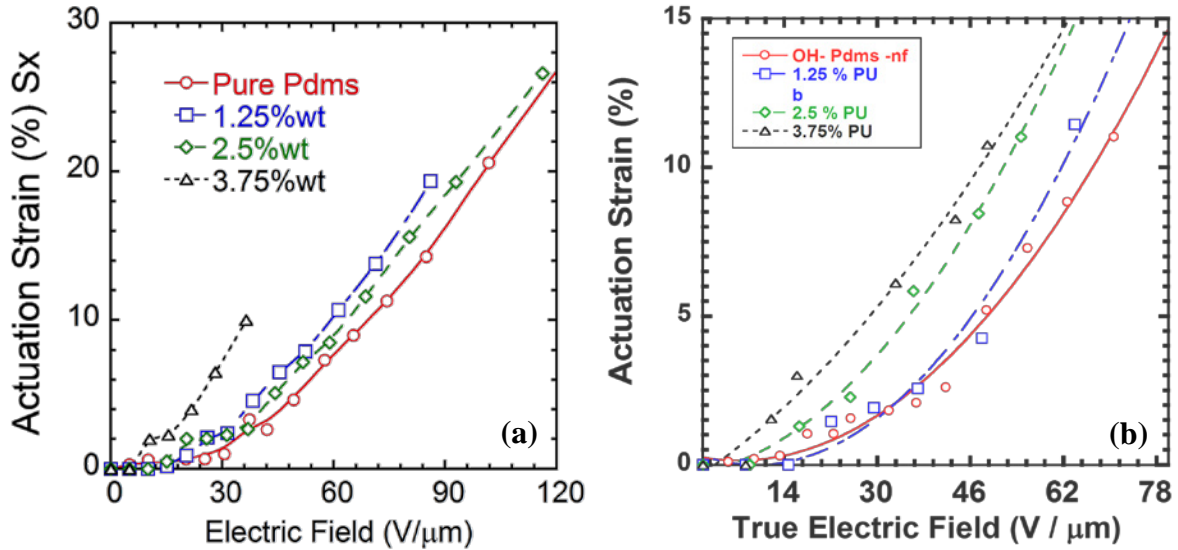


Figure 6.7 Actuation strain versus electric field for (a) Type I and (b) Type II PU/PDMS composite films.

For the Type I and Type II PDMS and composite elastomers created as part of our study, Figure 6.7(a-b) plot actuation strain (s_x) against true electric field. In general, the actuation strain results were similar to those for the control sample for all composite concentrations. However, composite dielectric strength decreased with increasing PU nanofiber filler weight concentration. The composites maximum actuation strain decreased from 20% to 10% with the increase in fiber weight concentration from 1.25% to 3.75%.

As shown in Figure 6.7(b), the actuation strain results for the Type II composite samples were also very similar to those for the control sample for all composite concentrations. Here too, composite dielectric strength decreased as PU nanofiber filler weight concentration increased. The maximum actuation strain of the composites decreased from 10% to 8% as fiber weight concentration increased from 1.25% to 3.75%.

All PU/PDMS composites showed lower dielectric strengths than that of pure PDMS. The dielectric strengths of these materials decreased further with the introduction of more PU nanofibers. The data used for calculations was recorded under the following conditions: ϵ_r was measured at 100 Hz, and Y was calculated at 30% strain of elastomers from stress-strain curves.

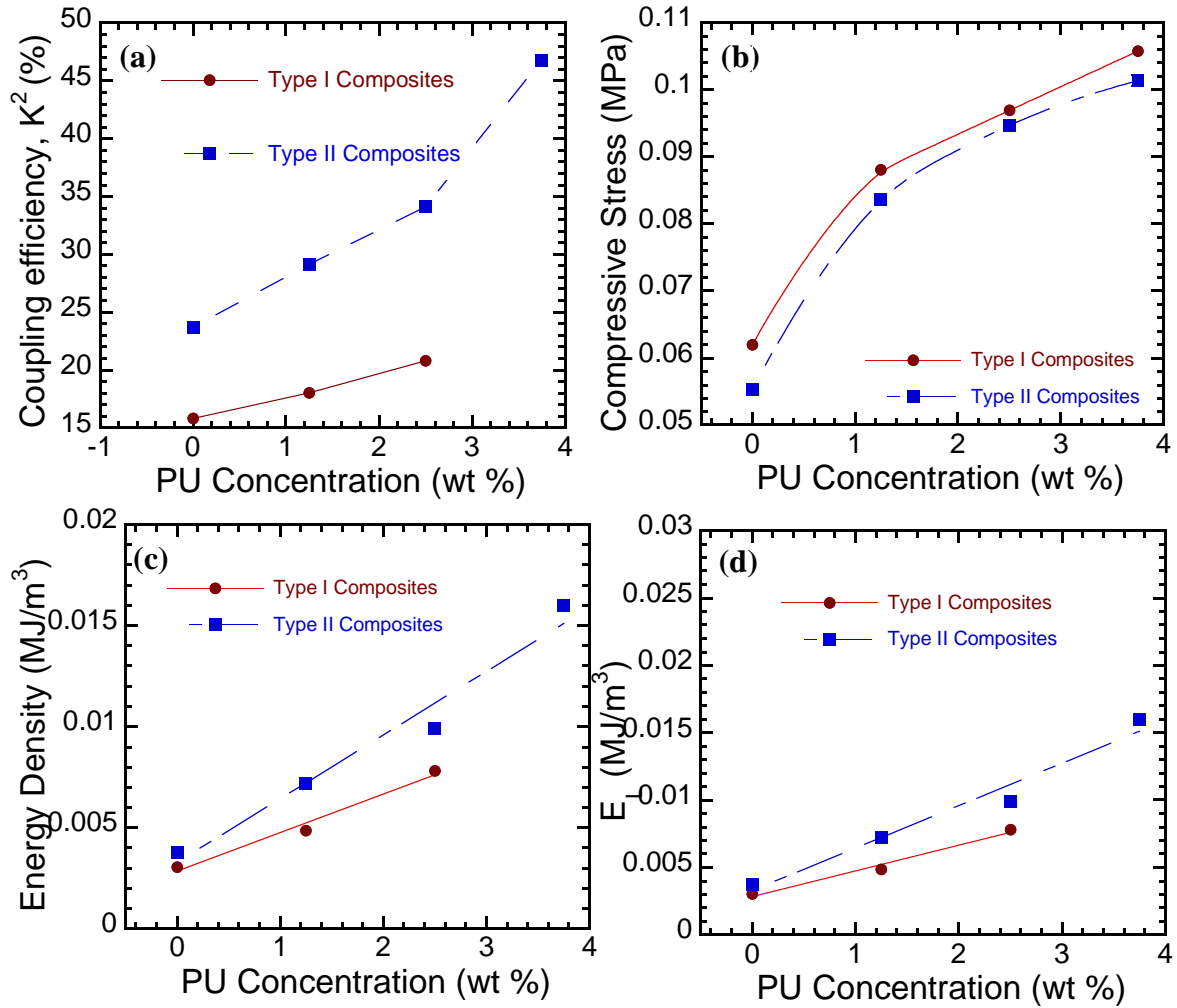


Figure 6.8 Plots of actuator performance of composites: (a) electromechanical coupling efficiency (K^2); (b) compressive (Maxwell) stress; (c) electromechanical energy density, as given by $[-P_{Maxwell}S_z/2]$ on a unit-volume basis; (d) electric energy density, E_L , $[-Y[s_z - \ln(1 + s_z)]]$, displayed in terms of PU weight concentration. For all plots, the magnitude of the electric field was 50 V/ μm . The lines serve as visual guides to eye.

Another important metric by which to evaluate the performance of a D-EAP actuator is electromechanical coupling efficiency, which is similar to energy conversion efficiency.

Figure 6.8(a) provides a plot of coupling efficiency as a function of PU weight concentration

for the Type I and Type II composites created in the course of this study. For both Type I and Type II PDMS, Figure 6.8(a) plots the coupling efficiencies of the composites and of pure PDMS, which acted as the control in this analysis. Pure Type I PDMS had a coupling efficiency of 15.82%, and the Type I composites with 1.25% and 2.5% concentrations of PU exhibited coupling efficiencies of 18.04 and 20.79%, respectively.

The composites made from Type II PDMS exhibited a similar improvement in coupling efficiency. With a K for pure Type II PDMS of 23.71%, the K^2 values of the composites with 1.25%, 2.5%, and 3.5% concentrations of PU were 29.16%, 34.13%, and 46.78%, respectively. Noting that the 3.5%-concentration composite exhibited almost a 100% increase in coupling efficiency over the pure Type II PDMS sample.

Both the Type I and Type II composites showed a similar improvement in Maxwell stress, or compressive pressure, over the pure PDMS control at 50 V/ μm . These values for pure Type I and Type II PDMS were 0.0620 MPa and 0.0553 MPa, respectively. The Type I composites' values ranged from 0.0881 MPa at 1.25% concentration PU to 0.1058 MPa at 3.5% concentration PU. The Type II composites exhibited slightly lower values, ranging from 0.0836 MPa at 1.25% concentration PU to 0.1013 MPa at 3.5% concentration PU. For both Type I and Type II composites, therefore, Maxwell stress was an increasing with the increasing concentration of PU.

Composite energy density also increased as a function of increasing concentration of PU (see Figure 6.8(c)), and Type II values always exceeded Type I values. For Type I and Type II pure PDMS, energy density was $3.30\text{E-}05$ MJ/m³ and $5.06\text{E-}05$ MJ/m³, respectively. For the

Type I composites, energy density ranged from 3.78E-05 MJ/m³ at 1.25% concentration PU to 4.4E-05 MJ/m³ at 2.5% concentration PU. Type II composite energy density ranged from 5.062E-05 MJ/m³ at 1.25% concentration PU to 10.81E-05 MJ/m³ at 3.75% concentration PU. As can be seen in Figure 6.8(c), energy density increased at a constant rate until 2.5% concentration PU; it then increased sharply at 3.75% concentration PU, at which point it represented greater than a 100% improvement over the pure PDMS sample's energy density.

Electromechanical sensitivity, β , was calculated using Equation 5.13. The electromechanical sensitivities for the Type I and Type II composites were compared to their corresponding pure PDMS control samples using the following formula:

$$\beta_r = \frac{\beta}{\beta_{PDMS}} \quad \text{Equation 6.2}$$

where β is the electromechanical sensitivity of a composite, β_{PDMS} is the electromechanical sensitivity of the pure PDMS material (Type I, 0.0030; Type II, 0.0020), and β_r is the relative electromechanical sensitivity of the composite to that of the pure PDMS sample. Calculated using data recorded under the following conditions: ε_r was measured at 1000 Hz, and Y was measured at 0% or 0.5% strain.

As with the other measures of physical properties discussed, β was an increasing with the increasing PU wt% in the composite. Among Type I composites, β_r ranged from 1.59 for the 1.25% concentration PU composite to 2.57 for the 2.5% concentration PU composite. The improvement in electromechanical sensitivity was even more pronounced for the Type II composites: The 1.25% concentration sample exhibited a value 4 times that of Type II pure

PDMS, the 2.5% concentration 8 times that of pure PDMS, and the 3.75% concentration 27 times that of pure PDMS. This increase represented a near exponential rate of growth in β as a function of PU wt% concentration.

The actuation performance for nanofiber composites were compared to other composite dielectric elastomer actuators in Table 6.2. According to this table, we can conclude that nanofiber PU/PDMS nanocomposites present a higher dielectric strength and lower Young's modulus than ceramic-elastomer composites. PU/PDMS composites also showed a higher dielectric strength than conductive filler-elastomer composites.

Table 6.2 Mechanical properties of the neat and composite film samples.

Type (specific)	Modulus (Mpa)	ϵ_r	Concentration (%)	$E_{\text{Breakdown}}$ (V/ μm)	Maximum strain (%)	Prestrain (%)
VHB4910 ²⁶	2	4.7	—	~235	60	300
PDMS	1.270	2.5	—	40	12	30
PDVB@PANi-PDMS ²⁷	5.4	7.7	42.3		11	30
(CB-BaTiO ₃)/PDMS ²⁸	1.9	10	CB 0.03, BT 0.60(wt)	30	6.1	30
P3HT-PDMS ²⁹	0.046	14	6 (wt)	8.5	0.02	0
PMN-PDMS ³⁰	17.3	36	108.1		<7	-
Dipoles-PDMS(Sylgard 184) ³¹	0.85	6.15	10,7	61	~2.8	-
Dipoles-PDMS(Elastosil) ³¹	0.14	5.56	10.7	30.7	~2.5	-
PDMS-PDVB ³²	11.7	~7.7	max:31.7(vol)	50	0.85	-
PDMS-PDVB ³²	0.5	~3.3	optimum:15 (vol)	50.9	10	-
PU-PDMS (in-situ syn) ³³		~16, tan Δ >1	40 (wt)	5.5	2.5	-
PU-PDMS (PU as nanofibers)	~0.9	~4.6	3.75 (wt)	45	10	30
BaTiO ₃ -PDMS	12.8	39.3	205.5		2.6	-
TiO ₂ -PDMS ³⁴	0.85	4.9	9 (vol)	60	~8	-
TiO ₂ -PDMS (plasticized) ³⁴	~0.2	3.8	4 (vol)	35	18	-
PZT - TPE ³⁵	~0.1	~6	80 (wt)	20.6	~7	-

The data have been reported from cited references for conditions that result in the best actuation behavior.

6.4 Conclusions

In this chapter, we described our fabrication of solution-cast PDMS film reinforced with electrospun polyurethane nanofiber and discussed the electromechanical, mechanical, dielectric, and morphological properties of the resulting composite films. PDMS was solution-cast inside

PU nanofibers. The dielectric constant and Young's modulus of the nanofiber composite films were increased. The dielectric properties and mechanical properties influenced actuator performance. The nanocomposite elastomers had desirable dielectric constant values but high dielectric loss; the dielectric strength of the composite films decreased with increasing percentage of nanofiber composition.

In summary, we have shown that nanofiber composites were able to improve the actuation behavior of PDMS elastomers in terms of coupling efficiency and energy density at a given electric field. These nanofiber composite elastomers can be produced and used in many engineering applications.

6.5 References

1. Bar-Cohen, Y. Electroactive polymer (EAP) actuators as artificial muscles. (SPIE Press, 2004).
2. Pelrine, R., Kornbluh, R., Pei, Q. & Joseph, J. High-speed electrically actuated elastomers with strain greater than 100%. *Science* **287**, 836–839 (2000).
3. Zhang, Q. M. et al. An all-organic composite actuator material with a high dielectric constant. *Nature* **419**, 284–287 (2002).
4. Baughman, R. H. *et al.* Carbon nanotube actuators. *Science* **284**, 1340–1344 (1999).
5. Mirfakhrai, T., Madden, J. D. W. & Baughman, R. H. Polymer artificial muscles. *Mater. Today* **10**, 30–38 (2007).
6. Shankar, R., Ghosh, T. K. & Spontak, R. J. Dielectric elastomers as next-generation polymeric actuators. *Soft Matter* **3**, 1116 (2007).

7. Carpi, F., Gallone, G., Galantini, F. & De Rossi, D. *Enhancing the dielectric permittivity of elastomers*. (Elsevier, 2008).
8. Brochu, P. & Pei, Q. Advances in dielectric elastomers for actuators and artificial muscles. *Macromol. Rapid Commun.* **31**, 10–36 (2010).
9. Biddiss, E. & Chau, T. Dielectric elastomers as actuators for upper limb prosthetics: challenges and opportunities. *Med. Eng. Phys.* **30**, 403–418 (2008).
10. Goulbourne, N., Frecker, M. I., Mockensturm, E. M. & Snyder, A. J. Modeling of a dielectric elastomer diaphragm for a prosthetic blood pump. in **5051**, 319–331 (2003).
11. Ahnert, K., Abel, M., Kollosche, M., Jørgensen, P. J. & Kofod, G. Soft capacitors for wave energy harvesting. *J. Mater. Chem.* **21**, 14492–14497 (2011).
12. Florian, P., Jena, K. K., Allauddin, S., Narayan, R. & Raju, K. V. S. N. Preparation and characterization of waterborne hyperbranched polyurethane-urea and their hybrid coatings. *Ind. Eng. Chem. Res.* **49**, 4517–4527 (2010).
13. Liu, H., Kameoka, J., Czaplewski, D. A. & Craighead, H. G. Polymeric nanowire chemical sensor. *Nano Lett.* **4**, 671–675 (2004).
14. Liu, H., Reccius, C. H. & Craighead, H. G. Single electrospun regioregular poly(3-hexylthiophene) nanofiber field-effect transistor. *Appl. Phys. Lett.* **87**, 253106 (2005).
15. Li, Y. *et al.* Ultra-low dielectric performance of polymer electrospun nanofiber mats. *Appl. Phys. A* **100**, 207–212 (2010).
16. Dagdeviren, C. & Papila, M. Dielectric behavior characterization of a fibrous-ZnO/PVDF nanocomposite. *Polym. Compos.* **31**, 1003–1010 (2010).

17. Liu, H. *et al.* Carbon nanotube array/polymer core/shell structured composites with high dielectric permittivity, low dielectric loss, and large energy density. *Adv. Mater.* **23**, 5104–5108 (2011).
18. Tijing, L. D. *et al.* Improved mechanical properties of solution-cast silicone film reinforced with electrospun polyurethane nanofiber containing carbon nanotubes. *Appl. Surf. Sci.* **264**, 453–458 (2013).
19. Li, X. *et al.* Preparation and dielectric property investigation of ferrocene/poly(vinyl pyrrolidone) composite membranes. *J. Nanosci. Nanotechnol.* **9**, 704–708 (2009).
20. Bashouti, M., Salalha, W., Brumer, M., Zussman, E. & Lifshitz, E. Alignment of Colloidal CdS Nanowires Embedded in Polymer Nanofibers by Electrospinning. *ChemPhysChem* **7**, 102–106 (2006).
21. Khan, W. S., Asmatulu, R. & Eltabey, M. M. Dielectric properties of electrospun pvp and pan nanocomposite fibers at various temperatures. *J. Nanotechnol. Eng. Med.* **1**, 041017–6 (2010).
22. Im, J. S., Kim, J. G., Lee, S.-H. & Lee, Y.-S. Effective electromagnetic interference shielding by electrospun carbon fibers involving Fe₂O₃/BaTiO₃/MWCNT additives. *Mater. Chem. Phys.* **124**, 434–438 (2010).
23. Vijayakumar, G. N. S., Devashankar, S., Rathnakumari, M. & Sureshkumar, P. Synthesis of electrospun ZnO/CuO nanocomposite fibers and their dielectric and non-linear optic studies. *J. Alloys Compd.* **507**, 225–229 (2010).
24. Li, W. K. & Wong, Y. W. Electrical properties of electrospun nanofibers of peo/carbon black composite. *Solid State Phenom.* **151**, 67–71 (2009).
25. Chanmal, C. V. & Jog, J. P. Electrospun PVDF/BaTiO₃ nanocomposites: polymorphism and thermal emissivity studies. *Int. J. Plast. Technol.* **15**, 1–9 (2011).

26. Kornbluh, R. D., Pelrine, R., Pei, Q., Oh, S. & Joseph, J. Ultrahigh strain response of field-actuated elastomeric polymers. in *Smart Structures and Materials 2000: Electroactive Polymer Actuators and Devices (EAPAD)* (ed. Bar-Cohen, Y.) **3987**, 51–64 (SPIE, 2000).
27. Liu, L. W., Kang, W. M. & Cheng, B. W. Preparation of polyurethane (PU)/polyaniline (PANI) compound nanofiber via electrospinning. *Adv. Mater. Res.* **332**, 1352–1356 (2011).
28. Zhao, H., Xia, Y.-J., Dang, Z.-M., Zha, J.-W. & Hu, G.-H. Composition dependence of dielectric properties, elastic modulus, and electroactivity in (carbon black-BaTiO₃)/silicone rubber nanocomposites. *J. Appl. Polym. Sci.* **127**, 4440–4445 (2013).
29. Carpi, F., Gallone, G., Galantini, F. & De Rossi, D. Silicone-poly(hexylthiophene) blends as elastomers with enhanced electromechanical transduction properties. *Adv. Funct. Mater.* **18**, 235–241 (2008).
30. Yang, D. *et al.* Lead magnesium niobate-filled silicone dielectric elastomer with large actuated strain. *J. Appl. Polym. Sci.* **125**, 2196–2201 (2012).
31. Risse, S., Kussmaul, B., Krüger, H. & Kofod, G. A versatile method for enhancement of electromechanical sensitivity of silicone elastomers. *RSC Adv.* **2**, 9029–9035 (2012).
32. Molberg, M. *et al.* High Breakdown Field Dielectric Elastomer Actuators Using Encapsulated Polyaniline as High Dielectric Constant Filler. *Adv. Funct. Mater.* **20**, 3280–3291 (2010).
33. Gallone, G., Galantini, F. & Carpi, F. Perspectives for new dielectric elastomers with improved electromechanical actuation performance: composites versus blends. *Polym. Int.* **59**, 400–406 (2010).

34. Zhao, H., Wang, D.-R., Zha, J.-W., Zhao, J. & Dang, Z.-M. Increased electroaction through a molecular flexibility tuning process in TiO₂-polydimethylsilicone nanocomposites. *J. Mater. Chem. A* **1**, 3140 (2013).
35. Molberg, M. *et al.* Elastomer actuators: systematic improvement in properties by use of composite materials. in **7642**, 76420M-76420M-9 (2010).

CHAPTER 7 Summary and Future Work

7.1 Summary

The aim of this research was to investigate elastomer blends and composites with respect to their applicability in dielectric elastomer actuators. The main goal was to develop soft nanocomposite elastomer materials with enhanced electromechanical response and improved actuation strain. In this context, we evaluated the use of the high-relative permittivity polymer polyurethane (PU) as filler and the low-elastic modulus and high-electric breakdown polymer polydimethylsiloxane (PDMS) as matrix. These PDMS materials were then further developed to improve the performance of the blends and composites. The approaches described here can aid in the development of useful materials with enhanced energy densities and electromechanical response for use in actuator applications.

Specifically, in this work, PU/PDMS dielectric elastomer actuator polymers (D-EAPs) were fabricated with different concentrations of PU, in a higher dielectric constant and enhanced electromechanical response. Polymer film fabrication from blends and fiber composites were performed. In both preparation methods, materials were commercially available and formulated elastomer.

We were able to obtain a substantial increase in relative permittivity, up to 70%, and in electrostatic energy density, up to 230%, while still sustaining very low dielectric loss. PU-PDMS blends and composites are suitable for energy-efficient applications requiring low electric fields, such as micro-robotic systems, micro-fluidic/haptic/biomedical devices (e.g., active braille and steerable catheters), and smart prosthetics.

7.2 Future Work

From the information collected and discussed in this study, a number of challenges and recommendations for future work can be identified. The successful design of enhanced energy density of nanocomposites based on use of high-permittivity PU requires detailed investigation of the structure of the polymer filler interface. This is particularly true for nanofiber composites, whose high surface area-to-volume ratio makes the interface critical in the determination of functional properties. Understanding the interactions in the interface of constituents will provide an opportunity to tailor the electromechanical properties of the nanocomposites. For example, enhanced compatibility between polymers could have a positive effect on the dielectric permittivity and electric breakdown strength of blends and composites.

Incorporating other polymer fillers that have high polarizability (e.g., PVDF and LC polymers, fluoropolymers, or copper metallocenes) or high conductivity (e.g., carbon or metal nanoparticles) would increase the dielectric constant of these fiber webs tremendously. The use of composite fibers in elastomer matrices can be expected to increase dielectric constant and mechanical properties of composite films. Such composites would show a low dielectric loss because of not percolating filler arrangement. The phase behavior of these suggested blends and composites can be studied to understand the chemistry and structures of the polymer-polymer and polymer-nanofiller interfaces.

Subramani et al.¹ recently demonstrated the production of Anisotropic D-EAP with tunability (ADEPT) composites using acrylic elastomer as matrix and various fibrous materials as reinforcements. The fibers were chosen to represent a wide range of mechanical and

dielectric properties as well as high dielectric permittivity. In an approach similar to theirs, unidirectional nanofiber-reinforced composites could be fabricated through a solvent-casting method. The electrospinning method can easily produce aligned nanofibers and so can be simply and easily applied into dielectric elastomer actuator fabrication method. Ultimately, the method of nanofiber composite production can be used with a wide variety of polymer fibers with fillers and matrices to meet the requirements of many applications.

7.3 References

1. Subramani, K. B., Cakmak, E., Spontak, R. J. & Ghosh, T. K. Enhanced electroactive response of unidirectional elastomeric composites with high-dielectric-constant fibers. *Adv. Mater.* **26**, 2949–2953 (2014).